Constraints on the Origin of Magnetic White Dwarfs

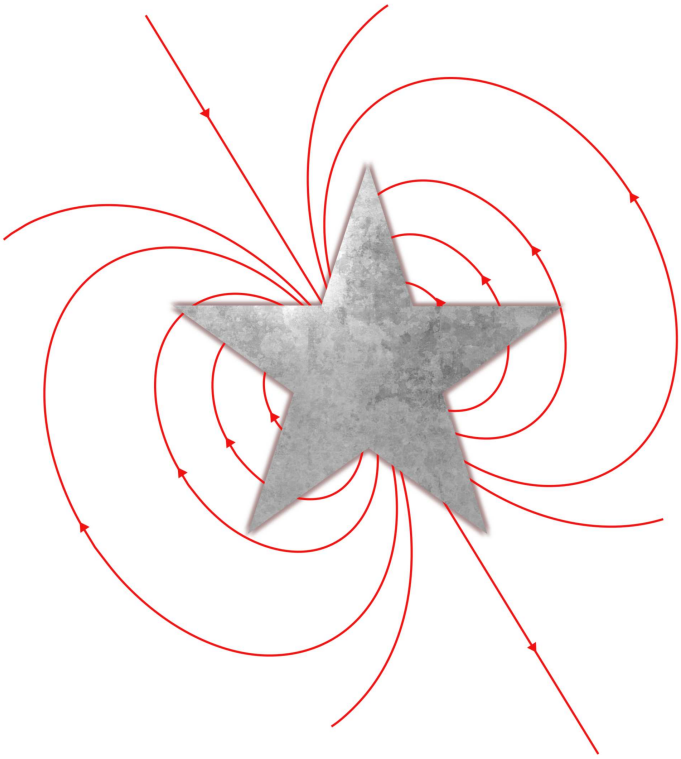

Referees: Priv-Doz. Stefan Jordan

Prof. Dr. Ralf Klessen

Dissertation

submitted to the

Combined Faculties of the Natural Sciences and Mathematics

of the Ruperto-Carola-University of Heidelberg, Germany

for the degree of

Doctor of Natural Sciences

Put forward by

Baybars Külebi

born in: Ankara, Turkey

Oral examination: 17^{th} December, 2010

Zusammenfassung

Das zentrale Thema dieser Arbeit ist das häufigste Endprodukt der Entwicklung magnetischer Sterne, die Magnetischen Weißen Zwerge (MWZe). Verbesserte statistische Untersuchungen, die auf neueren Himmelsdurchmusterungen sowie sehr präzisen Beobachtungen einzelner besonderer MWZe basieren, bieten die Möglichkeit, verschiedene Hypothesen zur Entwicklung dieser Objekte zu testen. Im ersten Teil unserer Arbeit identifizieren wir wasserstoffreiche MWZe (DAHs) im Sloan Digital Sky Survey (SDSS) und untersuchen die Bevölkerungsstatistik aller bekannten DAHs im SDSS. Zusätzlich untersuchen wir die Entwicklungsgeschichte einiger dieser Objekte mit Hilfe von Beobachtungen ihrer Doppelsternbegleiter oder aufgrund von deren Mitgliedschaft in Offenen Sternhaufen. Im zweiten Teil unserer Arbeit untersuchen wir den einzigartigen MWZ REJ 0317-853 mittels Messungen seiner Parallaxe mit dem *Hubble*-Weltraumteleskop und durch die zeitaufgelöste Modellierung der Spektren und Polarisationsbeobachtungen. Wir zeigen, daß die Annahme eines zentrierten Dipols für die Geometrie des Magnetfeldes für mehr als die Hälfte der untersuchten Objekte falsch ist; dies gilt insbesondere für den außergewöhnlichen Weißen Zwerg REJ 0317-853, welcher während einer Rotationsphase ein sehr homogenes Magnetfeld zeigt. Dies wird auch durch die erste Beobachtung von Zyklotronabsorption im Polarisationsspektrum eines Weißen Zwerges gestützt, die von uns mit Hilfe eines neuen selbstkonsistenten Models für die physikalische Behandlung dieses Absorptionsprozesses erklärt werden konnte. Darüberhinaus untersuchen wir den möglichen Einfluß des Magnetfeldes auf den Massenverlust während der Sternentwicklung und auf die Struktur des Sternes, was für das Verständnis der Natur des massereichen Weißen Zwerges REJ 0317-853 wichtig ist.

Abstract

The central theme of this work is the most frequent final stage of the evolution of magnetic stars, the Magnetic White Dwarfs (MWDs). Improved statistical investigations coming from new surveys and very precise observations of unique MWDs offer the possibility to test various hypotheses on the evolution of these objects. In the first part of our work we identify hydrogen-rich MWDs (DAHs) in the Sloan Digital Sky Survey (SDSS) and investigate the population statistics of all known DAHs in the SDSS. Additionally, we investigate the evolutionary histories of a few of these objects using constraints from the observations of their binary counterparts or through their membership in open clusters. In the second part of our work, we investigate the unique MWD REJ 0317-853, by a parallax measurement with the *Hubble* Space Telescope and by time resolved spectro-polarimetric modeling. We show that the assumption of centered magnetic dipoles for the field geometry is not correct for more than half of the objects in our sample; this is in particular true for REJ 0317-853 which shows a very uniform field during one rotation phase. This is validated by the first observation of cyclotron absorption in the polarization spectrum of a white dwarf, which is explained with a new model for the self-consistent physical treatment of this absorption process. Furthermore, we study the possible influence of magnetism on the mass loss during the stellar evolution and on the structure of the star which is of importance to understand the nature of the massive white dwarf REJ 0317-853.

"Wer baute das siebentorige Theben?
In den Büchern stehen die Namen von Königen.
Haben die Könige die Felsbrocken herbeigeschleppt?"

"Who built Thebes of the seven gates?
In the books you find the names of kings.
Did the kings haul up the lumps of rock?"

Bertold Brecht - "Fragen eines lesenden Arbeiters"

Contents

Introduction

Magnetic White Dwarfs

"Dumpster diving" would be the best way to describe white dwarf astrophysics. As stellar remnants they are the locked up masses of the galaxy, destined not to contribute anymore to the galactic evolution which warrants the "dumpster" or "trash" analogy. In fact more than 95-98 percent of the stars in our Galaxy are expected to become white dwarfs, hence as a population they carry important information on the stellar population and the environment of their origin. This implies, a better understanding of white dwarfs provides us with an improved picture of stellar evolution and the population of stars they succeed such as the globular and open cluster. Investigating the properties of white dwarfs has the potential to constrain the origin and evolution of our Galaxy (Koester & Weidemann, 1980). According to the current picture of stellar evolution, low to intermediate-mass hydrogen-burning stars ($0.8 - \sim 9\ \mathrm{M}_{\odot}$) are expected to end their life passively, shedding their envelopes and finally ending up with electron degenerate cores, unlike the heavier mass stars where the remnants are formed after a violent explosion (Weidemann, 2000, and references therein).

The interest on white dwarfs transcend the field of stellar evolution since they provide cosmic laboratories for matter under terrestrially unattainable conditions. Historically the existence of white dwarfs, have been the macroscopic demonstration of Pauli's principle and degenerate matter which obey Fermi-Dirac statistics. This qualifies the discovery of white dwarfs as the archetypal case for astrophysical tests of contemporary new theories. The uniqueness of the work of Chandrasekhar (1931), namely applying forefront physics to astrophysical questions, prompted Landau (1932) to predict the existence of stars supported by degenerate pressure of atomic nuclei which later became to be known as neutron stars. In addition to the extreme conditions in the white dwarf cores, at least ten percent of the white dwarf population show magnetic features up to field strengths 10^9 G (Wickramasinghe & Ferrario, 2000). This fact also makes them testbeds for calculations of atomic physics under the influence of magnetism, since these field strengths are hard to attain under lab conditions (the current limit for the implosive devices is about $20\,\mathrm{MG}$).

The relatively simple interiors and atmospheres of white dwarfs, allow for precise diagnostics of stellar parameters. Although faint, white dwarfs are observable in a large window of wavelength and this allows direct numerous possibilities for observing he surface structure. Observations combined with the advances in the spectral modeling of stellar atmospheres, yield reliable estimations on effective temperatures, surface gravities, element abundances, and indirectly provide information on masses, radii, and ages. The high accuracy modeling of white dwarf spectra which has confidence to the level of approximately 1% or even better of the absolute flux, prompts interest from various astronomical communities (Koester, 2002). One of the direct applications is the role white dwarfs as calibration

standards for spectrographs on spacecrafts such as International Ultraviolet Explorer (IUE), the *Hubble* Space Telescope (HST), the Extreme Ultraviolet Explorer (EUVE), the Far Ultraviolet Explorer (FUSE).

The precise age assessments of white dwarfs designates them as cosmochronometers (Winget et al., 1987). They can be used for determining the ages of specific populations, namely clusters or different components of the galaxy; be it thin disk, thick disk or halo. The usage of luminosity functions of white dwarfs have the potential to not only constrain the age of our galaxy but also yield information on the stellar formation history and the initial mass function.

White dwarfs are also identified as the progenitors of Supernova Ia (SNIa) explosions which are instrumental in observational cosmology due their property as standard candles (see e.g. Hillebrandt & Niemeyer, 2000). The investigations of white dwarf evolution, especially for the case of progenitor systems have been a topic of interest for the Supernova science. Although the underlying principles are well known, the theoretical uncertainties in the explosion mechanisms of SNIa and the necessity for lightcurve calibrations, provides further incentive on investigations on the structure of white dwarfs.

One subset of the whole white dwarf population is the class of magnetic white dwarfs (MWDs). White dwarfs with magnetic field strengths of between 10^4 and 10^9 G are understood to represent more than 10% of the total population of white dwarfs if observational biases are considered (Liebert et al., 2003; Kawka et al., 2007). Although not as exotic as neutron stars or black holes, they have the advantage of observability at multiple bands. The existence of circular polarization observations and detailed magnetic modeling enables the precise investigation of the surface magnetic fields.

There are multiple hypothesis for the origin of these objects. One of them, the "fossil field" hypothesis suggests that magnetic fields are products of an earlier stage of stellar evolution. In this picture, the field strengths are amplified due to the contraction of the core, during which the magnetic flux is conserved to a major extent. From the perspective of this hypothesis, chemically peculiar Ap and Bp stars were proposed to be the progenitors of MWDs (Angel et al., 1981).

The "fossil field" hypothesis has certain problems, the most important one being the incommensurable incidence of the magnetism in different stages of the stellar evolution. Namely, the inferred incidence of MWDs with respect to the total white dwarf population outnumbers the incidence of Ap/Bp stars within the A/B population (Kawka et al., 2007). One other problem of the fossil field hypothesis is the relatively massive nature of the MWDs (Liebert, 1988; Vennes & Kawka, 2008). While the mean value of the masses of the MWDs is $\sim 0.93\ \mathrm{M}_{\odot}$, the mean mass of the non-magnetic white sample is $\sim 0.56\ \mathrm{M}_{\odot}$ (Liebert, 1988). It has been suggested that this could be a result of the influence of magnetism on the mass loss. This possibility was tested by Wickramasinghe & Ferrario (2005) via population synthesis. Their conclusion was that current number distribution and masses of high-field magnetic white dwarfs (HFMWDs, $B \geq 10^6\,G$) are not mainly due to an inclusion of a modified IFMR but rather by assuming that $\sim 10\%$ of A/B stars have unobservable small scale magnetic fields.

The competing picture can be lumped into the wide category of dynamos which is expected to occur; during the red giant phase due to convective motions (Thompson & Duncan, 1993), during binary mergers of two double degenerates (Ferrario et al., 1997), or during a Common Envelope (CE) evolution for close binaries (Tout et al., 2008). The most recent and promising model is based on the CE phase that the cores of giants experience,

which is expected to occur during the evolution to the cataclysmic variables. During this phase, the orbital angular momentum is transferred to the envelope as the two cores spiral in toward each other. This process causes both differential rotation and convection within the CE, which are the key ingredients of magnetic field generation (see Tout et al., 2008, and references therein).

This Work

The answer to the question of the origin of MWDs depends on two different approaches: The first one relies on the analysis of the whole population of MWDs. Secondly, the detailed analysis of unique MWDs with as many possible observational methods and consistent physical models. By that proposed formation channels can be tested. In this work we hope to shed light on the origin of MWDs through new observations, methodology and theoretical additions to the spectral modeling.

The detailed outline of the thesis is as follows:

We start by describing the necessary theoretical framework to translate the observables to stellar parameters of white dwarfs. In Chapter 1, we will introduce the basic concepts through a historical treatise of white dwarfs, magnetic white dwarfs and the spectral classifications. Then an outline of the theory of white dwarfs will be presented, for the topics concerning the rest of this work. We will derive the historically important equations of white dwarf structure and basic cooling theory of white dwarfs, which will be followed by a discussion on the recent recent developments in the theory of white dwarf evolution. In the second part of this Chapter, we will introduce the polarized radiative transfer and the magnetic atmospheric modeling which is the most important tool in this work for estimating stellar parameters from the observations.

The first necessary ingredient for determining the properties of MWDs as a population, are most certainly observational data which, at this time provided abundantly by the Sloan Digital Sky Survey (SDSS). We will undertake the analysis of 97 known (Gänsicke et al., 2002; Schmidt et al., 2003; Vanlandingham et al., 2005) and 44 new hydrogen-rich MWDs in Chapter 2. The consistent modeling of a large number of MWDs will provide us with the opportunity to investigate the distribution of magnetic fields and the magnetic geometry. This will enable us to test the fossil field hypothesis from the perspective of the field geometry for the first time. This Chapter is based on Külebi et al. (2009).

The investigation undertaken in Chapter 2 relies solely on the magnetic field and the effective temperature information of the sample, which is not enough for an investigation of evolutionary histories. In Chapter 3 we rectify this deficiency by introducing two methods to estimate the distance of MWDs in the absence of a parallax measurement. These method enables us to estimate the radius of the MWDs, which in turn can be used to calculate the mass and the cooling age through theoretical input. We apply the two methods namely, cluster membership and common proper motion association of the MWDs to apply this method and discuss their individual evolutionary histories. Part of this Chapter is based on Girven et al. (2010) and discusses their results in detail.

In Chapter 4 we make a short detour to consider the free-free absorption in the MWD atmospheres which is important for the continuum spectrum. In this chapter we will propose using the classical plasma formalism for calculating the properties of the magnetised atmospheres. With the plasma approach, we will recalculate the cyclotron absorption cross-sections in the literature which are calculated with various methods and show the consistency of this new method. In the final part of this chapter we implement all the necessary

ingredients, to calculate the cyclotron absorption cross-section and the magneto-optical parameters to be used in polarized radiative transfer equations.

Finally in Chapter 5 we will continue to analyze individual MWDs. In this chapter, which is partly based on Külebi et al. (2010), we will investigate the evolutionary history of RE J 0317-853 using distance measurements, this time estimated from parallax observations made by the *Hubble* Space Telescope. RE J 0317-853 is a record holder in mass, rotation and level of circular polarization. We will also divulge the new magnetic structure by spectral modeling, taking advantage of the new treatment of free-free absorption and magneto-optical parameters. The fits made using the new free-free parameters show conclusively that the high circular polarization is due to cyclotron absorption which has never been confirmed in the spectra of MWDs before. We will finish by revisiting the question of the formation and evolution of RE J 0317-853 in the light of the new analyses.

Chapter 1

Theory of White Dwarfs

1.1 Introduction

In this chapter we outline the history and the underlying physics of white dwarfs and their magnetic subpopulation. The historical treatise on white dwarfs in Sec. 1.1.1 is followed by an introduction on the magnetic white dwarfs in Sec. 1.1.2. In Sec. 1.1.3 we outline the contemporary observational classifications of white dwarfs, that is elementary for the discussion of origin and evolution of these objects. The introduction section overall, is the basis of a thorough discussion on the theory of white dwarfs, namely the white dwarf structure in Sec. 1.2 and atmospheric modeling of magnetic white dwarfs in Sec. 1.3.

1.1.1 History of white dwarfs

The realization that white dwarfs are a separate class of objects was prompted by the discovery of 40 Eridani B (40 Eri B) in 1914 by Russell (1914). The position of this object in the Hertzsprung-Russell (HR) diagram was unexplained for years, since it was positioned well below the main sequence (Fig. 1.1). It was called "white" due its color in the optical bands, and "dwarf" due to its small radius.

A major question appeared with the discovery of a counterpart to the Sirius; Sirius B, which seemed to have similar properties (Adams, 1915). The determination of the spectral type allowed for the estimation of the radius. This information combined with the known mass of $1\ \mathrm{M}_{\odot}$ of the object allowed for the determination of the mean density as $5 \times 10^4\,\mathrm{g/cm^{-3}}$, which was also supported by the gravitational redshift measurements of Sirius B (Adams, 1925).

This motivated an investigation into the properties of the material out of which the white dwarfs consists. The relativistic state of the Fermi state, explaining the physical properties of these stars. The realization that degenerate electrons are providing the pressure support (Fowler, 1926) led to the application of the relativistic theory of condensed Fermi matter to white dwarfs (Anderson, 1929; Chandrasekhar, 1931) which led to the determination of a limiting mass above which there exists no stable configuration.

The unique approach of using cutting edge physics to the astrophysical questions immediately motivated Landau to predict the possibility of a star supported by the degenerate pressure of atomic nuclei (Landau, 1932) before the discovery of neutrons. Later, the existence and the structure of neutron stars were conceptualized by Landau (1938); Oppenheimer & Volkoff (1939). The application of new physical concepts to celestial problems,

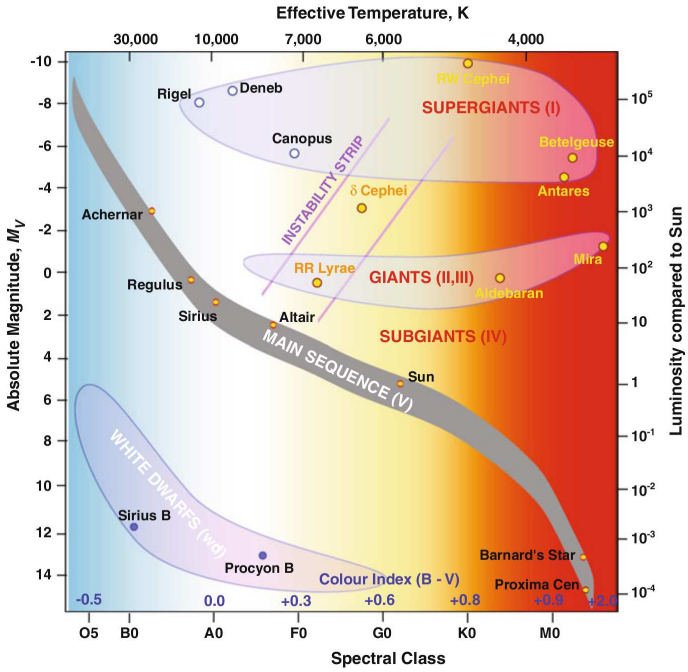

Figure 1.1: Hertzsprung-Russell diagram from R. Hollow, CSIRO. The spectral types and effective temperatures are drawn according to the color index to which they correspond. The position of white dwarfs are shown below the main-sequence.

became common place after Chandrasekhar, with white dwarfs being the template discovery.

1.1.2 Magnetic white dwarfs

The concept of Magnetic White Dwarfs (MWDs) is as old as the discovery of kilo Gauss (kG) magnetic fields in the atmospheres of early type stars, which are stronger than the Sun (Babcock, 1947a,b). These stars are currently known as peculiar A type stars and by assuming angular momentum conservation during the stellar evolution Blackett (1947) showed that white dwarfs might harbour field strengths as high as a million Gauss (MG).

This conjecture led to more speculation concerning the detection of these MWDs spectroscopically, and Blackett (1947) further argued that the lack of spectral lines in the spectrum of featureless DC white dwarfs might be attributed to the extreme broadening of the hydrogen lines in the spectra of hydrogen-rich (DA) stars. Building upon that he suggested three such stars to be investigated. One of the candidates, GRW+70°8247 had very shallow absorption features which were known as Minkowski bands (Minkowski, 1938). However, the faint nature of GRW+70°8247 (< 12 mag) postponed the test of magnetism for two more decades.

During this time, the other two stars, which were bright enough to be tested for magnetic broadening, splitting and shift of the lines; Wolf 1346 and 40 Eri B, were observed and gave negative results for the existence of magnetic effects (Thackeray, 1947; Babcock, 1948). Due to these null observations the search for MWDs fell from fashion, and was not pursued for decades (Liebert, 1988).

The rejuvenation of the MWD research happened after the discovery of the field strengths of the neutron stars (Ostriker & Hartwick, 1968; Ginzburg et al., 1969; Chow,

1969). On the conceptual basis of flux freezing (Cowling, 1945) and amplification of "fossil fields" due to the contraction of the star during stellar evolution, the existence MWDs were yet again considered.

Due to a lack of a consistent description of atomic transitions at high field strengths, the theoretical model that enabled Kemp (1970) to confirm the magnetic nature of GRW+70°8247 was his magnetoemission model (a toy model of harmonic oscillators), which predicted the level of continuum polarization. For a complete description, a consistent method for the atomic transition was needed. This was finally developed initially by Roesner et al. (1984); Greenstein et al. (1985) and then through consistent atmospheric modeling (Wickramasinghe & Ferrario, 1988; Jordan, 1992).

Since then ∼200 MWDs is the current number of known MWDs (see Külebi et al., 2009, and Chapter 2 for a recent count). These MWDs consist not only hydrogen-rich DAs but also MWDs with helium (Becken & Schmelcher, 2001) and carbon molecules (such as CH and C_2, Berdyugina et al., 2007; Hall & Maxwell, 2008; Vornanen et al., 2010) in their atmospheres.

1.1.3 Spectral types and evolution

Since the first discovery of Russell (1914) the number of white dwarfs increased to about $1\,000$ during the 70s. Currently this number has increased considerably up to $10\,000$ (Kleinman et al., 2004), which contributes greatly to both investigations which use white dwarfs and those that try to understand the nature of white dwarfs themselves.

The internal composition of a white dwarf reflects the evolutionary phases of its progenitor. Most of the mass of a white dwarf is concentrated inside the core which consists of the products of He burning, mainly carbon and oxygen. The massive white dwarfs $1.0-1.3\ \mathrm{M}_\odot$ most likely have cores composed of oxygen and neon. This core mixture is a result of an offset carbon ignition which either happens during the evolution of a $9\ \mathrm{M}_\odot$ mass star (Ritossa et al., 1996; García-Berro et al., 1997; Iben et al., 1997) or during a merger of two white dwarfs (Saio & Nomoto, 2004).

On top of this core small amounts of He and H remnant from the mass-loss phase is expected to exist. A He layer of $0.01\ \mathrm{M}_\odot$ resides under an even thinner layer of hydrogen of $10^{-4}\ \mathrm{M}_\odot$ if H even is present. This layering happens for stars in which radiative transfer is not effective and heavier atomic species sink deeper due to gravitational settling.

Due to this atmospheric structure, the main body of the white dwarf population can be separated spectroscopically into two categories according to the chemical component of the top atmospheric layer. The first group is called hydrogen-rich or DA and they mostly have H in their atmospheres and in some cases traces of other elements. They make up 85 percent of all known white dwarfs (Eisenstein et al., 2006). The other H-deficient family makes up 15 percent of all white dwarfs have mostly He in their atmospheres are called non-DAs. They are divided into subclasses depending on their effective temperatures. The hottest non-DAs are DO $200\,000\,K \geq T_{\mathrm{eff}} \geq 45\,000\,K$ which consist have He in their atmospheres. For lower effective temperature in the range $30\,000\,K \geq T_{\mathrm{eff}} \geq 11\,000\,K$, neutral He is observed for the type DB. And finally as with decreasing temperatures, $11\,000\,K \geq T_{\mathrm{eff}}$, metals start to show up in white dwarf spectra for types DC, DQ and DZ. The gap in the temperature intervals correspond to the "DB gap" where no DB star exists $45\,000\,K \geq T_{\mathrm{eff}} \geq 30\,000\,K$. There are also peculiar white dwarfs with oxygen rich atmospheres (Gänsicke et al., 2010) and hot DQs $T_{\mathrm{eff}} \approx 20\,000\,K$ (Dufour et al., 2007, 2008).

The correspondence of the effective temperatures and spectral types seems to suggest that there might be spectral evolution through the lifetime of a white dwarf. Although some of the these spectral types create problems for the theory of stellar evolution, in most cases the changing behaviour of the spectral type can be explained as a result of competing physical processes such as convection, mass-loss, accretion, gravitational settling and radiative levitation (for a recent review, see Althaus et al., 2010).

The basics of the white dwarf structure, under the assumption of zero temperature, is explained in Sec. 1.2.1, using the original approach of Chandrasekhar (1931) supplemented with additional physical effects, such as neutronization and magnetic fields. All of the calculations are made under the assumption of zero-temperatures and they are sufficient to explain the mechanical structure of a white dwarf.

However, the total energy of the white dwarfs in fact do change, or simply radiate away during the life-time of a white dwarf. As we have seen, white dwarfs do in fact have high temperatures and then gradually cool down, losing internal energy. This behaviour implies that white dwarfs are not static but rather go through some kind of evolution. Luckily the degenerate structure of the white dwarfs, simplifies the quantification of the evolution. More importantly, the question of evolution can be separated into two parts; the total energy of the star and secondly the rate at which the energy radiates away.

Due to this fact, in the discussion of the theory of white dwarfs and their evolution, in Sec. 1.2 we begin with a discussion of the structure of white dwarfs and then move to basic considerations for the cooling of the degenerate core. In Sec. 1.3 we examine white dwarf radiation with special consideration of magnetic fields in white dwarf atmospheres.

1.2 White Dwarf Structure

1.2.1 Mass-radius relations

One of the most important aspects of the white dwarf structure is the relationship between the mass and radius of the star. Initially predicted by Chandrasekhar (1931), unlike stars with non-degenerate matter cores, the radius of white dwarfs decreases with increasing mass. This is a natural consequence of the pressure support from degenerate electrons.

The solution for the mass-radius relationship is simply reached by using the structure equation inside the hydrostatic equilibrium. In Chandrasekhar's method the solution is reached with the inclusion of the equation of state. However, as the mass of the white dwarf increases, the gravitational force causes the radius to decrease and thus the density increases. In this manner, the equation of state becomes relativistic. When the matter inside is completely relativistic, we no longer have a mass-radius relationship. Rather there is a limiting mass known as the Chandrasekhar mass, which depends on the chemistry of the star.

Many important extensions to the mass-radius relationships were made, Hamada & Salpeter (1961) included realistic chemistry and made electrostatic corrections. Later Ostriker & Bodenheimer (1968) added the influence of differential and rigid rotation, and using same self-consistent field formalism (see Ostriker & Mark, 1968) effect of the magnetic fields Ostriker & Hartwick (1968).

Now we can start discussing the structure of white dwarfs from first principles. We will assume a zero-temperature and start from the property of the material inside. The Fermi state, conjectures that the fermions inside the matter occupy the lowest energy level

possible. The application of this type of matter is unique in the fact that degenerate fermions present a pressure source due to the fact that each electron fills a separate energy level, according to the Pauli's exclusion principle. This pressure present the main source of support for stars which stopped nuclear burning.

The property of the degenerate electrons are defined by their common value for momentum, that is p_F the Fermi momentum which depends on the total number of electrons per unit volume. The distribution function for Fermi gas is $2/h^3$, since h is the value corresponding to unit phase space and for unit space 2 spin levels (up, down) are filled.

$$f(p) = \begin{cases} \frac{2}{h^3}, & \text{for p} \leq \text{p}_\text{F} \\ 0 & \text{for p} > \text{p}_\text{F} \end{cases} \tag{1.2.1}$$

From probability density, we can get the number density

$$n_e = \int_0^{p_F} f(p)\, d^3p = \int_0^{p_F} \frac{2}{h^3} 4\pi p^2\, dp = \frac{8\pi}{3h^3} p_F^3 \tag{1.2.2}$$

This equality gives an expression for the Fermi momentum p_F;

$$p_F = \left(\frac{3n_e}{8\pi}\right)^{1/3} h \tag{1.2.3}$$

For this kind of statistical distribution, the energy can be calculated by integrating the energy of a single particle convolved with the number distribution of the particles over all possible momenta. If the energy of a particle is defined as $(p^2c^2 + m_e^2c^4)^{1/2}$, the thermodynamic energy becomes:

$$\begin{aligned} E &= 2\frac{V}{h^3}\int_0^{p_F} 4\pi dp p^2 (p^2c^2 + m_e^2c^4)^{1/2}, \qquad x_F = \frac{p_F}{mc},\ \eta = \frac{p}{mc} \\ &= 8\pi\frac{V}{h^3}\int_0^{x_F} \eta^2(1+\eta^2)^{1/2} d\eta \\ &= 8\pi\frac{V}{h^3} m_e^4 c^5 \frac{1}{8}[(1+x_F^2)^{1/2}(x_F + 2x_F^3) - \text{arcsinh}(\text{x}_\text{F})]. \end{aligned}$$

Due to our choice of relativistic energy for the single electron, this equation gives the most general case. From this we can derive the pressure using the thermodynamic equations. When we write the potential Ω for the grand canonical ensemble (see e.g. Landau & Lifshitz, 1968)

$$\Omega = -PV = E - TS - \mu N. \tag{1.2.4}$$

where P is pressure, T is the temperature, N is the number of particles and S the entropy which is zero for the degenerate matter and μ is the chemical potential which is equal to the Fermi energy for our case. This means the pressure is equal to

$$
\begin{aligned}
PV &= \mu N - E \\
&= m_e c^2 (1+x_F^2)^{1/2} N - 8\pi \frac{V}{h^3} \frac{1}{8} [(1+x_F^2)^{1/2}(x_F + 2x_F^3) - \sinh^{-1}(x_F)] \\
&= V \frac{8\pi}{3h^3} (m_e^4 c^5) [(1+x_F^2)^{1/2} - \frac{3}{8} [(1+x_F^2)^{1/2}(x_F + 2x_F^3) - \sinh^{-1}(x_F)] \\
&= V \frac{8\pi}{3h^3} (m_e^4 c^5) \frac{1}{8} [(1+x_F^2)^{1/2}(2x_F^3 - 3x_F) - 3\sinh^{-1}(x_F)] \\
P &= \frac{\pi}{3h^3} (m_e^4 c^5) [(1+x_F^2)^{1/2}(2x_F^3 - 3x_F) - 3\sinh^{-1}(x_F)] \qquad (1.2.5) \\
P &= A f(x) \\
A = \frac{\pi}{3h^3} m_e^4 c^5 &= 6.01 \times 10^{22}, \qquad f(x) = (1+x_F^2)^{1/2}(2x_F^3 - 3x_F) - 3\sinh^{-1}(x_F)
\end{aligned}
$$

This equation gives the most general equation of state for the matter composed of degenerate electrons at zero temperature. The cases for non-relativistic and relativistic cases can be found by approximating $f(x)$ for $x_F \ll 1$ and $x_F \gg 1$ respectively.

$$
\begin{aligned}
x_F &\ll 1 \\
P &= A \left[x_F^3 + \frac{x_F^5}{2} - 3 \left(\frac{x_F^3}{3} + \frac{x_F^5}{10} \right) \right] \\
&\approx A \frac{x_F^5}{5} \\
x_F &\gg 1 \\
P &= A \left[x_F^4 + \frac{x_F^2}{2} - 3 \left(\frac{x_F^4}{4} + \frac{x_F^2}{4} \right) \right] \\
&\approx A \frac{x_F^4}{4}
\end{aligned}
$$

To reach a familiar polytropic description for the equations of state, we need to substitute for the dimensionless Fermi momentum using equation 1.2.3 as $x_F \propto n_e^{1/3} \propto \rho^{1/3}$ where ρ is the density. This proportionality between mass and number density, can be specifically shown as $\rho = H \mu_e n_e$, where $\mu_e = A/Z$ is the atomic mass per electron.

$$
\begin{aligned}
\rho = H \mu_e n_e = H \mu_e \frac{8\pi m_e^3 c^3}{3h^3} x_F^3 \qquad (1.2.6) \\
\rho = B x_F^3, \qquad B = H \mu_e \frac{8\pi m_e^3 c^3}{3h^3}.
\end{aligned}
$$

Then when we insert the densities inside the pressure equations, we reach the familiar terms for non-relativistic and relativistic equations of state.

$$
P_{\mathrm{non-r}} = K'_{\mathrm{non-r}} \, x_F^5 = K_{\mathrm{non-r}} \, \rho^{5/3} \qquad (1.2.7)
$$

$$
P_{\mathrm{r}} \approx K'_{\mathrm{r}} \, x_F^4 = K_{\mathrm{r}} \, \rho^{4/3} \qquad (1.2.8)
$$

The correspondence to the non-relativistic $n = 3/2$ and the relativistic $n = 3$ case can be seen right away for the polytropic equation of state $P = K\,\rho^{1+1/n}$, where n is the polytropic index.

When the pressure of the Fermi gas inside a white dwarf is known, the stellar structure can be constructed with the combined use of hydrostatic equilibrium and the structure equation.

$$\frac{dP(r)}{dr} = -\rho\frac{GM(r)}{r^2} \qquad \frac{dM(r)}{dr} = -4\pi r^3\rho(r)$$

which combined, lead to

$$\frac{1}{r^2}\frac{d}{dr}\left(\frac{r^2}{\rho}\frac{dP}{dr}\right) = -4\pi G\rho(r) \tag{1.2.9}$$

where G is the gravitational constant. The solution of this differential equation exist in the form of Lane-Emden equations where the equations of state are polytropic. The most general solution for the case of white dwarfs are reached with the use of equation 1.2.5. Plugging in the simple descriptions for pressure and density we reach the differential equation:

$$\frac{1}{r^2}\frac{d}{dr}\left(\frac{r^2}{Bx^3}A\frac{df(x)}{dr}\right) = -4\pi GBx^3 \tag{1.2.10}$$

The left hand side can be simplified as:

$$\frac{1}{x^3}\frac{df(x)}{dr} = \frac{8x}{(x^2+1)^{1/2}}\frac{dx}{dr} = 8\frac{d\sqrt{x^2+1}}{dr}. \tag{1.2.11}$$

When we insert this inside 1.2.10 and change the variable as $y^2 = x^2 + 1$;

$$\frac{1}{r^2}\frac{d}{dr}\left(r^2\frac{d\sqrt{x^2+1}}{dr}\right) = -\frac{\pi GB^2}{2A}x^3$$

$$\frac{1}{r^2}\frac{d}{dr}\left(r^2\frac{dy}{dr}\right) = -\frac{\pi GB^2}{2A}(y^2-1)^{3/2} \tag{1.2.12}$$

we arrive at the following differential equation. With a simple change of variables we can further simplify

$$y = y_0\theta, \qquad r = \alpha\eta$$

$$y_0 = \sqrt{x_0+1}, \quad \alpha = \sqrt{\frac{2A}{\pi G}}\frac{1}{By_0}$$

$$\frac{1}{\eta^2}\frac{d}{d\eta}\left(\eta^2\frac{dy}{d\eta}\right) = -\left(\theta^2 - \frac{1}{y_0^2}\right)^{3/2} \tag{1.2.13}$$

and reach a more general version that is close to the Lane-Emden equation. For specific polytropic indicies the equation is described as Lane-Emden equation, which is solved numerically by using relevant boundary conditions,

$$\theta|_{\eta=0} = 1, \qquad \left.\frac{d\theta}{d\eta}\right|_{\eta=0} = 0. \tag{1.2.14}$$

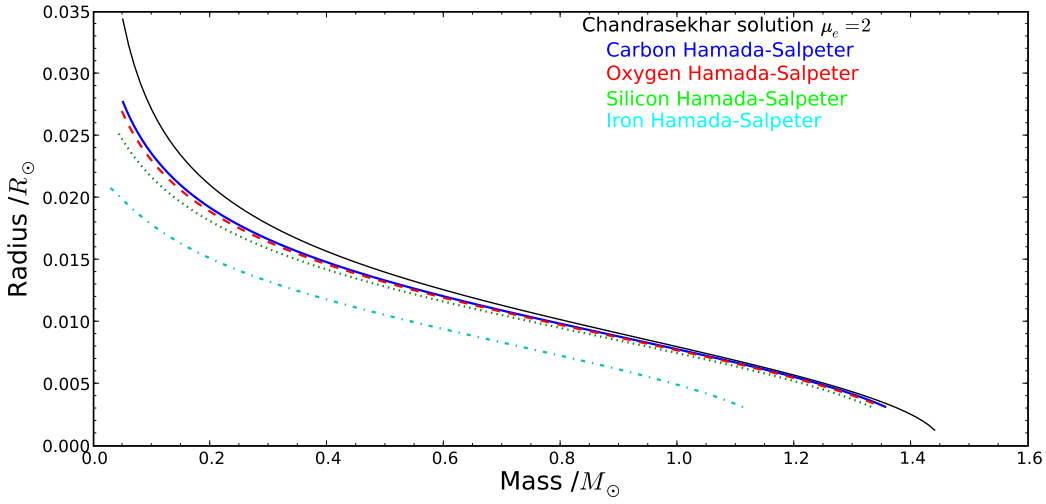

Figure 1.2: Theoretical zero temperature mass-radius relations for white dwarfs. The top curve is the original solution of Chandrasekhar, for $\mu_e = 2$ which corresponds to carbon cores. The curves in color are the zero temperature solutions of Hamada & Salpeter (1961). Notice with increasing atomic mass per electron, both the overall radii and the limiting Chandrasekhar mass decreases.

However, to understand the behaviour of the radius with respect to the mass, the solution for a single polytropic index is not appropriate. Each mass shell corresponds to a different density, hence a different equation state and a different polytropic index. Also as was previously mentioned, low mass white dwarfs have predominantly non-relativistic $n = 3/2$ polytropic indicies and they evolve gradually to ultra relativistic $n = 3$ white dwarfs when the limiting Chandrasekhar mass is reached.

The equation 1.2.13 was solved by Chandrasekhar and his numerical values were used widely for years. The mass-radius relationship calculated by Chandrasekhar is illustrated in Fig. 1.2.

The same differential equation can be reached by a different method, without the usage of the mass function, but rather through direct usage of the gravitational potential (see e.g. Landau & Lifshitz, 1968). This method, which is not parametrized with respect to Lane-Emden parameters but to the chemical potential, is more instructive to understand the behaviour the gradient of polytropic indicies per mass shell and can easily be used to derive physical parameters.

According to the divergence of the gravitational field, the gravitational potential depends on the source term which is the mass within the surface of divergence. Analogous to the Gauss' Law, the gravitational potential is described as:

$$\int_A g(r) \cdot dA = -4\pi GM \tag{1.2.15}$$

where A denotes surface and dA the surface element, $g(r)$ is the gravitational acceleration which changes according to radius. If all terms are written explicitly with ϕ being the potential, we can describe the mass of the whole star as

$$
\begin{aligned}
g(R) = -\nabla\phi = &- \left.\frac{\partial\phi}{\partial r}\right|_{r=R} \\
&- \left.\frac{\partial\phi}{\partial r}\right|_{r=R} 4\pi R^2 = -4\pi GM \\
&R^2 \left.\frac{\partial\phi}{\partial r}\right|_{r=R} = GM
\end{aligned} \tag{1.2.16}
$$

When we use the differential form of Gauss' Law, we are able derive an analogue of the equation 1.2.9. However it is now in terms of potential rather than pressure.

$$
\begin{aligned}
\nabla^2\phi &= 4\pi G\rho \\
\frac{1}{r^2}\frac{d}{dr}\left(r^2\frac{d\phi}{dr}\right) &= 4\pi G\rho.
\end{aligned} \tag{1.2.17}
$$

To derive an analogue of equation 1.2.10 we need to relate the properties of the matter to the potential of the star. For material in thermal equilibrium, the total thermodynamic potential per unit molecule equal to the addition of the field free chemical potential μ_0 and the potential induced by the external field (Landau & Lifshitz, 1968):

$$
\mu_0(P,T) + u(x,y,z) = \text{constant} \tag{1.2.18}
$$

For white dwarfs the potential is the gravitational potential and the equation becomes

$$
\mu + m_e\mu_e\phi = \text{constant} \tag{1.2.19}
$$

where μ_e is the atomic mass per electron as defined before, not to be confused with the chemical potential.

For brevity we will omit the subscript zero from the chemical potential. When we replace the potential in the equation 1.2.17 with equation 1.2.19, and insert the density from equation 1.2.6 in, we obtain

$$
\frac{1}{r^2}\frac{d}{dr}\left(r^2\frac{d\mu}{dr}\right) = -4\pi\mu_e m_e G\rho. \tag{1.2.20}
$$

In equation 1.2.6 we have already defined ρ in terms of dimensionless Fermi momentum x_F for the electrons in Fermi state. Additionally the chemical potential can be expressed in terms of x_F.

$$
\begin{aligned}
\mu = E_F &= (m_e^2c^4 + p_F^2c^2)^{1/2} \\
&= m_ec^2(1 + x_F^2)^{1/2} \\
x_F &= \left(\frac{\mu^2}{m_e^2c^4} - 1\right)^{1/2}
\end{aligned} \tag{1.2.21}
$$

This allows us to express ρ in terms of the chemical potential after which we are left with the familiar equation.

$$\frac{1}{r^2}\frac{d}{dr}\left(r^2\frac{d\mu}{dr}\right) = -4\pi m_e \mu_e GB\left(\frac{\mu^2}{m_e^2c^4}-1\right)^{3/2} \tag{1.2.22}$$

The above equation basically shows that our parameter y in the equation 1.2.12 is equal to rest energy normalized by the chemical potential μ/m_ec^2. This knowledge is useful, since any additional effects to the physical description can be conveniently added to this equation.

We can proceed further by calculating physically relevant limits. If we take the ultra-relativistic and non-relativistic limits, and follow the steps from equation 1.2.20, we obtain:

$$\begin{aligned} E_F = \mu_{\mathrm{non-r}} = \frac{p_F^2}{2m} = x_F^2\, mc^2 \qquad & \mu_{\mathrm{r}} = p_F c = x_F\, m_e c^2 \\ \mu_{\mathrm{non-r}} = \frac{(3\pi)^{2/3}}{2}\frac{\hbar^2}{\mu_e^{2/3}m_e^{5/3}}\rho^{2/3} \qquad & \mu_{\mathrm{r}} = (3\pi)^{1/3}\hbar\left(\frac{\rho}{\mu_e m_e}\right)^{1/3}. \end{aligned} \tag{1.2.23}$$

By substituting the density to get the limiting forms of equation 1.2.22, we arrive at:

$$\frac{1}{r^2}\frac{d}{dr}\left(r^2\frac{d\mu_{\mathrm{non-r}}}{dr}\right) = -\lambda\mu_{\mathrm{non-r}}^{3/2} \qquad \lambda = \frac{G(2m_e)^{7/2}\mu_e^2}{3\pi\hbar^3} \tag{1.2.24}$$

$$\frac{1}{r^2}\frac{d}{dr}\left(r^2\frac{d\mu_{\mathrm{r}}}{dr}\right) = -\lambda\mu_{\mathrm{r}}^{3} \qquad \lambda = \frac{4G(\mu_e m_e)^2}{3\pi c^3\hbar^3}. \tag{1.2.25}$$

It is apparent that the density profile determines the chemical potential of the star for each mass shell. To reach a sensible solution of the differential equation, we need to impose boundary conditions similar to the equation 1.2.10. At the radius of the object $\mu|_{r=R} = 0$ and at the center it should be constant which means $d\mu/dr|_{r=0} = 0$. This means, μ is defined with respect to the radius as

$$\frac{d\mu_{\mathrm{non-r}}}{dr} = -\frac{\lambda}{r^2}\int r^2\mu_{\mathrm{non-r}}^{3/2}\,dr \tag{1.2.26}$$

$$\frac{d\mu_{\mathrm{r}}}{dr} = -\frac{\lambda}{r^2}\int r^2\mu_{\mathrm{r}}^{3}\,dr. \tag{1.2.27}$$

With the use of dimensional analysis, we can define the function $\mu(r)$ accordingly. For the ultra-relativistic case λ has the dimension inverse square of length times energy (cm^{-2} erg^{-2}). This implies the chemical potential can be described with total radius of the object λ and a function which depends on the dimensionless radius.

$$\mu(r) = \frac{1}{R\sqrt{\lambda}}f(r/R).$$

where f represents the radius variation of the chemical potential.

This form immediately allows us to assess the dependencies of the density distribution with the use of relations between μ and ρ (equation 1.2.23).

$$\rho(r) = \frac{\text{constant}}{R^3}F(r/R).$$

What we are interested in is the mean density $\bar{\rho}$ which means we only need the average value of the function F over the stellar radius. $\bar{\rho} \propto R^{-3}$ means the total mass of the object is independent of the radius, i.e. the mass is constant at this limit. Since we know that this is the stability limit for the white dwarfs, this constant mass corresponds to the critical Chandrasekhar mass $M_{\rm ch}$.

To finally calculate the physical properties and the Chandrasekhar mass $M_{\rm ch}$, we further simplify the differential equation by the dimensionless parameter $\xi = r/R$, which scales the variability according to the total radius of the object. Then, we impose the boundary conditions and solve the differential equation numerically.

$$\frac{1}{\xi^2}\frac{d}{d\xi}\left(\xi^2\frac{df}{d\xi}\right) = f^3, \qquad f'(0) = 0, \qquad f(1) = 0 \tag{1.2.28}$$

The result for this regime is $f(0) = 6.897$ and $f'(1) = -2.1018$. The derivative of the function f at the surface is necessary to calculate the Chandrasekhar mass according to the Gauss' Law from equation 1.2.16.

$$\begin{aligned} GM_{\rm ch} &= R^2 \left.\frac{\partial\phi}{\partial r}\right|_{r=R} = \left.\frac{R^2}{\mu_e m_e}\frac{\partial\mu}{\partial r}\right|_{r=R} \\ &= \frac{R^2}{\mu_e m_e}\frac{-1}{R^2\sqrt{\lambda}}f'(1) \\ M_{\rm ch} &= \frac{3.1}{\mu_e m_e}\left(\frac{\hbar c}{G}\right)^{3/2} = \left(\frac{2}{\mu_e}\right)^2 1.4587 M_\odot \end{aligned} \tag{1.2.29}$$

This is the most important result of Chandrasekhar (1931) and has important implications for stellar evolution theory. This is the mass limit for the onset of collapse of a stellar core. Above this limiting mass, the electron degeneracy is insufficient to support the force of gravitation, and at the end of the lives of stars which host such massive cores, experience collapse and end up as core-collapse supernovae.

However the Chandrasekhar limit is an approximation under the assumption of zero-temperatures, simple chemistry and without the mechanical effects of angular momentum. The initial corrections to the chemistry of the white dwarf interiors were made by Salpeter (1961); Salpeter & Zapolsky (1967) which included the classical Coulomb energy of the ion lattice, Thomas-Fermi deviations from uniform charge distributions of electrons and the exchange energy due to spin-spin interactions.

An important outcome of the Salpeter (1961) corrections was that for high densities inverse β decays become important, and electrons tunnel into the nuclei to form neutrons which eventually change the effective chemical properties of the matter increasing the $\mu_{e,\rm eff}$. When the core density reaches a certain critical value, the electrons begin to be pushed inside the protons, which is also defined as the inverse β-process which creates neutrons and neutrinos.

Effectively the new nuclear structure inside the white dwarf core is changed. As the phase transition sets in, a part of the stellar core is composed of heavier nuclei, changing the effective adiabatic index of the star. However, surpassing the critical density, $\rho_{\rm cr}$, which causes the onset of the phase transition is not enough to start the instability. This requires either a large density difference between the core and the rest of the star (Ramsey, 1950),

i.e.

$$\frac{\rho_2}{\rho_1} = \frac{A_2 Z_1}{A_1 Z_2} > 1.5$$

or a chain of inverse β-processes between the electron and the nuclei due to the ever increasing heavier core.

This in turn induces an extra constraint to the maximum mass and effectively decreases it, which was shown explicitly by the zero-temperature models of Hamada & Salpeter (1961). For a pure Carbon core, this can be qualitatively demonstrated by

$$M_{\rm ch}^{\beta} = 1.396 M_{\odot} \text{ for } C^{12} \tag{1.2.30}$$

Another constraint that has an effect on the maximum Chandrasekhar mass is general theory of relativity (GTR). Initially suggested by Kaplan (1949) and later precisely calculated by Chandrasekhar (1964); Chandrasekhar & Tooper (1964), this effect is expected to break the dynamical stability at densities lower than what is expected from the Chandrasekhar zero-temperature limiting densities, and the white dwarf is expected to collapse at masses smaller than the Chandrasekhar zero-temperature limiting mass values.

$$M_{\rm ch}^{\rm GTR} = \left(\frac{2}{\mu}\right)^2 1.43 M_{\odot} \tag{1.2.31}$$

This has important implications for the pulsations on the dynamical stability and historically was proposed as a test for general relativity. However any additional effects, such as a deviation from the mass-radius models is not expected. This is because the estimated radii are three orders of magnitude larger than the Schwarzschild-radius: $GM/c^2 R_{WD} \sim 10^{-3}$. Hence, we do not expect any effect on our mass determinations, as also noted by Koester & Chanmugam (1990).

If we would compare the effects of the GTR versus the neutronization on the stability of the core, since GTR effects also depend on the chemistry of the matter, as a rule we would expect the critical densities to be as $\rho_{\rm neutr} < \rho_{\rm GTR}$, but the exact point of onset of instability is harder to calculate. This problem has been undertaken by Hamada & Salpeter (1961); Saakyan & Vartanyan (1964). The Chandrasekhar mass is decreased from 1.43 $\mathrm{M}_{\odot}$ to 1.367 $\mathrm{M}_{\odot}$ when both the GTR and Hamada & Salpeter (1961) corrections are considered (Cohen et al., 1969).

In addition to the chemistry of the matter inside white dwarfs, any mechanical effect on the pressure structure also implies a deviation from the theoretical zero-temperature radius. The most efficient way to support the white dwarf structure is through angular momentum. This extra support which causes a change in the pressure structure also effectively increases the critical mass of the white dwarf. Although for uniform rotation not more than a 4 percent change in the maximum limiting mass is expected, the situation drastically changes for differential rotation.

It was shown by Ostriker et al. (1966) that a stable configuration of arbitrary mass can always be constructed for a given angular momentum. However models with realistic physics and chemistry were calculated by Ostriker & Bodenheimer (1968) for white dwarfs with masses between 1.3-4.1 $\mathrm{M}_{\odot}$.

$$M_{\rm ch}^{T} = M_{\rm ch}\left(1 + \frac{3T}{|W|}\right) \tag{1.2.32}$$

where T is the rotational energy and W is the gravitational energy.

Although not as strong as the angular momentum, a similar mechanical effect exists for the influence of magnetism. As the magnetic energy $\mathcal{M}$ becomes comparable to the gravitational energy W, the magnetic pressure affects the stability of the white dwarf, increasing the radius fractionally by $|\mathcal{M}/W|$.

The stable configurations inside the stars were initially investigated by Woltjer (1960); Wentzel (1961) and later applied to the stellar structure and finally to mass-radius relations by Ostriker & Hartwick (1968)

The possibility of magnetic pressure inside the white dwarfs was used to explain the deviations from mass-radius relations by Mestel (1965). The additional effect of magnetic pressure can be most simply included by modifying the Chandrasekhar mass,

$$M_{\rm ch}^{B} = M_{\rm ch}\left(1 + \frac{3}{2}\frac{\mathcal{M}}{|W|}\right). \tag{1.2.33}$$

On the other hand the stable magnetic configurations were initially considered by Chandrasekhar (1956); Chandrasekhar & Prendergast (1956). However for our purposes, we will not deal with the specific geometry of the stable magnetic configurations but rather the overall magnetic energy. Even for the consideration of Ostriker & Hartwick (1968) where the magnetism vanishes on the surface, magnetic energies as high as ten percent of the gravitational energy are acceptable.

Since the mass estimate for a given radius depends on the (unknown) internal magnetic field strength of the white dwarf, precise calculations with mass-radius relations taking magnetism into account are beyond the scope of this work. We can use a simple energy argument from Shapiro & Teukolsky (1983) to look at the effect of the magnetic energy on the radius of the star. The total energy of the system is related to the gravitational energy W of the system as:

$$E = -\frac{3\Gamma - 4}{3(\Gamma - 1)} = -\frac{3 - n}{3}|W|$$

Approaching the extreme relativistic degeneracy limit, the star is near a $n = 3$ polytrope and this implies a small change in energy results in a large change in radius:

$$\frac{\Delta E}{E} = -\frac{\Delta R}{R}$$

The small change in energy can be supplied by a change in magnetic energy $\Delta\mathcal{M}$

$$\frac{\Delta R}{R} = \frac{3}{3 - n}\frac{\Delta\mathcal{M}}{|W|}$$

Defining δ as $\mathcal{M}/|W|$, hence $\Delta\delta = \Delta\mathcal{M}/|W|$ and assuming n to be constant as δ increases, we find the radius to be:

$$R = R_0 e^{\frac{3}{3-n}\delta} \tag{1.2.34}$$

In this formula, as the star approaches complete relativistic degeneracy at $n = 3$, This formula is not applicable since the radius rapidly increases. The same behaviour is also observed in the results of Nauenberg (1972) for the mass-radius relations under the influence of magnetism.

1.2.2 White dwarf cooling

One of the most useful applications of white dwarfs in astronomy is the age determination of certain stellar populations, be it clusters or the Galaxy itself. After our extended discussion on the fundamentals of the structure of white dwarfs, we can move towards the basic theory of cooling.

According to stellar evolution, white dwarfs are the degenerate remnants of stellar cores. Once nuclear burning ceases these cores contract until degeneracy pressure supports gravitation. Due to the virial theorem, contraction heats the white dwarf. Due to the degenerate conditions, the interior of white dwarfs are highly thermally conductive, which causes the internal temperature to be uniform. This forms the base temperature of the non-degenerate layers, in which each layer is in local thermodynamic equilibrium (see Sec. 1.3) and energy is lost through photon diffusion.

The dichotomy of the isothermal degenerate core and the heat sink non-degenerate surface allows the problem to be separated into two parts, in which the separate calculations of the total heat content and energy loss due to the luminosity of the white dwarf characterizes the cooling timescales. In this section we give an outline of the simple cooling theory and discuss shortly the recent literature on the cooling.

According to the elementary theory of cooling by Mestel (1965), the isothermal core of temperature T cools by photon luminosity L and the thermal energy inside the white dwarf is provided by the non-degenerate nuclei (see e.g. Shapiro & Teukolsky, 1983):

$$\begin{aligned} \dot{Q}_T = -L, \qquad Q_T &= \frac{3}{2} kT \frac{M}{A m_u} \\ t_{\rm cool} &= \frac{3}{5} \frac{kTM}{A m_u L} \end{aligned} \tag{1.2.35}$$

k is the Boltzmann constant, M is the mass of the white dwarf, A is the baryon number and m_u is the atomic mass. When we integrate this equation we obtain the cooling time, $t_{\rm cool} = t - t_0$, wherein t_0 is the time when the cooling starts at an initial core temperature T_0, after the envelope from the planetary nebula phase has been shed. Assuming a simple Kramers' Law (see e.g. Mihalas, 1978, and equation 1.3.35) for the opacity this result leads to a cooling age of

$$t_{\rm cool} \approx 9.41 \times 10^6 {\rm yr} \left(\frac{\rm A}{12}\right)^{-1} \left(\frac{\mu_{\rm e}}{2}\right)^{4/3} ({\rm M}/\,{\rm M}_\odot)^{5/7} \left(\frac{\rm L}{{\rm L}_\odot}\right)^{-5/7}. \tag{1.2.36}$$

There are other factors effecting the white dwarf cooling like neutrino losses and crystallisation and they are all taken into account in the detailed evolutionary models that we used. However, for some approximations in the following sections we will use this simplified

theory which is reasonably accurate on the hot end ($> 30\,000$ K) of the white dwarf cooling sequence.

One should note that all of these theoretical efforts were made under simple assumptions and for a zero temperature. For more precise models of white dwarf cooling we need more elaborate evolutionary models. First of all, luminosity is not the only energy loss mechanism, and depending on the temperature of the white dwarf, other effects such as nuclear burning, neutrino losses, and the gravitational energy released from physical separation processes in the core might affect the result. Also, at high temperatures, the assumption of degenerate cores being isothermal, does not hold. Additionally, the energy loss and the hydrostatic balance are coupled. Namely, the pressure balance depends on the temperature and density. This requires the simultaneous treatment of thermal and hydrostatic evolution. The implementation of these physical details makes self-consistent stellar evolution models necessary. This task has been undertaken by the models of Wood (1995); Althaus et al. (2005) in varying detail.

As mentioned before, the question of age assessment can be separated into two different problems, the evolution of the internal structure and the luminosity from the atmosphere. This means, to achieve estimates on the age of a white dwarf through observations depend on atmospheric modeling. In the literature, the collaboration of evolutionary models and the atmospheric modeling exists and the resulting calculations were made accessible to the community. Holberg & Bergeron (2006) used the carbon-oxygen (CO) core white dwarf evolutionary models of Wood (1995) for the basis of their thick layer ($M_{\mathrm{H}}/M_{*} = 10^{-4}$) atmospheric modeling and produced the synthetic magnitudes for white dwarfs of varying masses and ages[1]. For the white dwarfs with oxygen-neon (ONe) core cooling models with hydrogen layers of $M_{\mathrm{H}}/M_{*} = 10^{-6}$ exists (Althaus et al., 2007) that are based on models of Althaus et al. (2005) [2].

In the following chapter we will discuss the details of atmospheric modeling, however not for the aforementioned non-magnetic models but for the magnetized atmospheres which are focus of this work.

[1] http://www.astro.umontreal.ca/∼bergeron/CoolingModels
[2] http://www.fcaglp.unlp.edu.ar/evolgroup/tracks.html

1.3 White Dwarf Atmospheres

1.3.1 Radiative transfer

Photons are the most common tool for information transfer. This is true both for terrestrial and astronomical conditions. Unlike neutrinos, photons interact with normal matter easily and at the same time not as interactive as the ionized high energetic particles (i.e. cosmic rays) which interact with magnetic fields and cause showers in the upper atmosphere.

To get relevant information about astronomical objects we need a consistent theory of light and the propagation of light in matter. This has been one of the most important areas of research before and during the Copernican revolution. Our current understanding of light and seeing was developed starting from Alhazen (Ibn al-Haytham), Rene Descartes and Isaac Newton, who developed a theory of optics in addition to important discoveries in other topics. Finally, a wave theory of light was proposed by Christian Huygens, but James Clerk Maxwell was the one who implemented this concept completely. Maxwell's unification of electromagnetism, prompted the understanding of radiation as an electromagnetic wave.

In addition to the wave explanation, the corpuscular nature foreshadowed the photon as a particle, which eventually led to the complete picture of the interaction between light and matter with the advent of quantum physics. The nature of the photon as a particle with a spin of one, naturally explains the black body temperature and the quantized behaviour led to an understanding of emission and absorption of atomic lines.

To analyze and quantify radiation we start by defining the radiant energy (see e.g. Chandrasekhar, 1960), dE_ω emitted in a frequency interval $(\omega, \omega + d\omega)$, in a certain solid angle Ω, through an area $d\sigma$, during a time interval dt. The physical dimension that holds this energy is called intensity I_ω, hence the radiant energy is defined as:

$$dE_\omega = I_\omega \cos\theta d\omega d\sigma d\Omega dt \tag{1.3.1}$$

where θ is defined as the angle between the direction of the radiation and the normal to the surface $d\sigma$. As light passes through a medium it can be absorbed, emitted or scattered hence the amount of intensity depends on the position and the direction of the radiation.

To explain the change in radiation as it passes through a medium of thickness of ds in the direction of the propagation, we can start by defining:

$$dI_\omega = -\kappa_\omega \rho I_\omega ds \tag{1.3.2}$$

as the change of intensity. Furthermore now we can define the loss in energy as

$$\frac{dI_\omega}{ds} ds d\omega d\sigma d\Omega dt = -\kappa_\omega \rho I_\omega ds d\omega d\sigma d\Omega dt \tag{1.3.3}$$

where κ_ω is the (mass) absorption coefficient for a photon of frequency ω and ρ is the density of the material.

When the material is emissive the opposite case applies. The radiant energy from a mass dm of material, for the solid angle $d\Omega$, at a frequency interval $(\omega, \omega + d\omega)$ during the interval dt is $j_\omega dm d\omega d\Omega dt$.

If we prefer to use the density of the material where $\rho = dm/ds d\sigma$ we end up with a more familiar $j_\omega \rho ds d\sigma d\omega d\Omega dt$

The transfer of the photon is affected by absorption, emission and scattering. However, the question of scattering becomes negligible under the assumption of local thermodynamic

equilibrium (LTE). According to LTE for each point in the atmosphere, a local temperature T can be defined where absorption is proportional to emission with the factor being Planck's function for that local temperature, according to Kirchoff's law.

$$j_\omega = B_\omega(T)\kappa_\omega \tag{1.3.4}$$

where the source function $B_\omega(T)$ is defined as the Planck function:

$$B_\omega(T) = \frac{2h\omega^3}{c^2}\frac{1}{e^{h\omega/kT}-1}. \tag{1.3.5}$$

Here k is the Boltzmann constant and h is Planck's constant.

Using these assumptions and definitions we can write the radiation transfer equations through the energy equalities of equations 1.3.1 and 1.3.3.

$$\frac{dI_\omega}{ds} = -\kappa_\omega\rho I_\omega + j_\omega\rho.$$

In terms of the source function B_ω, this yields:

$$-\frac{1}{\kappa\rho}\frac{dI_\omega}{ds} = I_\omega - B_\omega(T). \tag{1.3.6}$$

Formally it is easy to solve this transfer equation with the use of optical depth τ

$$\tau(s,s') = \int_{s'}^{s} \kappa\rho ds$$

which in turn yields a solution of

$$I(s) = I(0)e^{-\tau(s,0)} + \int_0^s B(s')e^{-\tau(s,s')}\kappa\rho ds \tag{1.3.7}$$

If we solve these transport equations considering a plane-parallel system, we can easily use a coordinate system instead of the arbitrary s and s' displacements. z becomes the distance and θ the angle relative to the normal of the surface and ψ is the azimuth relative to the x axis.

$$-\cos\theta\frac{1}{\kappa\rho}\frac{dI(z,\theta,\psi)}{dz} = I(z,\theta,\psi) - B(z,\theta,\psi).$$

This equation is simply written as:

$$-\mu\frac{dI(\tau,\mu,\psi)}{d\tau} = I(\tau,\mu,\psi) - B(\tau,\mu,\psi). \tag{1.3.8}$$

with the description of τ analogous to the former case and $\mu = \cos\psi$.

The solution for the outward radiation becomes:

$$I(\tau,\mu,\psi) = I(\tau_1,\mu,\psi)e^{-(\tau_1-\tau)/\mu} + \int_\tau^{\tau_1} B(\tau,\mu,\psi)e^{-(t-\tau)/\mu}\frac{dt}{\mu} \tag{1.3.9}$$

These are the equations that form the basis of radiative transfer. Up to this point we have considered the whole flux of the light, however light carries different components of the electromagnetic vector. These different components might react differently when transferred inside an inhomogeneous medium, which is the case in a magnetised medium.

1.3.2 Polarized radiative transfer

Now we would like to construct the same transfer equations and their formal solutions for polarized light. Unlike the last section where we considered light as a ray of energy, we would like to consider different components of its electromagnetic vector. For this we need to understand the nature of light using the Maxwell's equations and see how different components of the electromagnetic vector decompose into different components. Let's start with the sourceless Maxwell's equations in vacuum.

$$\begin{aligned} \nabla \cdot \vec{B} &= 0 \\ \nabla \times \vec{B} &= \frac{1}{c}\partial_t \vec{E} \\ \nabla \cdot \vec{E} &= 0 \\ \nabla \times \vec{E} &= -\frac{1}{c}\partial_t \vec{B} \end{aligned} \tag{1.3.10}$$

∂_t is a shorthand for $\frac{\partial}{\partial t}$. Then we construct the wave equations by taking the curl of the induction equations:

$$\begin{aligned} \nabla \times (\nabla \times \vec{E}) &= -\frac{1}{c}\partial_t(\nabla \times \vec{B}) = -\frac{1}{c^2}\partial_t^2 \vec{E} \\ \nabla \times (\nabla \times \vec{B}) &= \frac{1}{c}\partial_t(\nabla \times \vec{E}) = -\frac{1}{c^2}\partial_t^2 \vec{B} \end{aligned}$$

We further use the vector equalities and the lack of divergence in the sourceless equations to simplify.

$$\begin{aligned} \nabla \times (\nabla \times \vec{B}) &= \nabla(\nabla \cdot \vec{B}) - \nabla^2 B \qquad \nabla \cdot \vec{B} = 0 \\ &= -\nabla^2 B \end{aligned}$$

This applies for both of the curled Maxwell equations:

$$\begin{aligned} \nabla^2 B = \tfrac{1}{c^2}\partial_t^2 B \qquad & \nabla^2 E = \tfrac{1}{c^2}\partial_t^2 E \\ \left(\nabla^2 - \tfrac{1}{c^2}\partial_t^2\right) B = 0 \quad & \left(\nabla^2 - \tfrac{1}{c^2}\partial_t^2\right) E = 0 \end{aligned}$$

The equations with the squared derivative of the position and time vectors are simply the Poisson equation in 4 dimensions in vacuum, where the unit vectors are $x_\mu = [x_1, x_2, x_3, ict] = [\vec{r}, ict]$. The derivative operators turn out to be,

$$\frac{\partial}{\partial^\mu} = \partial_\mu = \left[\partial_1, \partial_2, \partial_3, \frac{1}{ic}\partial_t\right]$$

The Poisson equation for both the electric and magnetic field shows that the solution is oscillatory. Since the electric field satisfies the wave equation, it is represented as $E(k^\mu x_\mu)$ where x_μ is again the position vector and the k^μ is the amplitude. k^μ like x_μ should be a null vector, i.e. $r^2 = c^2 t^2$. Meaning $k^\mu = [k^1, k^2, k^3, i\omega/c] = [\vec{k}, i\omega/c]$. The null condition yields the dispersion equation for electromagnetic waves in vacuum: $\vec{k}^2 = \omega^2/c^2$. In effect

the definition of the electric field becomes $E(k^\mu x_\mu) = E(\vec{k}\cdot\vec{r} - \omega t)$. Looking at the wave equation again the formal equation becomes:

$$\left(\nabla^2 - \frac{1}{c^2}\partial_t^2\right) E(\vec{k}\cdot\vec{r} - \omega t) = 0.$$

For this condition to be satisfied E needs to be a harmonic equation, meaning it needs to be proportional to $e^{i(\vec{k}\cdot\vec{r}-wt)}$. We are concerned with the real part of the harmonic function, $\Re(e^{i(\vec{k}\cdot\vec{r}-wt)}) = \cos(\vec{k}\cdot\vec{r} - wt)$ but the imaginary part also has an important use in order to describe the phase difference. Hence, an electromagnetic plane wave in vacuum is described as:

$$\vec{E} = E_0 e^{i(\vec{k}\cdot\vec{r}-wt)}. \tag{1.3.11}$$

With the use of this description the electric field can be separated into its vectoral components:

$$\vec{E_1} = \epsilon_1 E_1 e^{i(\vec{k}\cdot\vec{r}-wt)}$$
$$\vec{E_2} = \epsilon_2 E_2 e^{i(\vec{k}\cdot\vec{r}-wt)}.$$

The separation into two components is enough for the description of the electromagnetic wave in 3-dimensions since, with the $\vec{k}$ vector, they form a basis. Hence, any kind of 3-vector basis can be set up as long as the arbitrary 2 vectors form a plane, perpendicular to the vector $\vec{k}$.

This choice is made to be experimentally convenient since the Stokes parameters I, Q, U, V correspond to sums and differences of measurable quantities. Considering three sets of Cartesian planes as $(\hat{x}, \hat{y})$, $(\hat{a}, \hat{b})$ which is the same Cartesian plane only with 45°of rotation and finally $(\hat{l}, \hat{r})$ that corresponds to left handed and right handed rotation. This rotation is achieved by retarding one component against the other by using the phase difference induced through imaginary numbers. This simply means:

$$\hat{l} = \frac{\hat{x} + i\hat{y}}{\sqrt{2}} \qquad \vec{r} = \frac{\hat{x} - i\hat{y}}{\sqrt{2}}.$$

Finally the Stokes parameters are defined as:

$$\begin{aligned} I &= |E_x|^2 + |E_y|^2 \\ Q &= |E_x|^2 - |E_y|^2 \\ U &= 2\Re(E_x E_y^*) = |E_a|^2 - |E_b|^2 \\ V &= 2\Im(E_x E_y^*) = |E_l|^2 - |E_r|^2. \end{aligned}$$

Now we have description of the vectoral components of a plane electromagnetic wave in vacuum and we can start considering how these different components of the radiation is transferred. In fact the Stokes parameter I corresponds to the intensity I that we used in the transfer equations in the former chapter.

Due to the number of the Stokes parameters, the transfer equations for polarized light also consist of a set of differential equations. These equations include absorption coefficients for all Stokes parameters and additional parameters describing the phase shift between different polarization modes, which are called the magneto-optical parameters.

These equations as defined by Hardorp et al. (1976):

$$\mu\frac{d}{dl}\begin{pmatrix} I \\ Q \\ U \\ V \end{pmatrix} = \begin{pmatrix} \kappa_I \\ \kappa_Q \\ 0 \\ \kappa_V \end{pmatrix} B - \begin{pmatrix} \kappa_I & \kappa_Q & 0 & \kappa_V \\ \kappa_Q & \kappa_I & -\rho_R & 0 \\ 0 & \rho_R & \kappa_I & -\rho_W \\ \kappa_V & 0 & \rho_W & \kappa_I \end{pmatrix} \begin{pmatrix} I \\ Q \\ U \\ V \end{pmatrix}$$

As mentioned above, $\kappa_{I,Q,U,V}$ are absorption coefficients for specific Stokes components of the light and the $\rho_{R,W}$ parameters are the magneto-optical parameters which are called Faraday rotation and Voigt effect respectively. Finally l is the path length. This form was derived by Unno (1956), and with the use of μ, the solutions are generalized to arbitrary angles and accordingly with the convenient choices of reference κ_U was taken to be zero.

For simplicity let's construct the matrix forms of these differential equations:

$$\mu\frac{dI^\alpha}{dl} = S^\alpha - A^{\alpha\beta}I_\beta \tag{1.3.12}$$

The coupling in these sets of equations is induced by I_β. It can be rectified by taking out the diagonal component inside the matrix $A^{\alpha\beta} = \kappa_I\delta^{\alpha\beta} + \kappa_I M^{\alpha\beta}$ and defining the generalized source function Q^α accordingly;

$$Q^\alpha = B^\alpha - M^{\alpha\beta}I_\beta, \quad B^\alpha = \frac{1}{\kappa_I}S^\alpha, \quad d\tau = \frac{\kappa_I}{\mu}dl \tag{1.3.13}$$

With the use of these definitions we end up with a simple formula:

$$\frac{dI^\alpha}{d\tau} = I^\alpha - Q^\alpha \tag{1.3.14}$$

There are multiple methods to solve this set of equations. Initially Unno (1956) assumed that the opacities are constant and that the source function is linear in optical depth and solved the equations analytically. Martin & Wickramasinghe (1979) took advantage of these approximations and used the analytical solutions as boundary conditions at the lowest layer to solve for the whole atmosphere.

$$I^\alpha = I_a^\alpha + I_b^\alpha\tau + \sum_i^4 I_a^\alpha e^{a_i\tau} \tag{1.3.15}$$

$$B = B_a + \gamma\tau \tag{1.3.16}$$

This expansion is inserted into the set of transfer equation, then the coefficients and a_i in the exponential is evaluated by comparing the constant linear and exponential parts on both sides of the equation.

There are also more modern methods in solving the polarization transfer equations. Another numerical method called Accelerated Lambda Iteration (ALI) is outlined in Deetjen

et al. (2003). In this method, polarized radiative transfer equations are approximately solvable by lambda iteration, at each layer:

$$I^{\alpha} = \Lambda_d Q^{\alpha}. \tag{1.3.17}$$

However, the solutions of this method is not exact, and we can express the difference of with the formal solution:

$$\Delta I^{\alpha} = (I^{\alpha} - I^{\alpha}_{\rm FS}) = \Lambda_d \cdot (Q^{\alpha} - Q^{\alpha}_{\rm FS}) \tag{1.3.18}$$

With the usage of Takeda (1991), a good approximation of the ΔI^{α} can be solved. ALI provides a smooth solution and takes electron scattering into account.

Another method currently in usage is referred to as APPROX (Jordan & Schmidt, 2003) and it takes the advantage of the generalized Stokes parameters for the case of large Faraday rotation (Ramaty, 1969), which is always applicable for the MWD atmospheres. Large Faraday rotation implies the average phase difference between the polarization ellipses to be 0 and enables the decoupling of transfer equations.

$$\mu \frac{dI_{\pm}}{d\tau} = \alpha_{\pm} \left(\frac{B}{2} - I_{\pm} \right) \tag{1.3.19}$$

Here I_+ is the ordinary mode of radiation and I_- is called the extraordinary radiation. μ is again $cos\theta$, the angle between magnetic field vector and the normal vector to the surface. Finally B is the usual source function. The transfer equations are described simply by opacities $\alpha_{\pm}$. Then the formal solution is:

$$I_{\pm} = \frac{B}{2}(1 - e^{-\alpha_{\pm} l}) \tag{1.3.20}$$

where l is the path traveled by the photon. Moreover according to Ramaty (1969), Stokes parameters can be calculated simply as:

$$\begin{aligned} I &= I_+ + I_- \\ Q &= I_+ \left(\frac{1 - a_+^2}{1 + a_+^2} \right) + I_- \left(\frac{1 - a_+^2}{1 + a_+^2} \right) \\ U &= 0 \\ V &= I_+ \left(\frac{2a_+}{1 + a_+^2} \right) + I_- \left(\frac{2a_+}{1 + a_+^2} \right) \end{aligned} \tag{1.3.21}$$

where

$$a_{\pm}(\omega/\omega_H, \theta) = \frac{2(\omega/\omega_H)\cos\theta}{-\sin^2\theta \pm \sqrt{\sin^4\theta + 4(\omega/\omega_H)^2\cos^2\theta}}. \tag{1.3.22}$$

All of these solutions were compared in terms of accuracy and computational speed, and it was shown that they are equivalent (Jordan & Schmidt, 2003).

1.3.3 Opacity sources

Regardless of the method, we need the opacities to calculate the resulting flux. These opacities reflect different mechanisms which the photons induce on the atmospheric material. We have already noted that LTE is applicable to the white dwarf atmospheres, which means we are dealing with *thermal absorption processes* (Mihalas, 1978). As opposed to the contrary case of energy loss by *scattering*, in *absorption* the photon completely disappears, transferring its energy to the thermal energy of the medium.

The type of absorption that the photons are subject to is defined by the initial and final state of the electron with which the photon interacts.

Bound-bound opacities

The bound-bound opacities are the result of *photoexcitation*. Namely, photons exciting a bound electron to a higher energy level. This requires a knowledge on the energy levels of the atom. For the non-magnetic case, the calculation of the energy bands are rather simple due to the degeneracies of the energy levels of numerous quantum numbers. However, under the effect of external fields, the degeneracies of the spin and orbital quantum numbers are broken. Hence, due to the diverse energy states involved, the calculations become numerically complicated.

These transitions have been studied extensively using the advent of increased computational power, starting in the 80s by groups at Tübingen (Roesner et al., 1984; Forster et al., 1984; Wunner et al., 1985; Wunner & Ruder, 1987), Louisiana State University (Henry & Oconnell, 1984, 1985) . The most extensive review on the theoretical basis of the behaviour of atoms under high field strengths can be found in Garstang (1977).

The solution of the energy levels and transition probabilities inherently depend on the strength of the field. Accordingly, the Hamiltonian of the electrons under the influence of magnetic fields is constructed and investigated in relevant field regime. To construct the Hamiltonian we start by the field free energy of the Hamiltonian and than add the effect of the magnetic field.

Hamiltonian of a free electron is defined as $\vec{p}^2/2m$, and under the effect of the magnetic field the free momentum $\vec{p}$ becomes $\vec{p}+e\vec{A}$ according to the results of classical mechanics and $-e$ being the charge of an electron (Although the rest of the thesis is in CGS units, this part is calculated in SI units for brevity). Then our Hamiltonian becomes:

$$H = \frac{1}{2m}\vec{p}^2 \rightarrow \frac{1}{2m}(\vec{p}+e\vec{A})^2. \tag{1.3.23}$$

To put our Hamiltonian into a convenient form we need to construct the vector potential $\vec{A}$. The fundamental relation between $\vec{B}$ and $\vec{A}$ is,

$$\vec{B} = \nabla \times \vec{A} \tag{1.3.24}$$

For our purposes we assume that the magnetic field is homogeneous and directed along z axis: $\vec{B} = [0, 0, B_z]$. This implies, according to equation 1.3.24, that the vector potential $\vec{A}$ has only x and y components. This means, with a choice of Coulomb gauge, that:

$$\begin{aligned} \nabla \cdot \vec{A} &= 0 \\ \partial_x A_x + \partial_y A_y &= 0 \\ \partial_x A_x &= -\partial_y A_y \\ A &= -\mathcal{A} y \hat{x} + \mathcal{A} x \hat{y} \\ \vec{A} &= [-\mathcal{A} y, \mathcal{A} x, 0] \end{aligned} \tag{1.3.25}$$

neglecting the constants of integration. This assumption is physically admissible since $\vec{A}$ is gauge invariant and any additional constants do not imply a physical difference.

Inserting this result into the equation 1.3.24 we end up with

$$\begin{aligned} \vec{B} = B_z &= \partial_x A_y - \partial_y A_x = 2\mathcal{A} \\ \mathcal{A} &= \frac{B_z}{2} \\ \vec{A} &= \frac{1}{2}(-B_z y \hat{x} + B_z x \hat{y}) = \frac{1}{2}(\vec{B} \times \vec{r}). \end{aligned}$$

as the vector potential. Now we can continue with our exploration of the Hamiltonian.

$$H = \frac{1}{2m}(\vec{p} + e\vec{A})^2 = \frac{\vec{p}^2}{2m} + \frac{e^2}{2m}(\vec{p} \cdot \vec{A} + \vec{A} \cdot \vec{p}) + \frac{e^2 \vec{A}^2}{2m} \tag{1.3.26}$$

In this representation the Hamiltonian can be decomposed into three parts. The first part with only the momentum corresponds to classical kinetic energy H_{KE}. The terms with linear dependence to $\vec{A}$ correspond to $H_{\mathrm{mag^I}}$ and terms in quadratic dependence in $\vec{A}$ are grouped as $H_{\mathrm{mag^{II}}}$.

We continue by simplifying the $H_{\mathrm{mag^I}}$ according to our description of the vector potential. First, the vector potential, $\vec{A}$, and the momentum operator $p = -i\hbar\nabla$, commute. Thus, $H_{\mathrm{mag^I}} = e(\vec{p}.\vec{A})/m$ and:

$$\begin{aligned} \frac{e}{m}\vec{p}.\vec{A} = \frac{e}{2m}\vec{p} \cdot (\vec{B} \times \vec{r}) &= \frac{e}{2m}\vec{B} \cdot (\vec{r} \times \vec{p}) \\ &= \frac{e}{2m}\vec{B} \cdot \vec{l} \end{aligned}$$

where $\vec{r} \times \vec{p} = \vec{l}$ is the angular momentum of the electrons. Additional effects are expected to this part of the Hamiltonian from the spin interaction in addition to the orbital angular momentum defined above. The interaction of the spin with the magnetic field is defined as $(g_E e/2m)\vec{B} \cdot \vec{s}$ where $\vec{s}$ is the spin angular momentum which has eigenvalues of $\pm 1/2\hbar$. The addition of this term yields the linear Zeeman Hamiltonian:

$$H_{\mathrm{mag^I}} = \frac{e}{2m}\vec{B} \cdot (\vec{L} + g_e \vec{S}) \tag{1.3.27}$$

For a general definition, we refer to the total orbital angular momentum L and total spin angular momentum S in case of a system with multiple electrons.

Next we consider the quadratic Zeeman term which is relatively simpler which $\vec{B} \times \vec{r} = Br \sin\theta$. Considering the addition of the energies of many electrons, the Hamiltonian becomes;

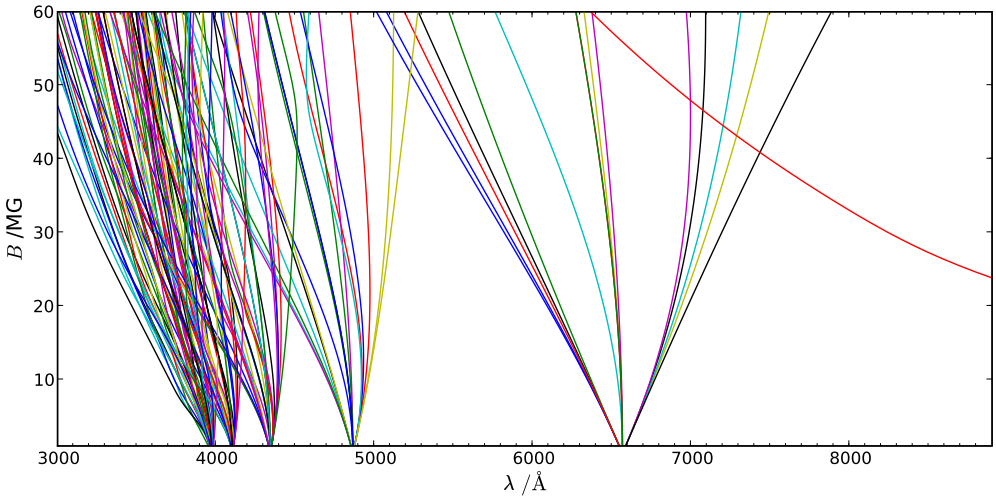

Figure 1.3: Paschen-Back regime for hydrogen transitions. The evolution of transition wavelengths with respect to increasing magnetic field strengths is shown.

$$H_{\mathrm{mag^{II}}} = \frac{e^2 B^2}{8mc^2} \sum r_i^2 \sin^2(\theta_i) \tag{1.3.28}$$

where the summation is over the atomic electrons and the angle is with respect to the direction of the magnetic field vector $\vec{B}$.

Furthermore, there are internal effects that need to be considered and the total Hamiltonian is written as

$$H = H_{\mathrm{KE}} + H_{\mathrm{C}} + H_{\mathrm{spin}} + H_{\mathrm{mag^{I}}} + H_{\mathrm{mag^{II}}} \tag{1.3.29}$$

in which H_{C} refers to the Coulomb potential, H_{spin} is the electron spin-orbit interaction term, and the terms $H_{\mathrm{mag^{I}}}$, $H_{\mathrm{mag^{II}}}$ are the aforementioned linear and quadratic Zeeman effects, respectively.

The method to solve for the transitions depends on the strength of the external field, where terms in the Hamiltonian can be neglected or approximately solved by perturbative methods wherever possible. Then, the common basis of the eigenvectors is found and the transition energy can be easily constructed. The perturbation calculations consists of identifying the unperturbed Hamiltonian, and the perturbative part of the Hamiltonian; constructing the eigenstates and eigenvalues of the unperturbed part. Then, the solution is simply reached by calculating the expectation value of the perturbation Hamiltonian (Sakurai & Tuan, 1994).

Now we will examine which states are applicable for the different field regimes and which parts of the Hamiltonian may be neglected or interpreted as a perturbative term.

For very weak magnetic fields, (i.e. $B \ll 5 \times 10^4 G$) the quadratic Zeeman effect ($H_{\mathrm{mag^{II}}}$) can be neglected and the linear Zeeman effect is smaller than the spin-orbit coupling ($H_{\mathrm{mag^{I}}} \ll H_{\mathrm{spin}}$). In this regime the good set of states, namely the states for which the Hamiltonian is diagnosable, are $|SLJM>$ and the deviation in the transitions are

mainly caused by the linear Zeeman effect. The transition energy ΔE becomes a deviation from the field free transition energy ΔE_0, where

$$\Delta E = \Delta E_0 + \frac{e\hbar}{2mc} B g_J M \tag{1.3.30}$$

and g_J is the Landé factor.

For stronger magnetic fields, the Paschen-Back effect becomes dominant and the spin-orbit coupling is broken, $H_{\rm C} \gg H_{\rm mag^I} \gg H_{\rm spin} \gg H_{\rm mag^{II}}$, and the states become $|SM_sLM_L>$. The first order effect is determined by the expectation value of the linear Zeeman effect ($H_{\rm mag^I}$).

$$\Delta E = \Delta E_0 + \frac{e\hbar}{2mc} B \Delta M_L. \tag{1.3.31}$$

This is true for transition rules of $\Delta M_L = 0, \pm 1$ (with $\Delta M_S = 0$). These selection rules imply that the transitions are split into three; one undisplaced central component and two components on the side, which are together called a *Paschen-Back Triplet*.

As the field strengths surpass $\geq 0.1\,MG$ the quadratic Zeeman effect ceases to be negligible, and must be included for the energy calculations as a first order correction. In this case the unperturbed states for a one-electron atom becomes $|nlm_lm_s>$ and the correction to the energy levels is,

$$\Delta E_Q = \frac{e^2 B^2 a_0^2}{8mc^2 Z^2} n^2 \frac{[5n^2 + 1 - 3l(l+1)][l^2 + l - 1 + m_l^2]}{(2l-1)(2l+3)}. \tag{1.3.32}$$

Here a_0 is the Bohr radius, and the transitions are defined according to the selection rule $\Delta l = 0, \pm 2$ (see Hamada & Nakamura, 1973; Garstang & Kemic, 1974). The energy correction has a dependence on quantum number n, which means that this regime is also applicable to weaker fields if the electrons are at higher n states.

The field strengths higher than 100 MG is usually called the intermediate regime since it is bordering between relatively simply described regimes of the quadratic Zeeman effect and the Landau regime where the Coulomb terms are neglected with respect to the magnetic terms. In this regime, the interaction energies of the magnetic fields are comparable to the Coulomb energies and the calculations are relatively simple (Yafet, 1956).

The lack of perturbative solutions prompted variational solutions of the atomics states, for field strengths up to 7×10^{11} G (Smith et al., 1972; Praddaude, 1972). The extensive calculations were undertaken later by numerous groups (Roesner et al., 1984; Forster et al., 1984; Wunner et al., 1985; Wunner & Ruder, 1987; Henry & Oconnell, 1984, 1985). In addition to all of these computationally expensive methods, a pseudo-spectral algorithm for the solution of one-,two- and three-electrons was proposed recently by Heyl & Thirumalai (2010) which is much simpler. Their calculation method is based on the work of Thirumalai & Heyl (2009) which solves the two-dimensional differential equations for the wave functions and potentials numerically for the intermediate regime. The simplicity of the method comes from the fact that the approximate solutions to the differential equations are polynomials and can be interpolated. However, we did not rely on this calculations in our work, hence we will not discuss the details of this here.

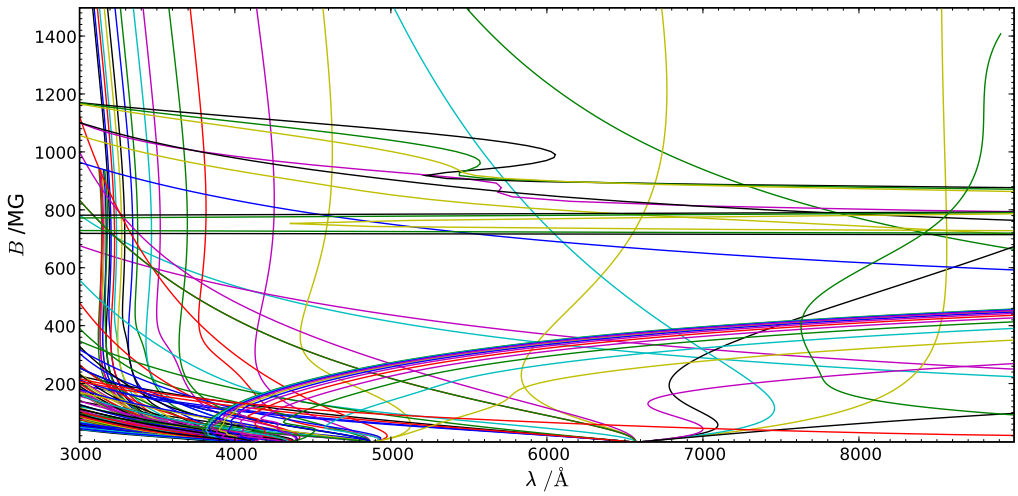

Figure 1.4: The behaviour of the hydrogen transitions under the influence of magnetic fields. The field strengths relevant to the MWDs are shown.

Bound-free opacities

When photons ionize the bound electrons of an atom, the final state is simply defined by the kinetic energy of the electron. This process is called *photoionization* and is yet another source of absorption.

The initial treatment of bound-free opacities was undertaken by Lamb & Sutherland (1974) in which they considered field strengths lower than $\leq 10\,\mathrm{MG}$ and a dipole approximation for the transition cross-sections is applicable.

$$\kappa_{\Delta m} = \mathrm{const} \times 4\pi^2 \frac{\mathrm{e}^2\omega}{\mathrm{c}} \sum_{\mathrm{i,f}} |< \mathrm{f}|\mathrm{d}_{\Delta\mathrm{m}}|\mathrm{i} >|^2 \, \delta(\mathrm{E_f} - \mathrm{E_i} - \hbar\omega), \;\; \Delta\mathrm{m} = 0, \pm 1$$

Here $\hbar\omega$ is the photon energy, E_i is the bound energy and E_f is the final free energy of the electrons. Δm is the change in the magnetic quantum number, m. Using the assumption of Lamb & Sutherland (1974) the wavefunctions are unchanged but the energies are Zeeman shifted. These shifts in energy are the same for transitions with same Δm and are proportional to the Larmor frequency ($\omega_L = eB/2mc$), i.e. $\Delta m = \hbar\omega_L$.

The matrix element part can simply be written as a function $f_{\Delta m}(\omega)$:

$$f_{\Delta m}(\omega) = \sum_{i,f} |< f|d_{\Delta m}|i >|^2 \, \delta(E_f - E_i - \hbar\omega) \tag{1.3.33}$$

$$f(\omega) = \frac{1}{\omega}\sigma(\omega) \approx \frac{1}{\omega} \sum_{i=1}^{4} \bar{\sigma_i} \tag{1.3.34}$$

Here the cross-section $\bar{\sigma_i}$ is defined as area per electron in an energy level of a principle quantum number n, and averaged over the angular momentum quantum numbers. The

cross-sections come from the field free consideration of Kramers' approximation (see e.g. Mihalas, 1978),

$$\sigma = \frac{64\pi^4 e^{10} m}{3\sqrt{3} c h^6 Z^4} \frac{\lambda^3}{c^3 n^5} g_{II} \tag{1.3.35}$$

where g_{II} is the gaunt factor.

For the calculation of the function f, cross-sections of levels only up to $n = 4$ are considered for $\lambda < 15\,000\,\text{Å}$. This is also due to pressure ionization, namely the separation between the particles are smaller than the Bohr radius at high levels. The bound-free absorption for low field strengths becomes:

$$\kappa_{\Delta m}(\omega) = \frac{\omega}{\omega - \Delta m \omega_L} \kappa_0 (w - \Delta\omega_L). \tag{1.3.36}$$

The shortcoming of the calculation of Lamb & Sutherland (1974) is the $10\,\text{MG}$ limit to the field strength. This is inherently connected to the simple approximation that considers the shifting of the field free bound states. Additionally, free electrons are subject to forces induced by the external magnetic field and they occupy Landau states. If the field is in z direction, the final momentum is only in z direction and the final energy is defined as $p_z^2/2m$. Thus, the energy corresponding to a perpendicular motion is quantized (Garstang, 1977).

$$E = \left(n + \frac{1}{2} m + \frac{1}{2} |m| \right) \hbar\omega_c + p_z^2/2m.$$

Here, ω_c is the cyclotron frequency ($eB/m_e c$). Since only $m \leq n$ is allowed, for positive m, $E_{min} = m\hbar\omega_c$ and for negative or zero m, $E_{min} = 0$.

A further correction is made by Jordan (1992) for the photoionization edge wavelengths. For the bound states in which energy calculations exists, the photoionization offsets can be calculated via transition to the lowest Landau level.

In this case, the Balmer edge splits into 12 components (4 for each Δm) in 8 different wavelengths. Beyond these determined absorption edges, the contribution of a transition to the absorption is approximated by the Lamb-Sutherland equation (1.3.36) again, but the contribution of each Δm transition to the opacities is distributed to the total using the Wigner-Eckart theorem (see Landau & Lifshitz, 1977). The absorption coefficient for transitions from bound state (n, l, m) to $(n', l', m + \Delta m)$ is then written as:

$$\kappa_{bf} = \kappa_{\Delta m} \begin{pmatrix} l & 1 & l' \\ -m & \Delta m & m + \Delta m \end{pmatrix}$$

where $\kappa_{\Delta m}$ is the same absorption coefficient from the Lamb-Sutherland method and the matrix corresponds to the resulting coefficient; *3 j symbols* calculated from Wigner-Eckart theorem. In our code this procedure is applied for transitions with quantum numbers n up to four.

A shortcoming of this method is the assumption that magnetic field completely dominates and the influence of the Coulomb force on the lower Landau states is ignored (Kara

& McDowell, 1981). However this picture is not applicable for fields strengths between $10 - 10^3$ MG. It has been noted that for a consistent picture, the effect of the Coulomb forces together with the influence of the magnetic fields need to be considered (see West, 1989, and references therein)

Photoionization cross-section studies with full quantum mechanical calculations were made by Delande et al. (1991) and Merani et al. (1995) with the use of a complex-rotation method. In addition to this, Merani et al. (1995) expanded the eigenvectors of the rotated Hamiltonians in Sturmian basis. Using this method, the complex matrix was diagonalized to calculate the photoionziation cross-sections of hydrogen in magnetic fields between 117 and 235 MG. In the work of Zhao & Stancil (2007), the rotated Hamiltonians are expanded in the Slater-Landau basis. The size of the basis is much smaller than the Sturmian basis.

Free-free opacities

When a photon is absorbed by an electron and the kinetic energy of the electron is altered with respect to the ion in its vicinity, this process is called a free-free absorption.

The transitions from one free state to another free state can be expressed as transitions in Landau states, which enumerate the quantized states in the direction perpendicular to the magnetic field. These quantized states correspond to the classical picture of helically moving electrons which move in the x-y plane on quantized orbits and propagate freely in the z direction.

The cross-section for the cyclotron absorption that was used for a long time in magnetic white dwarf atmospheric calculations is from (Lamb & Sutherland, 1971, 1974):

$$\sigma_+(\omega_H, \alpha) = \frac{4\pi^{3/2}}{|\cos\alpha|}\frac{e^2}{mc}\frac{1}{\omega}\left(\frac{mc^2}{2kT}\right)^{1/2}\frac{1}{1-e^{-\hbar\omega/k_BT}}e^{-\frac{mc^2}{2kT\cos^2\theta}\frac{(\omega-\omega_H)^2}{\omega^2}}.$$

The exponential term of the cross-section puts a tight constraint on the frequency dependency. Therefore, the major contribution to the cross-section is for frequencies near cyclotron frequency. Cross-section under the assumption of $\omega \approx \omega_H$, according to Lamb & Sutherland (1974) is:

$$\sigma_+(\omega_H, \alpha) \approx \frac{4\pi^{3/2}c}{|\cos\alpha|}\frac{e^2}{\hbar}\left(\frac{c}{\omega_H}\right)^2\left(\frac{mc^2}{2kT}\right)^{1/2}\frac{B}{B_q}\frac{1}{1-e^{-\hbar\omega_H/k_BT}}e^{-\frac{mc^2}{2kT\cos^2\theta}\frac{(\omega-\omega_H)^2}{\omega^2}}. \tag{1.3.37}$$

Here B_q corresponds to the quantum critical magnetic field, $B_q = \frac{m^2c^3}{e\hbar} = 4.414 \times 10^{13}\ G$. The subscript $+$ refers to a transition of $\Delta M = +1$, hence the cyclotron cross-section is only induced by right handed photon transitions.

The solution of Lamb & Sutherland (1971) is based on quantum calculations of the scattering cross-section using one electron. Later, this cross-section is convolved by the velocity of the electrons, which effectively broadens the cyclotron resonance due to the Doppler shift induced by the velocity distributions of electrons. This broadening is apparent in the equation 1.3.37 as a Gaussian with the argument $\frac{mc^2}{2kT\cos^2\theta}\frac{(\omega-\omega_H)^2}{\omega^2}$ where the factor $\frac{c^2}{2v_T^2\cos^2\theta}$ enumerates the angle dependent broadening due to the is the thermal velocity v_T of the electrons.

Another known contribution to the cyclotron cross-section is electron collisions. Bekefi (1966) derived the cyclotron cross-section via collisional broadening classically as:

$$\sigma_{\rm cyc} = \frac{e^2}{m_e c}(1+\cos^2\alpha)\frac{kT}{2\pi\hbar\omega}(e^{\hbar\omega/kT}-1)\frac{\nu_{\rm eff}}{(\omega_H-\omega)^2-\nu_{\rm eff}^2} \tag{1.3.38}$$

where $\nu_{\rm eff}$ is the effective collisions of the electrons.

The method of Bekefi (1966) was to first calculate the cyclotron emissivities and then use that to determine the cyclotron absorption using Kirchoff's law (equation 1.3.4). The cross-section under the effect of electron collisions has a Lorentzian profile. This can be combined with the Gaussian profile induced from the Doppler broadening of the resonance, to effectively have a Gaussian at the center and a Lorentzian at the wings of the profile. This heuristic argument, which was put forward by Martin & Wickramasinghe (1979) leads to line profiles with Voigt profiles.

$$H(a,v) = \frac{a}{\pi}\int_{-\infty}^{\infty} dy \frac{e^{(y+v)^2}}{y^2+a^2} \tag{1.3.39}$$

for our case it becomes:

$$H(\nu'_{\rm eff}, Z) = \frac{\nu'_{\rm eff}}{\pi}\int_{-\infty}^{\infty} dy \frac{e^{(y+Z)^2}}{y^2+\nu'^2_{\rm eff}}$$

where Z represents the angle dependent Doppler broadened resonance $(\omega-\omega_H)/(\sqrt{2}\omega\beta_T)$ and $\nu'_{\rm eff}$ is the dimensionless effective collision $\nu_{\rm eff}/(\sqrt{2}\omega\beta_T)$, β_T in both equations correspond to $\beta_T = v_T/c$. The reason for the choice of $\nu'_{\rm eff}$ will become clearer when we solve the cyclotron cross-sections using plasma physics formalism in Sec. 4.4. For simplicity, let's define the term that introduces Gaussian broadening as $\Delta_D = \sqrt{2}\omega\beta_T$. The Voigt function is used to describe the broadening of the lines using the formalism of Beckers (1969) and it was also explained in detail by Born et al. (1959).

One of the most important problems in synthesizing magnetic spectrum is the magnetic broadening due to the limited precision of the magnetic grids. Since the surface area of each single spectrum which represents the single magnetic field strength and direction has a size, the associated magnetic field strength also is not discrete but a distribution around the mean value. Only this fact itself causes the magnetic broadening of single field vector spectrum. The magnetic broadening of the cyclotron lines was conceived as a Gaussian profile and implemented accordingly to the Voigt profiles.

$$\sigma_{\rm cyc} = \sigma_+ H\left(\frac{\nu_{\rm eff}}{\Delta_D+\Delta_B}, \frac{\omega-\omega_H}{\Delta_D+\Delta_B}\right) \tag{1.3.40}$$

where Δ_B quantifies the Gaussian broadening due to the distribution of the magnetic field over a surface element ΔB. The influence of variation on the spectrum can be expressed in terms of frequency as,

$$\Delta_B = \frac{\Delta\omega_H}{\omega} = \frac{\Delta B e}{mc}\frac{1}{\omega}. \tag{1.3.41}$$

The magnetic broadening parameter can be decomposed into the variation of the cyclotron frequency with respect to the photon frequency due to the magnetic variation. This means broadening is only effective near the cyclotron frequency.

Additionally, in the free-free regime of the spectrum, the magneto-optical parameters need to be accounted for. When light is propagating in magnetized media polarization is expected occur due to the anisotropies induced by the fields in the plasma. To explain the dichroic nature of the material, the physical concepts of Faraday rotation (ρ_R) and Voigt effect (ρ_W) are used. Due to the broken symmetry of the dielectric tensor ϵ_{ij}, the electric vector of the electromagnetic wave rotates (ρ_R), and a phase retardation between linear polarizations occurs (ρ_W) .

ρ_R and ρ_W are defined proportional to the angle of rotation in their relevant polarization planes. These rotation angles are defined by Smith (1966) as:

$$\Theta = \frac{\omega l}{2c}(n_+ - n_-), \qquad \Phi = \frac{\omega l}{c}(n_\parallel - n_\perp)$$
$$\rho_R = -2\cos\alpha\frac{1}{\kappa_R}\frac{d\Theta}{dl}, \qquad \rho_W = -\frac{1}{\kappa_R}\sin^2\alpha\frac{d\Phi}{dl}$$

From Wittmann (1974):

$$\begin{aligned}\rho_R = \cos\alpha\frac{d(2\Theta)}{d\tau} &= 2\frac{\pi}{\lambda_0}(n_+ - n_-)\cos\alpha \\ &= \frac{\omega_H}{c}(n_+ - n_-)\cos\alpha \\ \rho_W = \cos\alpha\frac{d(\Phi)}{d\tau} &= \frac{2\pi}{\lambda_0}(n_\parallel - n_\perp)\sin^2\alpha \\ &= \frac{\omega_H}{c}(n_\parallel - n_\perp)\sin^2\alpha. \end{aligned} \tag{1.3.42}$$

Assuming $\omega \gg \omega_H$, $\omega \gg \omega_p$, $\nu_e = 0$ and taking from Pacholczyk (1977);

$$\begin{aligned}\rho_R &= -\frac{\omega_p^2\omega_H}{c\kappa_R(\omega^2 - \omega_H^2)}\cos\alpha \\ \rho_W &= -\frac{\omega_p^2\omega_H^2}{2c\kappa_R(\omega^2 - \omega_H^2)}\sin^2\alpha. \end{aligned} \tag{1.3.43}$$

These values are approximated for $\omega \neq \omega_H$, namely away from the cyclotron frequency by Pacholczyk (1977). The incompatibility of the Pacholczyk (1977) description of the magneto-optical parameters is apparent with respect to the cyclotron absorption coefficients, in which the effects of broadening due to velocity distributions of electrons and their effective collisions are taken into account. In addition to the lack of these broadening mechanisms, the resonance structure was oversimplified due to expansions on the basis of $\omega_H \ll \omega$.

There were various attempts made at including the effects of broadening for the magneto-optical parameters. One method was to implement the line broadening formulas for the bound-bound transitions, according to the broadening theory (Born et al., 1959; Wittmann, 1974; Beckers, 1969; Martin & Wickramasinghe, 1981). In the work of Jordan

et al. (1991) different methods to implement effective collisions and the magnetic broadening was developed. However a single consistent method to implement Doppler broadening, collisional broadening and the magnetic broadening to both cross-section and the magneto-optical parameters does not exist in the literature.

The details of the various methods for calculating cyclotron cross-sections will be discussed extensively in Chapter 4.

1.4 Summary

In this section we have outlined the theory of white dwarfs which is necessary to diagnose the observations and estimate physical properties of these objects. We have discussed the structure and the cooling of white dwarfs and showed that magnetism can influence the structure of a white dwarf. Furthermore, we have given an overview of radiation transfer in MWD atmospheres which is instrumental in determining the effective temperature and magnetic structure of MWDs. The formalism outlined here is the basis of the investigations undertaken in the following chapters. We will continue our investigation of the MWD population and their magnetic structures in Chapter 2. Later in Chapters 3 and 5 we will make use of the structure of white dwarfs to assess their evolutionary histories.

Chapter 2

Statistics of Magnetic White Dwarfs

2.1 Introduction

White dwarfs with magnetic field strengths of between 10^4 and 10^9 G are understood to represent more than 10% of the total population of white dwarfs (Liebert et al., 2003). The Sloan Digital Sky Survey (SDSS), the largest spectroscopic survey carried out to date, has discovered thousands of new white dwarfs, among them 102 with magnetic fields (MWDs) (Gänsicke et al., 2002; Schmidt et al., 2003; Vanlandingham et al., 2005). After the analysis of Data Release 3 (DR3), the number of known magnetic white dwarfs had increased from 65 (Wickramasinghe & Ferrario, 2000; Jordan, 2001) to 167 (Kawka et al., 2007). The first seven magnetic DAs (DAHs) uncovered from SDSS were visually identified in the area of the initial Early Data Release (EDR Gänsicke et al., 2002). Schmidt et al. (2003) added 46 objects in the DR1, 38 of them DAH, plus three new magnetic helium rich WDs (DBH), and five new MWDs with metallic and molecular lines. Vanlandingham et al. (2005) reported on 49 additional new MWDs from the DR2 and DR3, specifically 46 new DAH, two new DQAs and one DQ with molecular bands.

Schmidt et al. (2003) and Vanlandingham et al. (2005) determined the field strengths and the inclinations of the magnetic dipoles by visually comparing the observed spectra with model spectra. They used an extension of the modeling method of Latter et al. (1987) accounted for the effect of the change of magnetic field strength on line depths and the variation in the field strength over the stellar surface for only the unpolarized radiation flux, namely Stokes parameter I. Their analyses with this simplified method of radiation transport resulted in dipolar field strengths for the SDSS MWDs of between 1.5 MG and ~ 1000 MG. Including the pre-SDSS, formerly known as MWDs, their sample consisted of 111 MWDs, 97 being classified as DAHs.

In this chapter, we present the reanalysis of data of SDSS DAHs detected by Gänsicke et al. (2002), Schmidt et al. (2003), and Vanlandingham et al. (2005), plus the analysis of data for 44 new detection from all SDSS data until DR7 (DR4 until DR7 were not scanned systematically for MWDs).

2.2 SDSS Data

SDSS investigates five-band photometry of the Northern Galactic Polar Cap using the 2.5 meter telescope at Apache Point, New Mexico, with its special purpose instruments

(Fukugita et al., 1996). Follow-up spectroscopy of many stars is also performed with the twin dual-beam spectrographs (3900 - 6200 and 5800 - 9200 $\AA, \lambda/\Delta\lambda \sim 1800$), in particular of blue objects such as white dwarfs and hot subdwarfs (Harris et al., 2003; Kleinman et al., 2004). Since the energy distribution of strongly magnetic white dwarfs can differ from nonmagnetic ones, MWDs are found not only in the SDSS color categories for white dwarfs or blue horizontal-branch stars, but may also fall into the color categories for quasars (QSOs), "serendipitous blue objects", and hot subdwarfs. Based on their colors, objects are assigned to fibers for follow-up spectroscopic investigations (for spectroscopic target selection, see Stoughton et al., 2002).

To identify magnetic white dwarfs from these samples, different techniques were used. For white dwarfs selected by color cuts in the u-g versus g-r color-color diagram, Gänsicke et al. (2002) and Schmidt et al. (2003) used visual inspection. In the work by Vanlandingham et al. (2005), visual identification was complemented with the *autofit* process (Kleinman et al., 2004), which fits spectra and photometry of hydrogen and helium white dwarfs to theoretical models. We note that white dwarfs with magnetic fields above 3 MG are flagged because of the poor χ^2 fits in the *autofit* process and MWDs with weaker magnetic fields might therefore be overlooked (Vanlandingham et al., 2005).

In addition to the data from the former SDSS MWD papers (DR1-DR3), we analysed new data of nineteen additional objects from the HYPERMUCHFUSS (HYPER velocity or Massive Unseen Companions of Hot Faint Under-luminous Stars Survey; see Tillich et al., 2009). This survey aims to detect high velocity underluminous B stars and white dwarfs. The candidates were chosen by the selection criterion (u-g)<0.4 and (g-r)<0.1, and spectral fits were performed to determine the radial velocity. Some objects showed formally very high negative radial velocities ($\leq -100\,\mathrm{km/s}$) but turned out toward be DAHs. The reason for this is that the higher-order Balmer lines of magnetic white dwarfs are shifted systematically to the blue, even for relatively small magnetic fields ($\leq 20\,\mathrm{MG}$), because of the quadratic Zeeman effect, which mimicks a high radial velocity. Additionally, 34 DAHs were serendipitously found in the course of a visual inspection of blue stellar objects from DR7. The total number of DAHs from SDSS is likely to increase yet further once a systematic search of all DR7 spectra has been carried out.

The one-dimensional spectra used in this work were generated by SDSS's spectroscopic pipeline `spectro2d` and downloaded from the Data Archive Server.

2.2.1 Analysis

Our model spectra are calculated with a radiative transfer code for magnetized white dwarf atmospheres that, for a given temperature and pressure structure of a model atmosphere (T_{eff}, $\log g$) and a given magnetic field vector with respect to the line of sight and the normal on the surface of the star, calculates both theoretical flux and polarization spectra (see Jordan, 1992; Jordan & Schmidt, 2003).

To increase efficiency, we pre-computed a three-dimensional grid of Stokes I and V (V spectra were not used due to a lack of polarization measurements) model spectra with effective temperature $7\,000\,\mathrm{K} \leq T_{\mathrm{eff}} \leq 50\,000\,\mathrm{K}$ 14 steps, magnetic field strength $1\,\mathrm{MG} \leq B \leq 1.2\,\mathrm{GG}$ in 1200 steps, and 17 different directions of ψ relative to the line of sight, as the independent variables (9 entries, equally spaced in $\cos\psi$). All spectra were calculated for a surface gravity of $\log g = 8$. Since no polarization information is available from the SDSS, our analysis is limited to the flux spectra (Stokes parameter I). Limb darkening is accounted for by a simple linear scaling law (see Euchner et al., 2002).

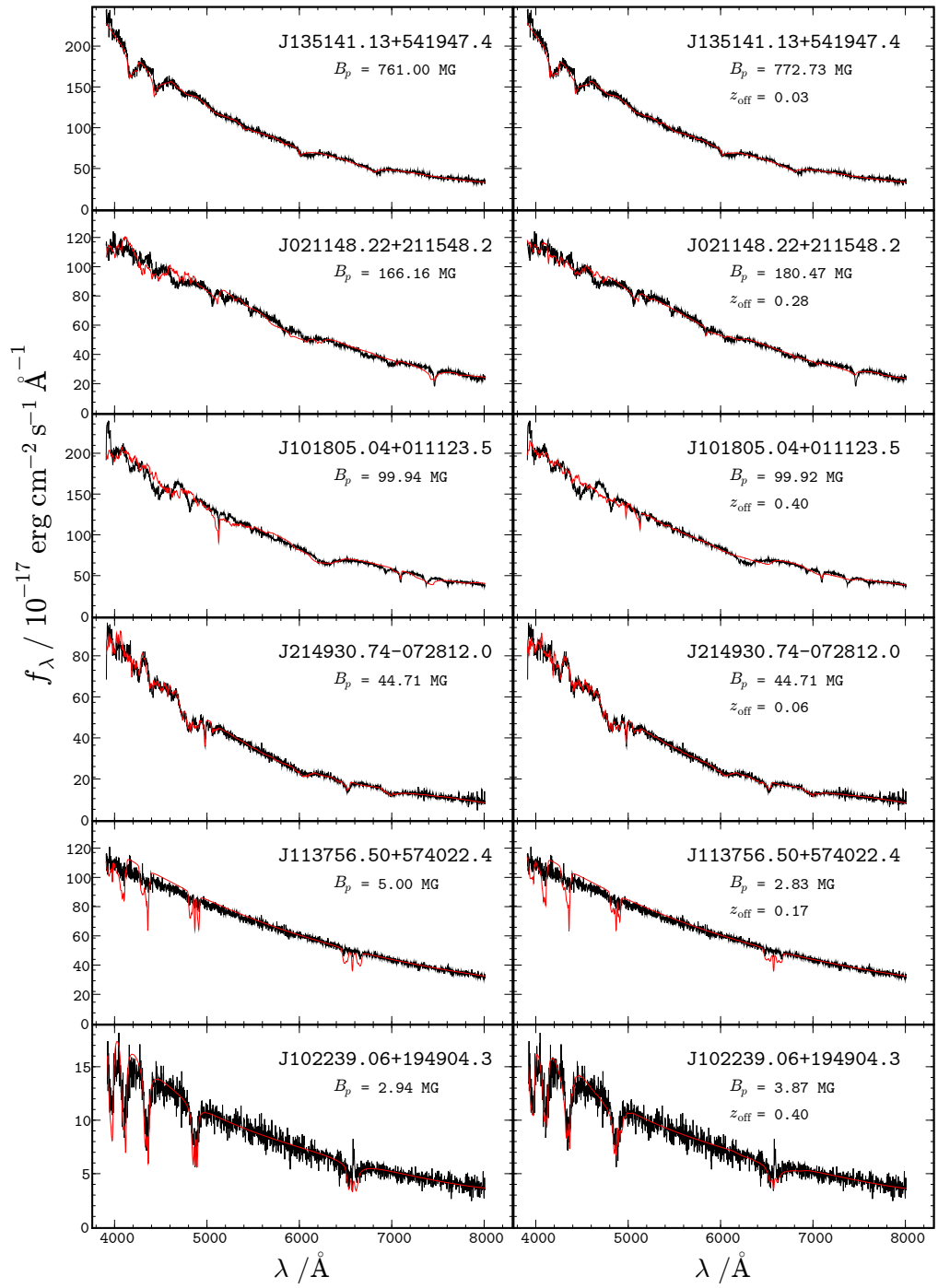

Figure 2.1: Fits of observed spectra of DAHs from the SDSS to centered magnetic dipoles with a polar field strength B_p (left) and dipoles shifted by $z_{\rm off}$ stellar radii along the dipole axis (right). Representative fits and objects mentioned in this chapter are chosen.

The magnetic field geometry of the DAHs was determined with a modified version of the code developed by Euchner et al. (2002). This code calculates the total flux (and circular polarization) spectra for an arbitrary magnetic field topology by adding up appropriately weighted model spectra for a large number of surface elements and then evaluating the goodness of fit. Magnetic field geometries are defined by multipole expansions of the scalar magnetic potential (Jacobs, 1987):

$$V_m(r,\theta,\phi) = \frac{a}{\mu_0}\sum_{l=1}^{\infty}\left(\frac{a}{r}\right)^{l+1}\sum_{m=0}^{l}(G_l^m\cos m\phi + H_l^m \sin m\phi)P_l^m(\cos\theta). \tag{2.2.1}$$

Where a is the radius of the white dwarf. From this equation the magnetic field vectors on the surface of the MWD ($r = a = 1$) are calculated to be

$$\begin{aligned}
B_r &= \mu_0\frac{dV_m}{dr} = -\sum_{l=1}^{\infty}\sum_{m=0}^{l}(l+1)A_l^m P_l^m(\cos\theta)\\
B_\theta &= \frac{\mu_0}{r}\frac{dV_m}{d\theta} = \sum_{l=1}^{\infty}\sum_{m=0}^{l}A_l^m\frac{d}{d\theta}P_l^m(\cos\theta)\\
B_\phi &= -\frac{\mu_0}{r\sin(\phi)}\frac{dV_m}{d\phi} - \frac{dV_m}{dr} = -\sum_{l=1}^{\infty}\sum_{m=0}^{l}mB_l^m\frac{P_l^m(\cos\theta)}{\sin\theta}
\end{aligned}$$

where A_l^m, B_l^m determine the amplitudes of the multipole components.

The individual multipole components can be independently oriented in azimuth (Θ_d) and in longitude (Φ_d) with respect to the rotation axis of the white dwarf and offset with respect to its center, allowing the modeling of rather complex surface field topologies. Components in a right handed spherical coordinate system can easily be transformed to Cartesian coordinates, where x is pointing to the observer and the z axis is where azimuth is zero. The dipolar component ($l = 0$, $m = 0$) can be defined in its Cartesian coordinates, where z' is pointing towards the pole.

$$\begin{aligned}
B_{x'}^p &= 3\frac{B_{\rm pol}^{\rm p}\,x'z'}{2r'^5}\\
B_{y'}^p &= 3\frac{B_{\rm pol}^{\rm p}\,y'z'}{2r'^5}\\
B_{z'}^p &= \frac{B_{\rm pol}^{\rm p}(3z'^2 - r'^2)}{2r'^5}.
\end{aligned} \tag{2.2.2}$$

Here $B^{\rm p}$ is the field strength at the pole and offsets to the multipoles $(x_{\rm off}, y_{\rm off}, z_{\rm off})$ are introduced in the x', y', z' coordinate system.

Additional free parameters are the white dwarf effective temperature and the inclination of the rotation axis with respect to the line of sight. Observed spectra are fitted using an evolutionary algorithm (Rechenberg, 1994) with a least-squares quality function.

In addition to the Zeeman effect, Stark broadening must be considered. When the electric and magnetic fields are parallel, Friedrich et al. (1994) estimated the effect on stationary line components, which are transitions that vary slowly in wavelength for large

intervals of magnetic field strengths. Stationary lines are more pronounced than non-stationary lines, since they are not smeared out extensively by the variation in the magnetic field strength over the stellar surface.

However, no atomic data for hydrogen in the presence of both a magnetic and electric field are available for arbitrary strengths and arbitrary angles between two fields. Therefore, only a crude approximation (see Jordan, 1992) is used in our model and systematic uncertainties are unavoidable, particularly in the low-field regime (≤ 5 MG), where the Stark effect dominates. Consequently, effective temperatures and surface gravities derived by fitting the Balmer lines alone are less reliable than in the case of non-magnetic white dwarfs. This may also produce disagreements with temperature estimates derived from the continuum slope.

Time-resolved analysis for rotating single magnetic white dwarfs was instrumental in determining rather complex field structures (e.g., VLT observations by Euchner et al., 2002, 2005, 2006). However, this usually relies on the preliminary knowledge of period, which is usually derived separately by photometry. Although the individual SDSS fiber spectra exists with 15 minute exposure time, because of a lack of information about spin period, we constrained ourselves to the coadded spectra, which includes 3 or more individual spectra with total exposure times of at least 45 minutes. With the possible exception of a few bright objects, the signal-to-noise ratio of the individual spectra would not be sufficient to find indications of rotational changes. Therefore, we had to restrict ourself to simple models for the magnetic field geometry, namely centered magnetic dipoles with only two free parameters or to dipoles offset along the magnetic axis with three free parameters. These parameters are the magnetic dipole field strength B_p,and the inclination of the dipole axis i for the centered dipole. For the offset dipole, there is an additional offset parameter along the magnetic axis $z_{\rm off}$ in terms of the stellar radius. For the 97 DAHs analysed, we used the literature values for $T_{\rm eff}$, which were determined by comparison to the theoretical non-magnetic DA colors in the u-g vs g-r plane (Schmidt et al., 2003; Vanlandingham et al., 2005). The temperature of the new DAHs presented in Table A.1 were estimated with synthetic SDSS color-color diagrams by Holberg & Bergeron (2006)[1], assuming that the influence of the magnetic field on the temperature determination is small, which is not always the case (see Schmidt et al., 1986; Gänsicke et al., 2001, and Sect.2.3.1).

All fits have reduced χ^2 values between 0.8 and 3.0 except for some high-field objects that obviously deviate from the assumed dipole geometry (see Sect. 2.3). We use the error calculation method of Zhang et al. (1986), which assumes that a small change in χ^2 could be approximated by a linear expansion of the covariance matrix; for complex χ^2 topologies, this approximation is inaccurate, final error in the inclination is often very large.

Final fit parameters with errors are noted in Table C.1 that is included in the appendix. In Figs. 2.1 and 2.2, we show fits of 12 DAHs, as an example. All of the fits to our remaining spectra can be found in the Appendix B (Fig. B.1-B.22 for the other DAHs).

2.3 Statistics of Magnetic White Dwarfs

Individual objects

Three objects analysed by Schmidt et al. (2003) and Vanlandingham et al. (2005) were omitted in our analyses. *J05959.56 +433521.3* (*G111-49*) was listed by Schmidt et al.

[1] http://www.astro.umontreal.ca/∼bergeron/CoolingModels/

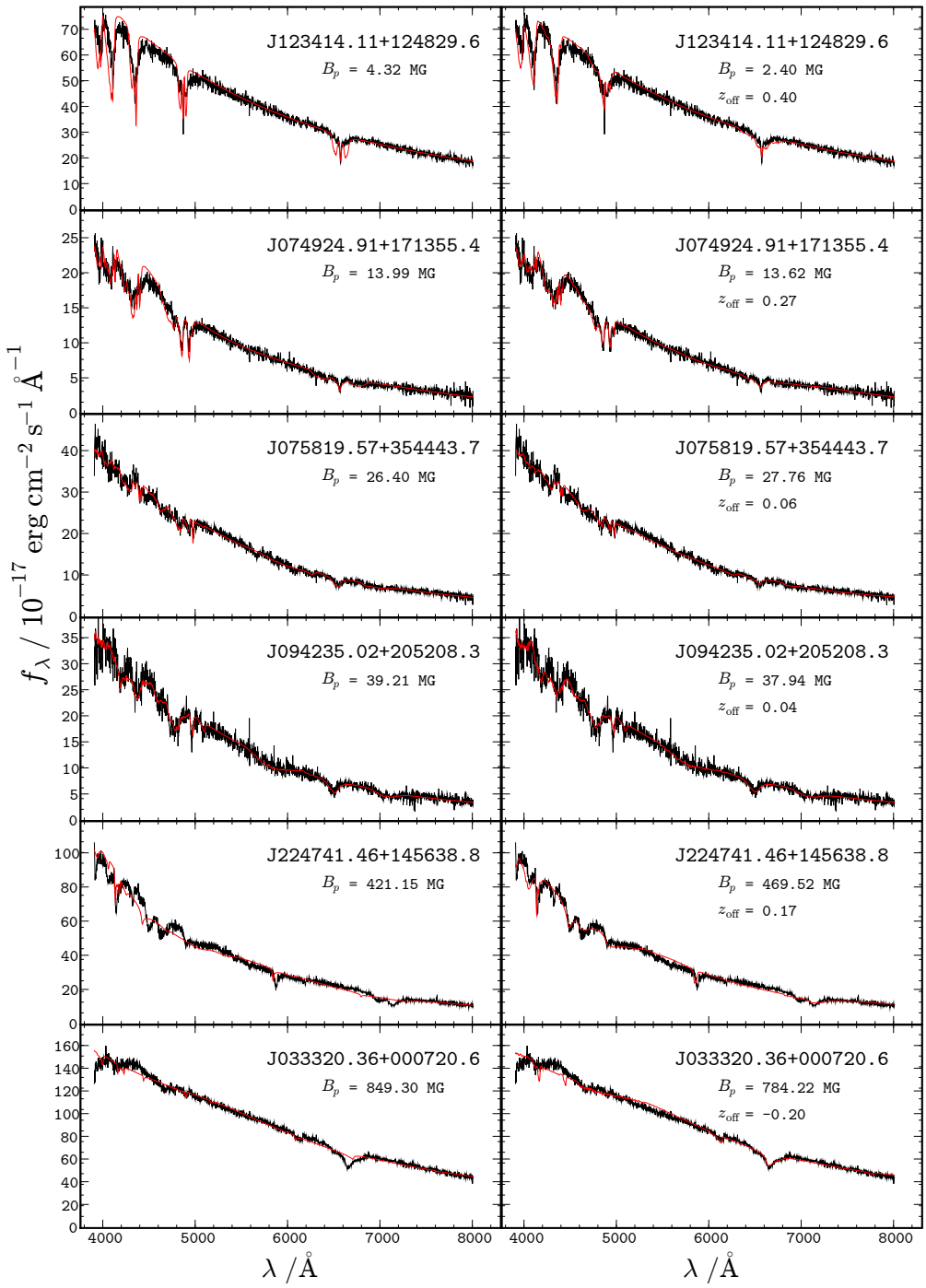

Figure 2.2: Fits of observed spectra of DAHs from the SDSS to centered magnetic dipoles with a polar field strength B_p (left) and dipoles shifted by $z_{\rm off}$ stellar radii along the dipole axis (right). Representative fits and objects mentioned in this chapter are chosen.

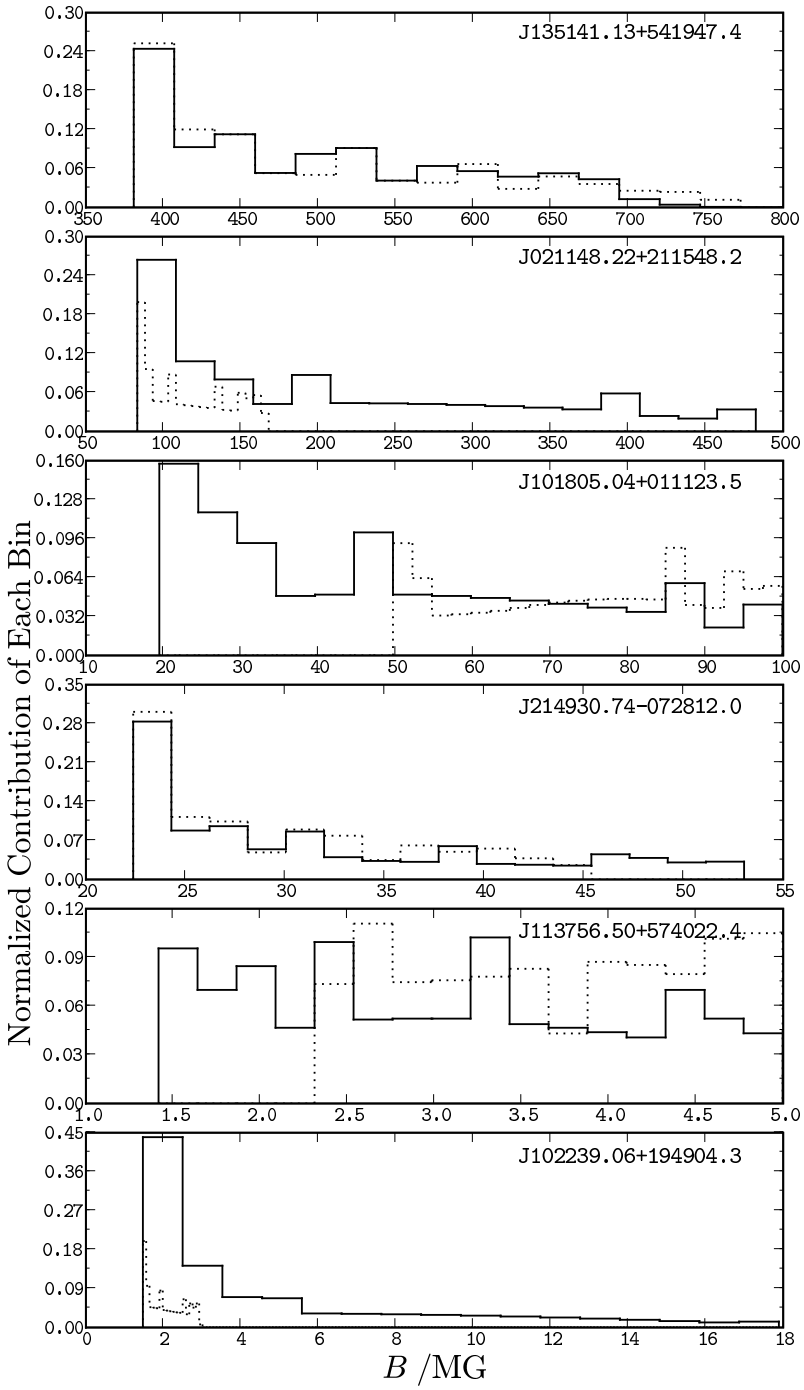

Figure 2.3: Normalized histograms of the magnetic field strength distributions over the visible hemisphere of the star used for calculation of the synthetic spectra shown on Fig. 2.1. Dotted lines represent the centered dipole models, solid lines indicate dipole models with offsets.

(2003) as a DAH, but is a carbon-rich (DC) MWD (Putney, 1995). *J084716.21 +148420.4* is a DAH+DB binary, in which the helium component in the spectrum is quite strong. This dilution of the hydrogen features prevented an accurate analysis of this object by our code. Finally, we were unable to model the SDSS spectrum of *J220029.08 -074121.5* due to the lack of any discernible features.

Emission lines were found in *J102220.69+272539.8* and *102239.06 +194904.3* (the latter being shown in Fig. 2.1) that are very similar to those of *J121209.31 +013627.7* which could indicate that these objects are EF Eri like, magnetic cataclysmic variables with a brown dwarf companion (Schmidt et al., 2005; Debes et al., 2006; Burleigh et al., 2006; Farihi et al., 2008).

The spectra of the high-field objects *J224741.41 +145638.8* and *J101805.04 +01123.5* (PG 1015+014, shown in Fig. 2.1) cannot be reproduced particularly well. At higher field strengths (> 50 MG), the spectra become very sensitive to the details of the magnetic field geometry, as was demonstrated by Euchner et al. (2002, 2005, 2006). The deviations of the observed spectra from our theoretical spectra assuming (offset) dipole models, therefore imply a magnetic field geometry that is more complex than a shifted dipole. A more comprehensive analysis of *J101805.04 +01123.5* showed that individually tilted and off-centered zonal multipole components with field strengths in the range 50-90 MG is needed to represent the global magnetic field (Euchner et al., 2006), which was consistent with our analysis.

The colors of MWDs with high field strengths (> 50 MG) are known to differ from non-magnetic white dwarf colors because the absorption in their spectral features as noted in Sect. 2.2. This behavior also affects temperature determinations from color-color diagrams. The analysis of *J224741.41 +145638.8* by Euchner et al. (2006) inferred an effective temperature of $T_{\rm eff} = 10000 \pm 1000$ K, unlike $T_{\rm eff} = 12\,000$ K that is derived from color-color diagrams. We used 10 000 K for our models, and this value provided better results, especially on the basis of line depths. When color-derived effective temperatures were used, a similar discrepancy with the slopes and line depths was also observed in *J224741.41 +145638.8*. The temperature 17 000 K was used in modeling by Schmidt et al. (2003), but the colors of *J224741.41 +145638.8* are outside the Holberg & Bergeron (2006) grid of $\log g$ - $T_{\rm eff}$ in u-g – g-r plane. In our procedure, we accomplished the best result with 50 000 K for this object on the basis of slope and line depths. On the other hand, some high-field objects in our sample such as *J135141.13 +541947* (Fig. 2.1) were fitted well and this discrepancy between the temperature derived by either colors or spectral fits was not observed.

In some of the optimal fits, the line depths of the observed and computed spectra strongly differ. These unsatisfactory fits are caused by two different kind of problems: either of the $\sigma^{\pm}$ components was shallower than expected on the basis of their sharp π counterparts in observed spectra, with respect to the models; or both $\sigma^{\pm}$ and π components of the lines were too shallow.

Sharp line cores within shallow wings in the spectra was already noted for *J123414.11 +124829.6* by Vanlandingham et al. (2005). It has been suggested that this might be caused by a deviation from centered dipole geometry, and our fits with offset dipole models proved to be considerably better than the centered dipole models in reduced χ^2. For lower magnetic strengths (< 50 MG), the smearing effect of offset dipole models affects only the $\sigma^{\pm}$ components of the lines. The reason is that in this field regime $\sigma^{\pm}$ components become more separated, while the π components are only slightly blue-shifted with increasing field strength. Therefore smeared-out wings with sharp-line cores can be synthesized by adding

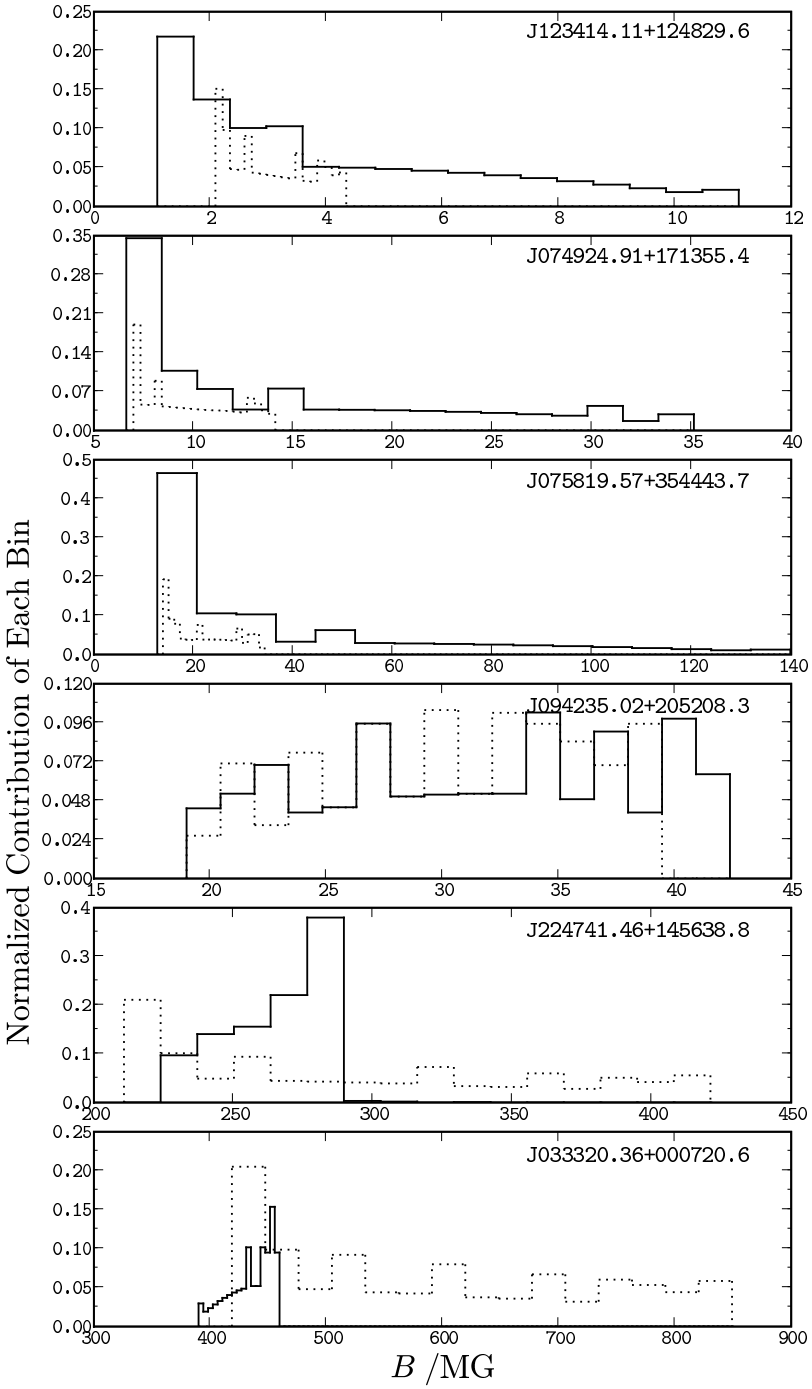

Figure 2.4: Normalized histograms of the magnetic field strength distributions over the visible hemisphere of the star used for calculation of the synthetic spectra shown on Fig. 2.2. Dotted lines represent the centered dipole models, solid lines indicate dipole models with offsets.

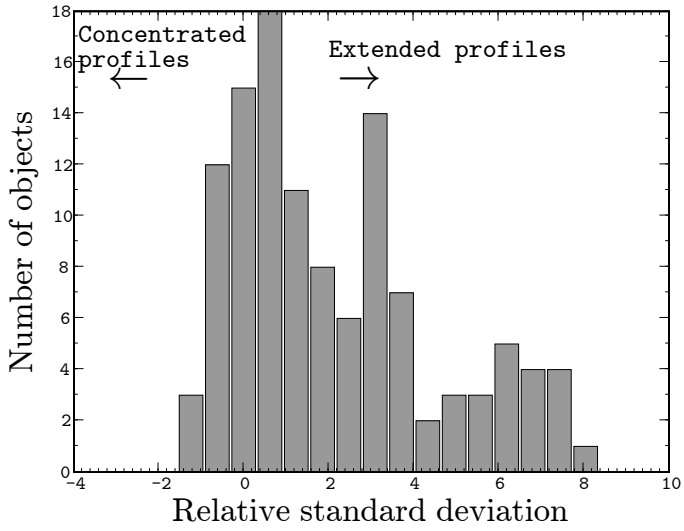

Figure 2.5: Histogram of the relative variance $\sigma_{\rm rel}$ (see Sect. 2.3.1) for known SDSS MWDs. Negative $\sigma_{\rm rel}$ indicates a magnetic field strength profile of the visible surface which is more concentrated than a centered dipole, whereas positive indicates profiles that are more extended.

spectra with a wider range of magnetic field strength values. Dipole models with offsets can generate such extended magnetic field distributions (see Sect. 2.3.1). Our fit to *J123414.11 +124829.6* was considerably tighter but we did not reproduce the exact profile. Another possible explanation of this spectrum is the contribution from a non-magnetic DA, which would dilute the $\sigma^{\pm}$ components causing an increased contrast between the wings and line cores. Offset dipole models improved our fits, although further analysis is needed to differentiate between the effect of geometry and the possible contribution from a non-magnetic DA.

The other case, *J113756.50 +574022.4* (see Fig. 2.1), has very shallow features with discernible magnetic wings. Neither a complicated geometry nor a change in effective temperature can explain its lack of line depth. Nevertheless, the magnetic field strength could be derived from the extent of the wings. We propose that this object is an unresolved spectroscopic binary (e.g., with DA+DC components), since in these situations hydrogen line strengths are known to be suppressed by the other component (Bergeron et al., 1990; Liebert et al., 1993a). The other objects with shallow features that belong to this category are: *J084716.21 +484220.4*, *J090632.66 +080716.0*, *J113215.38 +280934.3*, *J103532.53 +212603.5*, *J112328.49 +095619.3*, *J124806.38 +410427.2*, *J141906.19 +254356.5*.

One additional interesting outcome of this investigation was the results of modeling of *J033320.36 +000720.6*, which was formerly identified in the Hamburg/ESO survey for bright quasars as HE 03330-0002 (Reimers et al., 1998). Its magnetic properties were confirmed by Schmidt et al. (2001) by circular polarimetry; nevertheless, the modeling of the HE 03330-0002 was previously impossible, since the transitions in its spectrum were not understood to be caused either hydrogen or because of helium transitions. Although *J033320.36 +000720.6* was discovered in the EDR, because of this lack of knowledge about its atmosphere Gänsicke et al. (2002) did not attempt to model its data with a pure hydrogen atmosphere.

Table 2.1: The hydrogen transitions of SDSS J033320.36+000720.6 and their wavelengths at 446.5 MG.

Line	$nlm - n'l'm'$	$\lambda(\AA)$
Hα	$2s_0 - 3p_0$	6113.05
Hα	$2s_0 - 3p_{-1}$	7710.91
Hα	$2p_{-1} - 3d_{-2}$	6647.76

However, we noted that some of the lines in the spectrum of *J033320.36 +000720.6* possibly coincided with hydrogen stationary lines. Therefore we decided to model the spectrum with a 7 000 K DAH atmosphere. Our initial fits with a centered dipole inferred a dipolar field strength of ∼850 MG (see Fig 2.2), which reproduced the position but not the depths of the three transitions. More careful modeling with an offset dipole showed that the mean field strength over the visible surface is far more concentrated than for a regular dipole field geometry. Figure 2.4 shows that the mean field strengths are predominantly in the interval $390 - 470$ MG. When we consider the apparent peak value of this distribution, we infer line positions for three lines in the spectrum that are commensurate with those of Hα transitions (see Table 2.1).

The pure hydrogen atmosphere was unable to produce the red part ($\lambda < 5500\AA$) of the spectrum. There appear to be additional opacity contributions from different species of elements, to both the continuum and the features.

2.3.1 Magnetic field geometry

We have modeled a large sample of DAHs with dipole magnetic fields offset from the magnetic axis. However, the visualization of these model parameters is not straightforward. The effect of the dipole offset on the model spectrum depends on both inclination and the polar field strength. However, the polar field strength is not representative of the global magnetic field on the visible surface if the offsets are large. The most direct way to investigate a model geometry is to construct a diagram of the angle between the line-of-sight and the local magnetic field vector versus the magnetic field strength plot i.e., equivalent to the ZEeman BRoadening Analysis (ZEBRA) plots of (Donati et al., 1994). In our case, since we did not have polarization data, we only considered the magnetic field strength distribution histograms for simplicity.

In general, the effect of the offset dipole models is to either extend or reduce the range of magnetic field strengths across, the visible surface of the MWD, which is a fixed factor of two for centered dipole models (see Fig. 2.3). For offset dipoles, the range depends on both the values of B_p and the inclination i. To quantify the difference between the centered and off-centered dipole models, we determined the average and the standard deviation σ of the distribution of the magnetic fields for the parameters of our best-fit solution. The relative change in the standard deviations $\sigma_{\rm centered}$ and $\sigma_{\rm offset}$ is given by $\sigma_{\rm rel} = \frac{\sigma_{\rm offset} - \sigma_{\rm centered}}{\sigma_{\rm centered}}$.

The value $\sigma_{\rm rel} = 0$ indicates that the widths of the centered and offset dipole models are the same, $\sigma_{\rm rel} < 0$ indicates that more concentrated than a dipole field, and for $\sigma_{\rm rel} > 0$ the distribution of field strengths is more extended.

To present the magnetic field geometry of our sample, we plotted the histogram of $\sigma_{\rm rel}$ values for all known SDSS DAHs, except those discussed in Sect. 2.3 as possible binaries

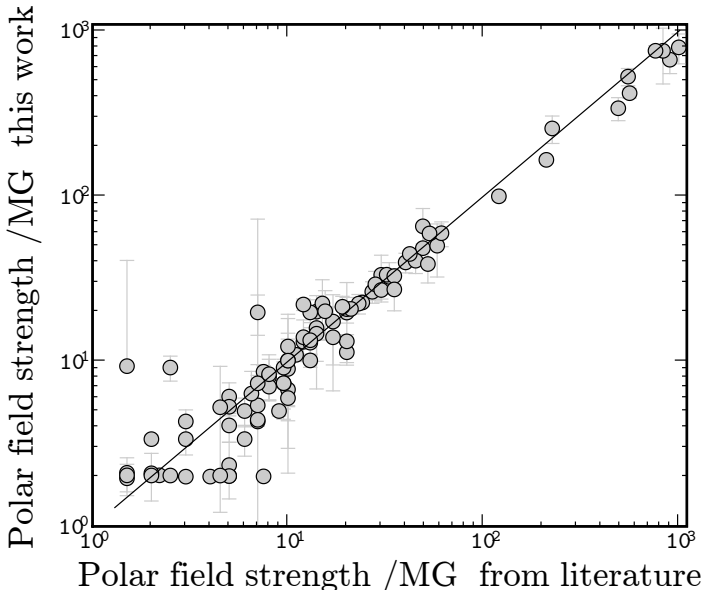

Figure 2.6: Comparison of centered dipole magnetic field fit values in this work versus Schmidt et al. (2003), Vanlandingham et al. (2005).

(Fig. 2.5). The average $\sigma_{\rm rel}$ for this sample was found to be 2.18. This implies that even for SDSS spectra of quite low signal-to-noise ratio, there is an overall tendency towards non-dipolarity for our sample of white dwarfs.

2.4 General Discussion

Overall, our results are consistent with previous analyses of DAHs (see Fig. 2.6), which shows that simple atmosphere models with pre-assumed dipole magnetic values are good approximations for these objects. In all cases, offset dipole models resulted in significantly tighter fits than models with centered dipoles. We noted in Sec. 2.3 that for some DAHs with high fields, completely satisfactory fits cannot be achieved with offset dipole models. This is indicative of a magnetic field geometry that is more complex than a shifted dipole.

The dipole magnetic field Ohmic decay timescale is 10^{10} yr. Even higher multipoles can live for such a long period of time (Muslimov et al., 1995). Therefore, no significant correlation between temperature and magnetic field strength is expected if temperature is assumed to be an indicator of age (Fig. 2.7). This lack of correlation supports the fossil ancestry of these fields inherited from earlier stages of stellar evolution. However for a clear conclusion, the field strengths and magnetic geometry of the MWD sample should be investigated with respect to the cooling ages, rather than $T_{\rm eff}$. The knowledge of cooling ages, depends on the mass estimates of MWDs. Estimating the masses of MWDs is beyond the scope of this Chapter, and relevant methods will be discussed in Chapter 3 (see Sec. 3.2).

In this chapter, we have analysed 141 DAHs, 97 of which had been previously analysed and 44 of which were being new. Gänsicke et al. (2002) conservatively estimated that the total number of MWDs would be tripled by the complete SDSS coverage. Before the end of the systematic search of the latest data releases, this expectation has already been

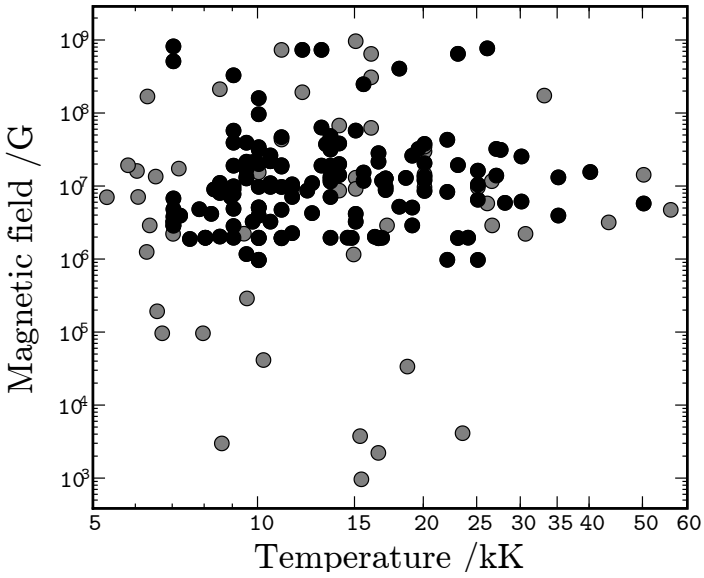

Figure 2.7: Scatter plot of dipole magnetic field value vs effective temperature. While black dots represent all known SDSS DAHs, grey dots indicate the DAHs from literature that were not analysed in this work. If $T_{\rm eff}$ is taken as a proxy for the cooling age, the random distribution of field strengths with respect to age indicator temperature is consistent with long decay timescale of DAHs with respect to their cooling age.

surpassed. In addition, our consistent modeling over the data releases show that within the SDSS DAH population, there is a tendency to deviate from simple centered dipoles. There are clear indications of deviations from centered dipole models for at least 50% of the SDSS DAHs (see Fig. 2.5).

The distribution of the magnetic field strengths of the MWDs in the Schmidt et al. (2003) sample is concentrated in the $\sim$5 – 30 MG interval. We have revised the magnetic field strengths of all known DAHs and created a histogram (Fig. 2.8). The values were taken from Jordan (2009), which is an extended and corrected version of Kawka et al. (2007). The same overabundance in the range $\sim$5 – 30 MG discussed in Schmidt et al. (2003) is apparent in Fig. 2.8, but overall, SDSS has nearly tripled the number of known DAHs and hence the completeness of the total MWD population is significantly affected by SDSS biases because of this high impact of SDSS.

High field MWDs are understood to be the remnants of magnetic Ap and Bp stars. If flux conservation is assumed, the distribution of the polar field strengths of high field MWDs should be most significant in the interval 50–500 MG. In our sample, objects with magnetic field strengths lower than 50 MG are more numerous than objects with higher magnetic field strengths (see Fig. 2.8). Part of this effect is caused by our biases (see Sec. 2.2). Nevertheless, it is consistent with previous results and supports the hypothesis that fossil magnetic fields from Ap/Bp stars alone are insufficient to produce high field MWDs (Wickramasinghe & Ferrario, 2005). Aurière et al. (2007) argued that dipole magnetic field strengths of magnetic Ap/Bp stars have a "magnetic threshold" due to large-scale stability conditions, and this results in a steep decrease in the number of magnetic Ap/Bp stars below polar magnetic fields of 300 G.

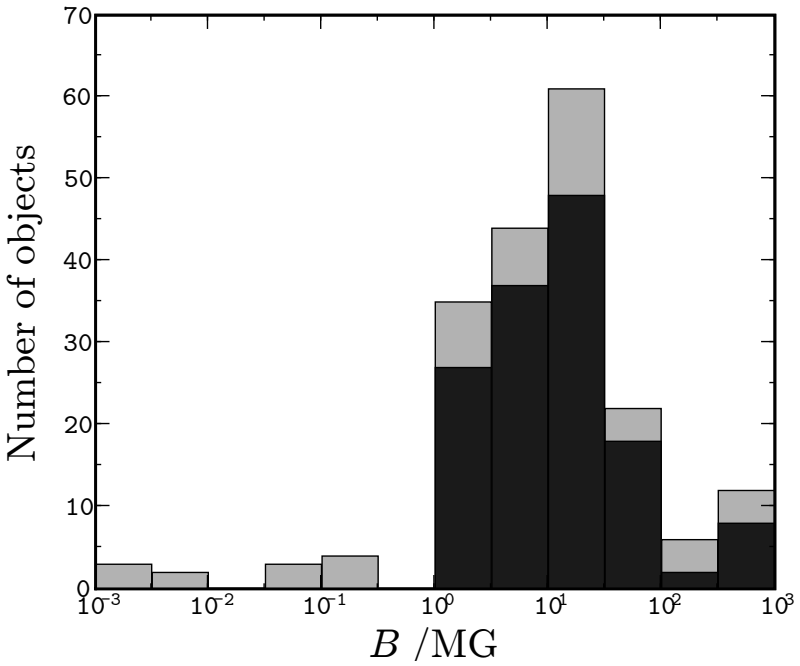

Figure 2.8: Histogram of the known magnetic white dwarfs in equal intervals of $\log B$. Gray columns represent the number of all known DAHs. Black shades represent the the contribution of SDSS to DAHs.

A possible progenitor population of MWDs with dipolar field strengths below 50 MG, is a currently unobserved population of A and B stars with magnetic field strengths of 10 – 100 G. Wickramasinghe & Ferrario (2005) suggested that if $\sim 40\%$ of A/B stars have magnetism, this would be sufficient to explain the observed distribution of MWDs. However, the existence of this population seems to be highly unlikely, since the the investigations of Shorlin et al. (2002) and Bagnulo et al. (2006) of magnetism in this population yielded null results, for median errors of 15 – 50 G and 80 G, respectively. Another candidate progenitor of these MWDs with lower field strengths is the yet undetected magnetic F stars (Schmidt et al., 2003). However, this conclusion is strongly affected by SDSS MWD discovery biases.

In our work, we have quantified the deviation from centered dipoles in our sample. To test the fossil field hypothesis, one can consider the statistical properties of the fields of Ap/Bp stars. One such statistical analysis was completed by Bagnulo et al. (2002). In their work, they used the mean longitudinal field, the crossover, the mean quadratic field and the mean field modulus to invert the magnetic field structure modeled by a dipole plus quadrupole geometry (the modeling procedure is explained in depth in Bagnulo et al., 1996; Landolfi et al., 1998). The aim of this analysis was to characterize the sample rather than find the best-fit solution for each object. Using the aforementioned observables, they analysed 31 objects and derived 147 "good fit" models. These models corresponded to the minima of the χ^2 hypersurfaces in their inversion procedure. Later model parameters were weighted by these reduced χ^2 values when assessing their statistical properties.

Bagnulo et al. (2002) investigated the relative importance of quadrupole and dipole in the magnetic field models by plotting weighted histograms of $B_{\rm d}/B_{\rm q}$, where $B_{\rm d}$ is the am-

plitude of dipole field strength (B_p in this work), and $B_{\rm q}$ is the amplitude of the quadrupole field strength. The main differences between our analysis and that of Bagnulo et al. (2002) was the usage of visual magnetic field distributions rather than the global magnetic field inferred from the time-resolved observations. The relationship between $B_{\rm d}/B_{\rm q}$ and to our relative variance parameter is not straightforward, since the structure of the total field depends on the angle between the dipole and quadrupole components. If we consider $B_{\rm d}/B_{\rm q} = 1$ as the point where the quadrupole component begins to dominate, 63% of the models can be considered predominantly quadrupolar (see Fig. 3 of Bagnulo et al., 2002). Hence, our conservative assessment that at least 50% of DAHs have non-dipolar fields, seems to be consistent with this result.

However one needs to be careful in considering the correspondence between the geometry between MWDs and their progenitors since theoretical models expect the field on the surface to evolve under certain conditions. Braithwaite & Spruit (2004) investigated the stable configurations of magnetic fields in stars with their magnetohydrodynamics code. Their work found that initial random fields decay within a few Alfvén timescales to a poloidal plus toroidal stable configuration. During the star's evolution, its toroidal field may diffuse outwards since the Ohmic diffusion timescale is within the order of the lifespan of an Ap/Bp star (Braithwaite & Nordlund, 2006). On the Ohmic timescale, the expected initial offset-dipole configuration of the surface magnetic field evolves to a simple centered dipole. Hence, Braithwaite & Nordlund (2006) hypothesized that Ap stars with centered dipole fields are likely to be older than Ap stars with non-dipolar geometries. It is important to mention that the concentration of the field inside the star is also an important parameter, which contributes to the structure of the surface magnetic field. A highly concentrated field results in a surface field structure with higher order multiples after the internal toroidal field formation. The relative importance of the Ohmic diffusion (i.e., the age) and concentration of the initial field on the surface magnetic field structure has yet to be further investigated. Nevertheless, if the Ohmic diffusion timescale affects the lifetime of an Ap star, then it would be more relevant to compare the field configurations of an older population of Ap stars with the magnetic field distribution of MWDs. This kind of work has not yet been undertaken for Ap stars.

If we neglect the possibility that older Ap stars may behave differently from the whole sample of this group and the field structure of MWDs do not evolve as Muslimov et al. (1995) suggested (see Sect. 2.4), then the global analysis of Bagnulo et al. (2002) imply that the distribution of field structures of chemically peculiar stars and DAHs are comparable, hence supporting the fossil field hypothesis.

In addition to the isolated evolution scenario, a binary star origin was proposed by Tout et al. (2008) for generating magnetic fields in WDs. In this picture, during the evolution to the cataclysmic variables (CVs) the cores of giants experience a common envelope (CE) phase. During this phase, the orbital angular momentum is transferred to the envelope as the two cores spiral in toward each other. This process causes both differential rotation and convection within the CE, which are the key ingredients of magnetic field generation (see Tout et al., 2008, and references therein).

A consistent account of the origins of magnetic fields in WDs awaits the finalization of the complete sample of SDSS MWDs.

Chapter 3

Constraining the Evolution of Magnetic White Dwarfs

3.1 Introduction

I have discussed the distribution of the magnetic field strengths and the magnetic field geometry of the hydrogen-rich magnetic white dwarfs (DAH) sample in the Sloan Digital Sky Survey (SDSS) in Chapter 2. However, to constrain the evolution of MWDs and how their magnetic fields were formed can only be assessed by additional evolutionary information.

To assess the evolution of a white dwarf, the most important piece of information needed is its age. If the cooling age and the progenitor age of the white dwarf is known, numerous questions about the origin of the object and the origin of the magnetic fields can be addressed. The results of the former chapter (Chapter 2) is not enough to draw such conclusions since the only information assessed was the $T_{\rm eff}$ and the magnetic structure.

Since cooling of white dwarfs is well constrained by the current theory (see Sec. 1.2.2), the physical properties of a white dwarf can be used to assess its age. According to simple cooling theory, the age of a white dwarf only depends on its heat content, namely its chemical composition, mass and temperature. Therefore, in order to evaluate the cooling age for a white dwarf of given composition we need to be able to measure the mass and the $T_{\rm eff}$. If the effective temperature is known, the emission of the white dwarf can be modelled. Comparison of the model flux and the absolute brightness of the object yields the radius, and through mass-radius relations, the mass can be estimated. In the case where direct measurements of distance, such as parallax measurements, do not exist or are not feasible, there are two different methods to obtain the distance in which the total evolutionary age, i.e. the progenitor age $t_{\rm prog}$ plus the cooling age $t_{\rm cool}$ is also accessible.

The first method is applicable when the MWD is in a binary, preferably with a non-magnetic white dwarf. In this case the surface gravity of the non-magnetic white dwarf can be evaluated with spectral fits to its Balmer lines and then with the help of theoretical mass-radius relations (see Sec. 1.2.1) the radius and mass of the non-magnetic white dwarf can be estimated. It is rather elementary to get the distance from the radius and the flux of the object, if the theoretical flux is known from atmospheric theory. The mass yields the cooling age, furthermore the total evolutionary age can be estimated by evaluating the progenitor mass from semi-empirical initial to final mass relation (IFMR). The information

on the progenitor mass enables us to assess the progenitor life time of the non-magnetic component, with the use of stellar evolution theory.

The second case is when the MWD is a member of a cluster. In this case, the distance to and the age of the cluster can be estimated independently by observations. This situation is more favourable since it does not demand the usage of the semi-empirical IFMRs and on the contrary, it is precisely the tool to determine and test it.

In the first section, I explain in detail the aforementioned methods to assess the evolutionary history of a white dwarf, specifically on deriving the masses and the cooling ages from the distance information. In the subsequent Sec. 3.3 I apply the cluster method to WD0836+201 and SDSS J0855+1640 which will be shown to be the Praesepe open cluster members. In the Sec. 3.4 the binary method will be applied to SDSS J130033.48+590407.0 (henceforth SDSS J1300+5904) which is shown to be in a Common Proper Motion (CPM) pair. In the final section I discuss the results and evaluate their implications for the stellar evolution in the context of IFMR.

3.2 Method

Due to the gravitational settling white dwarf atmospheres are subjected to, they are chemically simpler relative to the rest of the stellar population. In most of the cases, this enables robust physical diagnostics, based on the spectrum of a single species spectrum. The effective temperature, the surface gravity, radial velocity, the rotational velocity and the gravitational redshift can be measured based on the line profiles of the white dwarfs.

The spectral analysis consists of determining the effective temperature $T_{\rm eff}$ and surface gravity $\log g$ from χ^2 fits to the spectral lines. The model flux of the white dwarf with given physical parameters, enables the estimation of radius given the distance to the object.

$$\frac{f_\lambda}{F_\lambda} = \left(\frac{R_{\rm WD}}{d}\right)^2 \tag{3.2.1}$$

Where F_λ is the model flux, which depends on $\log g$, $T_{\rm eff}$ and f_λ is the observed flux. When the distance d of the object is known, the radius $R_{\rm WD}$ can be calculated. After this step, estimating the mass is then rather straightforward, given the surface gravity:

$$g = \frac{GM_{\rm WD}}{{R_{\rm WD}}^2}, \qquad M_{\rm WD} = \frac{gd^2}{G}\left(\frac{f_\lambda}{F_\lambda}\right)_{T_{\rm eff},g} \tag{3.2.2}$$

where G is the gravitational constant.

However for the magnetic white dwarfs this method is inadmissible since surface gravities can not be fitted in the MWD spectra with high confidence due to the simultaneous impact of the Zeeman and Stark effect on the shape of the spectral lines in the presence of the magnetic fields (for details see, Sec. 3.3.2).

Fortunately, even under the influence of $\log g$ uncertainties, a relatively accurate determination of the effective temperature is attainable if sophisticated models for the radiation transport through a magnetised stellar atmosphere are used. This enables the estimation of $R_{\rm WD}$ if we additionally make use of theoretical mass-radius relationships.

This type of analysis is common for MWDs in wide binaries (see e.g. Barstow et al., 1995) and magnetic cataclysmic variable primaries during their low accretion states (see e.g. Beuermann et al., 2000).

This method consists of two parts: Firstly, the determination of the effective temperature and the magnetic field strength and geometry from the observed spectra. For the three object of interest in this chapter, we already obtained the magnetic field geometry in Chapter 2 (Külebi et al., 2009) where $T_{\rm eff}$ was determined from the SDSS colours. In Sect. 3.3.2 we perform a more careful analysis to determine the $T_{\rm eff}$ spectroscopically.

In the second part we need values for the distance of the objects; which come either from the cluster distance or from the spectrum of the non-magnetic counterpart. Using the estimates for the distance, we first evaluate the absolute magnitude of the object and with the theoretical absolute magnitudes from model atmosphere calculations (Holberg & Bergeron, 2006; Althaus et al., 2007) which include implicitly the mass-radius relations and the white dwarf evolutionary models of Wood (1995); Althaus et al. (2005) respectively (see Sect. 3.3.3).

Furthermore, we can evaluate the progenitor age of a white dwarf by subtracting the cooling age from the total age. The origin of the total age of the system depends on the method used, which could either be the cluster age or the total age of the binary counterpart.

3.3 Magnetic White Dwarfs in Open Clusters

The stellar clusters are gravitationally bound systems of stars, which were formed at the same time in the same environment. This is supported observationally by the color-magnitude diagrams (CMD) of the stellar clusters, to which a single aged population, i.e. isochrones at a can be fitted. In these CMDs the termination of the main-sequence (MS turnoff) is apparent, which is used for estimating the total age of the cluster. In principle if the cluster is old enough, the evolutionary sequence extends all the way down to the cooling sequence of the white dwarfs.

Stellar clusters are divided into different types depending on how tightly they are bound by gravity. The globular clusters, are relatively old hence they are tightly bound and densely concentrated towards their center of gravity. Unlike globular clusters, open clusters are bound rather loosely. This property relieves the crowding effect in the fields of open clusters with respect to the globular clusters and allows the detection of faint members with relative ease, such as white dwarfs.

It is possible to assess the properties of the white dwarf progenitors in the cluster through the cluster properties when they are combined with the mass and cooling age of the member white dwarfs. This situation provides the possibility to test our understanding of stellar evolution. One of the most important representation of our current understanding of the theory of stellar evolution is the IFMRs, which link the progenitor mass of a star to the final white dwarf mass (Weidemann, 1977).

The IFMR is inherently connected to mass loss mechanisms (see e.g. Weidemann, 2000). The understanding of stellar evolution from the perspective of the IFMR enables us to constrain the critical mass necessary for Type II supernova explosions. This information can be used to estimate the birthrate and energetics of the supernovae, as well as the birthrates of the SN II products, the neutron stars (van den Bergh & Tammann, 1991). The precise IFMR also constrains the galactic chemical evolution (i.e. enrichment in the interstellar medium) which in turn contributes to the understanding of the star formation efficiency in these systems (Somerville & Primack, 1999).

The empirical determination of the IFMR were performed for the first time with the

cluster method (Weidemann, 1977; Koester & Weidemann, 1980). With now ∼40 white dwarfs associated with 11 clusters the empirical information on the IFMR has more than doubled within the last few years (see Ferrario et al., 2005a; Dobbie et al., 2006; Kalirai et al., 2008; Catalán et al., 2008; Casewell et al., 2009, for a recent discussion of cluster IFMR data). These observational studies established support for the already estimated general trend, in which higher stellar masses yield more massive white dwarfs. However the increased amount of data also resulted in a considerable scatter in the semi-empirical IFMR. This spread is argued to be the result of differences in the host environments. One effect was proposed to be metallicity by Marigo (2001), in which metal-rich stars was shown to undergo heavier mass loss and yield on average lighter white dwarfs. This was shown to be true conclusively by observations of white dwarf sequence in NGC 6791 (Kalirai et al., 2007).

Another physical process effecting the final mass of the white dwarf was proposed to be rotation. It was argued through very simple numerical methods (Dominguez et al., 1996) that angular momentum contributes as an extra pressure supporting against the gravity, causing the rotating core to expand and hence keep the maximum temperature lower than the temperature to ignite carbon. This lower temperature enables the growth of the C-O core in mass while avoiding carbon ignition. In this way ultra-massive (1.2-1.4 $\mathrm{M}_{\odot}$) white dwarfs can be formed from progenitors with masses between 6-8 $\mathrm{M}_{\odot}$.

Magnetic fields alongside angular momentum was also proposed to be an effective factor in the mass loss due after the discovery of a MWD WD0836+201 as a probable cluster member (Claver et al., 2001; Catalán et al., 2008). Under the condition that WD0836+201 is a Praesepe member, the estimated white dwarf mass was higher than expected for its progenitor mass. Up to now, only two MWD members have been discovered, one in Praesepe (WD0836+201, Claver et al., 2001) and one in NGC 6819 (NGC 6819-8, Kalirai et al., 2008) which are MWDs. However the spectrum of NGC 6819-8 has not been thoroughly analyzed with model spectra taking magnetism into account.

In order to assess the evolutionary histories of MWDs and prospectively investigate the possible effect of magnetism on the IFMR we tested whether any of the newly discovered magnetic MWDs in the Sloan Digital Sky Survey (SDSS) are open clusters members. The membership information provided us with information on the distance, which enables the estimation of the mass and the cooling age when $T_{\rm eff}$ from our magnetic models, their observed flux and the evolutionary models are used.

3.3.1 Cluster membership

Our aim is to discover possible cluster members which are magnetic and determine their masses and cooling ages. For non-magnetic white dwarfs the confirmation of cluster membership involves the coincidence of the their proper motion with the proper motion of the cluster, their position on the cooling sequence in color-magnitude diagrams, and by the commensurably of the observed flux at the distance of the cluster with the model flux estimated by $\log g$ and $T_{\rm eff}$of the white dwarf (see e.g. Kalirai et al., 2008).

We checked the membership of all SDSS DAHs which are analysed in Sec. 2 with the known open clusters in the Catalogue of Open Cluster Data (Kharchenko et al., 2005). For this purpose we used the proper motion data from SDSS data release 7 (DR7 Abazajian et al., 2009). One of the refinements of this data set compared to previous versions is the improvement of the astrometric calculations due to a cross calibration with the USNO CCD Astrograph Catalog (UCAC2) catalogue (Zacharias et al., 2004); by this the values for the

Table 3.1: Astrometric properties of the DAHs which are candidate members of Praesepe. The columns indicate the name of the object; the coordinates and the proper motions of the MWDs. Compare the proper motions of these objects with the proper motions of Praesepe RA p.m.$= -35.90 \pm 0.13$ mas/yr, Dec. p.m. $= -12.88 \pm 0.11$ mas/yr)

Object	RA	Dec.	RA p.m. / (mas/yr)	Dec. p.m. / (mas/yr)
WD0836+201	08 39 45.56	+20 00 15.7	-32.93±2.87	-15.98±2.87
SDSS J0855+1640	08 55 23.87	+16 40 59.0	-33.14±2.75	-14.71±2.75

proper motions could be computed from the combined SDSS and the Second US Naval Observatory (USNO-B Monet et al., 2003) positions.

For our investigations we compared the astrometric properties of 137 SDSS DAHs with the properties of 520 open clusters from the Catalogue of Open Cluster Data (Kharchenko et al., 2005). We looked for proper motion companions to the open clusters within 3σ of their observed tidal radius taken from the catalogue of Piskunov et al. (2008). The proper motions of the MWDs were acquired from the `CASJOBS SQL` interface (Li & Thakar, 2008).

As a result we obtained only two possible cluster members (see Tab. 3.1) and both belong to the same open cluster: NGC 2632 (Praesepe); one of the candidates is the formerly known member, WD0836+201 (EG 59; note, that the star was incorrectly labeled in Claver et al. (2001); Catalán et al. (2008) as noted in Casewell et al. (2009)) and the other candidate is SDSS J0855+1640.

Praesepe is a nearby open cluster which has been the subject of many white dwarfs studies and IFMR investigations (Luyten, 1962; Eggen & Greenstein, 1965; Claver et al., 2001). The current number of the white dwarfs, confirmed by radial velocity observations by Casewell et al. (2009), in this cluster is 9, including the known MWD WD0836+201. Compared to numerical simulations of the dynamics of open clusters (Portegies Zwart et al., 2001) the number of white dwarfs found in Praesepe is lower than expected, especially if compared to the number of observed giants. This result is similar to the work of Weidemann et al. (1992) in which the lack of white dwarfs and possible causes were discussed for the first time. Hence it is logical to expect more white dwarfs to be discovered to be a part of the Praesepe cluster if the search is extended at least up to the tidal radius.

The cluster membership can also be tested by the comparison of the radial velocity of the white dwarf with the radial velocity of the cluster. However for the MWDs the measurement of radial velocities it is not straightforward due to the shifts of the line cores induced by the magnetic fields. Moreover, the resolution of the SDSS spectra is not accurate enough to assess radial velocities.

The other constraint on possible membership is the position of the white dwarfs in the CMD; given the possible effective temperatures and surface gravities of white dwarfs, the colors can be constraint theoretically. We did not constrain the range of surface gravities to the typical masses of white dwarf because we do not want to miss possible low or high mass candidates.

Additional evolutionary constraints on the cluster membership comes from the estimated cooling age of the white dwarf: the cooling age must not be larger than the cluster age.

We have undertaken the analysis of all of the SDSS DAHs from Chapter 2 considering the aforementioned uncertainties, evaluated the cluster association and furthermore derived the masses of the MWDs in Praesepe.

Table 3.2: Photometric properties of the DAHs which are candidate members of Praesepe. The columns indicate the SDSS photometric magnitudes r, i, z which are relevant for this work (see Sec. 3.3.3).)

Object	r / mag	i / mag	z / mag
WD0836+201	18.11±0.01	18.36±0.01	18.66±0.04
SDSS J0855+1640	18.80±0.01	19.05±0.02	19.32±0.08

Table 3.3: Model fits with magnetic offset dipole models. The columns indicate the SDSS name of the object; the plate, Modified Julian Date and fiber ids of the observations; the offset dipole, the inclination with respect to the line of sight of the offset dipole, the offset along the axis of the magnetic field in terms of the stellar radius

MWD (SDSS+)	Plate-MJD-FiberID	$B_{\rm dipole}$ / MG	$z_{\rm off}$ / $r_{\rm WD}$	i / deg	$T_{\rm eff}$ / K
J083945.56+200015.7	2277-53705-484	2.83±0.19	0.26±0.02	26±4	17000±500
J085523.87+164059.0	2431-53818-522	12.61±1.03	0.25±0.02	44±6	20000±500

3.3.2 Effective temperatures from spectral analysis

All hydrogen-rich white dwarfs from the SDSS which have shown to be magnetic were analysed in Chapter 2, where we took advantage of pre-calculated model spectra for magnetized white dwarf atmospheres (see Jordan, 1992; Jordan & Schmidt, 2003). With an evolutionary fitting procedure we determined the magnetic field strength and geometry in terms of offset magnetic dipoles. For details of the fitting see Sec. 2.2.1, the resulting parameters of all objects are in Table C.1.

In this chapter we spectrocopically investigated the effective temperature rather than magnetic structure as in Chapter 2. For the non-magnetic case fits to the Balmer lines are undertaken in order to determine the $T_{\rm eff}$ and $\log g$. However for the MWDs, determining the effective temperatures and surface gravities by fitting the Balmer lines alone are less reliable than in the case of non-magnetic white dwarfs due to the lack of a realistic and easily applicable theory for the simultaneous impact of Stark and Zeeman effect on the spectral lines. This was investigated only for simple cases when the electric and magnetic fields are parallel (Friedrich et al., 1994), but no atomic data for hydrogen in the presence of both a magnetic and electric field are available for arbitrary strengths and arbitrary angles between two fields. Therefore, only a crude approximation (see Jordan, 1992) is used in our model and systematic uncertainties are unavoidable, particularly in the low-field regime (≤ 5 MG) where the Stark effect is strong relative to the Zeeman splitting. Therefore, we do not rely on any determination of $\log g$ from our spectral fits.

On the other hand, the determination of the effective temperature from the strength of the spectral lines is reliable and in particular at relatively small magnetic field strengths where the photo-ionization opacities are rather unaffected by the magntic field (Zhao & Stancil, 2006). The determination of $T_{\rm eff}$ through the line strengths has already been implemented by Gänsicke et al. (2002).

The determined parameters are in Tab. 3.3, the errors in $T_{\rm eff}$ is defined by the width of our grids. The fitted spectra are shown in Fig. 3.2, in observed values of fluxes. The fainter flux of SDSS J0855+1640 with respect to the flux of WD0836+201 despite its higher effective temperature hints for a smaller radius hence a more massive nature, if we assume both MWDs to be at the same distance.

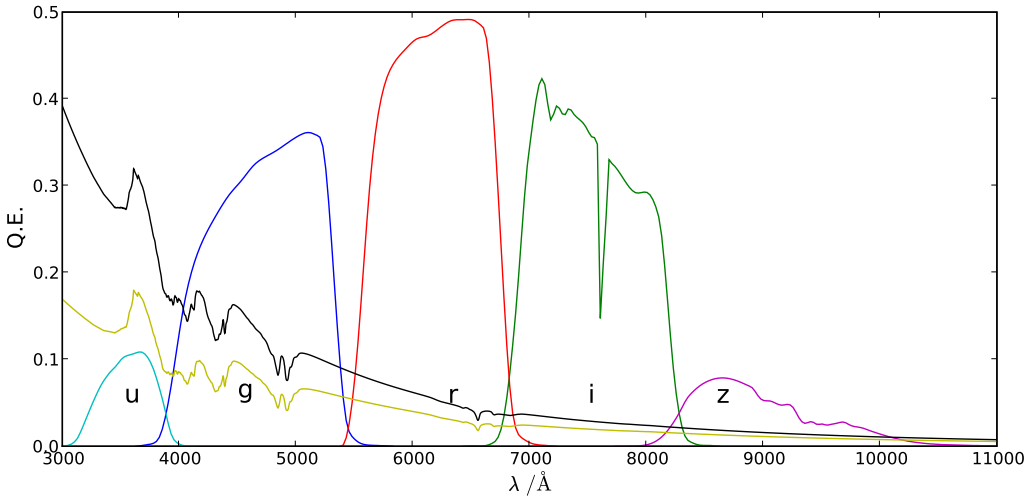

Figure 3.1: The diagram above shows the response curves of the $ugriz$ photometric pass-bands with applied 1.3 airmass correction, taken from the SDSS website (`http://www.sdss.org/dr7/`), compared to MWD spectra of different effective temperatures and same magnetic field geometry which for this case is the 12.61 MG offset dipole model of SDSS J0855+1640. The fluxes are in units, but the relative scale to each other is correct. The effective temperatures are 20 000 K (top), 15 000 K(bottom). The u, g and r bands cover the wavelengths which are effected by the magnetism in the MWD spectra for field strengths smaller than 50 MG. However this effect is minor for the r band.

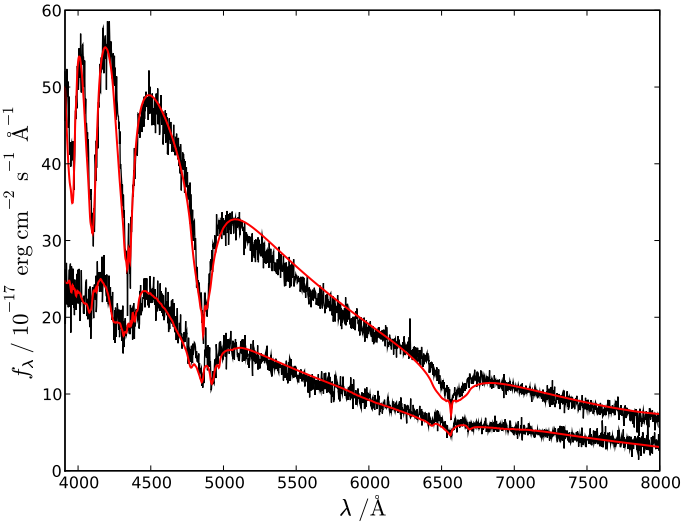

Figure 3.2: The spectral fits to WD0836+201 (top) and SDSS J0855+1640 (bottom) undertaken in this work. The parameters are given in Table. 3.3. Objects are plotted according to their observed fluxes for comparison. The inconsistencies in the WD0836+201 line fits are due to the simple treatment of relatively large Stark effect at the in the low-field regime ($B \leq 5$ MG). The fits are made to be sensitive to the continuum for assessing the effective temperature consistently.

3.3.3 Masses and cooling ages from photometric analysis

In order to determine the masses we used the synthetic magnitudes (in the *ugriz* photometric system of SDSS) for carbon-oxygen (CO) core white-dwarf cooling models with thick hydrogen layer ($M_{\rm H}/M_* = 10^{-4}$) masses (Wood, 1995; Holberg & Bergeron, 2006)[1]; since these are non-magnetic models the effect of the magnetism is not included in these calculations. As explained above, the MWD spectra show anomalous absorption under the effect of magnetic fields. Since both of the objects that we consider in this paper have relatively weak magnetic fields ($B_{\rm p} \leq 50\,{\rm MG}$) the modifications should be relatively small. Nevertheless, some regions of the spectrum and thereby some photometric bands are more affected by the magnetic field than others.

The photometric bands relative to a representative spectrum of a MWD in Paschen-Back regime ($0.5\,{\rm MG} \leq B_{\rm p} \leq 50\,{\rm MG}$) is shown in Fig. 3.1. The spectral position of the bound-bound transitions in this regime, with respect to magnetic fields are shown in Fig. 1.3. The u band is modified strongest by the magnetic field since it is close to the Balmer edge which is also split under the influence of the magnetic fields. The bands g and r are close to Balmer lines which are split under the influence of the magnetic fields so that we must assume a slight modification relative to the non-magnetic case. And finally i and z bands span over the continuum reasonably far away from the spectral line so that we can assume that these are almost equivalent to the non-magnetic values.

In order to minimise the uncertainties of our analysis we restricted ourselves to the use of i, r, and z. When comparing our mass determinations from the i band with those using u we obtain a difference as high as 8%; in the case of the g magnitude the differences decreases to 1%. The results for z and r magnitudes are consistent within 0.05%. This shows that the photometric magnitudes that correspond to spectral continuum are consistent with each other, thus we use the i band in our calculations.

We proceeded to calculate the absolute magnitudes using the known distance of Praesepe. There are multiple distance measurements of Praesepe; here we adopt the value of $184.5 \pm 6\,pc$ as the distance to the cluster center which was used by Casewell et al. (2009). It is the weighted mean of the Hipparcos-based distance measurement (Mermilliod et al., 1997), the ground-based parallax measurement of Gatewood & de Jonge (1994) and the photometric determination of An et al. (2007). It is not only a consistent approach to account for the multiple distance estimations in the literature, but also advantageous for us since we would like to compare our results to the ones of Casewell et al. (2009).

We interpolated the synthetic magnitude grids of Holberg & Bergeron (2006) at the spectroscopically determined effective temperature to find which mass and effective temperature yields this absolute i magnitude. The knowledge of mass together with $T_{\rm eff}$ yielded the cooling age straightforward from the evolutionary grids.

Furthermore we subtracted the estimated cooling ages from the total age of Praesepe which is 625 ± 50 Myr (Perryman et al., 1998, from isochrones fit with a metallicity of $Z = 0.024$) to calculate the progenitor ages of the MWDs. With this information at hand, estimating the initial masses is rather straightforward given the stellar evolution models. Hence we interpolated the Bertelli et al. (2009) stellar evolution grids with cubic splines to calculate the progenitor masses given the progenitor lifetime.

We have chosen a value of $Z = 0.027$ taken from Catalán et al. (2008) but our mass and age determinations do only weakly depend on the choice of metallicity: If we instead

[1] http://www.astro.umontreal.ca/~bergeron/CoolingModels

Table 3.4: $\log g$, mass, radii and cooling ages of Praesepe MWDs estimated with the photometric analysis.

MWD	$\log g$ / dex	$M_{\rm WD}$ / $\mathrm{M}_\odot$	radius / $0.01\,\mathrm{R}_\odot$	$t_{\rm cool}$ / Myr	$t_{\rm prog}$ / Myr	$M_{\rm i}$ / $\mathrm{M}_\odot$
WD0836+201	8.27±0.06	0.82±0.04	10.02± 0.49	222^{+30}_{-26}	403^{+58}_{-56}	$3.16^{+0.17}_{-0.14}$
SDSS J0855+1640	8.79±0.06	1.12±0.03	6.67± 0.31	391^{+39}_{-35}	234^{+62}_{-61}	$3.83^{+0.18}_{-0.20}$

use the lowest recent value for the metallicity of Praesepe $Z = 0.019$ (Claver et al., 2001; Casewell et al., 2009) the mass estimates become 0.03 $\mathrm{M}_\odot$ smaller and the progenitor age is 1% longer which is consistent with the result from Casewell et al. (2009).

We summarize our results in Table 3.4.

WD0836+201

Previous discussions of the properties of WD0836+201 (EG 59) are mostly based on the analysis by Claver et al. (2001) where the π components of the Zeeman splitted line cores were used for the determining $T_{\rm eff} = 17\,098\,K$ and $\log g = 8.32$. Using their values Catalán et al. (2008) re-estimated the mass and the progenitor mass of this object in order to discuss the effect of the magnetic field on IFMR. Casewell et al. (2009) mentioned that the analysis with non-magnetic model spectra may lead to uncertainties in the temperature determination. From the SDSS photometry ($u-g$, $g-r$) of WD0836+201, they determined an effective temperature of $15\,000\,\mathrm{K}$, and argued on this basis that the $T_{\rm eff}$ and $\log g$ determination from the spectroscopic fits with non-magnetic models are likely to be less robust.

With our model spectra for magnetised white dwarf atmospheres we obtain a more reliable fit of $T_{\rm eff} = 17\,000\,\mathrm{K}$ within the uncertainties discussed in Sec. 3.3.2. We used this temperature to estimate the mass, cooling age and the progenitor mass of WD0836+201 as explained in Sec. 3.3.3. Our results are summarized in Table C.1.

To check the consistency of our method, we compared our results with Claver et al. (2001) which implemented a similar analysis using the absolute V magnitude of the Praesepe white dwarfs at a given distance, and determined their radii from model atmospheres and then compared those with the radii from the evolutionary models of Wood (1995).

In this work, we used the distance modulus of 6.16 ± 0.05, labeled as rd1 in Claver et al. (2001) to calculate the mass of WD0836+201 and its progenitor for comparison purposes. Our result of $0.89 \pm 0.03\,\mathrm{M}_\odot$ corresponds to the 0.909 ± 0.015 $\mathrm{M}_\odot$ result of Claver et al. (2001) within the 3σ errors estimate. This shows that our results are consistent with the former analysis. Furthermore we show with our magnetic analysis that the temperatures assessed with non-magnetic colors are less reliable than spectroscopic analysis performed with models taking magnetic field into account.

SDSS J0855+1640

The question whether SDSS J0855+1640 belongs to the Praesepe cluster is less obvious than the case of WD0836+201 because SDSS J0855+1640 is further away from the cluster center and lies at the limb of the circular region defined by the tidal radius of the cluster. Different values for the tidal radius of the Praesepe have been determined in the literature:

Table 3.5: Coordinates, proper motions of the two WDs extracted from SDSS DR7.

Object	RA	Dec.	RA p.m. / (mas/yr)	Dec. p.m. / (mas/yr)
PG 1258+593	13 00 35.20	+59 04 15.6	42.4 ± 2.6	75.0 ± 2.6
SDSS J1300+5904	13 00 33.46	+59 04 06.9	41.8 ± 3.0	73.9 ± 3.0

Table 3.6: PSF magnitudes of the two WDs extracted from SDSS DR7.

Object	$u/$ mag	$g/$ mag	$r/$ mag	$i/$ mag	$z/$ mag
PG 1258+593	15.54 ± 0.01	15.20 ± 0.04	15.52 ± 0.02	15.76 ± 0.04	16.04 ± 0.02
SDSS J1300+5904	19.08 ± 0.03	18.23 ± 0.04	17.93 ± 0.02	17.80 ± 0.04	17.79 ± 0.03

Starting with 12 pc (Mermilliod et al., 1990), then a higher value of 16 pc was obtained (Adams et al., 2001), and finally an even higher value of 17.1 ± 1.2 pc (Piskunov et al., 2007) was found. In our work we used the 18.6 ± 1.4 pc value of Piskunov et al. (2008).

If we assume that SDSS J0855+1640 lies at 184.5 pc, which is the distance to the core of the cluster, its angular separation from the cluster center of 4.58° translates into a spatial distance of ∼14.7 pc. Within this radius the cluster members are expected to have the same kinematic properties of the cluster and high cluster proper motions relative to the field stars enables us to discriminate the members.

We also tested whether SDSS J0855+1640 can be a member of the Praesepe from an evolutionary point of view. When we estimate the radius hence the mass for a white dwarf with the observed flux of SDSS J0855+1640 and $T_{\rm eff} = 20\,000$ K (see Table 3.4), this yields cooling ages smaller than the age of Praesepe making a cluster membership possible.

It has been observed that the number of white dwarfs inside open clusters are lower than expected (Weidemann, 1977; Williams, 2002). The fact that white dwarfs tend to evaporate from the inner core of an open cluster due to galactic potential was already discussed for the case of the missing white dwarfs in Hyades (Weidemann et al., 1992). In this scenario, white dwarfs may leave the cluster by gaining small velocities (0.1 km/s) with respect to the cluster center.

Another reason for SDSS J0855+1640 to be at the tidal radius of the open cluster as a cluster member is the possibility of gaining a kick velocity of several km/s, due to asymmetric mass loss during the AGB phase (Fellhauer et al., 2003). This was tested observationally for the globular cluster NGC 6397 and found to be plausible (Davis et al., 2008).

If SDSS J0855+1640 is significantly far away from the cluster center, then the distance estimation based on the cluster membership might be erroneous. However, even if we assume SDSS J0855+1640 to be two tidal radii behind or in front of the center of Praesepe, SDSS J0855+1640 still can be assumed to be a member of the cluster since the inferred cooling ages in both cases are smaller than the cluster age.

Given the uncertainties of the analysis we have derived the evolutionary ages and the progenitor ages. We further evaluate the results these objects present, for the stellar evolution in the context of IFMR in Sec. 3.5.

3.4 Magnetic White Dwarfs in Wide Binaries

MWDs in wide binary systems provide important diagnostics to investigate the origin of magnetism, since it is yet another system in which mass and cooling age are measurable through investigation of the spectrum of the non-magnetic counterpart; hence the evolutionary time scales are known. Moreover, the components are probably did not interact during the binary lifetime hence a single star evolution can be assumed.

These kind of double degenerate systems with one magnetic and one non-magnetic white dwarf are currently rare. There are two flavours of possibilities due to the current picture of binary evolution. If the progenitor binary pair has a short enough orbital separation, the binary components go trough one or more phases of Common Envelope (CE) evolution. During the CE phase the system goes loses angular momentum due to the induced viscous braking, and the orbital separation shortens. These systems become close binaries or possibly even mergers if the loss of angular momentum continues due to gravitational wave radiation during the double degenerate phase (Iben & Tutukov, 1984, ,see also Sec. 5.5.2).

In the case in which the progenitor binary system starts with a large orbital separation and avoids a CE phase, the orbital separation does not shrink. After the mass-loss phase of the primary, the orbital separation increases and hence a wide binary system is formed.

Observationally, objects in a close binary are expected to exhibit unresolvable compound spectra in which the resolution of the instrument is not high enough to separate the individual components. On the other hand if the components of the binaries are well separated (100 to 1000 AU), depending on the distance and the resolution of the instrument they could be resolved separately. In this case their association to each other are confirmed by their common proper motion (CPM), hence they are defined as CPM pairs.

For the case where white dwarfs are in CPM pairs with F,G or K type stars the IFMR can be tested (Wegner, 1973; Oswalt et al., 1988; Catalán et al., 2008) using the age and metallicity of the main sequence component. This is a method in which the IFMR can be probed down to very low progenitor masses (initial mass of 1.5-2 $\mathrm{M}_{\odot}$) since the wide nature of the binary implies that the system was detached during its lifetime and a single star evolution is applicable.

For a double degenerate system, assessing the total evolutionary age depends on the progenitor age of the non-magnetic component. This means our age determinations depend on the semi-empirical IFMR. Within the assumptions we make for our estimates, the history of a non-interacting binary provides us with the possibility of test the fossil field hypothesis for magnetic field generation.

For this aim we have searched the SDSS database for proper motion companions and discovered SDSS J1300+590 to be a CPM pair with the well-studied hydrogen-rich (DA) white dwarf PG 1258+593. We analyzed this object with the constraints introduced by the non-magnetic counterpart to estimate the mass and the cooling age. According to the constraints introduced by the analysis of the non-magnetic component, we assess the origin of SDSS J1300+590.

3.4.1 Analysis of the Common Proper Motion system

To search for common proper motion pairs in the SDSS we have taken advantage of the UCAC2 astrometric catalogue as mentioned in the Sec. 3.3.1. This time we compared the proper motions of the white dwarfs against other white dwarfs in their vicinity and

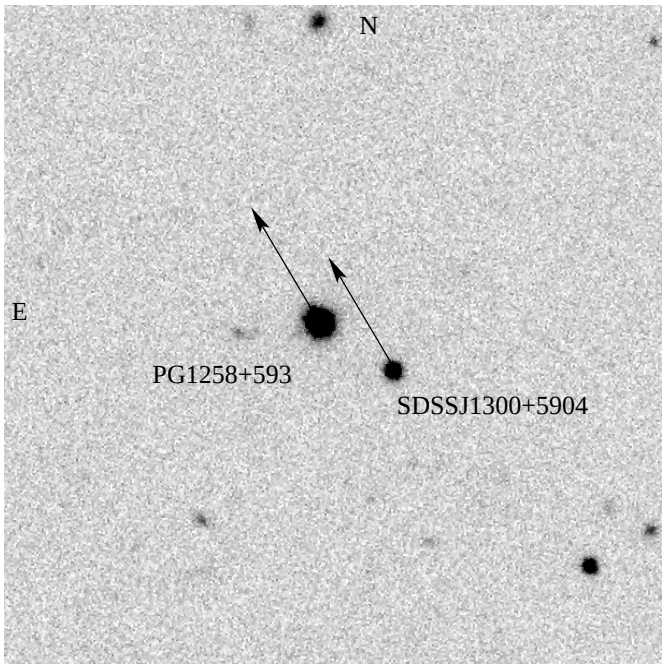

Figure 3.3: $2' \times 2'$ r band SDSS image of the WD CPM pair. Proper motions are indicated over 300 years. An SDSS fibre spectrum was obtained for the fainter component of the binary. Reproduced from Girven et al. (2010)

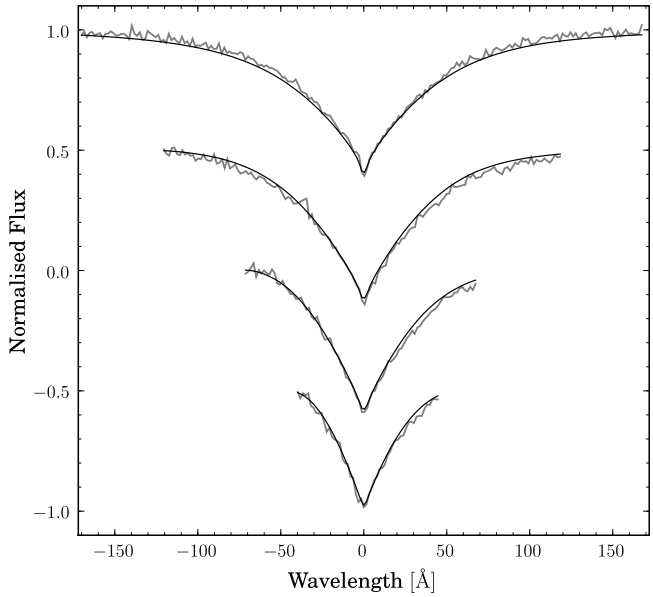

Figure 3.4: Normalised INT/IDS Hβ–Hϵ (top to bottom) line profiles of PG 1258+593 (gray line) and the best-fit model (black line) for $T_{\rm eff} = 14790$ K and $\log g = 7.87 \pm 0.02$. Reproduced from Girven et al. (2010).

Table 3.7: Atmospheric and stellar parameters for PG 1258+593 and SDSS J1300+5904.

	PG 1258+593	SDSS J1300+5904
$T_{\rm eff}$ / K	14790 ± 77	6300 ± 300
$\log g$ / dex	7.87 ± 0.02	7.93 ± 0.11
M / $\mathrm{M}_\odot$	0.54 ± 0.01	0.54 ± 0.06
R / 10^8 cm	9.85 ± 0.10	9.33 ± 0.64
$t_{\rm cool}$ / Myr	180 ± 7.00	1850 ± 50.0
B / MG	≤ 0.3	$\simeq 6$

discovered that the faint bluish SDSS J1300+5904 is a CPM companion to PG 1258+593[2]. Coordinates, proper motions, and $ugriz$ magnitudes of both white dwarfs are given in Tables 3.5, 3.6.

SDSS J1300+5904 had already been noted as a CPM companion by Farihi et al. (2005), however it was classified as a white dwarf with a featureless (DC) spectrum, based on a relatively poor spectrum. An investigation of the SDSS fibre spectrum confirms SDSS J1300+5904 as a DAH through the clear detection of a Zeeman-triplet in Hα (Fig. 3.5).

To be able to assess the evolutionary history of SDSS J1300+5904, it is necessary to know its distance and total evolutionary age which can be evaluated through the spectroscopic analysis of the non-magnetic counterpart PG 1258+593. In order to accomplish this, PG 1258+593 was observed on February 13, 1997, using the Intermediate Dispersion Spectrograph (IDS) on the Isaac Newton Telescope (INT). Two spectra of 20 min exposure time each were obtained with the R632V grating and a 1.5″ slit, covering the wavelength range $3680 - 5300$ Å at a spectral resolution of ~ 2.3 Å. The data were reduced and calibrated as described by Moran et al. (1999), and the normalised line profiles are shown in Fig. 3.4.

(Girven et al., 2010) analysed the INT/IDS spectrum of PG 1258+593 using DA model spectra from Koester et al. (2005) and the fitting routine described by Rebassa-Mansergas et al. (2007). The best fit is achieved for $T_{\rm eff} = 14790 \pm 77$ K and $\log g = 7.87 \pm 0.02$.

Compared with the analysis of Liebert et al. (2005) of PG 1258+593, which was done as part of their systematic analysis of the DAs from the Palomar Green Survey, our results are in excellent agreement. They quote $T_{\rm eff} = 14480 \pm 229$ K, $\log g = 7.87 \pm 0.05$, and 0.54 ± 0.02 $\mathrm{M}_\odot$. The distance to the CPM pair can be estimated as 68 ± 3 pc using the flux and equation 3.2.2. At this distance, the angular separation of 16.1 ± 0.1″ (Fig. 3.3) between the two objects translates into a minimum binary separation of 1091 ± 7 AU.

3.4.2 Analysis of the magnetic counterpart

The only information missing of SDSS J1300+5904 to estimate its mass and cooling age is the effective temperature. In order to estimate the $T_{\rm eff}$, we fitted the spectrum of SDSS J1300+5904 with centred magnetic dipolar models following the procedure outlined in Sec. 2.2.1 and Sec. 3.3.2.

As explained in Sec. 3.3.2, due to the lack of a consistent theory that describes Stark broadening in the presence of magnetic fields in this regime. Considering these uncertainties,

[2]Initially identified as a white dwarf candidate GD 322 by Giclas et al. (1967)

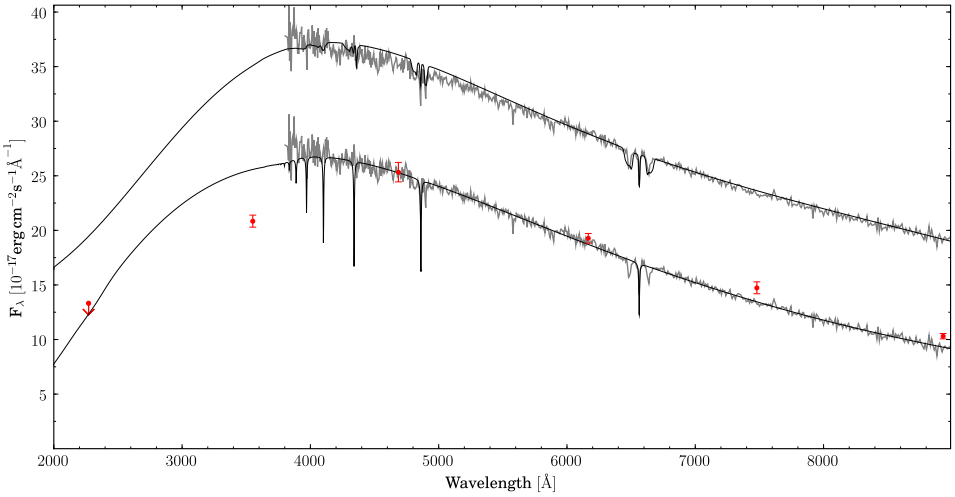

Figure 3.5: The SDSS spectrum of SDSS J1300+5904 with non-magnetic (bottom curves, $T_{\rm eff} = 6500\,K$, $\log g = 7.93$) and magnetic (top curves, $T_{\rm eff} = 6000$ K, $\log g = 7.93$) WD models. The top curves are offset by 10 flux units. The magnetic WD model is calculated for a centered dipole with polar strength of 6 MG at an inclination against the line-of-sight of 45 degrees. Shown in red are the fluxes corresponding to the SDSS $ugriz$ PSF magnitudes of SDSS J1300+5905. The left-most red point indicates the upper limit on the near-ultraviolet flux of SDSS J1300+5905 implied by the non-detection with GALEX. Reproduced from Girven et al. (2010).

we have used the approach of Gänsicke et al. (2002) and used two different methods to asses the effective temperature: Fitting only the Balmer lines (6000 K) and fitting the continuum slope (6800 K). In the case where only Balmer lines are fitted the slope of the model spectrum is normalized with respect to the observed continuum. The Zeeman splitting observed in Hα implies a magnetic field strength of $\simeq 6$ MG and suggests an intermediate inclination between the line-of-sight and the magnetic axis. Figure 3.5 shows a magnetic model spectrum for a offset dipole with polar strength of 6 MG with an inclination of ~ 45 degrees as an example of a satisfying fit (parameters given in Table C.1).

Afterwards, with the fitted value of $T_{\rm eff}$ and the photometric absolute magnitudes calculated using the distance and the observed magnitudes (Table 3.6); we estimated the radius, mass and the cooling age of the object by fixing the distance and using the atmospheric models of Holberg & Bergeron (2006), as explained in Sec. 3.3.3. Our results, that are summarized in Table 3.7, show that the MWD has a mass similar to the PG 1258+593. When we also consider the fact that SDSS J1300+5904 is the cooler counterpart, this immediately shows that the the progenitor mass of it should be more massive.

In contrast to PG 1258+593, SDSS J1300+5904 was not detected by GALEX but using the estimated distance of 68 pc, the limiting magnitude of GALEX, $m_{\rm nuv} = 20.5$, puts constraints on the $T_{\rm eff}$ between 6350 and $6650\,{\rm K}$ for a mass range from 0.47 to $0.63\ {\rm M}_{\odot}$. These limits are consistent with the results we obtained from fitting the $griz$ magnitudes for the same distance. The upper limits of the GALEX detection limits is also shown in Fig. 3.5

Within the errors, both WDs in this CPM pair have equal masses, but their different effective temperatures result in an age difference of 1.67 ± 0.05 Gyr, implying that their progenitor stars had rather different main-sequence life times. In this work we made use of this age difference PG 1258+593 and SDSS J1300+5904 to provide a semi-empirical upper

limit on the progenitor mass of SDSS J1300+5904.

Finley & Koester (1997) modelled the relatively massive white dwarf components of the CPM pair PG 0922+162, and they showed that that the estimated progenitor masses are consistent with the IFMR obtained from open clusters. In this part of the study, we adopted the main-sequence life times as a function of initial mass from the stellar evolution models of Pols et al. (1998). For any given choice of the progenitor mass of PG 1258+539 ($M_i^{\rm PG}$), the age difference of 1.67 ± 0.05 Gyr implies a progenitor mass for SDSS J1300+5904 ($M_i^{\rm SDSS}$). Figure 3.4.2 illustrates the relation between $M_i^{\rm PG}$ and $M_i^{\rm SDSS}$ for solar and half-solar metallicity models with and without overshooting. As the main-sequence life time is a very strong function of the initial mass, $M_i^{\rm SDSS}$ levels off very steeply for $1.4 \leq M_i^{\rm PG} \leq 1.8$, and in a most conservative interpretation, $M_i^{\rm PG} < 2.2$ M$_\odot$.

To investigate the influence of magnetism on the IFMR, we would like to estimate a value for the progenitor mass of the MWD. At a first look, the cooler nature of SDSS J1300+5904 implies that it is the result of a more massive progenitor, with respect to the binary companion PG 1258+593 of similar mass. To quantify the $M_i^{\rm SDSS}$, we can fix the estimate of $M_i^{\rm PG}$ according to the recent studies that probe down to low masses. Kalirai et al. (2008) accomplished that by investigating the very old cluster NGC 6791, which extended the semi-empirical IFMR down to initial masses of 1.16 M$_\odot$. The outcome of this investigation was a corresponding fit to all the cluster IFMR data:

$$M_f = (0.109 \pm 0.007) M_i + 0.394 \pm 0.025. \tag{3.4.1}$$

Here M_f is the final remnant mass and M_i the progenitor mass, in units of solar mass M$_\odot$. We can get a constrain for the $M_i^{\rm PG}$, by inserting in the estimated mass of 0.54 ± 0.01 into equation 3.4.1. Carefully propagating the errors, we end up with $M_i^{\rm PG} = 1.34 \pm 0.19$ as the progenitor mass. With this result we can further estimate the $M_i^{\rm SDSS}$ using the Fig. 3.4.2, to lie between $1.2-3.6$ M$_\odot$ including all the theoretical and observational uncertainties. For the most probable single value of $M_i^{\rm PG} = 1.34$, the MWD progenitor is $M_i^{\rm SDSS} = 1.61 \pm 0.14$ further propagation of errors to get error bars is not applicable for such a non-linear case and furthermore it is sufficient for our purposes to only consider the complete range of $1.2 - 3.6$ M$_\odot$.

3.4.3 Evolutionary status of the CPM pair

SDSS J1300+5904 and PG 1258+593 system belongs to a small population of spatially resolved double degenerates, in which one of the component is magnetic. All members of this group of objects are unique on their own. LB 11146, was the first pair and was discovered by Liebert et al. (1993b) who showed that its spectrum showed the properties of a featureless DC with weak hydrogen features. Subtracting a DA spectrum which could be diagnosed through the Balmer lines, yielded the featureless DC to be a MWD with hydrogen features around ~ 670 MG. The question of whether mass transfer existed in this system during the main sequence phase is still open, however a single star scenario is supported since Ap/A star binaries exist (Abt & Cardona, 1984; Schmidt et al., 1998) and magnetic field generation through CE phase or accretion is not necessarily need to be invoked, since the Ap/A eventually would lead to a MWD and a non-magnetic pair according to the "fossil field" hypothesis.

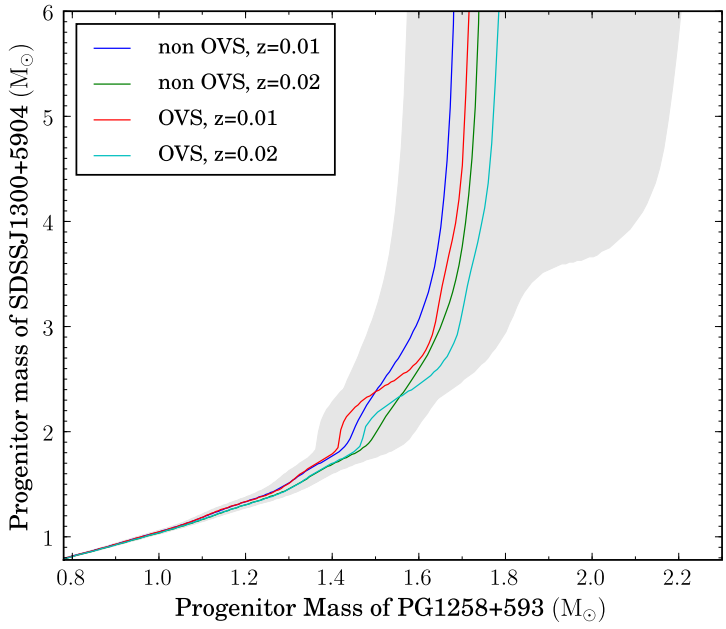

Figure 3.6: The mass of the SDSS J1300+5905 progenitor with respect to the mass of PG 1258+593 progenitor, according to the difference in cooling ages. The progenitor lifetimes are taken from Pols et al. (1998) and estimations are made for over-shoot (OVS) and non over-shoot models, as well as solar ($z = 0.02$) and half solar ($z = 0.01$) metallicities. The grey shaded area represents when 1σ errors on cooling times are considered. Reproduced from Girven et al. (2010).

Table 3.8: Known spatially resolved double degenerate systems with one magnetic component. Each double row represent a system, in which the second row has the properties of the DA counterpart

Name	MWD			separation		Ref.
	$T_{\rm eff}$ /K	$M_{\rm WD}/\,{\rm M}_{\odot}$	B /MG	["]	AU	
LB 11146	16000	0.9	670	~ 0.6	0.015	1,2,3,4
	14500	0.91 ± 0.07				
RE J0317-853	33800	1.32	340	~ 200	6.7	5,6,7,8
	16000	~ 0.93				
SDSS J1300+5904	6300 ± 300	0.54 ± 0.06	$\simeq 6$	16.1 ± 0.1	≥ 1091	9
	14790 ± 77	0.54 ± 0.01				

[1] Liebert et al. (1993b); [2] Glenn et al. (1994); [3] Schmidt et al. (1998); [4] Nelan (2007); [5] Barstow et al. (1995); [6] Ferrario et al. (1997); [7] Burleigh et al. (1999); [8] Vennes et al. (2003); [9] this paper.

The other MWD is such kind of system is the RE J 0317-853 which is unique in its own right since it is the most massive and the most rapid rotating single white dwarf known. Its evolutionary history is discussed in detail in Sec. 5.

Another flavour of double degenerate systems with one magnetic component, is the situation where the components are non-resolved. There two of such cases known up to date. One is EUVE J1439+75.0 (Vennes et al., 1999) where the surface gravity measurements imply masses of 1.0 and 0.9 $\mathrm{M}_{\odot}$ for the magnetic (B ~ 10 MG) and non-magnetic components respectively. These systems are so close that the disentangling of the spectra is problematic hence there were multiple possibilities for effective temperature and $\log\ g$ model parameters. The other double degenerate system is CBS 229 (SDSS J150813.20+394504.9) in which a preliminary analysis was undertaken by subtracting a non-magnetic component of $T_{\mathrm{eff}} = 15,000\,K$ and $\log\ g = 8.5$ from the composite spectrum hence showing the magnetic structure clearly. The composite spectrum of this object was analysed in Chapter 2 without the consideration of a binary and the implications were discussed in Sec. 2.3 (see also Fig. B.19).

The sample of known MWDs in binaries is quite few at this point, and MWDs with very strong fields seem to exist only in the resolved wide binary systems, however this could be an observational bias where the highest field MWDs are falsely classified as featureless DCs.

Evolutionarily, the existence of high field ($B \geq 100$ MG) MWDs in wide binaries shows that invoking the CE envelope scenario is not needed, however properties of the currently known objects introduces the possibility of binary interaction. Namely the relatively close orbit of LB 11146 implies a possible phase of mass transfer (Nelan, 2007), the high mass and angular momentum of RE J 0317-853 provides the possibility of a merger from an initial ternary system (Vennes et al., 2003, . The details of the RE J 0317-853/LB 9802 system is discussed extensively in Chapter 5).

The possibility of PG 1258+593/SDSS J1300+5904 having evolved from a ternary system like the one proposed for RE J 0317-853 might not be disregarded. According to this hypothesis, SDSS J1300+5904 might be the result of a merger of a close binary in which PG 1258+593 is the surviving third component at a wide orbital separation. The mass of SDSS J1300+5904 is typical for a single white dwarf, so any merger event would have been either due to the merger of two low mass white dwarfs possibly with helium cores, or had to involve a non-degenerate low mass star. In the case that SDSS J1300+5904 is the product of a merger, one would expect the MWD to be rapidly spinning, which could be confirmed by photometric variability (e.g. Brinkworth et al., 2004, 2005).

Additionally to the merger scenario, the PG 1258+593/SDSS J1300+5904 could be in a triple system in which the third component is unresolved. This contrived case was already observed for WD 1704+481 (Maxted et al., 2000). However the spectrum of SDSS J1300+5904 shows no evidence for an additional binary companion, unless it is a featureless DC (analogous to G62-46 Bergeron et al., 1993), or a very late type dwarf. Using the star spectral templates of Araujo-Betancor et al. (2005), a hypothetical unresolved late type companion to SDSS J1300+5904 would have to be of spectral type L5 or later to go unnoticed. White dwarf plus brown dwarf binaries are extremely rare (Farihi et al., 2005), hence discovering such a system in a CPM wide binary system appears rather unlikely. Moreover it is possible to rule out this hypothesis by infrared observations.

Setting aside the possibilities of an unresolved binary and an unrecognised merger, SDSS J1300+5904 differs from the two previously known MWDs in spatially resolved bina-

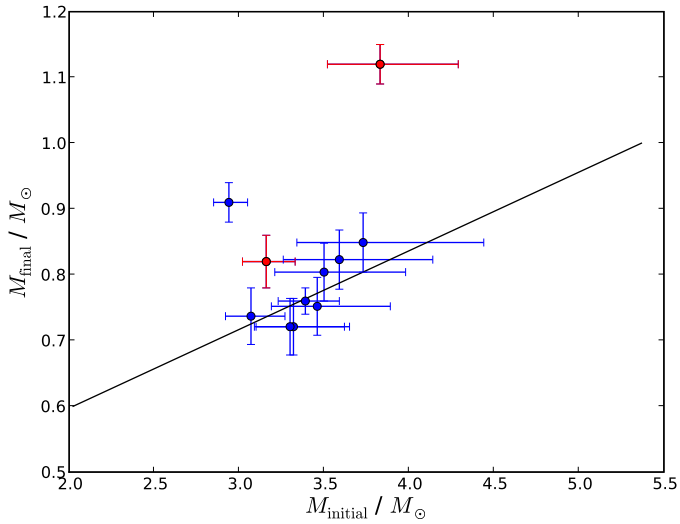

Figure 3.7: IFMR and the position of the Praesepe white dwarfs in this diagram from Casewell et al. (2009). The line is the best fit of Casewell et al. (2009), blue dots represent the regular white dwarfs and the red dots denote the position of the two MWDs in the Praesepe discussed in this paper and WD0636+197 is a known outlier.

ries that it appears to have evolved without interacting which implies a single star stellar evolution was in effect. In this case, it is more likely that the origin of the magnetic field is the fossil field from an Ap/Bp progenitor and not from dynamos from a CE phase (Tout et al., 2008). This is also consistent with the estimated progenitor mass of around $\sim 2\ \mathrm{M}_\odot$ (see Sec. 3.5) calculated from the total evolutionary ages.

3.5 Discussion on IFMR

In this study we were able to recover the formerly known Praesepe member WD0836+201 with our methods, and additionally we showed that our analysis is consistent with the literature. Furthermore with this method we discovered another prospective Praesepe member, SDSS J0855+1640 that probably is a part of the rare group of ultra-massive white dwarfs with masses above $1.1\ \mathrm{M}_\odot$. This group of objects are proposed to be final products of binary mergers and were observed numerously in EUV surveys (Bergeron et al., 1991; Marsh et al., 1997).

In addition to the massive ($1.12\ \mathrm{M}_\odot$) nature of SDSS J0855+1640 the evolutionary arguments show that it is the result of a $3.83\ \mathrm{M}_\odot$ progenitor which is consistent with the progenitor mass of the other white dwarfs in the system. However this puts the MWD as a strong outlier on the IFMR (see Fig. 3.7). Our assessments strongly depend on the assumed distance to the MWD. Especially since the SDSS J0855+1640 positioned along the center of the cluster but rather close to the tidal radius, it is worth considering the extreme limits for the assumed radius.

If SDSS J0855+1640 is two tidal radius behind the cluster, its mass is $1.2\ \mathrm{M}_\odot$ and it comes from a star of $\sim 7.4\ \mathrm{M}_\odot$. This results puts SDSS J0855+1640 approximately on the IFMR. In the case where SDSS J0855+1640 is two tidal radii in front of the cluster center,

mass of SDSS J0855+1640 is estimated as 1.0 $M_\odot$with a progenitor mass of $3.25\ M_\odot$, which makes SDSS J0855+1640 still an outlier in the IFMR diagram. Considering all the aforementioned possibilities, SDSS J0855+1640 is a strong outlier in the IFMR which might suggest that a merger scenario is more probable than single star evolution.

Our results in Sec. 3.4.1 (see also Fig. 3.4.2) shows that unlike the cluster MWDs, SDSS J1300+5904, which is a member of a CPM pair, lost considerably higher mass than its non-magnetic counterpart of the same mass. One should also note that a scatter for the estimated initial masses around $\sim 3\ M_\odot$ was observed for NGC 2099 (M 37 Kalirai et al., 2005) and the theoretical uncertainties of mass loss in this regime might also be the reason for this discrepancy. A similar type of scatter for the estimated initial masses around $\sim 3\ M_\odot$ was also observed for NGC 2099 (M 37 Kalirai et al., 2005).

This shows the current shortcomings of the mass loss theory. Furthermore testing the influence of the magnetism during the evolution of SDSS J1300+5904 awaits further studies of the low mass end of IFMR and better statistics for the MWDs in wide binaries.

The case of SDSS J0855+1640 and WD0836+201 seems to be more promising since all cluster white dwarfs except one seems to be consistent with the semi-empirical IFMR studies, and furthermore the masses of both MWDs are consistently higher than the rest of the cluster population. The observational result that MWDs are on average more massive than the non-magnetic white dwarfs (see Sec. 1.1.2; Liebert et al., 2003; Należyty & Madej, 2004), supports the possibility of the influence of magnetism on MWD masses.

The massive nature of MWDs can be explained by mergers which also is expected to generate magnetic fields due to dynamos induced by the internal shear and turbulent motions happening during the process (Piro, 2008). The larger masses of MWDs might also be the due to the influence of the fossil fields on the mass loss during stellar evolution. In this case magnetism could change the pressure structure, similar to the way angular momentum does (Dominguez et al., 1996), postponing the carbon ignition and allowing the core to grow which in turn results in an on average more massive white dwarf.

Our work shows that magnetism causes additional scatter in the IFMR however constraining the underlying physics that is in effect, depends on the careful considerations of hypothesis of stellar evolution under the influence of magnetism.

Chapter 4

Cyclotron Absorption

4.1 Introduction

The modeling of the Magnetic White Dwarf spectra for all the wavelengths in the optical range is far from complete. Although precise calculations of the bound-bound transitions exist (see Sec. 1.3.3), the rest of the spectral range, namely the continuum opacities relies on approximations based on the non-magnetic opacities (Lamb & Sutherland, 1974) or magnetic calculations for limited field ranges and angles (Merani et al., 1995; Zhao & Stancil, 2006).

Under the effect of magnetic fields, the electrons have a resonance at cyclotron frequency ($\omega_H = eB/m_e c$). This is classically explained as being due to specific electron orbits, that are induced by Lorentz force acting as the centripetal force for circular motion. Hence the transitions do not take place between quantum levels like in bound-bound case but between Landau levels, that are induced by the quantization of the electromagnetic field in the magnetized plasma. For the temperature regime where most of the MWDs are observed ($50\,000\,K > T_{\rm eff} > 6\,000\,K$) the transitions always collapse to the lowest $n = 1$ Landau level (see Sec. 1.3.3).

Classically free-free transitions can also be defined as magnetic bremstrahlung of a non-relativistic particle (as opposed to the relativistic version which is called synchrotron). The physical picture is the circular motion of the particles around the magnetic field hence the centripetal force cause radiation at an infinite number of harmonics, $s = \pm1, \pm2, \pm3$. The zeroth harmonic corresponds to a modified Cherenkov radiation.

Formerly the cross-section for cyclotron absorption was calculated quantum mechanically (Lamb & Sutherland, 1971, 1974), which only considers one electron and then convolves the absorption profile with the broadening due to velocity distribution of the electrons. Another approach that has been used for a long time in neutron stars is the calculation of the cyclotron absorption coefficient using the radiation transfer in anisotropic plasmas (see e.g. Mészáros, 1992).

There are mainly two approaches in absorption coefficient calculations, the first one is the calculation of the emissivity of a single photon propagating with arbitrary angle with respect to the magnetic field and integrating over the velocity distribution of the electrons. Then the cyclotron absorption coefficients are derived simply by Kirchoff's law (e.g. Bekefi, 1966) (equation 1.3.4). The second approach is a direct calculation of dielectric tensors. Both of the methods discussed in the context of accreting magnetic white dwarfs (see Chanmugam et al., 1989, for an overview).

Although the physical picture is simple, the free-free absorption is effective over most of the continuum spectrum, and most importantly impacts the level of the circular polarization, since the Landau levels are right handed which causes any free-free transition to effectively block one component of the polarization depending on the angle of the magnetic field vector. This fact has undeniable importance historically, in the discovery of the MWDs observationally. The confirmation of GRW+70°8247 as being magnetic depended on the first models of free-free transition (in that case, it was the harmonic oscillator model of Kemp, 1970; Kemp & Swedlund, 1970, see Sec. 1.1.2) and the interpretation of the circular polarization spectrum.

Currently the calculations of synthetic spectrum of MWDs, especially for the polarization, is problematic. This can be observed in the spectral fits to GRW+70°8247 (Jordan, 1992), which is the archetypical high-field MWD, and for RE J 0317-853 (see e.g. Vennes et al., 2003) which has the highest observed value of circular polarization. In order to fill this gap in the spectral modeling of high field MWDs, we reconsider the cyclotron opacities in the literature and introduce a self-consistent method of calculation for free-free transition parameters of MWD atmospheres.

In the first part of this Chapter, Sec. 4.2 I discuss the applicability of classical plasma calculations to MWD atmopsheres. Then in Sec. 4.3 I start introducing the plasma concepts and transfer of electromagnetic waves in plasmas. In this section I use the elementary theory to calculate the cyclotron absorption. In Sec. 4.4, I solve the Boltzmann equation and compare my results for the free-free parameters with the literature (outlined in Sec. 1.3.3) which are calculated by various methods. After showing that the classical plasma methodology is completely coincident with the former calculations; in Sec. 4.5 I use the results of the kinetic theory to self-consistently calculate the properties of the magnetized medium with increased parametrization which is needed for the MWD atmospheric conditions near the cyclotron frequency.

4.2 Applicability of Calculations in the Classical Regime for Magnetic White Dwarfs

Throughout this chapter the plasma formalism is used (see e.g. Ginzburg, 1964) This formalism starts from Maxwell's equations and includes either solving for the equation of motion for a charged particle, or the calculation of the transfer equation (the Boltzmann equation) for a distribution of particles. This basically implies the usage of classical electrodynamics, mechanics and statistical physics, leaving out relativistic and quantum calculations. Hence it should be explicitly shown, that under the physical conditions of a magnetized white dwarf atmosphere, relativistic and quantum calculations are not needed.

For the collisionless case the applicability limit is determined by the energy of the photons. For ($\hbar\omega \ll mc^2$) electrons may oscillate freely without any disruption, hence the classical picture completely accounts for the motion. This limit is valid up to soft X-rays ($\hbar\omega \sim mc^2 = 0.511$ MeV). However the refractive index of the media is determined by the internal collisions, or fundamentally the interaction of the electrons with photons. If we omit the cases of bound-bound and bound-free, we are left with free-free namely momentum transfer between free electrons and photons. For the classical limit to be valid for the non-relativistic electrons the kinetic energy of the electrons should be larger than the energy of the photon quanta ($\hbar\omega \ll kT$), which is not satisfied for optical wavelengths

(for $\hbar = 1.05 \times 10^{-27}$ erg sec, $k_b = 1.38 \times 10^{-16}$ erg/K; $\sim 0.5c/T \ll \lambda$)

The order of magnitude of the physical parameters relevant for MWD atmospheres are:

$$\omega_H = 1.76 \times 10^{15} B_8 \ \mathrm{s}^{-1} \tag{4.2.1}$$

$$\omega_p = 1.78 \times 10^{13} N_{17}^{1/2} \mathrm{s}^{-1} \tag{4.2.2}$$

$$\begin{aligned} \nu_{\mathrm{eff}} &= 7.751 \times 10^{15} P_e T^{-2/5} \times [-8.835 + 2\ln(T) - \frac{1}{2}\ln(P_e)]\mathrm{s}^{-1} \\ &= 7.751 \times 10^{10} P_{e5} T_4^{-2/5} [-8.835 + 18.42\ln(T_4) - 5.75\ln(P_{e5})\mathrm{s}^{-1}] \end{aligned} \tag{4.2.3}$$

where ω_H is the cyclotron frequency, ω_p the plasma frequency and ν_{eff} the effective collisions taken from Spitzer (1956). All of the parameters are represented in particle density N, magnetic field strength B, temperature T and electron pressure P_e. The subscripts represent the power to the ten value of the parameter, i.e. B_8 means magnetic field strengths in units of 10^8 Gauss, which is the magnetic field regime we are interested in for the aforementioned MWDs, RE J 0317-853 and GRW+70°8247.

Knowing the physical constraints introduced by the physical dimensions of the MWD atmospheres, we can proceed with basic considerations for the atmospheric medium using the elementary theory.

4.3 Elementary Theory of Wave Propagation in Magnetoactive Plasma

The propagation of electromagnetic waves inside a completely or partially ionized plasma depends on the properties of the medium. The motions, density and distribution of the charges inside, define the properties of any ionized medium, which can be described starting with Maxwell's equations.

$$\begin{aligned} \nabla \cdot \vec{H} &= 0 \\ \nabla \times \vec{H} &= \frac{4\pi}{c}\vec{j} + \frac{\partial_t \vec{D}}{c} \\ \nabla \cdot \vec{D} &= 4\pi\rho \\ \nabla \times \vec{E} &= -\frac{\partial_t \vec{H}}{c}. \end{aligned} \tag{4.3.1}$$

Hence $\vec{E}$ and $\vec{H}$ are the electric field and the magnetic field vectors, $\vec{D}$ is the electric displacement ($\vec{D} = \epsilon\vec{E}$), ρ is the charge density and $\vec{j}$ is the current density ($\vec{j} = \sigma\vec{E}$). ϵ is the permittivity (or dielectric constant) and σ is the conductivity. For plasmas the magnetic displacement $\vec{B}$ is not used since magnetic permeability is practically equal to unity.

The reciprocative nature of the electromagnetic waves and the charges inside the medium allows us to use the electromagnetic field as a probe. An electromagnetic wave is a harmonic function and its time dependent part is simply $e^{i\omega t}$ hence the time dependencies inside the Maxwell's equations are converted to $i\omega$ (see equation 1.3.11)

$$\begin{aligned}
\nabla \cdot \vec{H} &= 0 \\
\nabla \times \vec{H} &= \frac{4\pi}{c}\vec{j} + \frac{i\omega \vec{D}}{c} \\
\nabla \cdot \vec{D} &= 4\pi\rho \\
\nabla \times \vec{E} &= -\frac{i\omega \vec{H}}{c}
\end{aligned} \tag{4.3.2}$$

From this set the wave equation to be solved is reached simply by putting $\vec{H}$ expressed in terms of $\nabla \times E$ inside the equatuin$\nabla \times \vec{H}$.

$$\begin{aligned}
i\frac{\omega}{c}\nabla \times (\nabla \times \vec{E}) &= \frac{4\pi}{c}\vec{j} + \frac{i\omega\epsilon\vec{E}}{c} \qquad\qquad \vec{j} = \sigma\vec{E} \\
-\nabla \times (\nabla \times \vec{E}) - i\frac{4\pi\omega}{c^2}\sigma\vec{E} + \frac{\omega^2}{c^2}\epsilon\vec{E} &= 0 \\
\nabla^2\vec{E} - \nabla(\nabla \cdot \vec{E}) + \frac{\omega^2}{c^2}\left(\epsilon - i\frac{4\pi}{\omega}\sigma\right)\vec{E} &= 0 \\
\nabla^2\vec{E} - \nabla(\nabla \cdot \vec{E}) + \frac{\omega^2}{c^2}\epsilon'\vec{E} &= 0.
\end{aligned} \tag{4.3.3}$$

ϵ' is called complex permittivity which simply is $\epsilon' = \epsilon - i4\pi\sigma/\omega$. To solve the wave equation we need to have an expression for complex permittivity. The permittivity and the conduction is derived from the motions of the ions and electrons. To get a sense of conductivity we can have an elementary derivation from the current and equation of motions of the particles. The total current density from the motion of the charges is

$$\vec{j}_t = e\sum_{k=1}^{N}(\dot{\vec{r}}_k - \dot{\vec{r}}_k^{(i)})$$

in which e is the charge of an electron, $\dot{r}_k$ is the velocity of the electrons and $\dot{r}_k^{(i)}$ is the velocity of the ions. Here the plasma is assumed to be quasineutral meaning $N = N_- = N_+$, which is a good approximation for our case. The total current is the combination of conduction current density $\vec{j}$ and change in polarizability $\vec{P} = (\vec{D} - \vec{E})/4\pi$; $\vec{j} + \partial_t\vec{P}$,

$$\begin{aligned}
\vec{j}_t = \vec{j} + i\omega\vec{P} = \left(\sigma + i\frac{\epsilon - 1}{4\pi}\omega\right)\vec{E} &= i\frac{\omega}{4\pi}(\epsilon' - 1)\vec{E} \\
&= e\sum_{k=1}^{N}(\dot{\vec{r}}_k - \dot{\vec{r}}_k^{(i)})
\end{aligned} \tag{4.3.4}$$

When collisions between electrons between other electrons and ions are neglected the equation of motion for them can be written as:

$$\begin{aligned}
m\ddot{\vec{r}}_k = e\vec{E} &= e\vec{E}_o e^{i\omega t} \\
\partial_t^2\vec{r}_k &= \frac{e\vec{E}_0 e^{i\omega t}}{im\omega} \\
\vec{r}_k &= -\frac{e\vec{E}_0 e^{i\omega t}}{m\omega^2}.
\end{aligned}$$

Knowing the equation of motion of the charges allows us to write the expressions for the current densities with which the polarizability can be expressed according to equation 4.3.4.

$$\begin{aligned} P = \frac{\vec{D}-\vec{E}}{4\pi} = \frac{(\epsilon-1)\vec{E}}{4\pi} &= \int e\sum_{k=1}^{N}(\dot{\vec{r}}_k - \dot{\vec{r}}_k^{(i)})dt \\ &= e\sum_{k=1}^{N}(\vec{r}_k - \vec{r}_k^{(i)}) \\ &= -\frac{e^2}{\omega^2}\vec{E}\left(\frac{N}{m} - \sum_l \frac{N_l}{m_l}\right) \\ \epsilon = 1 - \frac{4\pi e^2}{\omega^2}\left(\frac{N}{m} - \sum_l \frac{N_l}{m_l}\right). & \end{aligned}$$

This description of complex permittivity yields purely real functions, which means the conductivity is zero. This result is inherently connected to the fact that we did not include the effects of collisions, hence there is no momentum transfer between the electrons and they freely oscillate in the field. If we want to involve collisions, we have to consider the momentum transfer, $m\dot{\vec{r}}\nu_{\text{eff}}$ as a contribution to the equation of motion. Here, ν_{eff} is the frequency of collisions (effective number of collisions per second).

$$m\ddot{\vec{r}}_k + m\nu_{\text{eff}}\dot{r}_k = e\vec{E}_o e^{i\omega t} \tag{4.3.5}$$

The velocity term simply represents a damping term to the oscillations of the electrons. The solution proceeds the same way, assuming oscillation for the electron trajectories and determining the amplitude.

$$\begin{aligned} \dot{\vec{r}}_k &= Ae^{iwt} \\ -\omega^2 mAe^{i\omega t} + im\omega Ae^{i\omega t}\nu_{\text{eff}} &= eE_0 e^{i\omega t} \\ A(-m\omega^2 + im\omega\nu_{\text{eff}}) &= eE_0 \\ A &= -\frac{eE_0}{m(\omega^2 - i\omega\nu_{\text{eff}})} \\ \dot{\vec{r}}_k &= -\frac{eE_0}{m(\omega^2 - i\omega\nu_{\text{eff}})}e^{iwt}. \end{aligned} \tag{4.3.6}$$

Repeating the steps of the collisionless case in which we equated the polarizability to the integral of the current, we reach the complex dielectric constant.

$$\begin{aligned}
\epsilon' &= 1 - \frac{4\pi e^2 N}{m(\omega^2 - i\omega\nu_{\text{eff}})} \\
&= 1 - \frac{4\pi e^2 N\omega}{m\omega(\omega^2 + \nu_{eff}^2)} + i\frac{4\pi e^2 N\nu_{\text{eff}}}{m\omega(\omega^2 + \nu_{eff}^2)} \\
\epsilon &= \Re(\epsilon') = 1 - \frac{4\pi e^2 N\omega}{m\omega(\omega^2 + \nu_{eff}^2)} \\
\sigma &= \Im(\epsilon') \cdot \frac{\omega}{i4\pi} = \frac{e^2 N\nu_{\text{eff}}}{m(\omega^2 + \nu_{\text{eff}}^2)}.
\end{aligned}$$

Now we can move away from the field free case to the constant magnetic field. Under a constant magnetic field, the charges are effected by a force which is analogous to the centrifugal force that induces gyration along the constant lies of force. This is parametrized by the gyration frequency $\omega_H = |e|H/mc$. More importantly the Lorentz force induces an anisotropy in the plasma, hence the complex dielectric constant becomes a complex dielectric tensor characterizing the direction dependence of these properties.

$$\epsilon'_{ik} = \epsilon_{ik} - i4\pi\sigma_{ik}/\omega, \qquad \vec{j}_i = \sigma_{ik}\vec{E}_k, \qquad \vec{D}_i = \epsilon_{ik}E_k.$$

If we take the direction of the constant magnetic field to be $\hat{z}$, the properties of the matter hence the dielectric tensor in the direction of the magnetic field and transverse to it will be different. This type of anisotropy is the direct consequence of the Lorentz force.

$$\begin{aligned}
& & m\ddot{\vec{r}} + m\nu_{\text{eff}}\dot{r} &= e\vec{E}_o e^{i\omega t} + e\dot{\vec{r}} \times \vec{H}/c \\
\dot{r}_z \times \vec{H} = 0, & & m\ddot{r}_z + m\nu_{\text{eff}}\dot{r}_z &= e\vec{E}_o e^{i\omega t} \\
\dot{r}_{x,y} \times \vec{H} = \mp\dot{r}_{x,y}H_z/c, & & m\ddot{r_{x,y}} + m\nu_{\text{eff}}\dot{r} &= e\vec{E}_o e^{i\omega t} \mp e\dot{r}_{x,y}H_z/c \\
& & r_z &= -\frac{eE_z\hat{z}}{m(\omega^2 - i\omega\nu_{\text{eff}})}e^{i\omega t} \\
& & \dot{r}_z &= \frac{eE_0}{m(i\omega + \nu_{\text{eff}})}e^{i\omega t}\hat{z} \\
& & r_{x,y} &= -\frac{eE_{x,y}}{m(\omega^2 - i\omega\nu_{\text{eff}} \pm \omega\omega_H)}e^{i\omega t}\hat{x}, \hat{y} \\
& & \dot{r}_{x,y} &= \frac{eE_0}{m(i\omega + \nu_{\text{eff}} \mp i\omega_H)}e^{i\omega t}\hat{x}, \hat{y}.
\end{aligned}$$

Total current density is given as $\vec{j}_t = eN\dot{\vec{r}}$ and independent from the field. When we write the longitudinal and transversal (to the field hence to $\hat{z}$) components of the current density:

$$\begin{aligned}
j_{tx} \pm ij_{ty} &= \frac{e^2 N(E_x \pm iE_y)}{m(i\omega + \nu_{\text{eff}} \mp i\omega_H)} \\
j_{tz}\pm &= \frac{e^2 NE_z}{m(i\omega + \nu_{\text{eff}})}
\end{aligned}$$

we can see that the currents in the direction of the magnetic field are unaffected and the induced acceleration is equivalent to equation 4.3.6, due to the transversal nature of the Lorentz force.

The description of the total current density directly leads to the calculation of the dielectric tensor:

$$\begin{aligned}
\epsilon'_{ik} &= \epsilon_{ik} - i4\pi\sigma_{ik}/\omega \\
\epsilon'_{ik}E_k &= \epsilon_{ik}E_k - i4\pi\sigma_{ik}E_k/\omega \\
&= D_k - i4\pi j_k/\omega = E_k + 4\pi P_k - i4\pi j_k/\omega \\
&= E_k + 4\pi j_{t_k}/i\omega.
\end{aligned}$$

By calculating each $E_k + 4\pi j_{t_k}/i\omega$, we can reach the transverse and longitudinal components

$$\begin{aligned}
(D_x - i4\pi j_x/\omega) \pm i(D_y - i4\pi j_y/\omega) &= \left(1 - \frac{\omega_p^2}{\omega^2 \mp \omega\omega_H - i\omega\nu_{\text{eff}}}\right)(E_x \pm iE_y) \\
D_z - i4\pi j_z/\omega &= \left(1 - \frac{\omega_p^2}{\omega^2 - i\omega\nu_{\text{eff}}}\right)E_z.
\end{aligned}$$

Here the plasma frequency ω_p is defined as $\omega_p^2 = 4\pi e^2 N/m$. From these descriptions we can calculate each component of the dielectric tensor one by one. We start by the simplifying our set of equations, also with the use of Hermitian property ($\epsilon_{ik} = \epsilon_{ki}^*$; even in the absence of the absorption):

$$
\begin{aligned}
D_z - i4\pi j_z/\omega = \epsilon'_{zk}E_k = \epsilon'_{zx}E_x + \epsilon'_{zy}E_y + \epsilon'_{zz}E_z \\
\epsilon'_{zx} = \epsilon'_{xz} = \epsilon' zy = \epsilon' yz = 0 \\
D_z - i4\pi j_z/\omega = \epsilon'_{zk}E_k = \epsilon'_{zz}E_z \\
\left(1 - \frac{\omega_p^2}{\omega^2 - i\omega\nu_{\text{eff}}}\right) E_z = \epsilon'_{zz}E_z \\
\epsilon'_{zz} = 1 - \frac{\omega_p^2}{\omega^2 - i\omega\nu_{\text{eff}}}
\end{aligned}
$$

$$
\begin{aligned}
\left(1 - \frac{\omega_p^2}{\omega^2 \mp \omega\omega_H - i\omega\nu_{\text{eff}}}\right)(E_x \pm iE_y) &= \epsilon'_{xx}E_x \pm \epsilon' xyE_y + i(\epsilon'_{yx}E_x + \epsilon'_{yy}E_y) \\
&= (\epsilon'_{xx} \pm i\epsilon' yx)E_x \pm i(\epsilon'_{yy} \mp \epsilon'_{xy})E_y \\
\epsilon'_{xx} \pm i\epsilon'_{yx} = \epsilon'_{yy} \mp \epsilon'_{xy} &= 1 - \frac{\omega_p^2}{\omega^2 \mp \omega\omega_H - i\omega\nu_{\text{eff}}}
\end{aligned}
$$

$$
\begin{aligned}
\epsilon'_{xx} = \epsilon'_{yy} &= 1 - \frac{\omega_p^2(\omega - i\nu_{\text{eff}})}{\omega[(\omega - i\nu_{\text{eff}})^2 - \omega_H^2]} \\
\epsilon'_{yx} = -\epsilon'_{xy} &= -i\frac{\omega_p^2\omega_H}{\omega(\omega + \omega_H - i\nu_{\text{eff}})(\omega - \omega_H - i\nu_{\text{eff}})}. \qquad (4.3.7)
\end{aligned}
$$

Above, we have the relations for the dielectric tensor of a magneto-active plasma. The dielectric tensors of inactive but anisotropic medium is symmetrical and in the absence of collisions they are also real. In the medium without external fields, $\vec{D}$ and $\vec{E}$ vectors are parallel in all three coordinates, but this is not the case for the magneto-active media. The two principle directions are the direction of the magnetic field where $D_z = \epsilon_{zz}E_z$, and the plane perpendicular to it, $D_x \pm iD_y = (\epsilon_{xx} \mp i\epsilon_{xy})(E_x \pm iE_y)$ the proportionality of the D vector with the E vector of the same plane is the characteristic physical feature of a gyrotropic medium.

One useful version of the dielectric tensor for radiative transfer is where the angle of the magnetic field is arbitrary. This can be calculated by rotating our original solutions

$$\epsilon'_{ik}(x_l) = \gamma_{im}\gamma_{kn}\epsilon'_{mn}(x'_l)$$

$$
\begin{aligned}
\epsilon'_{xx} &= 1 - \frac{v(1-is)}{(1-is)^2 - u} \\
\epsilon'_{yy} &= 1 - \frac{v[(1-is)^2 - u\sin^2\alpha]}{(1-is)[(1-is)^2 - u]} \\
\epsilon'_{zz} &= 1 - \frac{v[(1-is)^2 - u\cos^2\alpha]}{(1-is)[(1-is)^2 - u]} \\
\epsilon'_{xz} &= -\epsilon'_{zx} = \frac{i\sqrt{u(v\sin\alpha)}}{(1-is)^2 - u} \\
\epsilon'_{xy} &= -\epsilon'_{yx} = -\frac{i\sqrt{u(v\cos\alpha)}}{(1-is)^2 - u} \\
\epsilon'_{yz} &= \epsilon'_{zy} = \frac{uv\cos\alpha\sin\alpha}{(1-is)[(1-is)^2 - u]}
\end{aligned}
\tag{4.3.8}
$$

where $u = \omega_H^2/\omega^2$, $v = \omega_p^2/\omega^2 = 4\pi e^2 N/m\omega^2$, $s = \nu_{\text{eff}}/\omega$

If we apply the coordinate transform such as the axis of symmetry becomes the magnetic field vector and the waves are propagating with an angle α, then as mentioned above, we can simplify response of the material to the photons into two modes. To achieve that we need to solve the dispersion equation (see equation 4.3.3), which is a quadratic equation, from which we would end up with two roots for the complex index of refraction.

$$
\begin{aligned}
\vec{k}\times(\vec{k}\times\vec{E}) &= -\frac{\omega^2}{c^2}\vec{D} \\
(k^2\delta_{ij} - k_i k_j - \frac{\omega^2}{c^2}\epsilon_{ij})E^{ij} &= \Lambda_{ij}E^{ij} = 0 \\
\det(\mathrm{k}^2\delta_{\mathrm{ij}} - \mathrm{k_i k_j} - \frac{\omega^2}{\mathrm{c}^2}\epsilon_{\mathrm{ij}}) &= \det(\Lambda_{\mathrm{ij}}) = 0 \\
\text{where}\quad \Lambda_{ij} &= \tilde{n}^2\delta_{ij} - \tilde{n}_i\tilde{n}_j - \epsilon_{ij} \\
\Lambda_{ij} &= \begin{pmatrix}
\epsilon_{xx} - \tilde{n}^2\cos^2\alpha & \epsilon_{xy} & \epsilon_{xz} + \tilde{n}^2\sin\alpha\cos\alpha \\
-\epsilon_{xy} & \epsilon_{yy} - \tilde{n}^2 & \epsilon_{yz} \\
\epsilon_{xz} + \tilde{n}^2\sin\alpha\cos\alpha & \epsilon_{yz} & \epsilon_{zz} - \tilde{n}^2\sin^2\alpha
\end{pmatrix}
\end{aligned}
\tag{4.3.9}
$$

$$
\begin{aligned}
\det(\Lambda_{\mathrm{ij}}) = \Lambda &= \mathrm{A}\tilde{\mathrm{n}}^4 - \mathrm{B}\tilde{\mathrm{n}}^2 + \mathrm{C} \\
A &= \epsilon_{xx}\sin^2\alpha + \epsilon_{zz}\cos^2\alpha + 2\epsilon_{xz}\sin\alpha\cos\alpha \\
B &= A\epsilon_{yy} + \epsilon_{xx}\epsilon_{zz} - \epsilon_{xz}^2 + (\epsilon_{xy}\sin\alpha - \epsilon_{yz}\cos\alpha)^2 \\
C &= \epsilon_{xx}\epsilon_{yy}\epsilon_{zz} + \epsilon_{xx}\epsilon_{yz}^2 + \epsilon_{zz}\epsilon_{xy}^2 - \epsilon_{yy}\epsilon_{xz}^2 + 2\epsilon_{xx}\epsilon_{yz}\epsilon_{xz} \\
\tilde{n}_\pm^2 &= \frac{B \pm \sqrt{B^2 - 4AC}}{2A}.
\end{aligned}
\tag{4.3.10}
$$

Applying the above general solution of the dispersion equation to our dielectric tensor we end up with the two roots for the $\tilde{n}$ describing the two different modes: extraordinary (2,+) and ordinary (1,-).

$$n_{\mp} = n_{1,2} = 1 - \frac{2v(1-is-v)}{2(1-is)(1-is-v) - u\sin^2\alpha \pm \sqrt{u^2\sin^4\alpha + 4u(1-is-v)^2\cos^2\alpha}}. \tag{4.3.11}$$

This equation is applicable to frequencies that are far away from plasma and cyclotron frequencies. Moreover this description and the additional polarization coefficients derived from a similar condition (ignoring the collisions, $s \to 0$) are the basis of the radiative transfer prescription of Ramaty (1969) which was discussed in Sec. 1.3.2.

The index of refraction in equation 4.3.11 is also the basis for the magneto-optical parameter calculations of Pacholczyk (1976), under the assumption of cold plasma ($\omega \gg \omega_p$) and for frequencies far away from cyclotron frequency.

In the following section I will calculate the absorption coefficient for the cyclotron frequency as well as the indicies of refraction which naturally would be applicable for the frequencies in the vicinity of the cyclotron frequency.

4.4 Kinetic Theory of Wave Propagation in Magnetoactive Plasma

To solve the radiative transfer equations in the vicinity of the cyclotron frequency, knowing the cyclotron absorption cross-section is not sufficient. Furthermore, we need to know the response of the magnetized medium to the electromagnetic waves since the medium is birefringent. The calculation of the complex index of refraction is sufficient to provide the necessary information on both absorption and refraction.

In this section I represent the calculation of the parameters of free-free transitions, namely the absorption coefficients and the indicies of refraction that are used for calculating the magneto-optical parameters, with a self-consistent method. The methodology we adopt is based on the classical plasma calculations which are outlined in the fundamental work of Ginzburg (1964).

As mentioned in Sec. 1.3.3 the absorption cross-section and the magneto-optical parameters are calculated with various methods. Moreover, near the cyclotron frequency numerous approximations are used and the effects of velocity distribution of electrons and effective collisions are added qualitatively. There is yet to be a unifying description for the birefringent MWD atmospheres.

The derivations of the cyclotron absorption is already existing in the literature. Especially in the context of accreting white dwarfs Chanmugam (1980); Pavlov et al. (1980); Meggitt & Wickramasinghe (1982) the properties of the magnetized atmospheres were investigated from a plasma physics perspective (see Chanmugam et al., 1989, for an overview). As opposed to the accreting white dwarfs where shock temperatures are rather high hence cyclotron emission is observed and in neutron stars where relativistic and Quantum Electrodynamics (QED) effects such as vacuum birefringence are important, the situation for the MWDs are different and I will investigate the plasma properties for the correct regime and for the desired parameters relevant for the radiative transfer within this formalism.

For that, I will concentrate on the kinetic theoretical calculation of the dielectric tensor which is the most unifying form since many effects can directly be implemented inside. I

have already calculated the dielectric tensor from elementary theory, but to calculate it via velocity distribution first we need to start from the Vlasov equations which is basically a Boltzmann equation without the collision integral.

$$\begin{aligned}\frac{df}{dt} &= \frac{\partial f}{\partial t} + \frac{d\vec{r}}{dt}\frac{\partial f}{\partial r} + \frac{d\vec{p}}{dt}\frac{\partial f}{\partial p} \\ &= \frac{\partial f}{\partial t} + \vec{v}\frac{\partial f}{\partial r} + q\left(E_0 + \frac{1}{c}[v \times B_0]\right)\frac{\partial f}{\partial v}\end{aligned} \tag{4.4.1}$$

in which f is the velocity distribution of particles in which $dN = f(\vec{p}, \vec{r}, t)d^3rd^3p$ where N is the total number of particles. $\frac{d\vec{p}}{dt}$ is the force exerted on the particles, for our case where the particles are inside an external electric field $E_0 = 0$.

To further simplify, we assume the deviation of the distribution of the particles from the thermal equilibrium to be small. Thus f can be separated in two parts; f_0 is the equilibrium (Maxwellian) distribution of particles which is the result of stationary fields E_0 and B_0; the second part f' describes the deviation from Maxwellian distribution due to the effects of high frequency fields E' and B' (i.e. $\omega \gg \omega_p$). Now with $f = f_0 + f'$ we can linearize the Vlasov-Maxwell equations and solve f' in terms of f_0. f_0 does not depend on v or t but only p. The $\frac{df_0}{dt}$ is referred to as the collision integral I_{st} and for the Vlasov solution it is taken to be zero. Hence from linearization:

$$\partial_t f' + v\partial_r f' - e\left(E_0 + \frac{1}{c}[v \times B_0]\right)\partial_p f' = e\left(E' + \frac{1}{c}[v \times B']\right)\partial_p f_0 + I_{\text{st}} \tag{4.4.2}$$

$$I_{st} = \frac{df_0}{dt} = 0$$

$$\frac{df'}{dt} = \partial_t f' + \partial_t r + \partial_r f' + \partial_t p \partial_p f'$$

$$\partial_t r = v(t), \qquad \partial_t p = -eE_0 - \frac{e}{c}[v(t) \times B_0]$$

$$\frac{df'}{dt} = \partial_t f' + v(t)\partial_r f' - e\left(E_0 + \frac{1}{c}[v \times B_0]\right)\partial_p f'. \tag{4.4.3}$$

If we combine both the linearization (equation 4.4.2) and the chain rule for f' (equation 4.4.3) we end up with:

$$\frac{df'}{dt} = \frac{e}{m}\left(E'(r(t), t) + \frac{1}{c}[v(t) \times B'(r(t), t)]\right)\partial_v f_0 \tag{4.4.4}$$

$$f'(\vec{v}(t), \vec{r}(t), t) = \frac{e}{m}\int_{-\infty}^{t}\left(E'(r(t), t) + \frac{1}{c}[v(t) \times B'(r(t), t)]\right)\partial_v f_0 \, dt.$$

This is the main equation to be solved for the distribution function of the electrons. To do that we assume the radiation to be a plane wave and Fourier transform it.

$$E \sim E_i e^{i(k\cdot r - \omega t)}, \qquad B \sim B_k e^{i(k\cdot r - \omega t)}$$

$$f' = \frac{e}{m}\int_{-\infty}^{t}(E_k + \frac{1}{c}v \times B_k)\partial_v f_0 e^{i[k\cdot(r'-r) - \omega(t'-t)]} \, d(t - t').$$

From the Maxwell equation of a plane wave: $i\omega B/c = ik \times E$, $\frac{1}{c}v \times B_k = v \times (k \times E)/\omega$

$$f' = \frac{e}{m}\int_{-\infty}^{t}(\frac{E_k + v\times(k\times E)}{\omega})\partial_v f_0 e^{i[k.(r'-r)-\omega(t'-t)]}$$
$$f' = \frac{e}{m}\int_{-\infty}^{t}(\frac{[(\omega - v.k)\delta_{ij} + v_i k_j])\cdot E_i}{\omega})\partial_v f_0 e^{i[k\cdot(r'-r)-\omega(t'-t)]}\ d(t-t').$$

In order to write this tensor we need solve the kinematics of the electron under the influence of a magnetic field. The motion is simply described by an orbital motion around the axis of magnetic field direction with the cyclotron frequency ω_H. In our description magnetic field is directed in the z direction.

$$v_i = \begin{pmatrix} v_\perp\cos(\omega_H t) \\ v_\perp\sin(\omega_H t) \\ v_\parallel \end{pmatrix},\quad r'_i = r - \begin{pmatrix} v_\perp\sin(\omega_H t)/\omega_H \\ -v_\perp\cos(\omega_H t)/\omega_H \\ v_z t \end{pmatrix},\quad \partial_v f_{0i} = \begin{pmatrix} \partial_{v_\perp} f_0\sin(\omega_H t)/\omega_H \\ -\partial_{v_\perp} f_0\cos(\omega_H t)/\omega_H \\ \partial_{v_z} f_0 t \end{pmatrix}. \tag{4.4.5}$$

We can define the tensorial multiplicative part, simply as $h_i = [(\omega - v\cdot k)\delta_{ij} + v_i k_j]\partial_v f_0^j$ which explicitly becomes:

$$h_i = \begin{pmatrix} \omega - k_z v_z & 0 & v_\perp\cos(\omega_H t)k_z \\ 0 & \omega - v_\perp k_\perp\cos(\omega_H t) - k_z v_z & v_\perp\sin(\omega_H t)k_z \\ v_z k_\perp & 0 & \omega - v_\perp k_\perp\cos(\omega_H t) \end{pmatrix}\begin{pmatrix} \partial_{v_\perp} f_0\sin(\omega_H t)/\omega_H & -\partial_{v_\perp} f_0\cos(\omega_H t)/\omega_H & \partial_{v_z} f_0 t \end{pmatrix}$$
$$= \begin{pmatrix} \{\partial_{v_\perp} f_0(\omega - k_z v_z) + \partial_{v_z} f_0 k_z v_\perp\}\cos(\omega_H t) \\ \{\partial_{v_\perp} f_0(\omega - k_z v_z + \partial_{v_\perp} f_0 k_z v_\perp\}\sin(\omega_H t) \\ \{\partial_{v_\perp} f_0 v_z k_\perp + \partial_{v_z} k_\perp v_\perp\}\cos(\omega_H t) + \omega\partial_{v_z} f_0 \end{pmatrix}.$$

Here we used the a simplified wave vector $k = (k_x, 0, k_z)$ since the anisotropy is dichroic and hence axisymmetric. One vector is enough to describe the axisymmetric propagation of the electromagnetic wave transverse to the magnetic field.

And finally for the asymmetric part of the distribution which defines the current density, we simply have

$$f' = \frac{e}{m}\int_t^\infty \frac{E_k h_i(t')}{\omega} e^{(\vec{k}\cdot\vec{r}_0 - \omega(t-t'))}\ d(t-t').$$

Using the above transformations for r_0 and write $\vec{k}\cdot\vec{r}$ explicitly, the wave part can be expanded,

$$e^{i[k\cdot(r'-r)-\omega(t'-t)]} = e^{i[(k.r - \omega t - \frac{k_\perp v_\perp}{\omega_H}\sin(\omega_H t') + (\omega - k_z v_z)t')]}$$

then we use the identity:

$$e^{i\lambda\sin\phi} = \sum_{n=-\infty}^{\infty} J_n(\lambda)e^{in\phi}$$
$$e^{i[(k\cdot r - \omega t - \frac{k_\perp v_\perp}{\omega_H}\sin(\omega_H t') + (\omega - k_z v_z)t')]} = e^{i(k\cdot r - \omega t)}\sum_n J_n(\frac{k_\perp v_\perp}{\omega_H})e^{-in\omega_H t'}e^{i(\omega - k_z v_z)t'}.$$

hence simplifying our integral, now it can be expressed as:

$$f' = \frac{e}{m\omega}\int_0^\infty dt'\ E_k e^{i(\omega - k_z v_z)t'}\ \sum_n J_n(\frac{k_\perp v_\perp}{\omega_H})h_i(t')e^{i(\omega - n\omega_H - k_z v_z)t'}.$$

Remembering the fact that we are working in Fourier space which means $E_k e^{i(\omega-k_z v_z)t'} \sim E_i$ and take the electric field out of the integral in f', we can see that our solutions further simplify.

Continuing with the solution, we calculate the distribution function.

$$f' = \frac{e}{m\omega}E^i\sum_n J_n(\chi)L_i, \qquad \chi = \frac{k_\perp v_\perp}{\omega_H}$$
$$L_i = \int_0^\infty h_i(t')e^{i(\omega - n\omega_H - k_z v_z)t'}\ dt'.$$

The t' dependence of h_i consists of trigonometric terms like $\sin(\omega_H t')$ and $\cos(\omega_H t')$ which can be expressed as $(e^{i\omega_H t'} - e^{-i\omega_H t'})/2$ and $(e^{i\omega_H t'} + e^{-i\omega_H t'})/2$ for convenience. Assuming h_i consists of amplitudes and oscillatory parts, we can define it as

$$h_i = (|h_x|\cos(\omega_H t'), |h_x|\cos(\omega_H t', |h_z'|\cos(\omega_H t') + w\partial_{v_z} f_0).$$

Then we can express the integrals as:

$$\begin{aligned}
&\int_0^\infty \left\{ \begin{array}{c} \cos(\omega_H t) \\ \sin(\omega_H t) \end{array} \right\} e^{i(\omega - n\omega_H - k_z v_z)t'}\ dt' = \\
=&\frac{1}{2}\int_0^\infty \left\{ \begin{array}{c} e^{i[\omega-(n-1)\omega_H - k_z v_z]t'} + e^{i[\omega-(n+1)\omega_H - k_z v_z]t'} \\ e^{i[\omega-(n-1)\omega_H - k_z v_z]t'} - e^{i[\omega-(n+1)\omega_H - k_z v_z]t'} \end{array} \right\} dt' \\
=&-i\frac{1}{2}\left\{ \begin{array}{c} \mathrm{Pole(n-1) + Pole(n+1)} \\ \mathrm{Pole(n-1) - Pole(n+1)} \end{array} \right\}.
\end{aligned} \tag{4.4.6}$$

The function Pole(n) is the direct result of the integral and defined as:

$$\begin{aligned}
\int_0^\infty e^{i(\omega - a\omega_H - k_z v_z)t'}\ dt' &= -i\frac{e^{i[\omega - a\omega_H - k_z v_z]t'}|_0^\infty}{\omega - a\omega_H - k_z v_z} \\
&= -i\frac{1}{\omega - a\omega_H - k_z v_z} = -i\mathrm{Pole(a)}.
\end{aligned} \tag{4.4.7}$$

Now inserting all in L_i:

$$L^i = \left\{ \begin{array}{c} \sum_n J_n(\chi)(1/2)[\mathrm{Pole(n-1)+Pole(n+1)}][\partial_{\mathrm{v}_\perp}\mathrm{f_0}(\omega - \mathrm{k_z v_z}) + \partial_{\mathrm{v_z}}\mathrm{f_0 k_z v_\perp}] \\ \sum_n J_n(\chi)(1/2)[\mathrm{Pole(n-1)+Pole(n+1)}][\partial_{\mathrm{v}_\perp}\mathrm{f_0}(\omega - \mathrm{k_z v_z} + \partial_{\mathrm{v}_\perp}\mathrm{f_0 k_z v_\perp}] \\ \sum_n J_n(\chi)\{(1/2)[\mathrm{Pole(n-1)+Pole(n+1)}][\partial_{\mathrm{v}_\perp}\mathrm{f_0 v_z k_\perp} + \partial_{\mathrm{v_z}}\mathrm{k_\perp v_\perp}] + \mathrm{Pole(n)}\omega\partial_{\mathrm{v_z}}\mathrm{f_0}\} \end{array} \right\}.$$

To simplify the equations what we need to do is to make a change of dummy indicies to make all the pole terms $\mathrm{Pole(n)}$, furthermore the summation limits are unaffected by this change since they are from $-\infty$ to ∞. This method converts the terms with $\cos(\omega_H t')$ into $\frac{J_{n+1}+J_{n-1}}{2}$ and terms with $\sin(\omega_H t')$ into $\frac{J_{n-1}-J_{n+1}}{2}$ (for simplicity we dropped the arguments χ of the Bessel functions). Thus we can use the Bessel forms,

$$\frac{J_{n+1}(\chi)+J_{n-1}(\chi)}{2}=\frac{nJ_n(\chi)}{\chi}$$
$$\frac{J_{n-1}(\chi)-J_{n+1}(\chi)}{2}=J_n'(\chi) \tag{4.4.8}$$

where J_n' is the derivative of J_n. When we insert the Bessel functions inside the distribution function we end up with:

$$f'=-i\frac{e}{m\omega}\sum_n\frac{M^iE_i}{\omega-n\omega_H-k_zv_z},\ M^i=\begin{pmatrix}\{(\omega-k_zv_z)\partial_{v_\perp}f_0+k_zv_\perp\partial_{v_z}f_0\}\frac{n\omega_H}{k_\perp v_\perp}J_n\\ i\{(\omega-k_zv_z)\partial_{v_\perp}f_0+k_zv_\perp\partial_{v_\perp}f_0\}J'\\ \{v_zk_\perp\partial_{v_\perp}f_0+k_\perp v_\perp\partial_{v_z}f_0+(\omega-\omega_H)\partial_{v_z}f_0\}J_n\end{pmatrix}. \tag{4.4.9}$$

This is the most general description for the kinetic distribution function. Any kind of description can be used for the equilibrium distribution f_0 depending on the property of the matter. For our case we use the Maxwellian for the isotropic distribution function.

$$f_0(v)=n_0\left(\frac{m}{2\pi k_bT}\right)^{3/2}e^{-\frac{mv^2}{2k_bT}}$$
$$f_0(v_\parallel,v_\perp)=n_0\left(\frac{m}{2\pi k_bT_\perp}\right)^{3/2}\left(\frac{T_\perp}{T_\parallel}\right)^{1/2}e^{-\frac{mv_\parallel^2}{2k_bT_\parallel}}e^{-\frac{mv_\perp^2}{2k_bT_\perp}}$$

where k_b is the Boltzmann constant and the temperatures are separated into two due to anisotropies. Assuming that the anisotropies are small we can write the derivatives of the distribution function as:

$$\frac{\partial f_0}{\partial v^2}=\text{const f}_0$$
$$\frac{\partial f_0}{\partial v_\perp^2}=2v_\perp\text{const f}_0=2\text{v}_\perp\frac{\partial\text{f}_0}{\partial\text{v}^2}$$
$$\frac{\partial f_0}{\partial v_\parallel^2}=2v_\parallel\frac{\partial f_0}{\partial v^2}$$

hence reaching a more simplified M^i:

$$M^i=2\frac{\omega}{\omega_H}\begin{pmatrix}\frac{n\omega_H^2}{k_\perp}J_n\\ i\omega_Hv_\perp J'\\ \omega_Hv_\parallel J_n\end{pmatrix}\frac{\partial f_0}{\partial v^2}$$
$$f'=-i\frac{2e}{m\omega}\frac{\partial f_0}{\partial v^2}\sum_n\frac{J_n}{\omega-n\omega_H-k_zv_z}\begin{pmatrix}\frac{n\omega_H^2}{k_\perp}J_n\\ i\omega_Hv_\perp J'\\ \omega_Hv_\parallel J_n\end{pmatrix}E_i. \tag{4.4.10}$$

The important result of our calculations is the effect of the $\mathrm{Pole(n)}$ function; which explains the resonance of with respect to the cyclotron frequencies. The condition for resonance depends on the order of the Bessel functions n and the Doppler shift $k_zv_\parallel$.

Now that we have a description of the distribution function f' (remember that only the anisotropic part of the distribution function causes current to flow), we can calculate first the current density and then the dielectric tensor.

$$
\begin{aligned}
j_i &= -e \int dv\, v_i f', \quad f' = \mathcal{M}^i E_i \\
&= -e \int dv\, v_i \mathcal{M}^k E_k \\
\vec{D} &= \epsilon' \vec{E} = \vec{E} - i4\pi j/c \\
\text{in tensorial notation:} \quad \epsilon_i'^k E_k &= E_i + \frac{4\pi}{i\omega} j_i,\ j_i = \sigma_i^k E_k \\
&= E_i + \frac{4\pi}{i\omega} \sigma_i^k E_k \\
\epsilon_i'^k &= \delta_i^k + \frac{4\pi}{i\omega} \sigma_i^k \\
&= \delta_i^k - \frac{4\pi e}{i\omega} \int dv\, v_i \mathcal{M}^K.
\end{aligned}
$$

In our terms the dielectric tensor becomes:

$$
\epsilon_i'^k = \delta_i^k - \frac{4\pi e^2}{m\omega^2} \sum_n \int d^3v \left[(\omega - k_z v_z) \partial_{v_\perp} f_0 + k_z v_\perp \partial_{v_z} f_0 \right] \frac{\Pi_i^k}{\omega - n\omega_H - k_z v_z} \tag{4.4.11}
$$

where Π_i^k is the dyadic product of M^i with its complex conjugate. Here and

$$
\Pi_i^k = \begin{pmatrix}
\frac{n^2\omega_H^2}{k_\perp^2} J_n^2 & i\frac{n\omega_H}{k_\perp} v_\perp J_n J_n' & \frac{n\omega_H}{k_\perp} v_z J_n^2 \\
-i\frac{n\omega_H}{k_\perp} v_\perp J_n J_n' & v_\perp^2 J'^2 & -iv_\perp v_z J_n J_n' \\
\frac{n\omega_H}{k_\perp} v_z J_n^2 & -iv_\perp v_z J_n J_n' & v_z^2 J_n^2
\end{pmatrix}. \tag{4.4.12}
$$

Here we have shortened omitted the argument χ of the Bessel function J_n. Hence the definition of the general form of dielectric constant (equation 4.4.11) in the coordinate system where the z axis is points along the magnetic field and the x axis is in the plane of $\vec{k}$ and $\vec{B}$ (which is the same kind of coordinate system we used for the solution of the dispersion equation) depends on the integral over the Π_i^k which is evaluated in cylindrical coordinates $d^3v = 2\pi v_\perp\, dv_\perp\, dv_z$. The integration over dv_z is performed in the complex plane encircling the singularities at $v_z = (\omega - n\omega_H)/k_z$.

Since we are using the Maxwellian equilibrium distribution we have exponentials in our integrals. In order to solve their convolution with Bessel functions, we need to take advantage of the Weber integral (Watson, 1966)

$$
\int_0^\infty dt\, e^{p^2 t^2} J_n(at) J_n(bt) = \frac{1}{2p^2} e^{(a^2+b^2)/4p^2} I_n\left(\frac{ab}{2p^2}\right) \tag{4.4.13}
$$

for this integral to be correct $|\arg p| < \pi/4$ and here I_n denotes the modified Bessel function while I_n' its derivative.

$$I_n(\chi) = i^{-l} J_l(ix) = \sum_{m=0} \frac{1}{m!\Gamma(m+c+1)} \left(\frac{\chi}{2}\right)^{2m+l}$$
$$\text{if } 0 < \mathrm{x} \ll \sqrt{\mathrm{n}+1}$$
$$I_n(\chi) \approx \frac{1}{\Gamma(n+1)} \left(\frac{\chi}{2}\right)^{2m+l}$$

where the gamma function is defined as $\Gamma(n) = (n-1)!$

The addition of the Maxwellian to the complex pole integrals yield the plasma dispersion functions.

$$\int_C dv_z \, \frac{k_z}{k_z v_z - (\omega - n\omega_H)} = i\pi W(Z_n) \tag{4.4.14}$$

where the parameters are defined as

$$Z_n = \frac{\omega - n\omega_H}{\sqrt{2} k_z v_T} \qquad\qquad v_T^2 = \frac{k_b T}{m_e}. \tag{4.4.15}$$

The W_n function is a shorthand for $W(Z_n)$ and defined as Kramp, Fadeeva or complex error function in the area of plasma physics and it is commonly referred to as the plasma dispersion function and its properties are such that

$$W(Z_n) = \frac{i}{\pi} \int_C \frac{e^{-y^2}}{Z_n - y} dy = e^{-Z^2} \left(1 + \frac{2i}{\sqrt{\pi}} \int_0^{Z_n} e^{x^2} dx\right) \tag{4.4.16}$$
$$= e^{-Z^2}[1 + \frac{2i}{}erf(Z)] = e^{-Z^2}\mathrm{erfc}(-\mathrm{iZ})$$
$$\text{if } |Z_n| \ll 1$$
$$W(Z_n) \approx 1 + \frac{2i}{\sqrt{\pi}} + \ldots$$
$$\text{if } |Z_n| \gg 1$$
$$W(Z_n) \approx e^{-Z_n^2} + \frac{i}{\sqrt{\pi}} \left(\frac{1}{Z_n} + \frac{1}{2Z_n^3} + \frac{1}{4Z_n^5} + \ldots\right).$$

When the integrals are taken accordingly, the dielectric tensor turns out to be:

$$
\begin{aligned}
\epsilon'_{xx} &= 1+\sum_{n=-\infty}^{\infty}\frac{i\omega_p^2}{\omega k_z v_T}\sqrt{\frac{\pi}{2}}W_n e^{-\chi}\frac{l^2}{\chi}I_n(\chi)\\
\epsilon'_{yy} &= \epsilon'_{xx}+\sum_{n=-\infty}^{\infty}\frac{i\omega_p^2}{\omega k_z v_T}\sqrt{\frac{\pi}{2}}W_n e^{-\chi}2\chi[I_n(\chi)-I'_n(\chi)]\\
\epsilon'_{zz} &= 1+\sum_{n=-\infty}^{\infty}\frac{\sqrt{2}\omega_p^2}{\omega k_z v_T}e^{-\chi}I_n Z_n(1+i\sqrt{\pi}W_n Z_n)\\
\epsilon'_{xz}=\epsilon'_{zx} &= \sum_{n=-\infty}^{\infty}\frac{\omega_p^2}{\omega\omega_H}\frac{k_\perp}{k_z}(1+i\sqrt{\pi}W_n Z_n)\frac{l}{\chi}e^{-\chi}I_n(\chi)\\
\epsilon'_{xy}=-\epsilon'_{yx} &= -\sum_{n=-\infty}^{\infty}\frac{\omega_p^2}{\omega k_z v_T}\sqrt{\frac{\pi}{2}}W_n e^{-\chi}l[I_n(\chi)-I'_n(\chi)]\\
\epsilon'_{yz}=-\epsilon'_{zy} &= -\sum_{n=-\infty}^{\infty}\frac{i\omega_p^2}{\omega\omega_H}\frac{k_\perp}{k_z}(1+i\sqrt{\pi}W_n Z_n)e^{-\chi}[I_n(\chi)-I'_n(\chi)].
\end{aligned}
$$

The tensor can be put in a more convenient form with $u=\omega_p^2/\omega^2$, $\beta=v/c$,

$$
\begin{aligned}
\epsilon'_{xx} &= 1+\frac{i\sqrt{\pi}u}{\sqrt{2}\beta|\cos\alpha|}e^{-\chi}\sum_n\frac{l^2}{\chi}I_n(\chi)W_n\\
\epsilon'_{yy} &= \epsilon'_{xx}-\frac{i\sqrt{\pi}u}{\beta|\cos\alpha|}\sqrt{2}e^{-\chi}\sum_n\chi[I'_n(\chi)-I_n(\chi)]W_n\\
\epsilon'_{zz} &= 1+\frac{u}{\beta|\cos\alpha|}\sqrt{2}e^{-\chi}\sum_n I_n Z_n(1+i\sqrt{\pi}Z_n W_n)\\
\epsilon'_{xz}=\epsilon'_{zx} &= u\frac{\omega}{\omega_H}\tan\alpha e^{-\chi}\sum_n\frac{l}{\chi}I_n(\chi)(1+i\sqrt{\pi}Z_n W_n)\\
\epsilon'_{xy}=-\epsilon'_{yx} &= \frac{\sqrt{\pi}u}{\sqrt{2}\beta|\cos\alpha|}e^{-\chi}\sum_n l[I'_n(\chi)-I_n(\chi)]W_n\\
\epsilon'_{yz}=-\epsilon'_{zy} &= iu\frac{\omega}{\omega_H}\tan\alpha\ e^{-\chi}\sum_n[I'_n(\chi)-I_n(\chi)](1+i\sqrt{\pi}W_n Z_n).
\end{aligned}
$$

The function Z_n describes the resonance structure of the cyclotron absorption. For our case, i.e. in magnetic white dwarfs the higher harmonics are negligible, hence we only concentrate on $n=1$. Additionally the thermal velocity of the electrons is described as $v_T=\sqrt{k_b T/m_e}\approx 3.89\times10^7\,T_4^{1/2}$ cm/s. For the temperature range of the known magnetic white dwarfs $\beta_T=v_T/c=1.30\times10^{-3}T_4^{1/2}$ is always much smaller than 1.

χ is the dominant parameter for these calculations. For the radiation around the cyclotron frequency ($\omega\approx\omega_H$); $\chi=k^2\sin^2\alpha v_T^2/\omega_H^2=\beta_T\sin^2\alpha$ is always smaller much than one. We will assume $\chi\ll1$ and expand the exponential terms and the Bessel equations (equation 4.4.8) in the dielectric tensor ($k_\perp=k\sin\alpha$, $k_z=k_\parallel=k\cos\alpha$).

$$\begin{aligned}
\epsilon'_{xx} = \epsilon'_{yy} &= 1 + i\sqrt{\frac{\pi}{8}}\frac{\omega_p^2 W(Z_1)}{k_z \omega v_T} \\
\epsilon'_{zz} &= 1 \\
\epsilon'_{xy} = -\epsilon'_{yx} &= -\sqrt{\frac{\pi}{8}}\frac{\omega_p^2 W(Z_1)}{k_z \omega v_T} \\
\epsilon'_{yz} = \epsilon'_{zy} = \epsilon'_{xz} = \epsilon'_{zx} &= 0.
\end{aligned} \tag{4.4.17}$$

This is the expression that appears in Zhelezniakov & Zlotnik (1980) and was also used by Pavlov et al. (1980). From the dielectric constant, the complex index of refraction can be calculated with the help of dispersion equation 4.3.10. For a diaxial birefringent cold magnetized plasma, the dielectric tensor in the general from is:

$$\epsilon_{ij} = \begin{pmatrix} \epsilon_{xx} & \epsilon_{xy} & 0 \\ -\epsilon_{xy} & \epsilon_{xx} & 0 \\ 0 & 0 & \epsilon_{zz} \end{pmatrix}$$

and according dispersion tensor can be constructed with the use of equation 4.3.9:

$$\Lambda_{ij} = \begin{pmatrix} \epsilon_{xx} - n^2\cos^2\alpha & \epsilon_{xy} & 0 \\ -\epsilon_{xy} & \epsilon_{xx} & 0 \\ 0 & 0 & \epsilon_{zz} - n^2\sin^2\alpha \end{pmatrix}.$$

In order to study the solution for the different mode of polarizations, one can assume the simple cases, transverse ($\alpha \approx \pi/2$) and longitudinal ($\alpha \approx 0$) propagation.

$$\begin{aligned}
\alpha &= 0 \\
n_\pm &= \epsilon_{xx} \pm i\epsilon_{xy} \\
\alpha &= \frac{\pi}{2}
\end{aligned} \tag{4.4.18}$$

$$n_\perp = \epsilon_{xx} + \frac{\epsilon_{xy}^2}{\epsilon_{xx}}, \qquad n_\parallel = \epsilon_{zz}. \tag{4.4.19}$$

Now we can solve for the case for arbitrary angle of propagation of the electromagnetic waves with respect to the magnetic axis. For simplicity we define $b = \sqrt{\frac{\pi}{8}}\frac{\omega_p^2 W(Z_1)}{k_z \omega v_T}$

$$\begin{vmatrix} k_z^2 - \frac{\omega^2}{c^2}(1+ib) & -\frac{\omega^2}{c^2}b & -k_x k_z \\ \frac{\omega^2}{c^2}b & k_z - \frac{\omega^2}{c^2}(1+ib) & 0 \\ -k_x k_z & 0 & k_x^2 - \frac{\omega^2}{c^2} \end{vmatrix} = 0.$$

We can solve the determinant simply by taking into account the dispersion relation derived in equation 4.3.10 and the simple proportionality $k = \tilde{n}\frac{\omega}{c}$

$$\tilde{n}_+ = 1 + ib(1+\cos^2\alpha), \qquad \tilde{n}_- = 1. \tag{4.4.20}$$

This solution shows that there is no correction to the ordinary wave (-) propagation from the kinetic theory, whereas for the extraordinary waves (+) the absorption κ and the refraction n coefficients depend on the real and imaginary parts of b, or namely the plasma dispersion function $W(Z)$ inside b. This is corroborated by the elementary theory since the cyclotron absorption is caused only by one mode of the radiation.

To compare this result with the cross-sections in the literature we need to know the relationship between the absorption coefficient κ and the cross-section μ (which corresponds to κ in the radiative transfer section) which is defined as the damping of the energy flux of the electromagnetic field by a factor of e, i.e. $\mu = \frac{2\omega\kappa}{c} = 2\mathrm{Im}(\tilde{n})$. If we explicitly describe the situation:

$$\vec{E} = E_0 e^{\pm\omega\kappa z/c} e^{i(\omega t \pm \omega n z/c)}$$

and look at the energy, namely the Poynting vector $\vec{S}$ of the electromagnetic wave

$$\vec{S} = c\vec{E} \times \vec{H}/4\pi\alpha e^{-2\omega\kappa z/c} \propto e^{-\mu z}$$

we can see the relation between the κ induced damping and the commonly used cross-section μ.

Now it is simple to calculate the cyclotron absorption coefficient for extraordinary mode in the vicinity of the cyclotron frequency. We are only concerned with the first harmonic of the cyclotron absorption, which corresponds to $n = 1$ according in our notation, and not the other cyclotron harmonics. Hence:

$$\begin{aligned} Z_1 &= \frac{\omega - \omega_H}{\sqrt{2}k_z v_T} = \frac{\omega - \omega_H}{\sqrt{2}\omega\beta_T|\cos\alpha|} \\ \mu_+ &= \sqrt{\frac{\pi}{8}}\frac{\omega_p^2}{k\omega v_T}\frac{1+\cos^2\alpha}{|\cos\alpha|}\Re[W(Z_1)]. \end{aligned}$$

The part of the cross-section equation that determines the resonance behaviour is the real part of the plasma dispersion function ($\Re[W(Z_1)]$). Since we know from equation 4.4.16 that the plasma dispersion function is a combination of the Gaussian in the real and the error function times the Gaussian in the imaginary, the real part simply yields a Gaussian with Z_1 as its argument.

$$\begin{aligned} W(Z_1) &= e^{-Z_1^2}\left(1 + \frac{2i}{\sqrt{\pi}}\mathrm{erf(Z_1)}\right) = e^{-Z_1^2}\mathrm{erfc(-iZ_1)} \\ \Re[W(Z_1)] &= e^{-Z_1^2}. \end{aligned}$$

When we insert the values of the parameters, for the extraordinary mode we end up with the result:

$$\begin{aligned} \mu_+ &= \sqrt{\frac{\pi}{8}}\frac{4\pi e^2 N}{m_e}\frac{m_e c^2}{2kT}\frac{1+\cos^2\alpha}{|\cos\alpha|}e^{-Z_1^2} \\ &= 4\pi^{3/2}\frac{e^2 N}{m_e c}\frac{1+\cos^2\alpha}{2}\left(\frac{m_e c^2}{2kT\cos^2\alpha}\right)^{1/2} e^{-\frac{mc^2}{2kT\cos^2\alpha}\frac{(\omega_H-\omega)^2}{\omega^2}}. \end{aligned} \tag{4.4.21}$$

When divided by the electron density N (to transform from absorption coefficient to cross-section) this result is almost identical to the Lamb & Sutherland (1971) (see equation 1.3.37) result (see Sec. 1.3.3), except the Planck distribution but since $\hbar\omega > kT$, the contribution of the Planck term is smaller than an order of magnitude. Additionally we have an angular term $(1+\cos^2\alpha)/2$ which varies between values $1/2$ ($\alpha \approx \pi/2$) and 1 ($\alpha \approx 0$) compared to the Lamb & Sutherland (1971). It comes from the consistent solution of the index of refraction for all directions, whereas Lamb & Sutherland (1971) calculated the parallel angles ($\alpha \approx 0$) and than used the angular part only for the broadening.

It is also easy to show that the Bekefi (1966) cyclotron cross-section of equation 1.3.38 can be reached directly by the dispersion method, solving the dielectric tensor of magnetoactive plasma from the elementary theory under the effect of collisions for the direction of the photon coincident with the direction of the magnetic field (i.e. $\alpha = 0$), and finally allow for absorption as $\tilde{n}^2 = (n - i\kappa)^2$:

$$\begin{aligned}
\epsilon'_{\pm} = (n_{\pm} - i\kappa_{\pm})^2 &= 1 - \frac{v}{1 \mp \sqrt{u}} \\
\Re(\epsilon'_{\pm}) = n_{\pm}^2 - \kappa_{\pm}^2 &= 1 - \frac{v(1 \mp \sqrt{u})}{(1 \mp \sqrt{u})^2 + s^2} \\
\Im(\epsilon'_{\pm}) = 2n_{\pm}\kappa_{\pm} &= \frac{sv}{(1 \mp \sqrt{u})^2 + s^2}.
\end{aligned}$$

If we are investigating photons with frequencies much higher than the characteristic plasma frequency, ω_p we can invoke the cold plasma approximation. This assumption holds for MWD atmospheres for photons with energies larger than that of microwaves since $N \approx 10^{17}\, cm^{-3}$, $\omega_p \approx 10^{11}\ s^{-1}$, $\lambda_p \approx 20\,\mathrm{cm}$. In this regime the index of refraction is approximately one ($n_{\pm} \sim 1$) as seen in equation 4.4.20. This is also true when we take into account the fact that the square of the absorption term is also small. Although κ is small, it is now calculable simply from the imaginary part of the dielectric tensor. In the collisionless case the extraordinary waves cause the resonance absorption. If we only consider ϵ_+ then we end up with

$$\begin{aligned}
2n_{\pm}\kappa_1 &= \frac{sv}{(1-\sqrt{u})^2 + s^2}, \qquad\qquad n_1 \sim 1 \\
\mu_1 &= \frac{2\omega\kappa}{c} = \frac{\omega}{c}\frac{sv}{(1-\sqrt{u})^2 + s^2} \\
&= \frac{\omega}{c}\frac{\omega_p^2}{\omega^2}\frac{\nu_{\mathrm{eff}}}{\omega}\frac{\omega^2}{(\omega_H - \omega)^2 + \nu_{\mathrm{eff}}^2} \\
&= \frac{\omega_p^2}{c}\frac{\nu_{\mathrm{eff}}}{(\omega_H - \omega)^2 + \nu_{\mathrm{eff}}^2} = 4\pi\frac{e^2 N}{mc}\frac{\nu_{\mathrm{eff}}}{(\omega_H - \omega)^2 + \nu_{\mathrm{eff}}^2}.
\end{aligned}$$

Again we were able to derive the former results (see equation 1.3.38 in Sec. 1.3.3) except for the exponential factor which represents the distribution of the Planck term $\frac{1}{1-e^{-x}}$, where $x = \hbar\omega/kT$ which is small since we are in the classical regime (see Sec. 4.2). If we expand it as $\sum_{n=0}^{\infty} e^{-nx} \approx 1 + e^{-x}$ we can see that this factor is neglectable.

The original Bekefi (1966) cross-section was calculated by the cyclotron emission and its equivalence to absorption through Kirchoff's law (equation 1.3.4), whereas now I used the index of refraction from the "elementary theory" to reach an identical result. The

shortcoming of this solution is that it does not include the angular dependency of the of the electromagnetic wave and more importantly the velocity distributions of the electrons. Since now it is shown that the effective collision prescription of the plasma theory is equivalent to the collision treatment in the literature, calculations of increasing detail can be undertaken within the plasma formalism.

Up to this point I have shown the alternative solutions to the cyclotron absorption cross-sections in the literature. Both solutions were reached through the same formalism but with different dielectric constants that are solutions of the dispersion equation. The quantum result is reached via the kinetic solution of the electron distribution function and inserting that for the total current, and the absorption coefficients from collisional broadening are reached simply including absorption terms in the wave equations and collisional terms in the electron equation of motion. So if we have a dielectric constant that describes both of these effects, not only we will have the cyclotron absorption that includes both effects but also we would be able to calculate consistent magneto-optical parameters from the fact that $\rho_R \propto n_2 - n_1$ and $\rho_W \propto n_{\parallel} - n_{\perp}$.

4.4.1 Kinetic theory under the effect of collisions

The problem of including the effects of the effective collisions ($\nu_{\rm eff}$) to the properties of the magnetized plasma without the inclusion of heuristic considerations (see Sec. 1.3.3) but from initial principles includes the consideration of the collision integral in the Boltzmann transport equation.

Classically the $\nu_{\rm eff}$ is the damping term added to the equation of motion of the elementary theory. We know that the inclusion of $\nu_{\rm eff}$ into the elementary theory of plasma is applicable to MWD atmospheres. However, we need to discuss whether this is also applicable to the collision integral of the Boltzmann equation since we would like to include both the effects of the velocity distribution and the effective collisions in the calculation of the dielectric tensor from the kinetic theory.

The collision integral in the Boltzmann equation is a nonlinear term in the equations and exact solution of it is rather complicated. The collision term in the Boltzmann equation (4.4.2) is

$$I_{st} = \left.\frac{df}{dt}\right|_{\rm coll}. \tag{4.4.22}$$

However with certain assumptions this integral can be simplified. The most simple case, the equilibrium case where $n'n'_1 - nn_1 = 0$ the energy and the momentum is conserved and the integral yields a distribution of $f_0 = ce^{-A(v-u_0)^2}$ which is the Maxwellian distribution.

According to Boltzmann's H-theorem (see e.g. Huang, 1987) after a sufficiently long duration the distribution function will approach the equilibrium distribution. With this at hand we can linearize our distribution function which we did in the former chapter. Qualitatively the effective collision frequency of electrons is inherently related to the relaxation time of the plasma. Which is the time scale after which due to the close interactions the velocity distribution of the particles is changed. In the non-magnetized medium, as one electron passes near another electron or ion, its trajectory is changed in a way that effectively the electron "forgets" its initial orbit.

The aforementioned relaxation to the equilibrium state can be qualitatively shown by solving the Vlasov equations. It is easy to see it from the linearized distribution function assumption since the deviation from the equilibrium condition is small,

$$f = f_0 + \frac{\vec{v}\dot{f}_1(v)}{v}$$
$$\partial_t f_1 + \frac{e\vec{E}}{m}\partial_v f_0 + \nu(v) f_1 = 0.$$

where f_0 is a Maxwellian distribution. The collisions damp the anisotropic part, which can be expressed as $f_1(v,t) = f_1(v,0)e^{\nu(v)t}$ in the case where $\vec{E} = 0$.

Going back to the non-magnetic case, the collisional frequencies calculations are connected with the Coulomb integrals in which the maximum impact parameter that causes the relaxation and the minimum impact parameter that corresponds to the greatest effect in the change of the trajectory are considered. They are Debye length ($r_D = \sqrt{k_b T/4\pi N e^2}$) that is responsible of shielding the effect of the charge inside the sphere of an ion electron mixture, and the minimum parameter is inherently related to the Coulomb force, where electrons kinetic energy is comparable to it, hence the maximum deflection is attained (see e.g. Spitzer, 1956).

$$r_D = \left(\frac{k_b T}{4\pi N e^2}\right)^{1/2} = 2.19 \times 10^{-6}\, T_4^{1/2}\, N_{17}^{-1/2}$$
$$r_s = \frac{e^2}{kT} = 1.67 \times 10^{-7}\, T_4^{-1}.$$

The $\nu_{\rm eff}$ used in the literature for MWD photospheres (Jordan et al., 1991) comes from Spitzer (1956) as:

$$\nu_{\rm eff} = 8 \times 0.714\pi \frac{e^4 N}{m^{1/2}(3k_b T^{3/2})} \ln\Lambda$$
$$= 3.77 \times 10^{11} N_{17} T_4^{-3/2} \ln\Lambda.$$

If the kinetic description of Ginzburg (1964) is used almost the same result is attainable:

$$\nu_{\rm eff} = \frac{4\sqrt{(2\pi)}}{3}\pi \frac{e^4 N}{m^{1/2}(k_b T^{3/2})} \ln\Lambda$$
$$= 3.63 \times 10^{11} N_{17} T_4^{-3/2} \ln\Lambda.$$

The Coulomb integral term ($\ln\Lambda$) depends on the maximum and minimum impact parameter ($\Lambda = b_{\max}/b_{\min}$) which in turn depends on the physical properties of the system. As explained above in the classical picture maximum and minimum impact parameters correspond to respectively Debye length r_D and r_s (distance for strong Coulomb collisions). This holds up to the point where the de'Broglie wavelength of the thermal electron ($\lambda_{\rm B} = \hbar/mv_T = 2.97 \times 10^{-8}\, T_4^{1/2}$) becomes smaller than the r_s, i.e. at $T > 3.16 \times 10^5 K$.

$$\Lambda = \begin{cases} \frac{r_D}{\lambda_B} & T > 3.16 \times 10^5 K \\ \frac{r_D}{r_s} & T < 3.16 \times 10^5 K \end{cases} .$$

For the MWD photospheres where the optical depth is of the order of one, we are always dealing with r_D/r_s. As the magnetic field strength increases, the Larmor radius (gyration radius, $r_B = v_T/\omega_B$) decreases, becoming smaller than the Debye radius. This causes the electrons to lose their orbital information at smaller scales than the Debye shielding effect. Hence without losing generality the maximum impact parameter (as the largest scales that scatter the electron) becomes the Larmor radius. Then the Coulomb integral is $\ln\Lambda = \ln(r_B/r_s)$, or more precisely through numerical calculations $\ln(0.47 r_B/r_s)$ (Zheleznyakov et al., 1999). As the temperature exceeds $T > 3.16 \times 10^5\, K$ quantum calculations are needed.

The limiting magnetic field strength depends on the limit where $r_B > r_D$, which is $B_6 N_{17}^{-1/2} > 1$. If we fix the particle density as $10^{17}\, cm^{-3}$, this corresponds to field strengths greater than $\sim 1\, MG$ which is the magnetic field range for the high field MWDs. As the field strengths increase further at a certain point ($B > 13.4 T_4^{3/2}\, MG$) the Larmor radius becomes smaller than the r_s. This means the gyration of the electrons not only effect the distant encounters, but also the curvature of the trajectory of the electron during close collisions. Since in this case the effect of the magnetic field is not only for the distant interactions but for all distances, the assumptions in the calculation of the Coulomb integral are violated. An analysis of this case was made by Zheleznyakov et al. (1999), through calculation of the limiting cases of the ν_{eff} in r_B dominant vs r_s dominant cases. Once the qualitative study yielded the Coulomb integral-like dependencies, the functions are scaled with constants to make the transition from one case to the other continuous and smooth.

$$\nu_{\text{eff}} \approx \nu_{\text{ei}} = \begin{cases} \frac{2\sqrt{2\pi}}{5e} N v_T \left(\frac{mc^2}{B^2}\right)^{2/3} & B_6 > 6.3 T_4^{3/2}\, K \\ \frac{8\sqrt{2\pi}}{15} \frac{me^4 N}{v_T^3} \ln\frac{r_B}{r_s} & B_6 < 6.3 T_4^{3/2}\, K \end{cases} .$$

According to Ginzburg (1964) the calculation of the transport collision frequencies (which are frequency dependent) as the effective collision frequency is acceptable for certain limits where $\omega^2 \ll \nu_{\text{eff}}^2$ or $\omega^2 \gg \nu_{\text{eff}}^2$. As we can see from the physical arguments above, for the optical frequencies this is always true in the MWD photospheres.

Now we can go ahead and attempt to calculate a unified description of the magnetoactive media which includes both the effects of the electron velocity distribution and effective collisions. The most direct way of attaining this is to solve the Boltzmann equation directly rather than the Vlasov equation as done in Sec. 4.4. However finding a concise result for the formal solution is inhibited by the frequency dependent nature of the collision integral in the kinetic theory, making the calculations nonlinear.

Since we know that, it is physically feasible to represent collisions as frequency independent effective collisions ν_{eff}, we can use one of the various simple representations of collision integral. One popular method for solving the Boltzmann equation is to assume a weak collision limit and approximate the collision integral as $I_{st} = -\gamma(f - f_0)$ where the collision integral is equal to a loss term γ times the deviation of the distribution function from the thermal equilibrium. This method initially implemented by Bhatnagar et al. (1954) and is called conveniently the Bhatnager-Gross-Krook (BGK) model.

In the linearized Boltzmann equation, the deviation in the distribution function corresponds to the linearized small departure f', and now we add the γ term which has the dimension of time^{-1} hence can be represented as the effective collision frequency ν_{eff}.

$$\frac{\partial f}{\partial t} + \vec{v}\frac{\partial f}{\partial r} - e\left(E + \frac{1}{c}[v \times B]\right)\frac{\partial f}{\partial v} = -\nu'_{\text{eff}} \tag{4.4.23}$$
$$\partial_t f' + v\partial_r f' - e\left(E_0 + \frac{1}{c}[v \times B_0]\right)\partial_p f' + \nu_{\text{eff}} f' = e\left(E' + \frac{1}{c}[v \times B']\right)\partial_p f_0.$$

Let's go back and do the same steps undertaken to reach equation 4.4.4, adding the chain rule of f' (equation 4.4.3) with the linearized Boltzmann equation (4.4.23) above.

$$\frac{\partial f'}{\partial t} + \nu_{\text{eff}} f' = e\left(E' + \frac{1}{c}[v \times B']\right)\partial_p f_0. \tag{4.4.24}$$

The equation for the anisotropic part of the distribution function is almost identical to the equation 4.4.4 (linearized Vlasov case), except the ν_{eff} term which appears in the function as a damping term. However the equation still is a linear differential equation and the solution is very simple.

$$\frac{df'}{dt} + \nu_{\text{eff}} f' = g(\vec{v}, t)$$
$$f' = e^{\nu_{\text{eff}} t}\int e^{-\nu_{\text{eff}} t'} g(\vec{v}, t) dt'.$$

In the convenient form it is described as

$$f'(\vec{v}(t), \vec{r}(t), t) = \frac{e}{m}\int_{\infty}^{0} e^{-\nu_{\text{eff}} t}\left(E'(r(t), t) + \frac{1}{c}[v(t) \times B'(r(t), t)]\right)\partial_v f_0\, dt \tag{4.4.25}$$

Note that the constants of the integration are included in the boundary conditions. When we follow the prescription of the former chapter, adopt the Fourier transform and the arrangement of the parameters (position,velocity) according to the cyclotron equations of motion inside the integral (see equations 4.4.5), the final version of the distribution function would look like

$$f' = \frac{e}{m\omega}\int_0^{\infty} dt'\; E_k e^{i(\omega - k_z v_z)t'} \sum_n J_n(\frac{k_\perp v_\perp}{\omega_H}) h_i(t') e^{i(\omega - n\omega_H - k_z v_z - i\nu_{\text{eff}})t'}. \tag{4.4.26}$$

Since our damping term is not affected by the change of the coordinate system, the f' integral in the Krook prescription is basically an addition to the to the argument of the exponential as $\omega - n\omega_H - k_z v_z - i\nu_{\text{eff}}$, which defines the poles of the complex integrals further in the calculation.

Taking the integrals with respect to time yields the same form of equations as in equation 4.4.6. Only the definition of the function Pole(n) has changed (see equation 4.4.7). This description of the pole which has an additional constant term $-i\nu_{\text{eff}}$ is carried as it is,

$$f' = -i\frac{2e}{m\omega}\frac{\partial f_0}{\partial v^2}\sum_n \frac{J_n}{\omega - n\omega_H - k_z v_z - i\nu_{\text{eff}}} M^i E_i \tag{4.4.27}$$

first through the velocity integrals where M^i is defined as in the collisionless case in equation 4.4.10 for calculating the current density and then all the way to the dielectric tensor (equation 4.4.11)

$$\epsilon_i'^k = \delta_i^k - \frac{4\pi e^2}{m\omega^2}\sum_n \int d^3v\,[(\omega - k_z v_z)\partial_{v_\perp} f_0 + k_z v_\perp \partial_{v_z} f_0]\frac{\Pi_i^k}{\omega - n\omega_H - k_z v_z - i\nu_{\text{eff}}} \tag{4.4.28}$$

where again Π_i^k is the same as described in equation 4.4.12.

Compared to the Vlasov solution, in this case the integral of Π_i^k with respect to dv_z needs to be taken over a complex pole to calculate the dielectric tensor. It is performed again, according to the integral 4.4.14. However, this time due to the complex nature of the pole, the argument of the plasma dispersion function, Z_n has changed with respect to the equation 4.4.15.

$$Z_n^* = \frac{\omega - n\omega_H + i\nu_{\text{eff}}}{\sqrt{2}\omega\beta_T|\cos\alpha|} = Z_n + i\nu'_{\text{eff}}. \tag{4.4.29}$$

In this situation the solution for the complex index of refraction is identical to the equation 4.4.20, with a minor difference to the plasma dispersion function. In the case where effective collisions are present, the argument of the plasma dispersion function Z_n becomes complex according to the equation 4.4.29. It was already shown that the real part of the plasma dispersion function with a real argument yields a Gaussian. However, for the case where the resonance condition Z_1^* is complex due to the effective collisions, the situation is not so simple. In this case, the real part of the plasma dispersion function yields a combination of a Gaussion due to the resonance term Z, plus a Lorentzian that is induced by the effective collision ν_{eff}. For convinience we will drop the index n.

This explanation is equivalent to the former heuristic arguments of Martin & Wickramasinghe (1979) and later of Pavlov et al. (1980) in the context of neutron stars and accreting magnetic white dwarfs, which quantitatively yield the Voigt profile (equation 1.3.39).

$$\begin{aligned}
W(Z^*) &= \frac{i}{\pi}\int_{-\infty}^{\infty} dy\,\frac{e^{-y^2}}{Z^* - y}, \qquad Z^* = Z + i\nu'_{\text{eff}} \\
&= \frac{i}{\pi}\int_{-\infty}^{\infty} dy\,\frac{e^{-y^2}}{(Z + i\nu'_{\text{eff}}) - y} = \frac{i}{\pi}\int_{-\infty}^{\infty} dy\,\frac{e^{-y^2}}{(Z-y)^2 + \nu'^2_{\text{eff}}}(Z - i\nu'_{\text{eff}}) \\
\Re[W(Z^*)] &= \frac{\nu_{\text{eff}}}{\pi}\int_{-\infty}^{\infty} dy\,\frac{e^{-y^2}}{(Z-y)^2 + \nu'^2_{\text{eff}}} \\
\Im[W(Z^*)] &= \frac{Z}{\pi}\int_{-\infty}^{\infty} dy\,\frac{e^{-y^2}}{(Z-y)^2 + \nu'^2_{\text{eff}}}.
\end{aligned}$$

To reach the Voigt profile we need to make a change of variables ($y' = y - Z$) so that

$$\Re[W(Z^*)] = \frac{\nu_{\text{eff}}}{\pi}\int_{-\infty}^{\infty} dy'\,\frac{e^{-(y'+Z)^2}}{y'^2 + \nu'^2_{\text{eff}}} = H(\nu'_{\text{eff}}, Z). \tag{4.4.30}$$

With this result the rederivation of the various cyclotron absorption prescriptions that are used in the current magnetic white dwarf literature is complete. I was able to show that the heuristic arguments in the literature which are used to combine the effects of velocity distribution of electrons and their collisions are consistent can be quantitatively represented with the plasma formalism.

With this physically and parametrically flexible formalism, we will be able to calculate the according indicies of refraction for the relevant modes of polarizations. In the next section, I calculate the indicies of refractions and discuss their implications for the radiation transfer in the MWD atmospheres.

4.5 Applications of the Kinetic Theory in Radiative Transfer

In the former sections I have reproduced each of the cyclotron absorption coefficients in the literature step by step. The final and the most sophisticated method used was the solution of the linearized Boltzmann equations with the BGK model for the collisions in the magnetized medium, which produced cross-sections that are coincident with the current literature for the relevant limiting cases. As mentioned before, the major advantage of this method is the self-consistent calculation of the properties of the medium. In this section we will take advantage of this fact and calculate the magneto-optical parameters from the indicies of refraction consistently with the absorption cross-sections.

Taking from Sec. 1.3.3, according to equation 1.3.42 the magneto-optical parameters are described most generally as:

$$\begin{aligned}\rho_R =& \frac{\omega_H}{c}(n_+ - n_-)\cos\alpha \\ \rho_W =& \frac{\omega_H}{c}(n_\parallel - n_\perp)\sin^2\alpha.\end{aligned}$$

As we have seen in Sec. 4.4.1 the ad hoc broadening of the cross-section is physically consistent with the kinetic theory. For a self-consistent simple description of the magneto-optical parameters all that needs to be done is to insert the values of the indices of refraction for n_+, n_-, $n_\parallel$, $n_\perp$.

The indicies of refractions for different polarization modes can be easily calculated from the dielectric tensor of a cold plasma. According to equation 4.4.17, the complex indicies of refractions are given by:

$$\begin{aligned}\epsilon_{xx} = \epsilon_{yy} = 1 + ib, \qquad \epsilon_{xy} = b \\ \tilde{n}_\pm = \epsilon_{xx} \pm i\epsilon_{xy} = 1 + ib \pm ib \\ \tilde{n}_-^2 = 1, \qquad \tilde{n}_+^2 = 1 + 2ib \\ \tilde{n}_\perp^2 = \epsilon_{xx} + \frac{\epsilon_{xy}^2}{\epsilon_{xx}} = 1 + ib + \frac{b^2}{1+ib} \\ \tilde{n}_\parallel^2 = \epsilon_{zz} = 1.\end{aligned}$$

where b is defined as:

$$b = \sqrt{\frac{\pi}{8}}\frac{\omega_p^2 W(Z_1^*)}{\omega^2 \beta_T |\cos\alpha|}$$

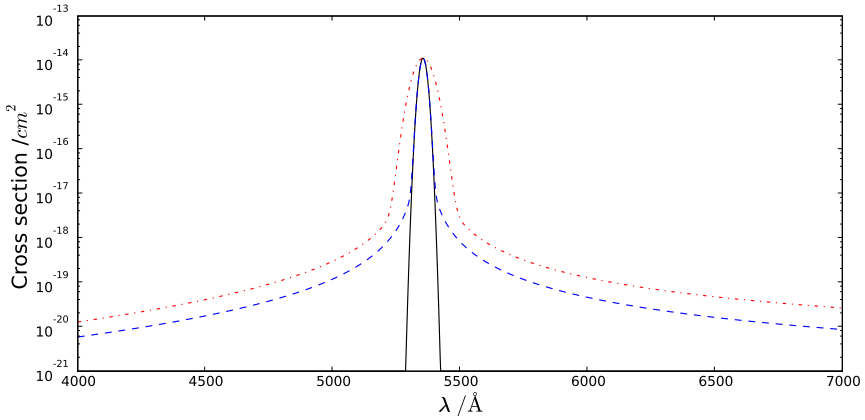

Figure 4.1: The comparison of cyclotron cross-sections calculated using different effects. The black solid line includes only thermal broadening which is calculated by the kinetic theory and identical to the Lamb & Sutherland (1974) result. Opacities for the cyclotron peak towers over the rest of the continuum. The blue dashed line includes the effective collision $\nu_{\rm eff}$ term and finally red dot dashed curve shows the additional magnetic broadening.

and Z_1^* according to equation 4.4.29.

These indices are complex variables, and in order to obtain a simple description of the real part, hence the index of refraction that is applicable to MWD atmospheres, we approximate according to the fact that ω_p/ω_H is at least one order of magnitude smaller than β_T and $\omega_p^2/(\omega_H^2\beta_T) \ll 1$, hence neglecting b^2.

The property of the medium for specific polarization mode can be calculated using the relatively simple solutions of the dispersion equation described by the equations 4.4.18

$$\begin{aligned}
\tilde{n}_- &= \sqrt{1+2ib} \approx 1+ib \\
n_- &= 1+\Im(b) \\
\tilde{n}_\perp &= \sqrt{1+ib+\frac{b^2}{1+ib}} \approx \sqrt{1+ib} \approx 1+i\frac{b}{2} \\
n_\perp &= 1+\frac{\Im(b)}{2}.
\end{aligned}$$

Inserting these results and b in, we end up with the magneto optical parameters

$$\begin{aligned}
\rho_R &= \frac{\omega_H}{c}(n_+ - n_-)\cos\alpha = -\frac{\omega_H \Im(b)}{c}\cos\alpha \\
&= -\frac{\omega_H}{c}\frac{\sqrt{\pi}}{2}\frac{\omega_p^2}{\omega^2\sqrt{2}\beta_T|\cos\alpha|}\Im[W(Z^*)]\cos\alpha \\
\rho_W &= \frac{\omega_H}{c}(n_\parallel - n_\perp)\sin^2\alpha = \frac{\omega_H \Im(b)}{2c}\sin^2\alpha \\
&= \frac{\omega_H}{c}\frac{\sqrt{\pi}}{4}\frac{\omega_p^2}{\omega^2\sqrt{2}\beta_T|\cos\alpha|}\Im[W(Z^*)]\sin^2\alpha.
\end{aligned}$$

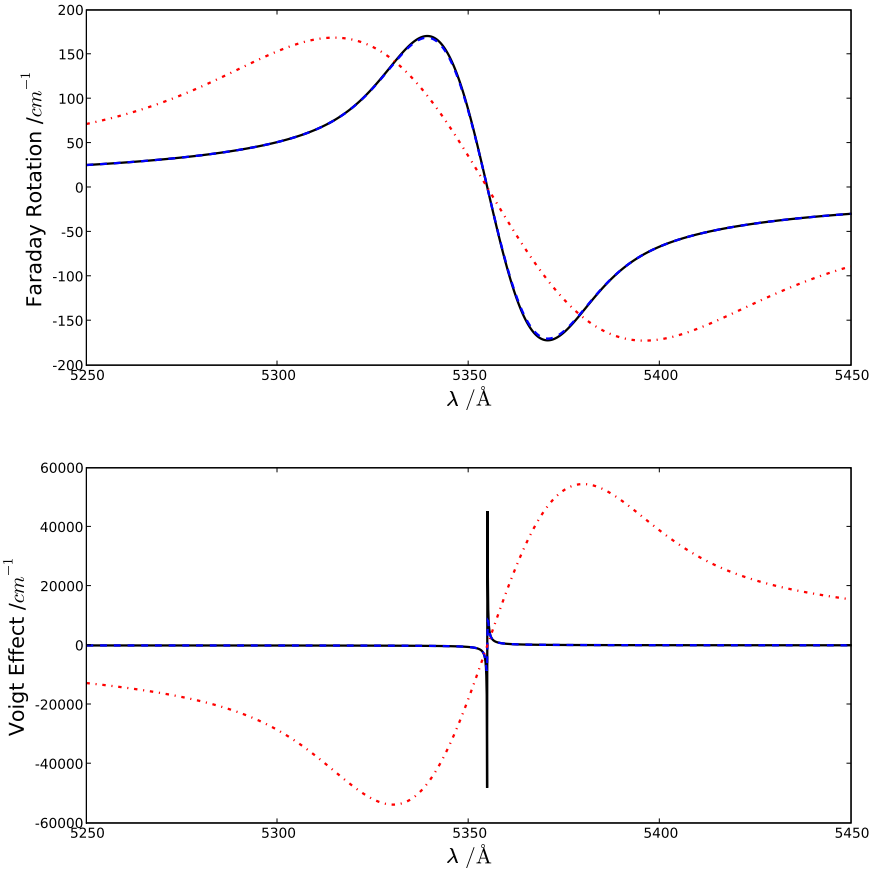

Figure 4.2: The comparison of cyclotron magneto-optical parameters calculated with different effects, same as Fig. 4.5. Faraday rotation calculated at $\alpha = 0$ while Voigt effect was calculated at $\alpha = \pi/2$

Here Z^* is the familiar complex term in the kinetic solution with the subscript 1 dropped. The real part of the plasma dispersion function is the Voigt function, in which the central region is a Gaussian and the wings are described by a Lorentzian.

Martin & Wickramasinghe (1982) exploited this fact to draw physical analogy to the magneto-optical parameters in the formalism of line formation which takes advantage of the function F (Wittmann, 1974). We should note that, although the imaginary part of the complex dispersion function corresponds to the Voigt profile, the real part of it does not coincide with the F function of Wittmann (1974). This shows the necessity for a description for the cyclotron absorption independent of the line formation theory, especially accounting for the refractive behaviour of the magnetized medium which we were able to generate with a through consideration of the plasma formalism.

With our use of the kinetic theory, we were able to derive the magneto-optical parameters which have the the properties of both Doppler and collisional broadening as a natural outcome of the formalism. The additional advantage of self-consistency with the calculations of the absorption cross-sections enables us to implement the already existing physically admissible improvements in the literature to our results.

As discussed in Sec. 1.3.3 one major question for the synthetic MWD spectra is the problem magnetic broadening (see e.g. Jordan et al., 1991). For the cyclotron absorption cross-section, this problem was addressed by additional broadening in the Gaussian part of the Voigt profile. To draw the analogy with our formalism we need to consider the argument of the plasma dispersion function Z^* in equation 4.4.29, in which the denominator $\sqrt{2}\beta_T|\cos\alpha|$ corresponds to the Doppler broadening Δ_D due to velocity distribution of the charges (see Sec. 4.4). When we compare our result of cyclotron cross-section with equation 1.3.40, we see that it is appropriate to add the magnetic broadening term Δ_H (equation 1.3.41).

This conjecture effectively modifies the complex argument of the plasma dispersion function, Z^*

$$\begin{aligned} Z' &= \frac{\omega - \omega_H + i\nu_{\rm eff}}{\omega\sqrt{2}\beta_T|\cos\alpha| + \Delta He/mc} \\ &= \frac{\omega - \omega_H + i\nu_{\rm eff}}{\omega(\Delta_D + \Delta_H)} \end{aligned} \tag{4.5.1}$$

The new Z' not only enables us to calculate the magnetically broadened absorption cross-section, but more importantly magnetically broadened magneto-optical parameters consistently.

$$\begin{aligned} \kappa_+ &= \sqrt{\frac{\pi}{8}}\frac{\omega_p^2}{\omega^2\beta_T|\cos\alpha|}\Re[W(Z')] \\ \sigma_{\rm cyc} &= \sqrt{\frac{\pi}{2}}\frac{\omega_p^2}{c\omega\beta_T|\cos\alpha|}\Re[W(Z')] \\ \rho_R &= -\frac{\omega_H}{c}\frac{\sqrt{\pi}}{2}\frac{\omega_p^2}{\omega^2\sqrt{2}\beta_T|\cos\alpha|}\Im[W(Z')]\cos\alpha \\ \rho_W &= \frac{\omega_H}{c}\frac{\sqrt{\pi}}{4}\frac{\omega_p^2}{\omega^2\sqrt{2}\beta_T|\cos\alpha|}\Im[W(Z')]\sin^2\alpha. \end{aligned} \tag{4.5.2}$$

4.6 Summary

In this chapter, I have discussed and rederived the cyclotron cross-sections with the use of plasma formalism. After proving the closure of the numerous methods in the literature and the kinetic theory of plasmas, I applied it for the calculation of the complex index of refraction which enables the self-consistent calculation of both the refractive and the absorptive properties of the MWD atmospheres.

With this new formalism and the free-free parameters at hand one can reassess the atmospheric properties of MWDs. As mentioned before, the continuum structure of especially the circular polarization spectrum strongly depends on the free-free transitions. In the following section I will enumerate this fact, observationally through magnetic modeling, specifically for the case of RE J 0317-853.

Chapter 5

The Evolutionary Status of REJ 0317-853

5.1 Introduction

RE J 0317-853 is a unique hydrogen-rich white dwarf, which was discovered as an EUV source by the ROSAT Wide Field Camera (Barstow et al., 1995). An analysis of follow-up spectroscopy established that the stellar surface is covered by a very strong magnetic field with a range of about 170-660 MG, implying that RE J 0317-853 has one of the strongest magnetic fields detected so far in a white dwarf.

The optical spectrum together with UV observations taken with the IUE satellite and the *Hubble* Space Telescope indicated that RE J 0317-853 possesses a very high effective temperatures in the range from 30 000 to 55 000 K; Barstow et al. (1995) achieved their best fit for about 49 000 K. A careful analysis of the extreme UV spectrum taken by the Extreme Ultraviolet Explorer (EUVE) satellite using the interstellar medium Lyman lines to account for the interstellar extreme ultraviolet absorption implied an effective temperature of $33\,800$ K (Vennes et al., 2003). Within these constraints, RE J 0317-853 is one of the hottest known magnetic white dwarfs (MWDs); in any case, it has the highest known temperature of all MWDs with a field strength above 20 MG (Kawka et al., 2007; Külebi et al., 2009).

Barstow et al. (1995) performed high-speed photometry demonstrating that the optical brightness of RE J 0317-853 varies almost sinusoidally with a period of 725.4 ± 0.9 sec and an amplitude of more than $0\overset{\mathrm{m}}{.}1$; these results were confirmed by Vennes et al. (2003), who inferred a period of 725.727 ± 0.001 sec from the variation in the circular polarisation. The only reasonable explanation for these results is rotation, implying that RE J 0317-853 rotates more rapidly than any other known white dwarf that is not a member of a close binary. The photometric variation must be caused by differences in the brightness on the various parts of the stellar surface. Since no strong absorption lines are detected in the optical, a possible explanation may be a variation in the effective temperature over the stellar surface; the reason for this temperature inhomogeneity is currently not well understood but is probably connected to stronger or weaker contributions to the magnetic pressure in the stellar atmosphere at different locations on the stellar surface with unequal magnetic field strengths.

To achieve a clearer insight into the evolution of RE J 0317-853, Burleigh et al. (1999)

obtained phase-resolved far-UV spectra with the *Hubble* Space Telescope (HST) Faint Object Spectrograph. They found that the previous optical results could generally be confirmed, but that the splitting of the Lymanα component into subcomponents implied that the field is probably more complicated than indicated by the mean optical spectrum. By compiling a time series of spectra, a model for the magnetic field morphology across the stellar surface was produced using the radiation-transfer models through a magnetised stellar atmosphere from Jordan (1992, see paper for a basic description of the methods) and an automatic least squares procedure. The magnetic geometry could be equally well described by an offset magnetic dipole ($x_{\rm off} = 0.057$, $y_{\rm off} = 0.004$, and $z_{\rm off} = -0.220$ stellar radii), which produces a surface field strength distribution in the range 140-730 MG or an expansion into spherical harmonics up to $l = 3$ in which the surface field strengths are constrained to be within the range 180-800 MG .

The mass of the white dwarf was determined according to the method introduced in Sec. 3.2 by estimating the absolute magnitudes (or absolute fluxes) calculated from the spectroscopic fit parameters $T_{\rm eff}$, $\log g$ and white dwarf evolutionary models (e.g. Wood, 1995; Benvenuto & Althaus, 1999). The determination of the mass of RE J 0317-853 is, not straightforward because of the effects of the strong magnetic field; the usual method of using the Stark broadening of the spectral lines to determine $\log g$ fails in the presence of a magnetic field of several hundred MG (see Sec. 2.2.1).

Nevertheless, the mass determination procedure of RE J 0317-853 could be improved by the knowledge of its distance. RE J 0317-853 is inferred to be in a wide-binary double-degenerate system together with its visual companion, which is a non-magnetic DA white dwarf (LB 9802) 7″ away. The spectrum of LB 9802 was analysed initially by Barstow et al. (1995), and later by Kawka et al. (2007) (for fit parameters see Table 5.3). Barstow et al. (1995) derived a distance in the range 33−37 pc with these parameters using the white dwarf evolutionary models of Wood (1992). The physical companionship of LB 9802 and RE J 0317-853 has recently been confirmed by *Spitzer* IRAC obsevations (Farihi et al., 2008) that demonstrated the common proper motion nature of the system.

With an effective temperature of 50 000 K and assuming a distance of 36 pc Barstow et al. (1995) concluded that the radius of RE J 0317-853 is about $0.0035\ {\rm R}_{\odot}$ with a corresponding extreme mass of $1.35\ {\rm M}_{\odot}(\log g = 9.5)$, derived from the mass-radius relations of Wood (1995). Later Vennes & Kawka (2008) derived a mass of $1.32 \pm 0.03\ {\rm M}_{\odot}$ using $T_{\rm eff} = 33\,800$ K, $\log g = 9.4$ and 27 pc for the distance (for details see Table 5.1). If these mass determinations are true, RE J 0317-853 would not only be one of the hottest known MWD but also the most massive ($\approx 1.35\ {\rm M}_{\odot}$) isolated (due to the large separation of RE J 0317-853 and LB 9802 we can assume that both stars did not interact during stellar evolution) white dwarf discovered so far; only two other white dwarfs are known with masses in excess of $1.3\ {\rm M}_{\odot}$: LHS 4033 with a mass in the range 1.31-1.34 ${\rm M}_{\odot}$(Dahn et al., 2004) and the magnetic white dwarf PG 1658+441 with $1.31 \pm 0.02\ {\rm M}_{\odot}$ (Schmidt et al., 1992).

From the theory of stellar evolution, there are two different ways to produce such massive white dwarfs: either by single-star evolution of a star with an initial mass higher than 7 or 8 ${\rm M}_{\odot}$ (Dobbie et al., 2006; Casewell et al., 2009; Salaris et al., 2009) or from the merger of two white dwarfs with C/O cores (see e.g. Segretain et al., 1997). The latter scenario is supported by the rapid rotation of RE J 0317-853.

Jordan & Burleigh (1999) measured the circular polarisation to have a degree of 16% at a wavelength of 5760 Å, the strongest ever found in a MWD. Together with the assumed small radius and strong gravity in the stellar photosphere, this also made RE J 0317-853 a

test object for setting limits on gravitational birefringence predicted by theories of gravitation, which violate the Einstein equivalence principle (Preuss et al., 2005).

In this chapter we want to discuss the evolutionary status of RE J 0317-853 with the use of various diagnostics. In the first part we will model the spectro-polarimetric observations from Anglo-Australian Telescope (AAT) with our atmospheric calculations in order to assess the magnetic structure of RE J 0317-853. In the second part of this chapter we present the analysis of the parallax measurement with HST's Fine Guidance Sensor (FGS). Since the mass determination of RE J 0317-853 was based entirely on the uncertain spectroscopic distance of the system, we used the observed trigonometric parallaxes of the white dwarf binary system to either confirm or disregard the conclusions of Barstow et al. (1995). In the final Section, we summarise the results of both parallax and spectro-polarimetric analyses and assess their implications on the evolutionary history of RE J 0317-853.

5.2 Time-resolved spectro-polarimetry of RE J 0317-853

5.2.1 Observations at the AAT

Optical spectro-polarimetric observations of RE J 0317-853 were obtained with the 4 m telescope at the AAT on 1996 October 16/17. Jordan & Burleigh (1999) used the RGO spectrograph and a Tektronic CCD, with a modulator consisting of a rotating super-achromatic quarter wave-plate. A calcite block analyser was positioned behind the slit to produce two spectra corresponding to orthogonal polarization states (the ordinary and extraordinary rays). Two background spectra were obtained simultaneously through a second aperture. The quarter wave-plate was rotated regularly between two positions 90° apart to average out flat field variations. The star and background were also periodically swapped between the two apertures for the same reason. Each pair of spectra taken at the two wave-plate positions were background-subtracted, extracted and co-added to give intensity and polarisation spectra. Jordan & Burleigh (1999) obtained the spectra using the 250B grating over a wavelength range of 3350 Å−7080 Å with a spectral resolution of ≈7 Å and a time resolution of ≈1 minute. The spectra were co-added in phase to cover the 725 second rotation period.

5.2.2 Spectroscopic analysis

In the literature time-resolved spectra of RE J 0317-853 has been fitted with offset dipoles and multipoles; however, these fits were not satisfactory, especially in the low field phase (Ferrario et al., 1997; Burleigh et al., 1999; Vennes et al., 2003, see Table 5.1). It has already been noted that the magnetic structure of the low field phase is very uniform (~ 185 MG) based on analysis of the spectral lines (Ferrario et al., 1997), but the synthetic MWD atmospheric models left the circular polarisation peak at the same phase unexplained. However, it was neglected in the previous modeling that the strong peak at ~ 5760 Å corresponds to the cyclotron feature for a uniform field strength of ~ 185 MG, according to $\lambda_H = 10\,700\,\text{Å}/B_8$.

With our new description for the dichroic continuum opacities from Chapter 4, we can now calculate the circular polarisation peak at the cyclotron frequency consistently with the spectral modeling. In order to test the new continuum opacities we recalculated our data base of theoretical spectra and polarisation data for effective temperatures between $30\,000$

Table 5.1: Results of the spectroscopic analyses of RE J 0317-853 in the literature. Burleigh et al. (1999) also applied multipole models to the spectrum. Note that Vennes et al. (2003) did not fit the RE J 0317-853 spectra but modeled the results of Ferrario et al. (1997) and multipole fit parameters of Burleigh et al. (1999).

	B95[1]	F97[2]	B99[3]	V03[4]
$T_{\rm eff}$/ K	$49\,250^{+2150}_{-1200}$	40 000	40 000	33 000
log g/ dex	≈9.5	9.52	≈9.5	9.3
Mass/ $M_\odot$	1.35	1.35	1.35	1.35
$\lvert B\rvert$ /MG	200-600	190-820	140-730	190-820
B_p /MG	340	450	363	450
$z_{\rm off}/R_{\rm WD}$	-0.2	-0.35	-0.22	-0.35
$x_{\rm off}/R_{\rm WD}$	–	–	0.057	-
$y_{\rm off}/R_{\rm WD}$	–	–	-0.04	-
i /°	-	60	40	60

[1] Barstow et al. (1995); [2] Ferrario et al. (1997); [3] Burleigh et al. (1999); [4] Vennes et al. (2003)

and $50\,000$ K and for $\log g = 9.5$ (Jordan, 1992); the field geometry was then obtained with the fitting procedure described by Euchner et al. (2002) (see also Sec. 2.2.1).

For an initial analyses we restricted ourselves to the spectro-polarimetric data of the low-field phase of RE J 0317-853 and modelled it with a simple offset dipole. The result of the fit is shown in Fig. 5.1. The difference between the synthetic flux and polarization spectrum calculated with magneto-optical parameters of Jordan et al. (1991) versus the magneto-optical parameters from Sec. 4.5 is apparent in the plots. The magnetic field geometry of the both spectral fits are identical; however, due to the inconsistencies of the theoretical treatment of the magneto-optical parameters and the cyclotron opacities the polarization peak near 5760 Å could not be fit in the former case.

Even if we consider only the low field phase, we could conclusively show the existence of cyclotron absorption. While the cyclotron line is indiscernible in the flux spectrum, the peak in circular polarization is indicative of strong dichroism. Although cyclotron emission is a well known phenomenon for accreting white dwarfs, cyclotron absorption is observed for the first time in the atmosphere of a MWD.

In a next step we have undertaken the fitting of the time-resolved flux and polarization spectra and binned the observations into 8 different phases. We used a modified version of the code developed by Euchner et al. (2002) (see Sec. 2.2.1). The initial fits with an off-centered magnetic dipole model yielded satisfactory fits for the low-field phase; however, the opposite phase of RE J 0317-853 where a strong field is dominant, lacks a good fit. The flux and circular polarization spectra for all phases are shown in Fig. 5.2. The parameters of our fits are rather similar to the literature since it is a dipole of strength $\sim 380\,MG$ with a large on axis offset $(0.29\,R_{\rm WD})$. In this model the field strengths are distributed between $140 - 485$ MG.

Although the overall fit quality is not very high, our models are able to reproduce the overall polarization level of circular polarization. This has not been accomplished by the former analyses of RE J 0317-853, and our success is indicative of the physical consistency of our theoretical description for the free-free opacities and magneto-optical parameters.

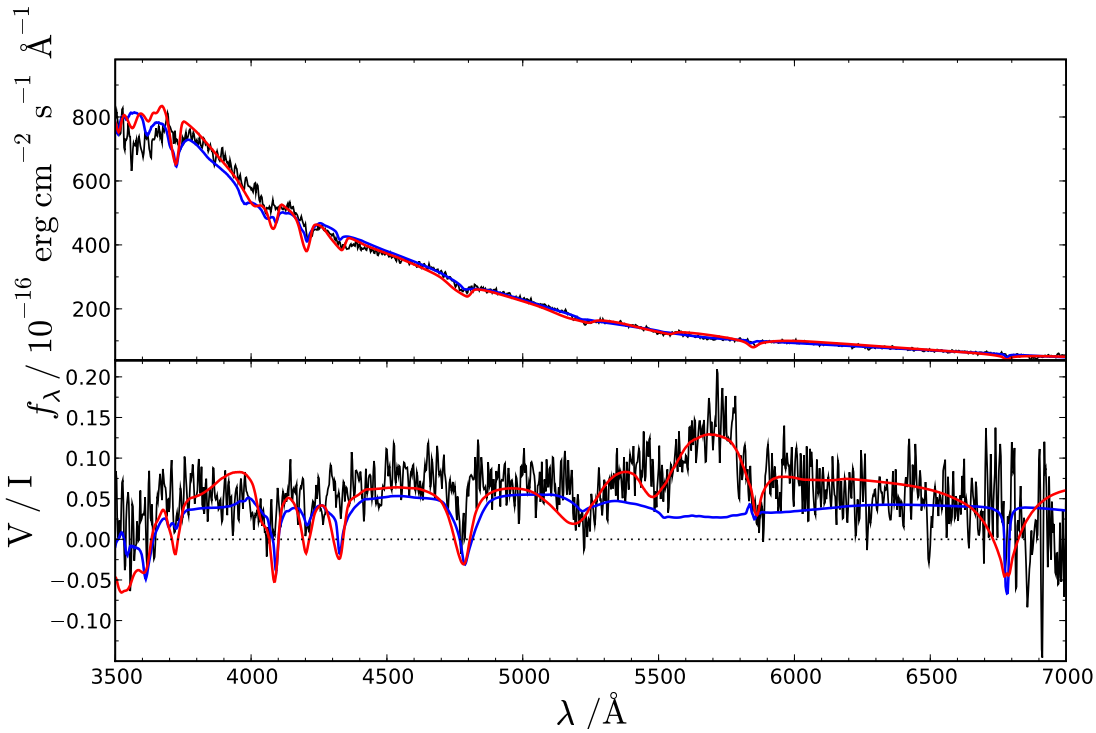

Figure 5.1: The comparison of the model spectra using the free-free opacities and magneto-optical parameters of Jordan et al. (1991) (see also Sec. 1.3.3) versus the ones derived in Sec. 4.5. The model fit using the old opacities and magneto-optical parameters are shown in blue, whereas the synthetic spectrum and polarization calculated with the new magneto-optical parameters are shown in red.

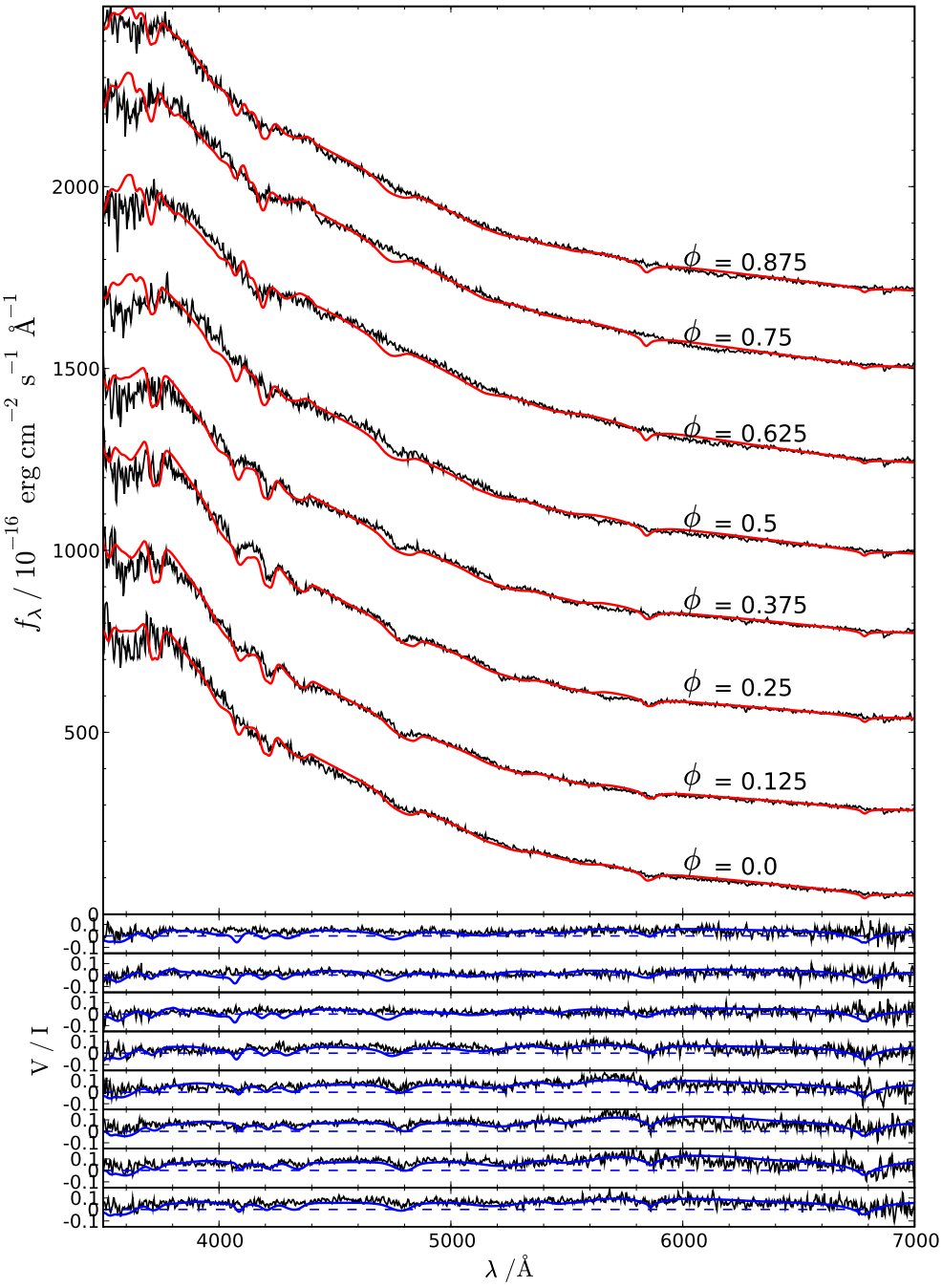

Figure 5.2: Observed phase-resolved spectra (above) and degrees of circular polarisation (bottom) of RE J 0317-853 (in black) fitted with off-centered, non-aligned magnetic dipole models (in red).

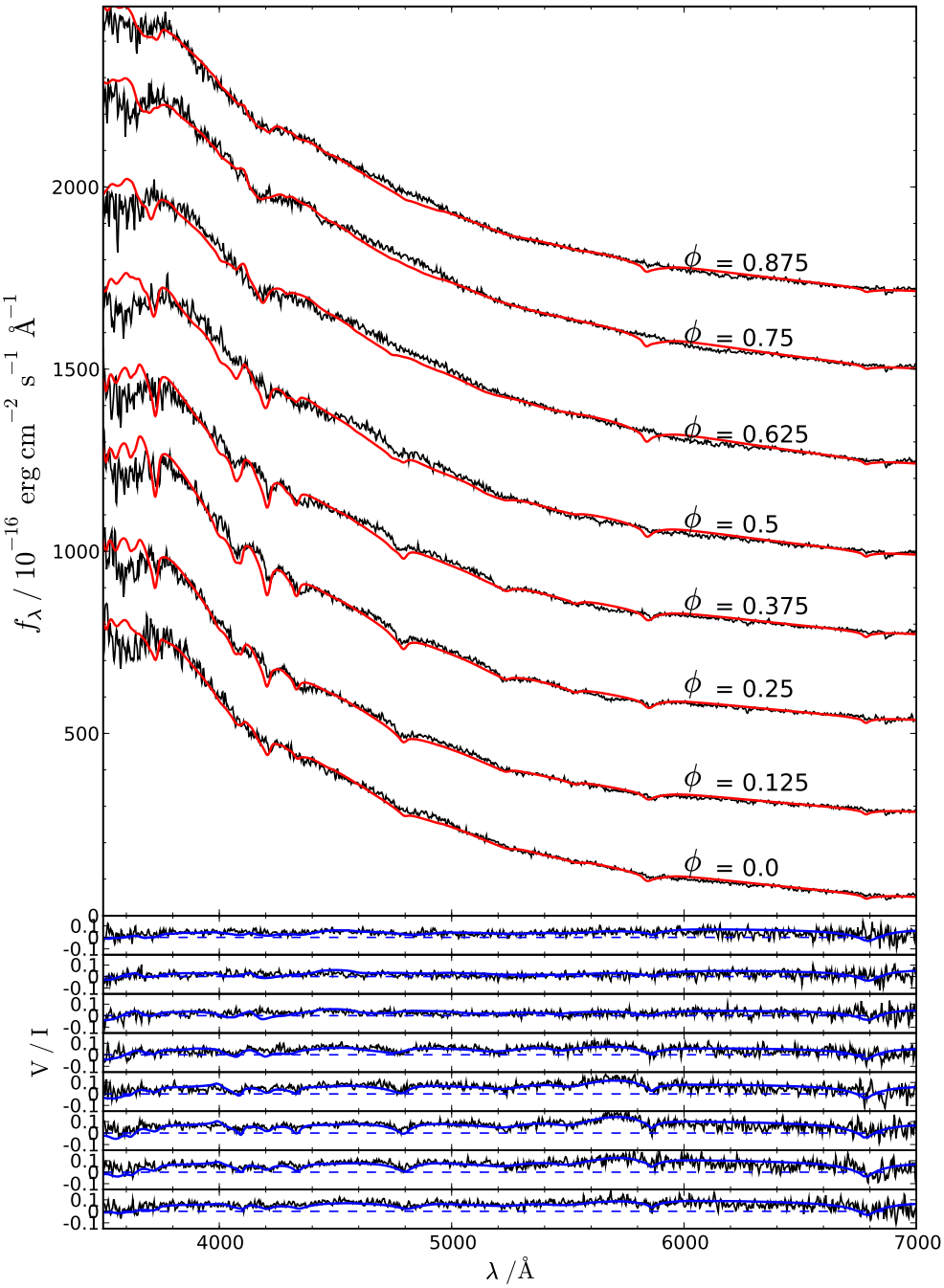

Figure 5.3: Observed phase-resolved spectra (above) and degrees of circular polarisation (bottom) of RE J 0317-853 (in black) fitted with off-centered, non-aligned magnetic dipole, quadrupole and octupole models (in red).

Table 5.2: Magnetic fit parameters of RE J 0317-853. The parameters are explained in the text.

B_p /MG	Θ_d /°	Φ_d /°	B_q /MG	Θ_q /°	Φ_q /°	B_o /MG	Θ_o /°	Φ_o /°	$x_{\rm off}$ /$R_{\rm WD}$	$y_{\rm off}$ /$R_{\rm WD}$	$z_{\rm off}$ /$R_{\rm WD}$	i /°
(1)												
384	-54	75	–	–	–	–	–	–	-0.029	-0.007	0.291	39
(2)												
380	-41	-70	267	-8	20	147	5	-11	-0.168	0.048	0.197	35

Table 5.3: Spectroscopically derived parameters of LB 9802.

Ref.	V /mag	$T_{\rm eff}$ /K	$\log g$	d_L /pc
1	14.11	$16\,030 \pm 230$	8.19 ± 0.05	33-37
2	-	$16\,360 \pm 80$	8.41 ± 0.02	30
3	13.90	$15\,580 \pm 200$	8.36 ± 0.05	27

[1]Barstow et al. (1995); [2]Ferrario et al. (1997); [3] Kawka et al. (2007)

However, for the phase with strong field, some strong bound-bound features are apparent in the model spectra, which means that the geometrical model used for the global magnetic field is too simple and hence insufficient in creating a large enough magnetic field gradient over the different phases.

To approach a better fit for the observations, we further pursued more complicated models, i.e. an off-centered $(x_{\rm off}, y_{\rm off}, z_{\rm off})$ non-aligned combinations of magnetic dipoles (polar field strength of dipole B_p, quadrupole (B_q), and octupoles (B_o)). We have used the prescription of Euchner et al. (2002) where alignment of the dipole (Θ_d, Φ_d), the quadrupole (Θ_q, Φ_q) and the octupole (Θ_o, Φ_o) are defined with respect to the rotation axis. In this model the transition from the low to the high field phase was much more consistent with the observations with respect to the offset dipole models, as seen on Fig. 5.3. Although not completely satisfactory the fits to the phase with the high field, imply a very strong magnetic field which extend to $943\,MG$ (the distribution of the global magnetic field strengths is between $144 - 943$ MG). The existence of a strong field spot has been proposed in the literature (Ferrario et al., 1997; Burleigh et al., 1999) and we confirm this diagnosis with our fits. Moreover, with such a high field strength found, RE J 0317-853 can almost compete with PG 1031+234 in which Oestreicher et al. (1992) found the highest magnetic field strength (1 GG) ever observed in a white dwarf.

5.3 Parallax Study

5.3.1 Observations with the FGS of the HST

The observations of the magnetic white dwarf RE J 0317-853 ($\alpha_{\rm ICRS} = 03^{\rm h}17^{\rm m}16\overset{\rm s}{.}1750$, $\delta_{rmICRS} = -85°32'25\overset{''}{.}45$) and its non-magnetic white dwarf companion LB 9802 ($\alpha_{\rm ICRS} = 03^{\rm h}17^{\rm m}19\overset{\rm s}{.}3050$, $\delta_{rmICRS} = -85°32'31\overset{''}{.}15$) with the *Hubble* Space Telescope were per-

Table 5.4: HST orbits for HST proposal 10930 and 11300.

proposal ID	start time	end time	visit
10930	Mar 24 2007 17:54:01	Mar 24 2007 18:53:25	01
10930	Mar 24 2007 19:29:48	Mar 24 2007 20:29:12	02
10930	Sep 27 2007 03:28:55	Sep 27 2007 04:28:19	03
10930	Sep 29 2007 01:47:19	Sep 29 2007 02:46:43	04
11300	Mar 29 2008 02:00:30	Mar 29 2008 02:59:53	01
11300	Mar 29 2008 03:36:19	Mar 29 2008 04:35:42	02

formed with the Fine Guidance Sensor 1r (FGS 1r) at three epochs (March 2007, September 2007, and March 2008, see Table 5.4). The Fine Guidance Sensor is a two-axis, white-light shearing interferometer that measures the angle between a star and HST's optical axis by transferring the star's collimated and compressed light through a polarising beam splitter and a pair of orthogonal Koesters prisms (see Nelan et al., 1998; Nelan, 2010, for a description of the instrument design). When FGS 1r is operated as a science instrument, HST pointing is held fixed and stabilized by FGS2 and FGS3 which operate as guiders.

To derive an astrometric solution for position, proper motion, and parallaxes, RE J 0317-853, LB 9802, and the reference field stars had to be observed at a minimum of three epochs, preferably at the seasons of maximum parallax factor to allow us to cleanly separate their parallaxes from their proper motions. These seasons are separated by about six months.

Fortunately, the epochs of maximum parallax factor also resulted in HST roll angles (which are constrained by date) such that the two white dwarf stars and the optimal set of astrometric reference stars could be observed at all epochs. Figure 5.4 shows the parallactic ellipse and the orientations of the FGS aperture at the times of the observations (there were two March epochs, 2007 and 2008). Experience shows that a minimum of two orbits per epoch are required to achieve the highest possible accuracy in the final parallaxes. Table 5.4 provides the dates of the six orbits for our HST programme. Since the two white dwarfs are only $\approx 7''$ apart, we were able to use the same reference stars for the two white dwarfs using no more HST orbits than would be necessary for a single parallax measurement. Using identical reference stars also ensured that the parallax difference between the two putative companion stars was measured more precisely than their absolute parallaxes since the measurements share the same correction of relative to absolute parallax. In addition, their relative proper motions can be measured to provide an additional check on whether or not the two white dwarfs constitute a bound pair.

5.3.2 Spectroscopy of the astrometric reference stars

Since only relative parallaxes can be measured with HST, we had to estimate the parallaxes of a sample of reference stars in the vicinity of our target objects which comprise our local reference frame (see Figure 5.5). Ref4 and Ref5 were not observed by the FGS 1r since they were not needed.

Spectra of these surrounding stars of similar (or somewhat larger) brightness than RE J 0317-853 were taken in service mode with the Boller & Chivens spectrograph of the 1.5m SMARTS telescope, located on Cerro Tololo at the Interamerican Observatory in Chile,

in two nights between February 16 and 18, 2008. To ensure that the whole optical range is covered, we performed exposures with two gratings (9/Ic and 32/Ib). Both observing nights were affected by passing clouds and the relatively high airmass (> 1.8) due to the large declination difference between the observatory's zenith and the target field. Since this could not fully be corrected by flux standards, the energy distribution in the blue channel may be compromised.

The classifications for the reference stars were performed by comparing the flux-calibrated spectra to the templates of Pickles (1998). Since the Pickles library does not cover all spectral subtypes, interpolation by eye was performed where appropriate. For late G- and especially K stars, the MK class III templates were also looked at because in some cases the star actually turned out to be a giant; giants can be clearly distinguished from dwarfs, which show an indentation at 5200 Å that the giants do not or only slightly exhibit. The few metal-poor and metal-rich templates were also used, although the difference in the Pickles spectra is too small to really make a discrimination in this respect.

The absolute magnitude determination was based on an interpolation of the data taken from Lang (1992) and Allen's astrophysical quantities (Cox, 2000). It was achieved by parametrising the spectral type so that spectral type F corresponds to 0, G to 1, K to 2, and M to 3, and the spectral type subdivisions correspond to the first decimal, i.e. an G2 star would be represented by 1.2. A 5th degree polynomial is then fitted to determine the M_V - spectral type relation shown in Fig. 5.6. This was performed for both luminosity class III and V, assuming that all our stars come from these two luminosity classes. The absolute magnitudes of the reference stars were then calculated using these two functions with their spectral class parametrised in the same way as an argument.

The determination of the errors is not straightforward, since not all error sources can be easily quantified. The error in the determination of the spectral type was roughly quantified by calculating the absolute magnitude of the spectral subtypes closest to the determined ones were calculated using the same fit function (for those stars where the derived spectral type was in-between two subdivisions, i.e. in the cases of reference stars 1, 3, and 9 the second next subtype was chosen). The difference between this absolute magnitude and the absolute magnitude obtained for the star is then our estimate of the error in the absolute magnitude caused by the uncertainty in the spectral classification. This assumes that the error in the spectral type is not larger than one subdivision, which might not be true in all cases but should generally be the case. It was generally found that the difference in absolute magnitude between the measured spectral type and its neighbours is about 0.2 mag, so this value was assumed in all subsequent calculations. This error of 0.2 mag corresponds to an error of 12% in distance (see Table 5.6, 7th column). The corresponding error in the parallax was used for the correction of the relative parallaxes.

Table 5.5: Coordinates and photometry of stars in this work.

name	$\alpha_{\rm ICRS}$	$\delta_{\rm ICRS}$	V /mag	$B-V$ /mag	$U-B$ /mag	$V-R$ /mag	$V-I$ /mag	GSC2 F[2] mag
RE J 0317-853	$03^{\rm h}17^{\rm m}16\overset{\rm s}{.}1750$	$-85°32'25\overset{''}{.}45$	14.90 ± 0.02	-0.16[1]	-1.13[1]	0.01[1]	-0.11[1]	15.09
LB 9802	$03^{\rm h}17^{\rm m}19\overset{\rm s}{.}3050$	$-85°32'31\overset{''}{.}15$	14.11 ± 0.02	$+0.07$[1]	-0.68[1]	-0.06[1]	-0.18[1]	14.22
Ref1[3]	$03^{\rm h}20^{\rm m}12\overset{\rm s}{.}918$	$-85°34'56\overset{''}{.}175$	9.42	0.38				
Ref2[4]	$03^{\rm h}18^{\rm m}52\overset{\rm s}{.}01$	$-85°35'20\overset{''}{.}8$	12.27	0.50[4]				12.55
Ref3	$03^{\rm h}18^{\rm m}03\overset{\rm s}{.}1$	$-85°36'02''$	14.60	1.14[5]				
Ref6	$03^{\rm h}13^{\rm m}59\overset{\rm s}{.}7$	$-85°30'16''$	14.00	1.04[5]				
Ref7	$03^{\rm h}15^{\rm m}55\overset{\rm s}{.}9$	$-85°30'20''$	15.00	0.84[5]				
Ref8	$03^{\rm h}16^{\rm m}46\overset{\rm s}{.}3$	$-85°29'48''$	14.37	1.10[5]				
Ref9	$03^{\rm h}18^{\rm m}55\overset{\rm s}{.}1$	$-85°36'42''$	14.36	0.63[5]				

[1] From Barstow et al. (1995); [2] http://tdc-www.harvard.edu/catalogs/gsc2.html; [3] =HD 23298=TYC9495-788-1(Høg et al., 1998); [4] =GSC0949500756; [5] theoretical $B-V$ values interpolated for spectral type and MK class, see Table 5.6

Table 5.6: Results of the analysis of the reference stars (V magnitude, spectral type and luminosity class, absolute magnitude, distance modulus, distance, quantifiable distance error (see text), and parallax and its errors (the subscripts "$-$" and "$+$" refer to the distances).

star	V /mag	spectral type	M_V /mag	$m_V - M_V$ /mag	$B-V$ /mag	d /pc	δd /pc	$\pi^{\delta\pi_-}_{\delta\pi_+}$ /mas
Ref1	9.95	F3-4V	3.48	6.47	0.41	197	24	$5.08^{+0.69}_{-0.55}$
Ref2	12.27	F7V	3.95	8.32	0.50	461	55	$2.17^{+0.29}_{-0.23}$
Ref3	14.60	K1-2III	0.48	14.12	1.14	6668	800	$0.15^{+0.02}_{-0.02}$
Ref6	14.00	K4V	6.96	7.04	1.04	256	31	$3.91^{+0.53}_{-0.43}$
Ref7	15.00	K0V	5.98	9.02	0.84	637	76	$1.56^{+0.22}_{-0.16}$
Ref8	14.37	K1III	0.55	13.82	1.10	5808	720	$0.17^{+0.02}_{-0.02}$
Ref9	14.36	G3-4V	4.81	9.55	0.63	813	98	$1.23^{+0.23}_{-0.17}$

Given the relation between parallax and distance, the error in the former is not symmetric if that of the former is. The asymmetric nature of the parallax error is represented in column 8 of Table 5.6. The errors given in Table 5.6 do not represent the overall error. A main source of error will most likely be the photometry, which is not of the highest precision. Moreover, our spectra do not allow us to determine the exact evolutionary status of the objects, which influences the accuracy of the absolute magnitude. For the same reason, the influence of metallicity cannot be taken into account, and all stars are assumed to be of solar abundance. Adding these uncertainties with some margin leads to an overall error in distance of 20-30%, with the stars Ref7-9 having the larger errors, since we only have one spectrum (red of Ref7, blue for the other two) for these objects. Since the parallax is the reciprocal of the distance, the stars with a large distance are the more reliable ones, especially the two giants (Ref3 and 8).

5.3.3 Analysis of the FGS data

Our astrometric measurements used FGS 1r in position mode to observe RE J 0317-853, LB 9802, and the associated reference field stars. At each of the three epochs, two HST orbits were used. Within each orbit, FGS 1r sequentially observed each star several times in a round-robin fashion for approximately 30 seconds. The standard FGS data reduction algorithms (Nelan & Makidon, 2002) were employed to remove instrumental and spacecraft artifacts (such as photon shot noise, spacecraft jitter and drift, optical distortion of the FGS, differential velocity aberration, etc). The calibrated relative positions of the stars in each of the six visits were combined using a six parameter overlapping plate technique that solves for the parallax and proper motion of each star. This process employed the least squares model GaussFit (Jefferys et al., 1988) to find the minimum χ^2 best solution.

The results of the FGS measurements for RE J 0317-853, LB 9802, and the reference stars are given in Table 5.7. The σ_ξ and σ_η are the $1\,\sigma$ errors of the fit of the stars onto the "master plate". Likewise, the parallax and proper motion errors are the $1\,\sigma$ dispersion in those values measured for the individual observations (e.g. RE J 0317-853 and LB 9802 were observed approximately four to five times each in every HST orbit, for a total of 24 to 30 individual measurements). The errors quoted in Table 5.7 are typical of the performance of the FGS 1r (for comparison see e.g. Benedict et al., 2007), indicating that

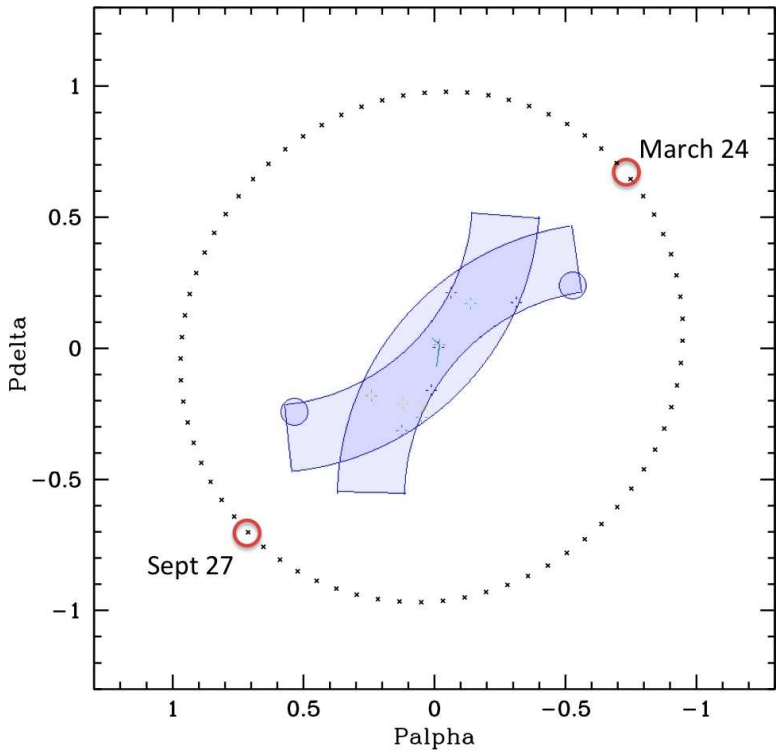

Figure 5.4: The parallactic ellipse of the RE J 0317-853 field and the orientation of the FGS 1r field of view at the dates of the observations. The X-axis of the FGS 1r is nearly parallel to the line connecting the circles that mark the epochs at which the observations were made.

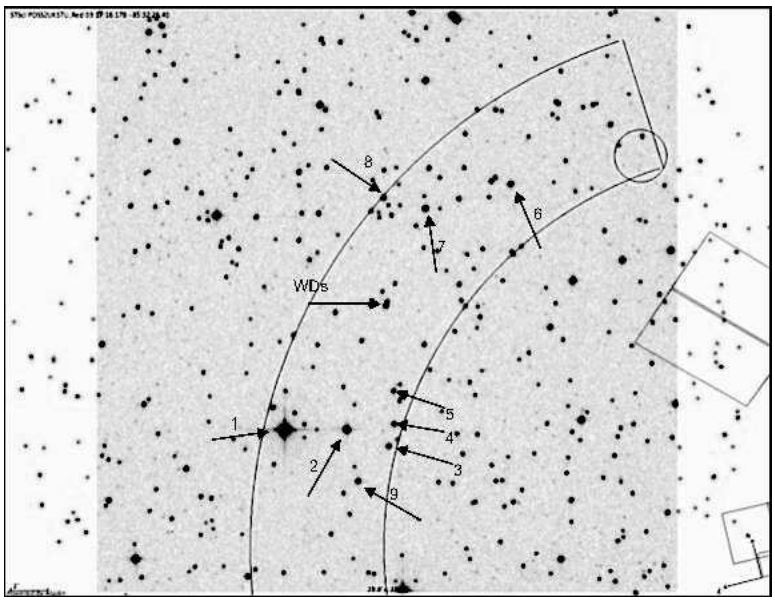

Figure 5.5: The field of the binary WDs RE J 0317-853 and LB 9802 and the reference stars Ref1, . . . , Ref9. Ref4 and Ref5 were later omitted since they were too faint.

Table 5.7: Astrometric results for RE J 0317-853, LB 9802. and the astrometric reference stars: parallax, proper motion in right ascension, proper motion in declination, the standard errors of the proper motion, and the standard errors in the fiducial coordinates ξ and η of the FGS.

star name	π/mas	μ_α/mas yr^{-1}	μ_δ/mas yr^{-1}	σ_ξ/mas	σ_η /mas
RE J 0317-853	34.380±0.260	-91.165±0.435	-15.344 ±0.451	0.3427	0.2085
LB 9802	33.279±0.238	-78.894± 0.424	-27.041±0.412	0.3042	0.2030
Ref1	4.62±0.39	10.76 ±0.782	19.50±0.731	0.4544	0.1541
Ref6	3.51 ±0.40	0.00 ±0.000	0.00±0.000	0.4862	0.4936
Ref7	1.57 ± 0.00	-21.01±0.698	-8.01±0.702	0.4552	0.3535
Ref8	0.17 ± 0.00	0.00 ±0.000	0.00±0.000	0.4713	0.3859
Ref9	1.23 ±0.00	0.00 ±0.000	0.00±0.000	0.4471	0.2317

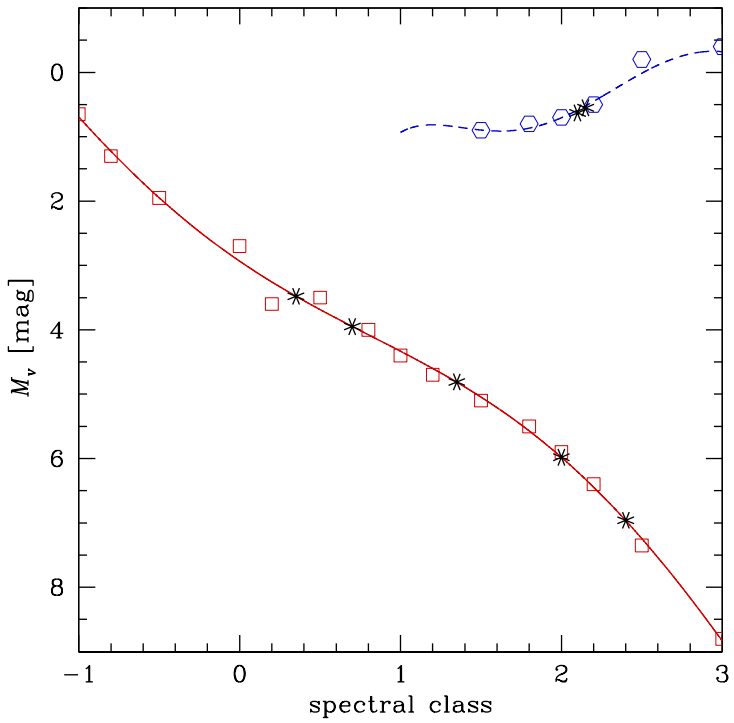

Figure 5.6: The spectrophotometric determinations of the absolute magnitude of the reference stars. The abscissa denotes the spectral type encoded in a way that F0 corresponds to 0.0, G0 to 1.0, K0 to 2.0 etc. and the spectral type subdivisions being given by the first decimal. The (red) open squares are the loci of main-sequence stars in this HR-diagram, and the (blue) open hexagons represent the giants (luminosity class III); the two curves show the resulting fits for both luminosity classes. The asterisks show the reference stars of this program. The spectral (sub)type was determined using low resolution spectra and the absolute magnitude was calculated using the fitted polynomial.

our observations are nominal. The best solution was obtained by directly solving for the trigonometric parallax of Ref1 and Ref6, for which we obtain values consistent with their predicted spectroscopic parallaxes. Likewise, we derive the optimal solution when we use the FGS 1r data to solve for the proper motion of Ref6 and Ref7. The bulk proper motion of the field is constrained by setting Ref6, Ref8, and Ref9 to have no proper motion. The astrometric reference star Ref2 was not used because FGS 1r resolved it to be a wide binary system, which caused an acquisition failure in the second epoch.

The parallaxes for RE J 0317-853 and LB 9802 differ by 1.101 mas, which is about four times the $1\,\sigma$ of their individual errors. This result includes an application of the standard "lateral colour" correction that removes the apparent shift of an object's position in the FGS field of view due to the refractive elements in the instrument's optical train. The correction is given as $\delta x = (B-V) \cdot lcx$ and $\delta y = (B-V) \cdot lcy$. The coefficients $lcx = -1.09$ mas and $lcy = -0.68$ mas are derived from the observed relative positions of two calibration stars, LATCOL_A ($B-V = 1.9$), and LATCOL_B ($B-V = 0.2$), at several HST roll angles. However, RE J 0317-853 is significantly hotter and bluer than the blue calibration star LATCOL_B. It is clear from Fig. 5.4 that an error in the lateral colour correction (especially in this case, along the FGS X-axis, which is nearly aligned with the line connecting the two circles marking the dates of the observations) will produce an error in the measured parallax. To evaluate the validity of applying the standard lateral colour correction (which is based solely on a star's value of B-V) to RE J 0317-853, we revisited the interpretation of the astrometric results of the lateral colour calibration observations. Details of this "plausibility" investigation will be published as an STScI FGS Instrument Scientist Report (Nelan, in preparation) but summarized here.

The spectral energy distribution (SED) of the two lateral colour calibrations stars, in addition to LB 9802, and RE J 0317-853 were convolved with the wavelength-dependent sensitivity of the FGS over its bandpass (the sensitivity decreases from $\approx 20\%$ at 4000 Å to $\approx 2\%$ at 7000 Å in a near linear fashion, where sensitivity refers to the probability that a photon will be detected). The number of photons observed (i.e., actually detected) by the FGS for each star at a given wavelength ($N_{photons}(\lambda)$) was normalized to unity at (for the moment) an arbitrary λ_o. The effective FGS colour of each star was then defined to be the ratio of the wavelength weighted sum ($\sum((\lambda_o - \lambda) * N_{photons}(\lambda))$ for all $\lambda < \lambda_o$ (the "blue" sum) to the similar "red" sum ($\sum((\lambda - \lambda_o) * N_{photons}(\lambda))$ for all $\lambda \geq \lambda_o$ over the FGS bandpass. The value of λ_o is the boundary between the blue and red such that for a source emitting the same number of photons at every wavelength the blue and red wavelength weighted sums are equal and the colour ratio is unity. For the FGS, we find that $\lambda_o = 5092$ Å.

The SEDs of both the red calibration star LATCOL_A and RE J 0317-853 were represented as black body curves with $T = 2\,900$ K and $T = 50\,000$ K, respectively, while LATCOL_B and LB 9802 were represented by stellar model atmospheres using a code based upon the Kurutz models. For LATCOL_B, a solar abundance, $T_{\rm eff} = 8\,000$ K, and $\log g = 4.1$ were assumed. For LB 9802, we assumed a hydrogen-atmosphere white dwarf with $T_{\rm eff} = 16\,030$ K and $\log g = 8.2$. Using these SEDs, we computed for each star the wavelength weighted blue/red ratio described above, for which we found (blue/red) = 0.13, 1.42, 1.79, and 2.54 for LATCOL_A, LATCOL_B, LB 9802, and RE J 0317-853, respectively. (A more precise estimate of the blue/red ratios for these four stars will use observed SEDs, which are currently unavailable. Here we simply evaluate the plausibility of this concept.)

If we assume that the lateral colour shift in the relative position of two stars is pro-

portional to the difference in their blue/red ratios, we can use the the astrometric results of the lateral colour calibration, which found that the blue star LATCOL_B was shifted by -1.87 mas relative to LATCOL_A, and their blue/red ratios to determine the proportionality constant $\alpha = -1.85/(1.42 - 0.13) = -1.44$ mas. Applying this to RE J 0317-853 and LB 9802, we find the lateral colour-induced shift in the position of RE J 0317-853 relative to LB 9802 to be -1.08 mas. The parallax result cited in Table 5.7 already includes a lateral colour correction of -0.25 mas in the position of RE J 0317-853 relative to LB 9802 (based solely upon the (B-V) of each star). This differs by -0.83 mas when using the difference in their blue/red ratios. If we apply this correction, the parallax difference of the two stars is reduced to 0.27 mas, which is $\approx 1\,\sigma$ of the individual measurements. We conclude that the two white dwarfs have the same parallax, and that this 0.27 mas difference is caused by the imprecise model SEDs used to construct the blue/red ratios.

The measured parallax of LB 9802 is also affected by errors in the lateral colour correction, but to a lesser extent since at (B-V)$= 0.07$ it is closer to the colour of the blue calibration star LATCOL_B (B-V$= 0.2$). Nonetheless, the parallax quoted in Table 5.7 may be too large by up to 0.4 mas, based on the difference in the predicted relative shift between two stars with (B-V) $= 0.2$ and 0.07 using the standard lateral correction and the blue/red ratio correction. Given the imprecision of the (blue/red) based correction, we take the parallax of LB 9802 to be $\pi = 33.279 \pm 0.238$ mas using the standard lateral colour correction.

LB 9802 is $7''$ distant from RE J 0317-853 at a position angle P.A. $= 145.856°$ as measured by FGS 1r. From the measured proper motions (Table 5.7), LB 9802 is moving away from RE J 0317-853 at 16.26 ± 0.86 mas yr^{-1} along a position angle of $133.62°$, which is nearly aligned with the line of sight between the two stars. The computation of the proper motions is dominated by the observations from the first and third epochs, which were performed at the same HST orientation. Therefore the uncertainty in the lateral colour correction has no effect. At a distance of 30.05 pc (calculated from the parallax of LB 9802), this corresponds to 0.489 ± 0.026 AU yr^{-1}, i.e. 2.33 ± 0.12 km s^{-1}. We compare this tangential space velocity with an estimated orbital speed. If we assume that this is a bound binary system with a separation of $7''$ (210 AU at 30.05 pc), and with the total mass ranging from 2.02-2.31 $M_\odot$ (see Sect. 5.4.1), a circular orbit yields a period of 2004 yr (for the higher mass estimate) to 2143 yr (for the lower mass); this corresponds to orbital speeds of 3.12-2.92 km s^{-1} for LB 9802 with respect to RE J 0317-853. These estimates are comparable to the tangential space velocity measured by FGS. This result and the close spatial proximity of the two stars supports the conclusion that LB 9802 and RE J 0317-853 constitute a bound system.

Although the FGS photometry shows a peak-to-peak amplitude variation between $V = 14.60$ and $V = 14.84$ (with 0.01 accuracy estimated using LB 9802 as a reference) consistent with the result from Barstow et al. (1995), the sampling was not good enough to confirm the 725 second photometric variability quantitatively by means of a Fourier analysis of this sparse data set.

5.4 Determination of the stellar parameters

5.4.1 Mass and radius determinations of RE J 0317-853 and LB 9802

To determine the mass of RE J 0317-853, we used synthetic bolometric colours and absolute magnitudes for carbon-oxygen (CO) core white-dwarf cooling models with thick hydrogen layers ($M_{\rm H}/M_* = 10^{-4}$) (Wood, 1995; Holberg & Bergeron, 2006)[1]; when required, we used oxygen-neon (ONe) core white-dwarf cooling models with hydrogen layers of $M_{\rm H}/M_* = 10^{-6}$ (Althaus et al., 2005, 2007)[2].

We determined the "observed" absolute visual magnitude $M_V^{\rm obs} = V + 5\log\pi - 5 = 12.51$ mag from $V = 14.90$ and $\pi = 0.033279''$. For a given effective temperature and surface gravity, the theoretical bolometric magnitude $M_{\rm bol}$, the bolometric correction B.C.$=M_{\rm bol} - M_V$, and mass m for RE J 0317-853 were calculated. The theoretical absolute visual magnitude was defined by

$$M_V^{\rm theo}(T_{\rm eff}, m) = M_{\rm bol}(T_{\rm eff}, m) - {\rm B.C.}(T_{\rm eff}, m). \tag{5.4.1}$$

The contour plots for $|M_V^{\rm obs} - M_V^{\rm theo}|$ are shown in Fig. 5.7 for the two possible core compositions. For both compositions, a satisfactory minimum could be reached only for parts of the range of effective temperatures between 30 000 and 50 000 K because the tables were limited to an upper value of $\log g = 9.5$ for the case of the CO cores ($\log g = 9.5$ corresponds to a mass of 1.37 $\rm M_\odot$ for 30 000 K and a mass of 1.46 $\rm M_\odot$ for 50 000 K) and to an upper limit of 1.28 $\rm M_\odot$ for the ONe models.

We calculated the minimum of $|M_V^{\rm obs} - M_V^{\rm theo}|$ for a given mass of our range of effective temperatures; when a mass solution could not be reached inside the calculated grids, we extrapolated the theoretical magnitudes.

For an effective temperature of 30 000 K, we estimated masses of 1.32 ± 0.02 (CO core) and 1.28 ± 0.02 (ONe core). Our CO-core calculations are consistent with the estimates of 1.31-1.37 $\rm M_\odot$ (Ferrario et al., 1997), who assumed a distance of 30 pc. The highest temperature for which we could obtain a solution in the $|M_V^{\rm obs} - M_V^{\rm theo}|$ diagram is about 48 000 K from which we inferred a mass of 1.46 $\rm M_\odot$. Any additional extrapolation may introduce substantial uncertainty because we are then approaching the Chandrasekhar limit.

In the grid of theoretical values for ONe cores, we performed significant extrapolation to obtain solutions above 30 000 K (see Fig. 5.8). For $T_{\rm eff} = 30\,000$ K, we obtained a mass of 1.28 $\rm M_\odot$ and inferred an error of ± 0.015 from the uncertainty in the observed visual magnitude and the parallax. For an effective temperature of 50 000 K, we derived 1.38 $\rm M_\odot$ with a slightly higher error estimate of 0.020 $\rm M_\odot$ due to the uncertainty of the extrapolation. The results are summarised in Table 5.8.

We applied the same procedure to LB 9802 by using our new parallax measurements and the information from the literature outlined in Table 5.3. Our mass estimate for the visual magnitude given by Barstow et al. (1995) is consistent with the former results (Ferrario et al., 1997; Kawka et al., 2007, see Table 5.9) although we find that our calculations with the visual magnitude provided by Kawka et al. (2007) is incompatible with our mass determination if we assume that the spectroscopically determined masses for LB 9802 are correct.

[1] http://www.astro.umontreal.ca/~bergeron/CoolingModels
[2] http://www.fcaglp.unlp.edu.ar/evolgroup/tracks.html

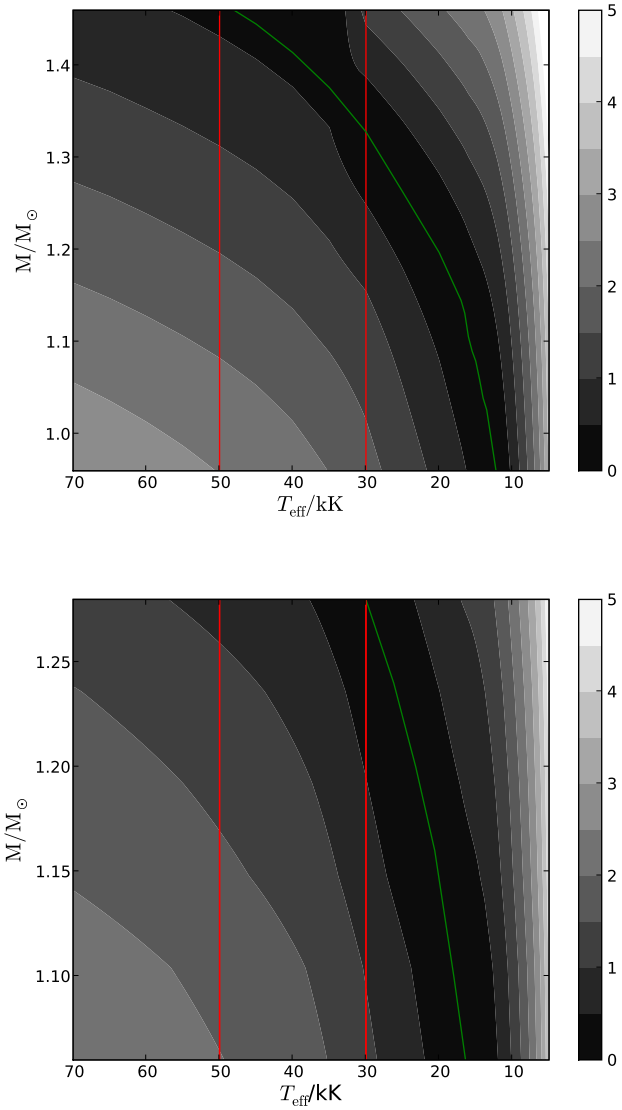

Figure 5.7: Contour plots for $|M_V^{\rm obs} - M_V^{\rm theo}|$/mag as a function of mass in $\rm M_\odot$ and $T_{\rm eff}$ for CO (top), ONe (bottom) core compositions constructed according to Eq. 5.4.1 and theoretical models from Wood (1995), Holberg & Bergeron (2006) for the CO models, and Althaus et al. (2005, 2007) for the ONe models. The bar to the right indicates the colour coding for the magnitude differences, the line in the darkest region $|M_V^{\rm obs} - M_V^{\rm theo}| < 0.5$ mag delinating $M_V^{\rm obs} - M_V^{\rm theo} = 0$ and the vertical lines the possible range of effective temperatures (30 000-50 000 K).

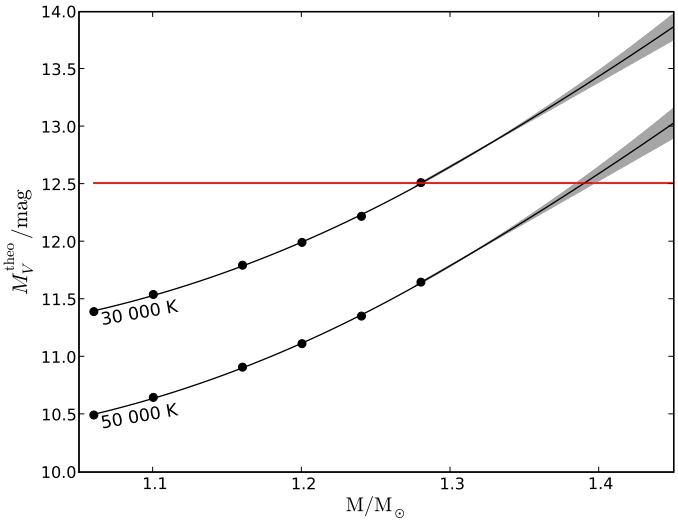

Figure 5.8: The mass of RE J 0317-853 versus absolute V magnitudes for an ONe white dwarf. The different curves correspond to the effective temperatures 30 000-50 000 K. Above 1.28 $\mathrm{M}_\odot$, we have to perform an extrapolation for $T_{\rm eff} > 30\,000$ K. Since we cannot strictly estimate the extrapolation error, we visually added some uncertainty to the extrapolated values, which was subsequently used to estimate the errors in Table 5.8. The horizontal red line denotes the "observed" M_V.

With the knowledge of the $M_{\rm bol}$ for a given mass, the radius can be directly estimated at a given $T_{\rm eff}$. The radius estimates yield slightly different values when two core models are considered (see Table. 5.8). This is caused assuming the assumption for the hydrogen layer mass to be $M_{\rm H}/M_* = 10^{-4}$ in the CO cooling models (Wood, 1995) versus the $M_{\rm H}/M_* = 10^{-6}$ content in the ONe cooling models (Althaus et al., 2005). This produces different luminosities for a given effective temperature.

5.4.2 Age determination of RE J 0317-853 and LB 9802

The assessment of the cooling ages of RE J 0317-853 and LB 9802 is important to the understanding of the evolutionary history of the system. It was possible to evaluate the cooling ages of both objects with the mass estimates that we determined.

For our estimations, we used the grids of white dwarf cooling sequences for CO and ONe cores (e.g. Wood, 1995; Benvenuto & Althaus, 1999) for their respective range of grid parameters; for masses above the available values, we extrapolated the age values in a way similar to that for the visual magnitudes (see Figs. 5.8 and 5.9).

Surprisingly, the difference in the cooling age of the two binary components is smaller than formerly estimated. For both assumed chemical compositions, the cooling age of the non-magnetic white dwarf LB 9802 is within the error bars of the cooling age of the magnetic and very massive RE J 0317-853 (see Tables 5.8 and 5.9). For the case of an ONe core with an effective temperature as high as 50 000 K, our conclusion is poorly constrained due to the extremely large uncertainties introduced by the extrapolation.

Previous age estimates were unreliable because they inferred a cooling age of RE J 0317-853 shorter than that of LB 9802, simply based on its higher effective temperature. If we use the elementary theory of cooling by Mestel (1965) assuming for a fixed effective temperature of

Table 5.8: Mass and age estimations for RE J 0317-853 using different core compositions and temperatures. The differences in radius estimates are caused by the different hydrogen content for different core models (see Sec. 5.4.1).

Core	$T_{\rm eff}$/K	mass/ $\mathrm{M}_\odot$	radius/$0.01\,\mathrm{R}_\odot$	$t_{\rm cooling}$/Myr
CO	30 000	1.32 ± 0.020	0.405 ± 0.011	281^{+36}_{-31}
	50 000	> 1.46	0.299 ± 0.008	> 318
ONe	30 000	1.28 ± 0.015	0.416 ± 0.011	303^{+40}_{-38}
	50 000	1.38 ± 0.020	0.293 ± 0.008	192^{+110}_{54}

Table 5.9: Mass and age estimations for LB 9802 using different V magnitudes in the literature and an average effective temperature of 16 000 K.

V/mag	mass/ $\mathrm{M}_\odot$	$t_{\rm cooling}$/Myr
14.11[1]	0.84 ± 0.05	279^{+68}_{-39}
13.90[2]	0.76 ± 0.05	223^{+36}_{-30}

[1] using the visual magnitude from Barstow et al. (1995); [2] using the visual magnitude from Kawka et al. (2007)

the white dwarf, the cooling age is a function of the mass and radius $t_{\rm cool} \propto M/R^2$. This means that the cooling age for low-mass white dwarfs ($< 0.5\ \mathrm{M}_\odot$) is simply proportional to mass $M^{5/3}$. As the mass of the white dwarf approaches the Chandrasekhar limit the radius asymptotically approaches zero, which means that ages for a given effective temperature depend even more strongly on the mass.

The masses estimated here are quite close to the Chandrasekhar limit ($\geq 1.30\ \mathrm{M}_\odot$) where post-Newtonian corrections should be considered for the stellar equilibrium (Chandrasekhar, 1964; Chandrasekhar & Tooper, 1964). However, these corrections mostly affect the dynamical stability of the star, leading to collapse before reaching the Chandrasekhar limit, but induce only small corrections to mass-radius relationship. This is because the estimated radii are three orders of magnitude larger than the Schwarzschild-radius: $GM/c^2 R_{WD} \sim 10^{-3}$. Hence, we do not expect any effect on our mass determinations, as also noted by Koester & Chanmugam (1990).

5.5 The Evolutionary History of the LB 9802 and RE J 0317-853 System

The projected distance of 210 AU between the two white dwarfs and their small relative proper motion suggest that they are companions and therefore share a common origin. The ages of both objects should therefore be equal or comparable within the error bars; this condition must be fulfilled for the correct evolutionary schemes of both white dwarfs.

The case of LB 9802 is straightforward because its evolutionary history is not complicated by either a strong magnetic field or an extreme mass. Therefore, the simple single-star evolution of LB 9802 places constraints on the total age of RE J 0317-853.

As mentioned above, previous analyses suggested a younger age for RE J 0317-853 than LB 9802 and for this reason the system was assumed to have an "age dilemma" (Ferrario et al., 1997). Therefore, an alternative scenario was proposed in which RE J 0317-853 is a result of the merging of two white dwarfs that have lower-mass progenitors.

5.5.1 Single-star origin of RE J 0317-853

With our new results, we undertook a more precise investigation. We firstly considered the single-star scenario for RE J 0317-853. To determine the total age of LB 9802 and RE J 0317-853 from the zero-age main-sequence (ZAMS) to their current stage, we used the latest semi-empirical initial-to-final-mass relations (IFMR) (Casewell et al., 2009; Salaris et al., 2009) to estimate their initial masses. By considering a diverse range of the theoretical schemes to calculateg the IFMR (metallicity, overshoot parameter, etc.), we deduced the progenitor mass of LB 9802 to be in the range $4.0 - 4.5\ \mathrm{M}_{\odot}$.

For the extremely high (final) mass of RE J 0317-853, the corresponding IFMR is quite uncertain. Theoretically, it was shown that 9-10 $\mathrm{M}_{\odot}$ mass stars would evolve into massive oxygen-neon (ONe) white dwarfs because of the off-centred carbon ignition in the partially degenerate conditions of their cores (Ritossa et al., 1996; García-Berro et al., 1997). With these constraints in mind, we consider more carefully a possible range of initial masses between 8 and 10 solar masses.

The total age (time on the main-sequence plus the white dwarf cooling time) of LB 9802 depends strongly on its initial mass. For the $0.84\ \mathrm{M}_{\odot}$ mass LB 9802, the initial masses in the range $4.0 - 4.5\ \mathrm{M}_{\odot}$ yield main-sequence lifetimes of 170-130 Myr (the progenitor ages were calculated using the evolutionary tracks from Bertelli et al. (2009) for solar metallicity). This means that the total evolutionary age of LB 9802 is in the range $410 - 450$ Myr.

With 40-30 Myr, the pre-white-dwarf lifetime is extremely short for progenitor masses in the range between 8 and $10\ \mathrm{M}_{\odot}$, respectively. For an effective temperature of $30\,000$ K and our resulting mass of $1.28 - 1.32\ \mathrm{M}_{\odot}$ for RE J 0317-853 (which would be the progeny of a 8 $\mathrm{M}_{\odot}$ star, see Casewell et al., 2009; Salaris et al., 2009), we derive total ages in the range $320 - 340$ Myr.

If alternatively we assume an effective temperature of $50\,000$ K for RE J 0317-853 and a CO core, we end up with a total lifetime of ≈ 350 Myr; for the ONe core case, the corresponding value would be ≈ 220 Myr. We reiterate that our estimate for the errors is rather large in the ONe case at $50\,000\,K$ (see Table 5.8) because of the uncertainties in the extrapolation. Hence, omitting the case with ONe core at $50\,000$ K, we can say that the total age of RE J 0317-853 is in the range $320 - 350$ Myr.

There are additional theoretical uncertainties in the IFMR due to magnetism and rapid rotation that should be important for an extreme case such as RE J 0317-853. The effect of both of these factors on the IFMR has been the subject of some discussion. Dominguez et al. (1996) argued that rapid rotation has a positive effect on the core growth, such that a rapidly rotating star of mass 6.5 $\mathrm{M}_{\odot}$ may produce a white dwarf of mass 1.1-1.4 $\mathrm{M}_{\odot}$. Observational evidence of this was found by Catalán et al. (2008). RE J 0317-853 is the fastest rotating isolated white dwarf and this rotation may be a relic of a rapidly rotating progenitor.

The assumption of a 6.5 $\mathrm{M}_{\odot}$ mass star as the progenitor does not relieve the "age dilemma" considerably since the progenitor age for this case is ~ 70 Myr, which does not differ much from the 40-30 Myr estimated for 8-10 $\mathrm{M}_{\odot}$ mass stars. Catalán et al. (2008) also argued that MWDs are relatively more massive than expected on the basis of their

inferred progenitors via the IFMR of non-magnetic white dwarfs. However, Wickramasinghe & Ferrario (2005) and Ferrario et al. (2005b) both concluded based on their population synthesis studies this effect is of only minor importance. Since the effect of rotation and magnetism on the evolutionary age is unclear or rather small, we did not consider them in our age estimations.

Based on these considerations, we conclude that the total age of LB 9802 is $410 - 450$ Myr at least ~ 100 Myr older than the respective value for RE J 0317-853 ($320 - 350$ Myr). This discrepancy implies that the single-star evolution scenario might not be applicable to RE J 0317-853.

However, the mass estimates leading to the cooling ages determined above neglected the influence of magnetism. The magnetic nature of RE J 0317-853 is likely to affect the determination of its mass because of the mass-radius relation. Ostriker & Hartwick (1968) discussed the effect of magnetism and rapid rotation on white dwarfs. Both magnetism and rotation act against the gravitation, causing an extended radius; hence, white dwarfs with strong internal magnetization have larger radii for a given mass.

To calculate the cooling tracks from synthetic colours and magnitudes of white dwarfs, mass-radius determinations are used implicitly. Hence our estimates of the masses and ages are impaired by the lack of mass-radius relations taking into account the effect of the magnetic field. We have already discussed the influence of magnetism on the structure in Sec. 1.2.1. According to equation 1.2.34 where the radius is increased by a factor $\mathrm{e}^{\frac{3}{3-n}\delta} = \mathrm{e}^{3.5\delta}$, where δ is the ratio of the magnetic energy to the gravitational energy of the star, and n is the polytropic index (Shapiro & Teukolsky, 1983). In the case of RE J 0317-853, an internal magnetization of $< B >= 10^{12} - 10^{13}$ G seems plausible; this would imply that $\delta \approx 0.1$ and therefore an increase in the radius by $\sim 40\%$. The influence of magnetism was first disccused by Ostriker & Hartwick (1968) for the case of a white dwarf of 1.05 $\mathrm{M}_{\odot}$mass. Since RE J 0317-853 has an even higher mass, n is in this case close to 3 and thereby the increase in radius for a given mass might be even higher than $\sim 40\%$.

For an effective temperature of 30 000 K, our measured radius is $0.410 \times 10^{-2}\ \mathrm{R}_{\odot}$, whereas for 50 000 K it is $0.295 \times 10^{-2}\ \mathrm{R}_{\odot}$. When we correct the influence of the magnetic field on the radius we end up with a higher mass than determined in Sect. 5.4.1. If RE J 0317-853 were of higher mass the cooling time would increase so that the age dilemma no longer exists for the assumption of single-star evolution.

As an initial consideration, cooling ages of ~ 400 Myr, which would diminish the age inconsistency, are possible for RE J 0317-853, if it has a mass of 1.32 $\mathrm{M}_{\odot}$ rather than 1.28 $\mathrm{M}_{\odot}$ (ONe case; 0.04 $\mathrm{M}_{\odot}$ discrepancy), or 1.38 $\mathrm{M}_{\odot}$ rather than 1.32 $\mathrm{M}_{\odot}$ (CO case; 0.06 $\mathrm{M}_{\odot}$ discrepancy), for an effective temperature of $30\,000$ K. The corrected radius of $R_0 = 0.32 \times 10^{-2}\,\mathrm{R}_{\odot}$ implies a mass of 1.38 $\mathrm{M}_{\odot}$ from the mass-radius relationship. This value implies that the corrections are plausibly high enough to account for the missing evolutionary age as discussed above.

If we consider $T_{\mathrm{eff}} = 50\,000$ K for RE J 0317-853, the mass estimates based purely on the total evolutionary age of the system would imply values well above the Chandrasekhar limit. Although it is known that strong internal magnetic field strengths also modify the Chandrasekhar limit (Ostriker & Hartwick, 1968), it is still difficult to quantitatively assess the masses and their effect on cooling ages in this regime.

5.5.2 Binary origin of RE J 0317-853

The merger scenario for ultra-massive white dwarfs was initially proposed by Bergeron et al. (1991) for GD 50, Marsh et al. (1997) proposed that this scenario could explain the properties of the hot and massive white dwarf population. For RE J 0317-853, it was similarly proposed to explain both the high angular momentum and high mass of this star (Ferrario et al., 1997). Vennes et al. (2003) also suggested that the scenario could produce a strong and non-dipolar magnetic field. They argued qualitatively that the high angular momentum is a result of the total orbital momentum of a coalescing binary and that the strong non-dipolar magnetic field can be generated by dynamo processes due to the differential rotation caused in turn by the merging.

The type of binary evolution that can lead to a double-degenerate system has been investigated in detail, since it represents a channel for producing SN Ia explosions (Webbink, 1984; Iben & Tutukov, 1984). In this scenario, a binary system consisting of two intermediate-mass stars (5-9 $\mathrm{M}_{\odot}$) goes through one or two phases of a common envelope (CE) and evolves to a double white dwarf system. If the final double-degenerate system has orbital periods in the range between 10 s and 10 h, it will lose angular momentum through gravitational radiation and merge in less than a Hubble time. The merging process leads to a massive central product with a surrounding Keplerian disk. Depending on the total mass of the system, the temperature in the envelope and the accretion to the merger product, the system can evolve either to a SN Ia or by an accretion-induced collapse (AIC) to a neutron star. When the total mass of the system is insufficient to create the density and the temperature to burn carbon under degenerate conditions, the system will end up as an ultra-massive white dwarf.

To test whether this scenario is indeed applicable to the case of RE J 0317-853, we have to trace back to the point in the stellar evolution where the merging could have happened, using the cooling age of RE J 0317-853 and subtracting it from the total evolutionary age of LB 9802. Using this progenitor age estimate and the theoretical constraints from the theory of binary star evolution, we can estimate the masses of the possible merging counterparts.

We begin by estimating the mass of the (secondary) binary component that needs longer to become a white dwarf. To obtain a lower limit to its mass, we assume the longest time from the main-sequence to the merging process considering the mass transfer episodes predicted by the binary scenario. After both white dwarfs are formed, the time needed for the binary to merge due to gravitational radiation depends strongly on the orbital parameters and mass of the double-degenerate system. Depending on the properties of the system, coalescence can be as fast as 0.1 Myr or as slow as 200 Myr (Iben & Tutukov, 1984). To obtain a lower limit to the total evolutionary time for the system, we neglect the time needed for the double-degenerate system to coalesce.

Iben & Tutukov (1985) discussed the evolution of 3 to 12 $\mathrm{M}_{\odot}$ stars that experience two phases of mass transfer. The phase of the mass transfer can take as long or even longer than the time the star spends on the main-sequence. For a 5 $\mathrm{M}_{\odot}$ star, the main-sequence phase lasts ∼90 Myr (Bertelli et al., 2009), while in the binary-evolution scenario it takes 114 Myr from the main sequence until the formation of the white dwarf. This means that ∼200 Myr are needed for a 5 $\mathrm{M}_{\odot}$ star to evolve into a white dwarf rather than the 100 Myr that we assumed for single-star evolution.

The possible cooling ages considered for LB 9802 (280 Myr) and RE J 0317-853 (280 - 320 Myr, when we assume an effective temperature of about 30 000 K) imply that the maximum time needed for binary evolution is at most the main-sequence age of LB 9802,

which is 130-170 Myr (for 4.0-4.5 $\mathrm{M}_{\odot}$). The upper limit of 170 Myr is comparably short relative to the 230 Myr of binary evolution time. This provides a lower mass limit for the system. The resulting mass of a white dwarf that is a product of a 5 $\mathrm{M}_{\odot}$ star in this binary evolution scheme is 0.752 $\mathrm{M}_{\odot}$ (Iben & Tutukov, 1985), which is lighter than inferred from the IFMRs determined for single-star evolution.

Since the pre-white-dwarf evolution is too long for an initial 5 $\mathrm{M}_{\odot}$, star we need a more massive progenitor hence should end up with a secondary white dwarf more massive than 0.752 $\mathrm{M}_{\odot}$. For the primary star, we assume that it has only a slightly higher mass than the secondary to deduce a lower limit to the total coalescing mass.

However, this assumption leads to serious inconsistencies, because the total mass of two components would result in more than $1.5\ \mathrm{M}_{\odot}$ being above the masses estimated for RE J 0317-853. This lower limit is also robust when we consider mass loss. Firstly, smoothed particle hydrodynamic (SPH) simulations show that only a very small mass loss is expected during merging ($\sim 10^{-3}\ \mathrm{M}_{\odot}$, see e.g. Lorén-Aguilar et al., 2009), and secondly, we expect almost all of the Keplerian disk to be accreted on the merger product. Wind mass-loss from the Keplerian disk is assumed to be lower than 10% of the accretion rate (Mochkovitch & Livio, 1990); this means that at least 90% of the disk is expected to be accreted. Lorén-Aguilar et al. (2009) also estimate $0.1-0.3\ \mathrm{M}_{\odot}$ for the disk masses, which would imply a total mass loss of $\leq 0.01-0.03\ \mathrm{M}_{\odot}$.

We note that infrared studies have detected possible disks surrounding massive white dwarfs (Hansen et al., 2006). This included RE J 0317-853 for which no convincing evidence of a disk was found in the *Spitzer* IRAC bands (see also Farihi et al., 2008). If RE J 0317-853 were the product of a merger of two white dwarfs, all of the matter from the Keplerian disk should have been accreted. In this scenario, total mass limits well above the estimated RE J 0317-853 mass cannot be avoided. This estimation eliminates the possibility of a binary origin for RE J 0317-853 with a current effective temperature as low as 30 000 K.

However, if the total mass of the binary system does not exceed the estimated value for RE J 0317-853, the time needed for the accretion of all the material from the disk is much longer than the evolutionary timescale. The accretion rate is expected to be $\leq 10^{-12}$ $\mathrm{M}_{\odot}$/yr for flows with laminar viscosity (Lorén-Aguilar et al., 2009). For disk material of $0.1-0.3\ \mathrm{M}_{\odot}$, that its complete accretion time of $1-3\times10^{5}$ Myr is three orders of magnitude longer than the evolutionary timescale.

If the binary scenario were correct, the Keplerian disk should have been observed unless the accretion rate of the disk was much higher than theoretically predicted. Only accretion rates higher than $10^{-10}\ \mathrm{M}_{\odot}$/yr would lead to a total disappearance of the disk.

When two equal-mass white dwarfs merge, the symmetry of the process leads to a rotating ellipsoidal composed of CO around the white dwarf rather than a Keplerian disk. If RE J 0317-853 were still in the process of accretion we would have observed CO in the spectra but this is not the case. On the other hand, if all the material of the surrounding ellipsoid had already been accreted (mass-loss can be neglected as discussed above) the mass of RE J 0317-853 would be higher than observed (above the Chandrasekhar limit).

We also considered the possible effect on the cooling ages of additional heating of the white dwarf core due to the merging process. Recent SPH simulations indicate the possibility of heating to $\sim 10^{9}\,K$ in the core (Yoon & Langer, 2005; Lorén-Aguilar et al., 2009). However, because of the $T^{-5/2}$ dependence of the cooling age according to the elementary theory (Mestel, 1965), the effect of this extra heating on the cooling ages is expected to be small (~ 2 Myr) and can be neglected.

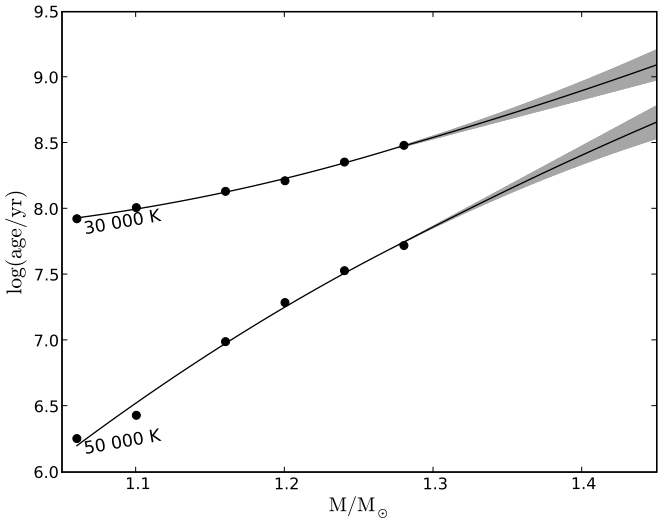

Figure 5.9: The mass of RE J 0317-853 versus logarithmic age in years for an ONe core white dwarf. The different curves correspond to the effective temperatures 30 000-50 000 K. Since we cannot strictly estimate the extrapolation error we visually added some uncertainty to the extrapolated values, which was subsequently used to estimate the errors in Table 5.8.

When we consider the ONe core case for an effective temperature of $50\,000$ K, leading to an average cooling age of ~ 190 Myr, we end up with an upper limit to the evolution time of the secondary of 220-260 Myr; the 40 Myr spread in evolutionary time is only due to the uncertainty in the LB 9802 progenitor mass (between 4.0-4.5 $\mathrm{M}_{\odot}$). Our estimated upper limit to the total age is comparable to the evolutionary timescale of a 5 $\mathrm{M}_{\odot}$ star in a binary system as considered above. However, the cooling time estimate for RE J 0317-853 in this case is considerably uncertain (see Table 5.8) due to the extrapolation. Within these large error margins, we would in principle be able to obtain a sub-Chandrasekhar mass for the merger product, but this process is very unlikely when we consider the time needed for the white dwarfs to merge ($10 - 100$ Myr Iben & Tutukov, 1984). Nevertheless, the possibility of a binary origin for an ONe core RE J 0317-853 at $T_{\mathrm{eff}} = 50\,000$ K cannot be entirely excluded.

We note that the effect of magnetic field strength on the structure of the white dwarf, considered in Sect. 5.5.1 is also important to binary evolution. The implementation of this effect leads to an inference of slower cooling for RE J 0317-853 as in the single-star scenario. This would yield shorter progenitor timescales for a constant evolutionary time, leading to the lower limits on the total mass of the coalescing white dwarfs becoming even more massive. This diminishes again the probability of binary evolution for $T_{\mathrm{eff}} = 30\,000$ K. However, for $T_{\mathrm{eff}} = 50\,000$ K the uncertainties still permit the possibility of merging. Furthermore, the effect of magnetism on the stellar structure ensure that this scenario remains favourable due to the higher Chandrasekhar mass limit (Ostriker & Hartwick, 1968; Shapiro & Teukolsky, 1983).

5.6 Discussion and Conclusions

RE J 0317-853 belongs to the very rare population of ultra-massive white dwarfs with masses exceeding $1.1\ \mathrm{M}_{\odot}$. The competing theoretical explanations of the origin of these white dwarfs are single-star evolution versus the merging of two degenerate stars. Without considering mass-loss during stellar evolution, it is known that an upper limit of $1.1\ \mathrm{M}_{\odot}$ for the final white dwarf mass would exist because of the ignition of carbon in the core of the progenitor star. However, taking into account the effect of mass loss, high-mass ONe-core white dwarfs can be produced (see Weidemann, 2000, for a review). Furthermore, it was proposed that even 9 to 10 $\mathrm{M}_{\odot}$ mass stars evolve into ONe core white dwarfs of mass 1.26 and 1.15 respectively, because of the off-centred carbon ignition in the partial degenerate conditions of their cores (Ritossa et al., 1996; García-Berro et al., 1997).

In the light of our current results, we have undertaken a more precise investigation of the possible evolutionary scenarios for RE J 0317-853. We have shown that the cooling ages are almost the same for the two components, contrary to the the previous studies (Ferrario et al., 1997). The detailed analysis very much depends on a precise determination of the effective temperature; for $T_{\mathrm{eff}} = 30\,000\,\mathrm{K}$, we can use the calculations by Wood (1995) and Benvenuto & Althaus (1999) and conclude that within the limits of the uncertainties RE J 0317-853 is at least as old as LB 9802. For a consistent interpretation of the system, we also have to take into account the time scales of the pre-white-dwarf evolution. The more massive progenitor of RE J 0317-853 should evolve more rapidly than the progenitor of LB 9802. Taking this into account, the total age difference between LB 9802 and RE J 0317-853 amounts to $\sim 100\,\mathrm{Myr}$ if single-star evolution is considered.

On the other hand, the alternative binary merger scenario proposed by Ferrario et al. (1997) and Vennes et al. (2003) as a solution to this age dilemma has severe drawbacks. When the evolutionary timescales are considered, the progenitor age of RE J 0317-853 yields lower limits on the mass of the merger product that is considerably higher than its estimated mass for all cases. For RE J 0317-853, we have large uncertainties in the cooling age estimate only for an effective temperature of $50\,000\,\mathrm{K}$, so that we cannot fully exclude the binary scenario.

We have also considered the effects of the magnetic fields on both of the scenarios. Magnetic fields cause an increase in radius, hence an underestimate of the mass, which would imply longer cooling ages than estimated. For the case of $T_{\mathrm{eff}} = 30\,000\,\mathrm{K}$, the influence of magnetism makes the single-star scenario possible while further eliminating the binary merger origin; for the high T_{eff} of $50\,000\,\mathrm{K}$, even the inclusion of magnetic effects does not ensure possibility of a single-star; furthermore the binary scenario remains possible within our large uncertainties.

In addition to the effects of magnetism on the mass determinations under the assumption of $T_{\mathrm{eff}} = 30\,000\,\mathrm{K}$, there is evidence of influence of magnetism also when $T_{\mathrm{eff}} = 50\,000\,\mathrm{K}$ is assumed since the estimated masses are larger than field-free Chandrasekhar mass. We know from Sec. 1.2.1 when the effects of GTR and Hamada & Salpeter (1961) corrections are simultaneously employed to a carbon core white dwarf, the limiting mass reduces to $1.367\ \mathrm{M}_{\odot}$ (Cohen et al., 1969). For our cases of CO and ONe cores, due to the increased atomic weight per electron μ_{eff}, the limiting mass should even be lower. This implies all of the determined masses at $T_{\mathrm{eff}} = 50\,000\,\mathrm{K}$ are larger than the modified Chandrasekhar limit. Since we do not expect an error in our mass estimations due to the lack of post-Newtonian treatment (see Sec. 5.4.2), these large masses can be considered as

evidence of a Super-Chandrasekhar mass white dwarf, possibly with structures supported by strong internal magnetic fields (see equation 1.2.33).

With our measurement of the parallaxes and relative proper motion of RE J 0317-853 and LB 9802 with HST's FGS, we have established that the wide binary system of these two stars is indeed a bound system. We have estimated the masses and ages of RE J 0317-853 and LB 9802 based on the current white dwarf cooling tracks for different core compositions and hydrogen layer masses. Owing to the magnetic nature of this object, the temperature determination of RE J 0317-853 remains difficult.

In this work we were able to fit the formerly unexplained circular polarization peak of RE J 0317-853 with a cyclotron absorption feature, through successful modeling of the uniform low-field phase. This is the first time, cyclotron absorption is observed in MWD atmospheres. The effect of cyclotron opacities on the MWD atmospheric structure has been a topic of interest especially for GD 229 (Zheleznyakov et al., 1996). Also the differences in the $T_{\rm eff}$ diagnostics for different wavelengths in the spectrum of GRW+70°8247, PG 1031+234 and also GD 229 was attributed to the radiative pressure caused by cyclotron absorption (Zheleznyakov & Serber, 1994).

It should be worth noting that our models do not explain the variability, possibly due to our single temperature models. Barstow et al. (1995) have suggested that the variability of the RE J 0317-853 can be explained by radiation-drivon diskon model. In this model, when the cyclotron peak corresponds to the black body peak at the spectrum of a MWD, the atmosphere is affected by the radiation pressure and incidentally causing a disk to form around the magnetic equator of the star which obscures the light, causing the overall variability (Mitrofanov & Pavlov, 1982; Bespalov & Zheleznyakov, 1990; Zheleznyakov et al., 1996). However the uniform ~ 185 MG is expected not to influence the atmospheric structure, since the thermal peak of the RE J 0317-853 spectrum is even bluer than far-ultra-violet ranges.

Another possibility for modification in the atmospheric structure is the influence of magnetism on the hydrostatic balance. A force-free magnetic dipole does not influence the force balance in the atmosphere (Stepien, 1978), and the only contribution through the decay of the dipolar term which was proposed by Landstreet (1987) has been ruled out by Jordan (1992). However it was shown that in the case of even a small deviation from the force-free dipolar structure, it is plausible that the force balance in the atmosphere is affected (Fendt & Dravins, 2000).

In addition to the discoveries of magnetic spots on MWDs, and the ubiquitous nature of non-dipolarity in the SDSS MWD population (Chapter 2), we have shown that the strongly variable RE J 0317-853 has a field geometry that strongly deviates from a dipole. The amassing information on the non-dipolarity in the MWD population (Euchner et al., 2005, 2006; Beuermann et al., 2007, see also Sect. 2.3.1) combined with the temperature inconsistencies in the broadband spectrum, prompts a revisit to the hydrostatic structure of MWD atmospheres in the future.

In the absence of precise $T_{\rm eff}$ estimates, we have considered the highest and lowest possible temperature for our mass and radius determinations. With these estimates we have discussed the evolutionary history and the possible origin of RE J 0317-853. Our results show that for a solution at the cooler end of the possible range of effective temperatures for RE J 0317-853, the binary scenario can be excluded within our uncertainties. We also proposed that the "age dilemma" can be solved for this case when the effects of the magnetism on the structure of the white dwarf is considered. Only at the very hot end of

our uncertainty range of effective temperatures, the binary origin scenario becomes more plausible.

Summary and Outlook

In this work we assessed the validity of hypotheses on the origins of MWDs through population statistics and analyses of individual objects. For this aim, we have exploited the database of SDSS, used high resolution time-resolved spectro-polarimetric observations, devised one new method of age determination of MWDs and improved the theory of magnetized atmospheres.

In Chapter 2, we analyzed 141 DAHs, 97 of which had been previously analyzed and 44 of which were being newly discovered. Through our work, the number of known MWDs have more than tripled. In addition, for the first time, the off-centered magnetic dipole models have been applied to such a large set of data. Our consistent modeling over the data releases showed that at least 50% of the SDSS DAH population, has a tendency for deviations from centered dipole field geometry. This is indicative of a magnetic field geometry that is more complex than a centered dipole, which is consistent with the field distributions of Ap/Bp stars (Bagnulo et al., 2002). Although this fact supports the "fossil field" hypothesis, the distribution of magnetic field strengths imply that the magnetic flux cannot fully be conserved if we assume the progenitors of MWDs solely as Ap/Bp stars.

To assess the evolutionary histories of individual objects we need distances, and in the absence of parallax measurements, we showed in Chapter 3 that it is possible to infer the necessary information through binary counterparts or cluster memberships. We carried out a systematic search for MWDs in clusters for the first time, using such a kinematic approach. We proposed that this method could be used as a way to investigate the influence of magnetism on the mass-loss during stellar evolution. Although our study showed that magnetism results in additional scattering in the IFMR, the results were not sufficient to draw conclusions on the physical mechanisms at this point. While the cluster member WD0836+201 shows evidence of hindered mass-loss, SDSS J1300+5904 which exists in a CPM system seems to have has experienced stronger mass loss. This could be a relic of the uncertainties which are already observed for non-magnetic white dwarfs, especially in the mass regime of SDSS J1300+5904. In Chapter 3, we also suggested that SDSS J0855+1640 should not be considered for the discussion of mass-loss since its ultra-massive nature suggests the history of a binary merger.

In Chapter 5 we used parallax measurements to investigate the various evolutionary scenarios for RE J 0317-853 as a result of the different models with different physical parameters. For all of the scenarios we showed that magnetism might influence the structure, either through changing the mass-radius relation or by increasing the Chandrasekhar mass limit.

Since magnetism is an important contributor to the modeling of RE J 0317-853, we have undertaken a multi-phase spectro-polarimetric analysis of this object. In addition to the ubiquitous nature of non-dipolarity in the SDSS population, we have shown that the

rapidly rotating, massive and highly magnetised object RE J 0317-853 has a field geometry that strongly deviates from a dipole. We have diagnosed the decade long unexplained circular polarization peak as cyclotron absorption with the use of the new plasma formalism derived in detail in Chapter 4. Our analysis shows that the cyclotron feature is indicative of a very homogeneous field structure.

Outlook

The scanning of MWDs in the SDSS sample is not yet complete. For a consistent population synthesis to check the origin of MWDs, especially in the context of single-star evolution and the "fossil field" hypothesis, data on a complete sample is necessary, and the number of reported -although not analyzed- MWDs is rapidly increasing. The increasing statistics prompt interesting questions on the influence of magnetism on stellar evolution. The influence of magnetism on mass-loss and core structure before the carbon ignition are themes which have not been thoroughly investigated in the literature. Additionally, the field decay during the cooling lifetimes of white dwarfs might be plausible. Although the magnetohydrodynamic simulations of stars have recently been undertaken (Braithwaite & Nordlund, 2006; Braithwaite & Spruit, 2004), the theoretical answer is not yet given conclusively. Observations on the basis of $T_{\rm eff}$ versus field strengths, imply that no such correlation exists (see Fig. 2.7), however the assumption of $T_{\rm eff}$ as a proxy for cooling ages is not precisely correct. To test a possible evolution of field strength and field geometry investigations of MWDs on the basis of cooling ages and detailed field structure needs to be taken into account. With this work we improved the number of MWDs with known ages. In the future, the increased statistics be an important incentive for the theoretical studies on the stellar structure.

The consistent calculation of cyclotron cross sections and the magneto-optical parameters through plasma methodology, provides an important diagnostic. The existence of RE J 0317-853 with its confirmed homogeneous field provides the possibility of tests of new physics. Due to the rather robust constraint of magnetic geometry, compliment of the successful diagnosis of the cyclotron feature, different physics can be tested without the worry of complicated magnetic geometry or magnetic smearing of spectral profiles. One such avenue of research would be the search for signals of pseudo-scalar particles in MWD atmospheres. Chelouche et al. (2009) already considered the possibility of photon, pseudo-scalar particle oscillations in the atmospheres of compact objects and calculated the properties of the magnetised plasma. The calculated properties of the MWD atmospheres in this work, enables the implementation of the pseudo-scalar particle influence in the radiation transfer equations. This implies, the atmospheric modeling of MWDs can, in principle, be test beds for direct signals from dark matter candidates and eliminate, if not constrain the masses of pseudo-scalar particles.

Although the magnetic structure of RE J 0317-853 is well understood, the temperature and pressure structure of its atmosphere is still in question. Now that we know the magnetic structure of RE J 0317-853 deviates strongly from a centered dipole, akin to most of the MWD population, the magnetic field in its atmosphere might not be force-free. This means that the force balance in the atmosphere could be influenced by magnetism (Fendt & Dravins, 2000). Although simple models of magnetic structure are not unique, the diagnostics on the magnetic geometry will provide clues on the complicated hydrostatic structure of MWD atmospheres.

One of the problems of our diagnostics of RE J 0317-853 was the lack of consistent

structural modeling near the Chandrasekhar mass limit. This fact is understandable since RE J 0317-853 is probably the most massive white dwarf rivaling only with PG1658+441 which is also magnetic. There are, in total, only four white dwarfs which are more massive than $1.3\ \mathrm{M}_{\odot}$ (additionally WD1653+256 and 1RXSJ0557−1635; Vennes & Kawka, 2008). In one of the hypothesis the ultra-massive MWDs are results of "failed" SNIa explosions, and precise diagnostics of all these objects would be important for testing hypothesis on binary mergers.

The question of ultra-relativistic degenerate stellar structure has its echo in the contemporary SNIa studies where rapid differential rotation delay the carbon detonation, allowing for larger than Chandrasekhar mass explosions (Yoon & Langer, 2005) which are currently observed (Howell et al., 2006). This scenario has been disputed, due to instability of differential rotation which partly results in the generation of magnetic fields (Piro, 2008). Considering the fact that magnetic fields also support against pressure, the interplay of magnetism and angular momentum might be important to answer the questions of inhomogeneity of SNIa lightcurves.

Appendices

Appendix A

The Photometric Properties of Hydrogen-rich Magnetic White Dwarfs in Sloan Digital Sky Survey

Table A.1: Photometric properties of the new confirmed DAHs and their temperatures. The columns indicate the SDSS name of the object; the plate, Modified Julian Date, and fiber ids of the observations; the SDSS photometric magnitudes u, g, r, i, z; and finally the temperatures derived from their colors.

MWD (SDSS+)	Plate-MJD-FiberID	u / mag	g / mag	r / mag	i / mag	z / mag	$T_{\rm eff}$ / K
J023420.63+264801.7	2399-53764-559	18.70	18.38	18.59	18.76	19.03	13500
J031824.19+422651.0	2417-53766-568	18.59	18.23	18.32	18.43	18.67	10500
J032628.17+052136.3	2339-53729-515	18.69	18.93	19.30	19.60	19.61	25000
J033320.36+000720.6	0415-51879-485	17.07	16.52	16.39	16.35	16.44	7000[12]
J074924.91+171355.4	2729-54419-282	18.78	18.78	19.13	19.44	19.64	20000
J075234.96+172525.0	1920-53314-106	18.78	18.44	18.44	18.50	18.64	9000
J080359.93+122943.9	2265-53674-033	17.24	17.23	17.53	17.83	18.08	9000
J081716.39+200834.8	2082-53358-444	18.91	18.34	18.15	18.12	18.23	7000
J083448.63+821059.1	2549-54523-135	18.07	18.32	18.74	19.06	19.49	27000
J083945.56+200015.7	2277-53705-484	18.11	17.83	18.11	18.36	18.66	15000[3]
J085106.12+120157.8	2430-53815-229	17.35	16.96	17.14	17.30	17.56	11000
J085523.87+164059.0	2431-53818-522	18.78	18.55	18.80	19.05	19.32	15500
J085550.67+824905.3	2549-54523-066	18.40	18.60	18.91	19.23	19.46	25000
J091005.44+081512.2	1300-52973-639	17.38	17.54	17.96	18.28	18.65	25000
J091833.32+205536.9	2288-53699-547	18.73	18.41	18.66	18.92	19.22	14000
J093409.90+392759.3	1215-52725-241	18.72	18.35	18.40	18.50	18.55	10000
J094235.02+205208.3	2292-53713-019	18.41	18.42	18.80	19.05	19.26	20000
J100657.51+303338.1	1953-53358-415	19.22	18.83	18.90	19.04	19.18	10000
J100759.80+162349.6	2585-54097-030	18.01	17.70	17.80	17.96	18.19	11000
J101428.09+365724.3	52993-1426-021	19.26	18.87	18.97	19.09	19.43	10500

Table A.1: continued.

MWD (SDSS+)	Plate-MJD-FiberID	u / mag	g / mag	r / mag	i / mag	z / mag	$T_{\rm eff}$ / K
J102220.69+272539.8	2350-53765-543	20.47	20.05	20.16	20.38	20.69	11000
J102239.06+194904.3	2374-53765-544	19.43	19.01	19.01	19.11	19.13	9000
J103532.53+212603.5	2376-53770-534	17.98	17.40	17.23	17.19	17.21	7000[2]
J105709.81+041130.3	0580-52368-274	18.09	17.67	17.58	17.60	17.70	8000
J112030.34-115051.1	2874-54561-512	18.65	18.73	19.05	19.34	19.75	20000
J112257.10+322327.8	1979-53431-512	19.60	19.37	19.50	19.68	19.92	12500
J112328.49+095619.3	1222-52763-625	18.15	17.70	17.74	17.87	18.02	9500
J113215.38+280934.3	2219-53816-329	17.50	16.99	16.88	16.87	16.92	7000[2]
J124836.31+294231.2	2457-54180-112	18.44	17.80	17.59	17.54	17.56	7000[2]
J125434.65+371000.1	1989-53772-41	16.01	15.97	16.35	16.64	16.95	10000
J125715.54+341439.3	2006-53476-332	17.14	16.78	16.81	16.92	17.11	8500
J134820.79+381017.2	2014-53460-236	17.26	17.54	18.04	18.33	18.70	35000
J140716.66+495613.7	1671-53446-453	19.03	19.13	19.43	19.75	19.97	20000
J141906.19+254356.5	2131-53819-317	17.80	17.41	17.46	17.53	17.69	9000
J143019.05+281100.8	2134-53876-423	18.03	17.68	17.68	17.74	17.92	9000
J151130.17+422023.0	1291-52738-615	18.20	17.98	18.01	18.20	18.48	9500
J151415.65+074446.5	1817-53851-534	19.16	18.84	18.88	18.99	18.88	10000
J152401.60+185659.2	2794-54537-410	18.39	18.15	18.34	18.54	18.8	13500
J153843.10+084238.2	1725-54266-297	18.24	17.90	17.94	18.22	18.20	9500
J154305.67+343223.6	1402-52872-145	18.08	18.32	18.75	19.10	19.46	25000
J165249.09+333444.9	1175-52791-095	19.11	18.63	18.63	18.65	18.92	9000

Table A.1: continued.

MWD (SDSS+)	Plate-MJD-FiberID	u / mag	g / mag	r / mag	i / mag	z / mag	$T_{\rm eff}$ / K
J202501.10+131025.6	2257-53612-167	18.91	18.76	19.07	19.28	19.74	17000
J220435.05+001242.9	0372-52173-626	19.66	19.38	19.47	19.54	19.71	22000
J225726.05+075541.7	2310-53710-420	17.09	17.11	17.31	17.44	17.65	40000

[1] HE 0330-0002
[2] The temperature from fits to the color-color diagram is uncertain.
[3] WD 0837+199 (LB 393, EG 61)

Appendix B

Fits to the Spectra of Hydrogen-rich Magnetic White Dwarfs in Sloan Digital Sky Survey

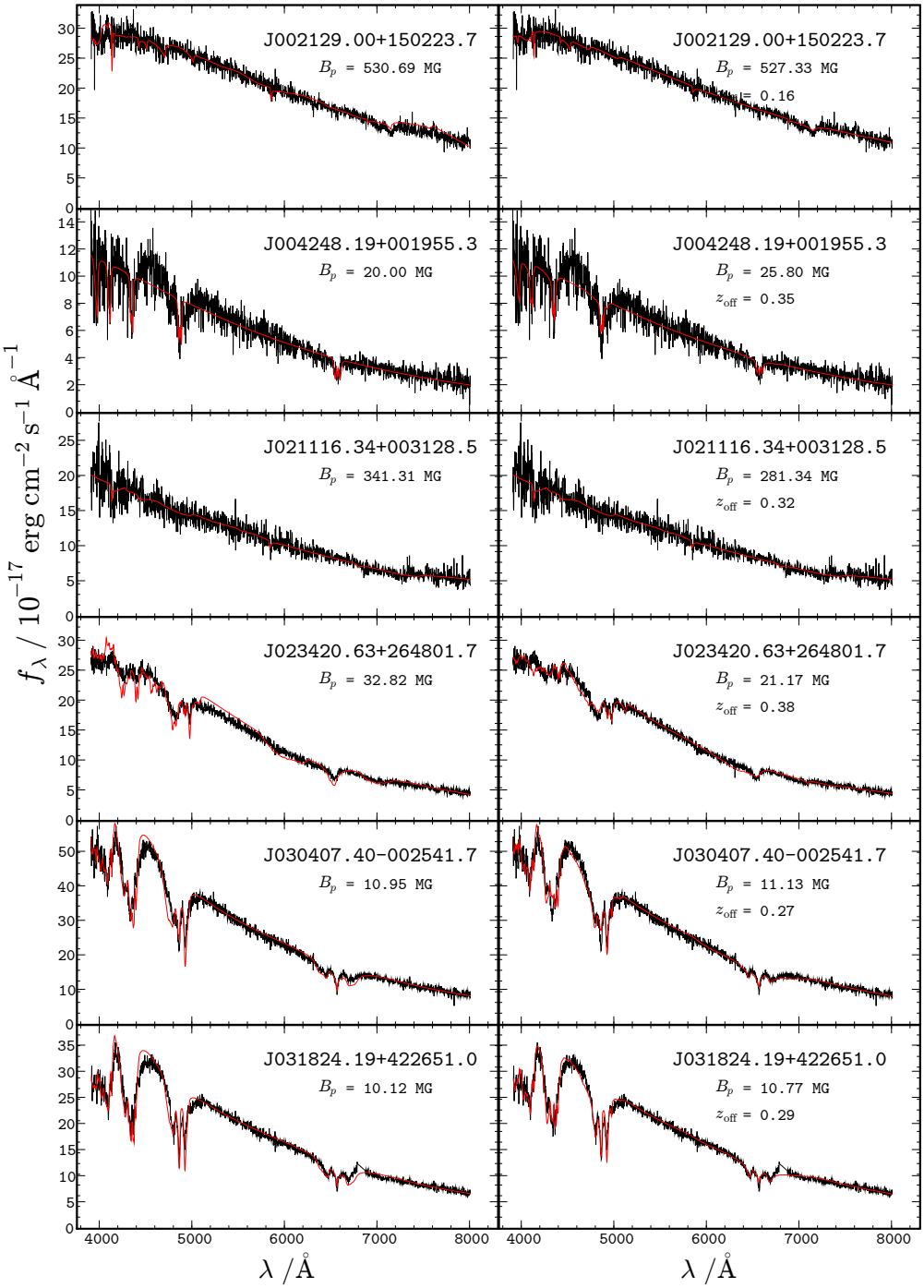

Figure B.1: Fits of observed spectra of DAHs from the SDSS to centered magnetic dipoles with a polar field strength B_p (left) and dipoles shifted by $z_{\rm off}$ stellar radii along the dipole axis (right).

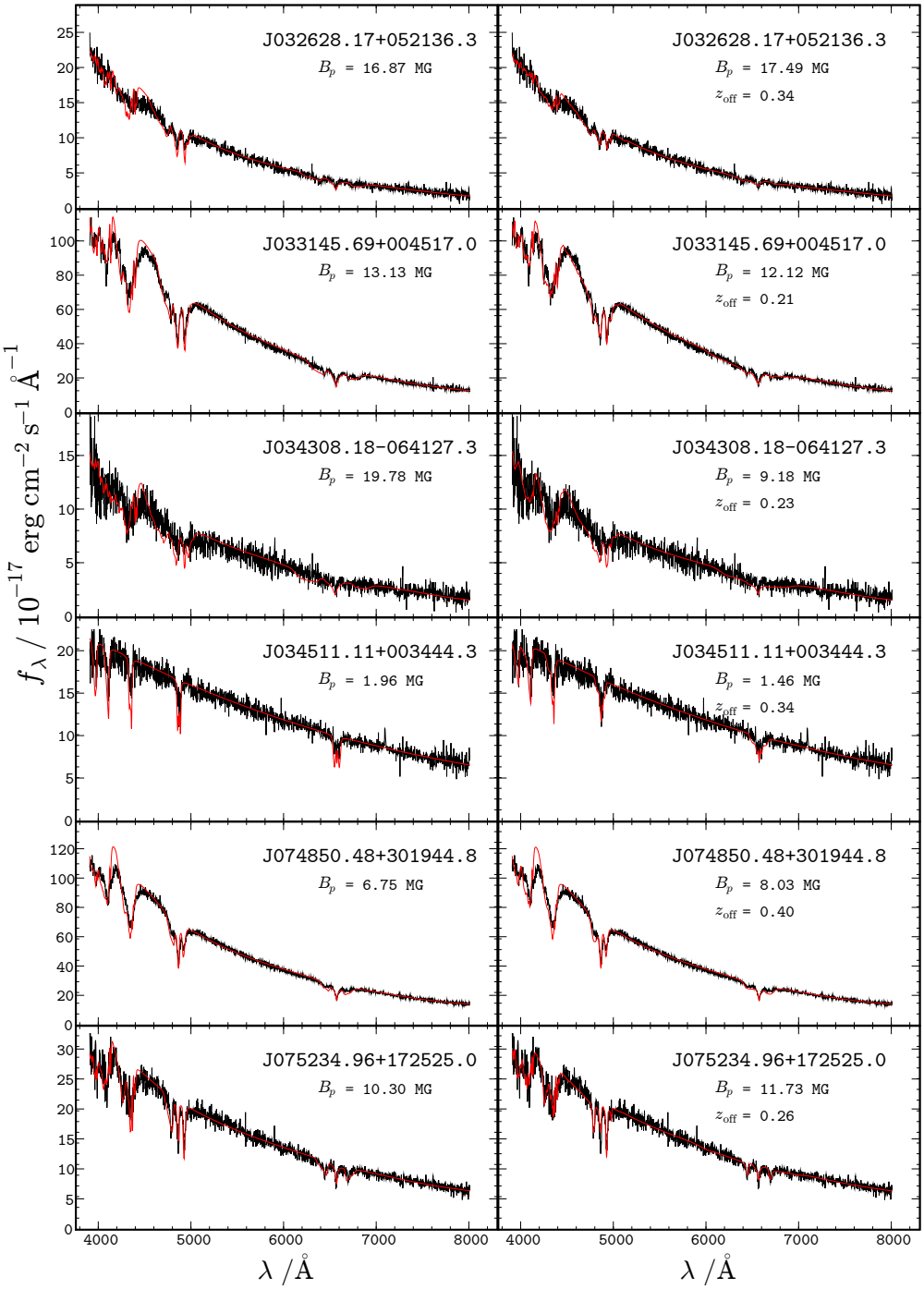

Figure B.2: Fits of observed spectra of DAHs from the SDSS to centered magnetic dipoles with a polar field strength B_p (left) and dipoles shifted by $z_{\rm off}$ stellar radii along the dipole axis (right).

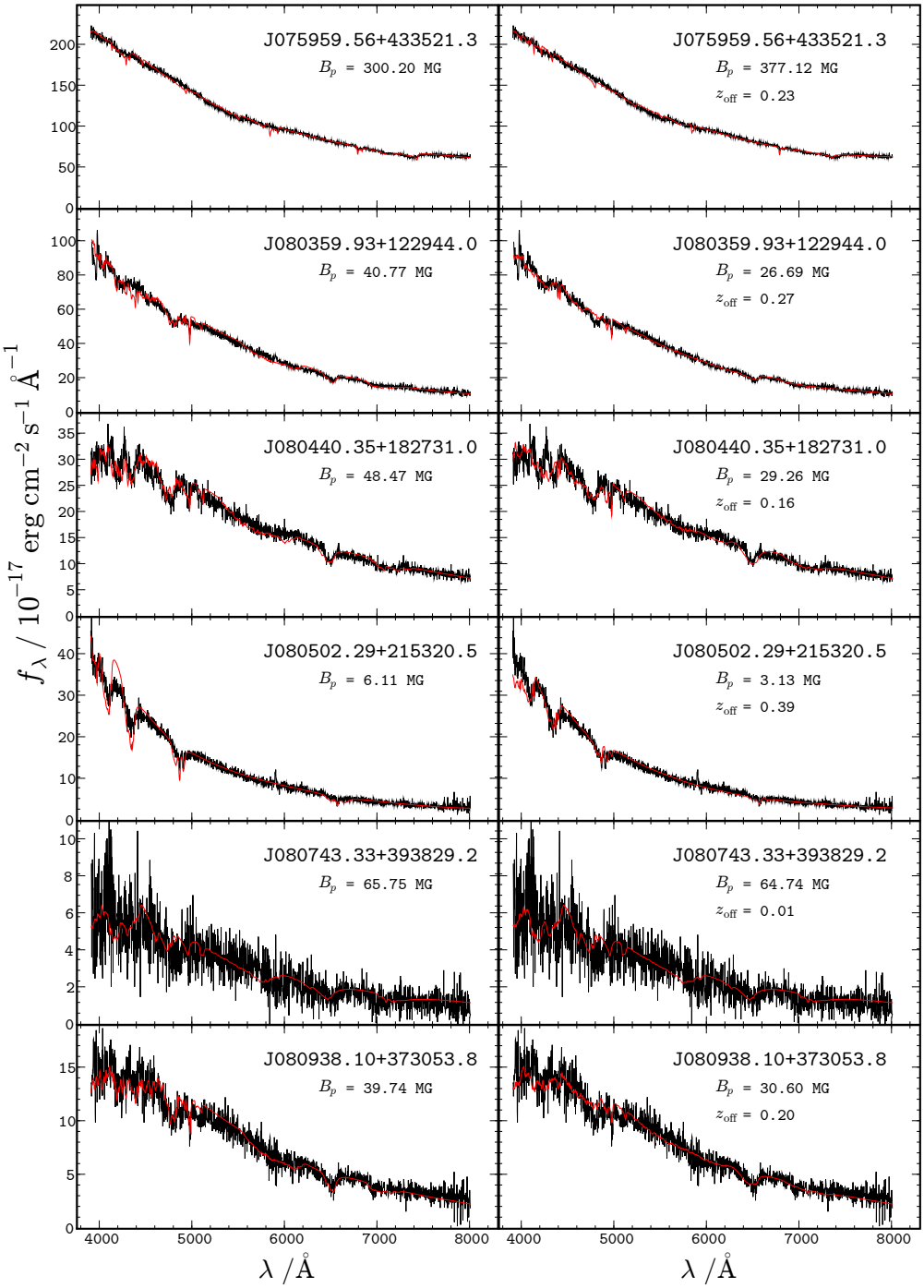

Figure B.3: Fits of observed spectra of DAHs from the SDSS to centered magnetic dipoles with a polar field strength B_p (left) and dipoles shifted by $z_{\rm off}$ stellar radii along the dipole axis (right).

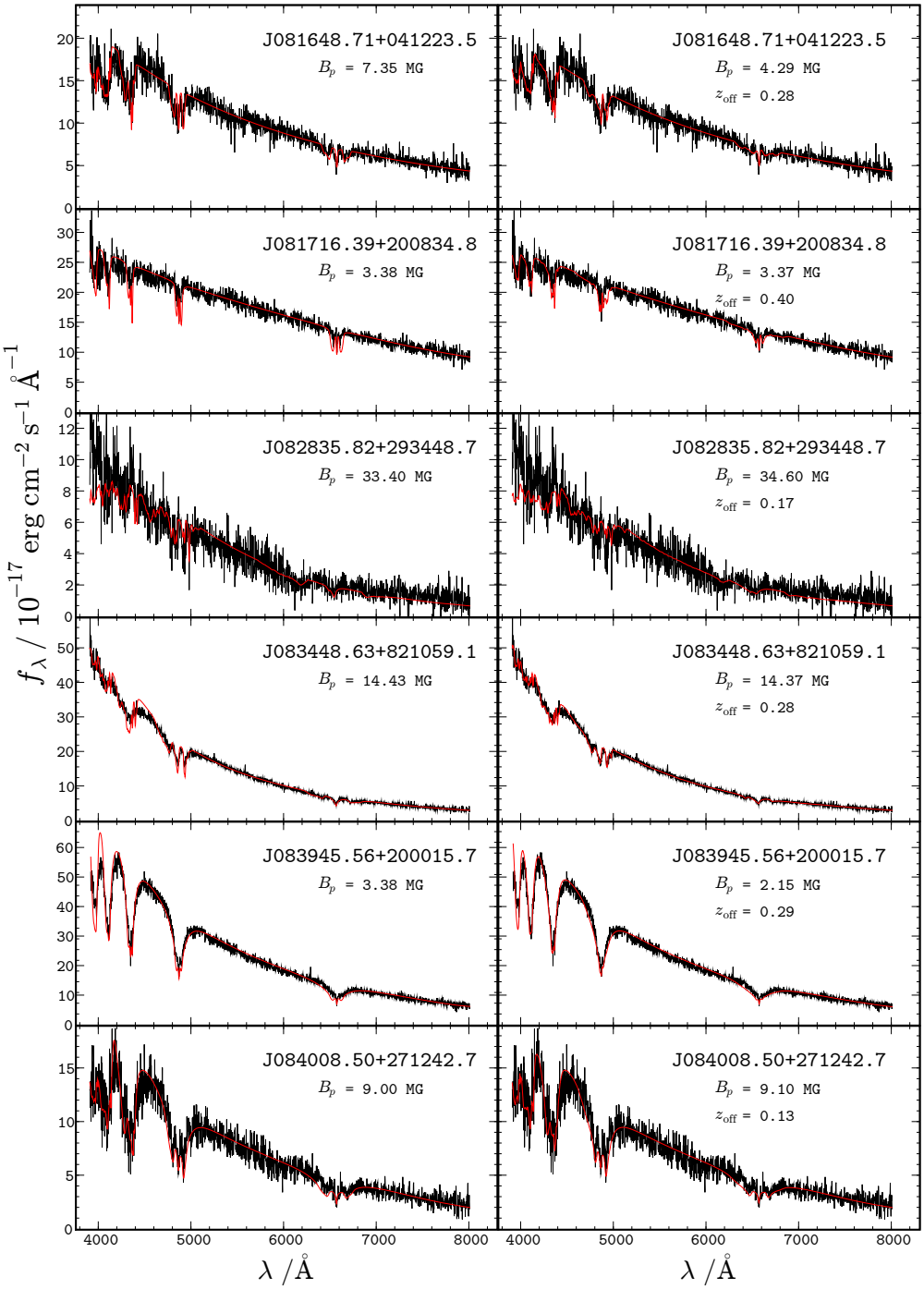

Figure B.4: Fits of observed spectra of DAHs from the SDSS to centered magnetic dipoles with a polar field strength B_p (left) and dipoles shifted by $z_{\rm off}$ stellar radii along the dipole axis (right).

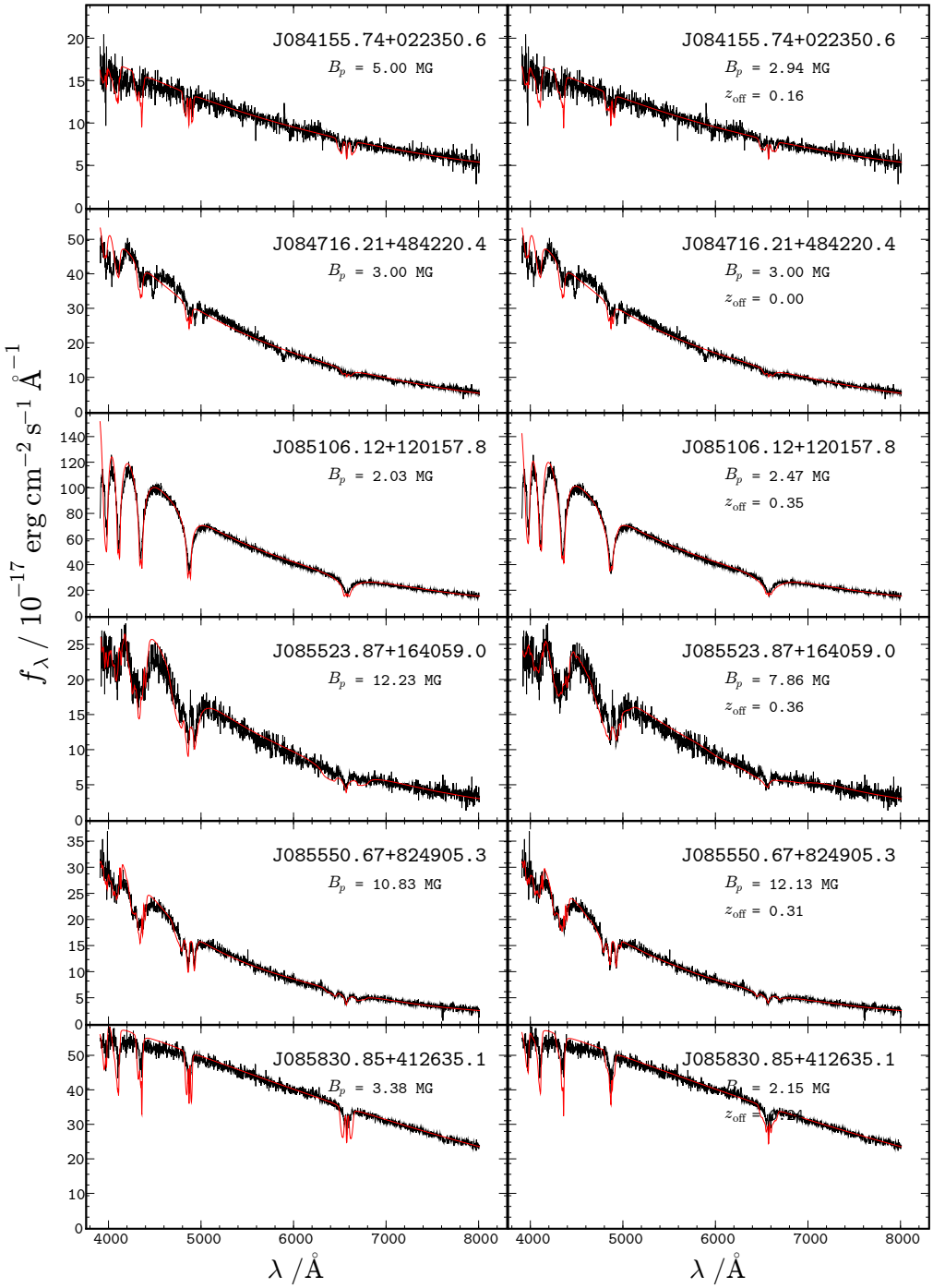

Figure B.5: Fits of observed spectra of DAHs from the SDSS to centered magnetic dipoles with a polar field strength B_p (left) and dipoles shifted by $z_{\rm off}$ stellar radii along the dipole axis (right).

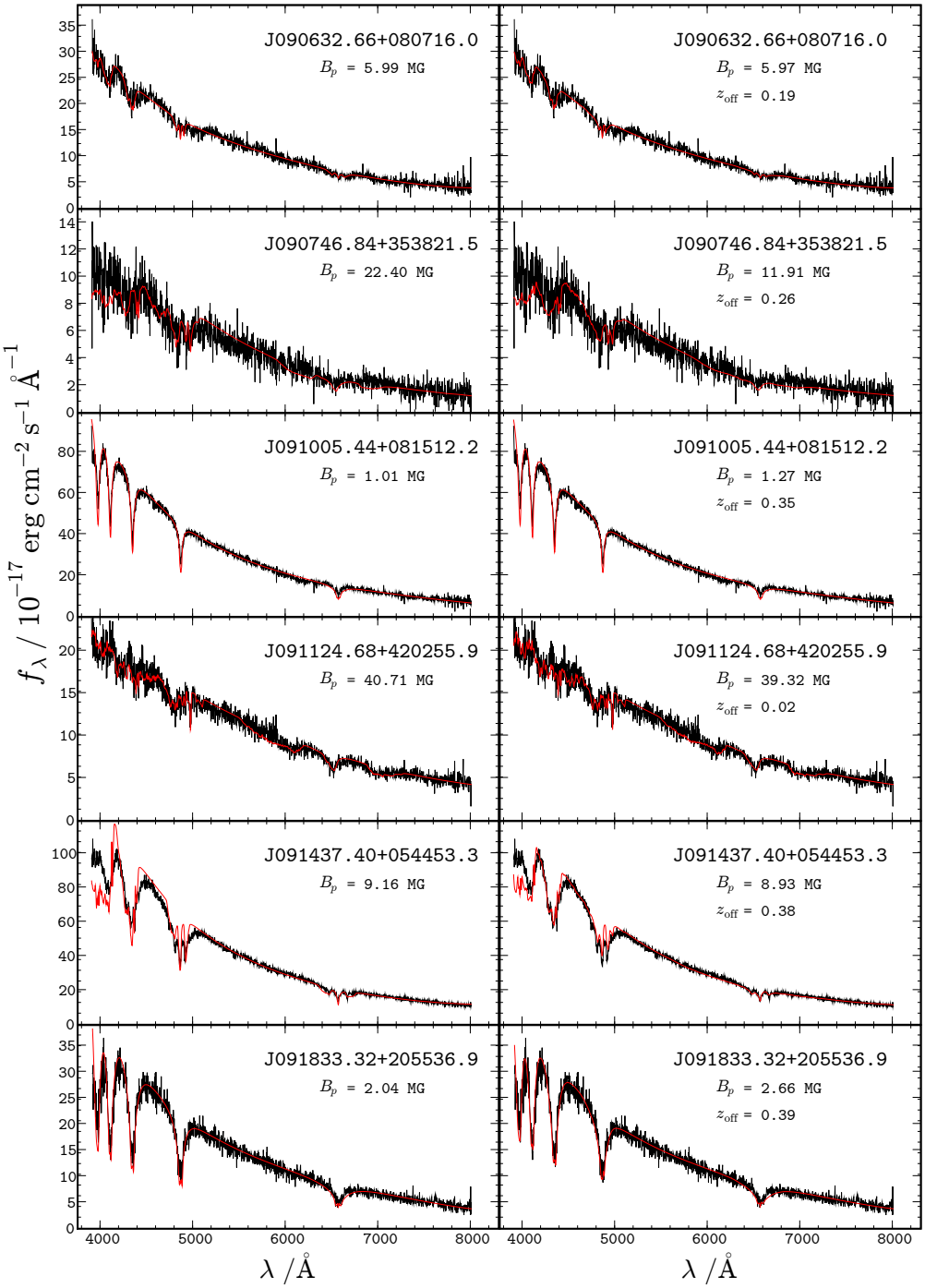

Figure B.6: Fits of observed spectra of DAHs from the SDSS to centered magnetic dipoles with a polar field strength B_p (left) and dipoles shifted by $z_{\rm off}$ stellar radii along the dipole axis (right).

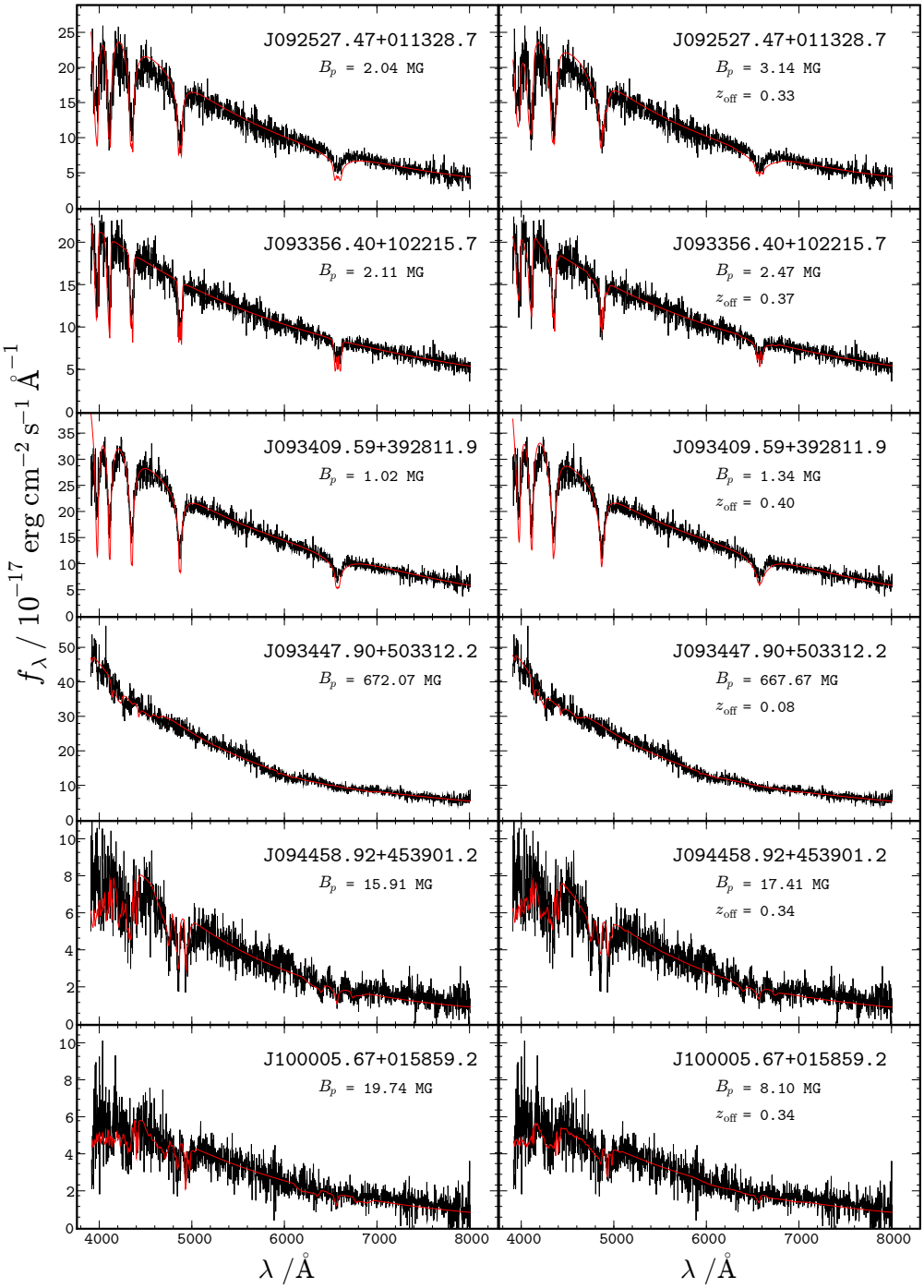

Figure B.7: Fits of observed spectra of DAHs from the SDSS to centered magnetic dipoles with a polar field strength B_p (left) and dipoles shifted by $z_{\rm off}$ stellar radii along the dipole axis (right).

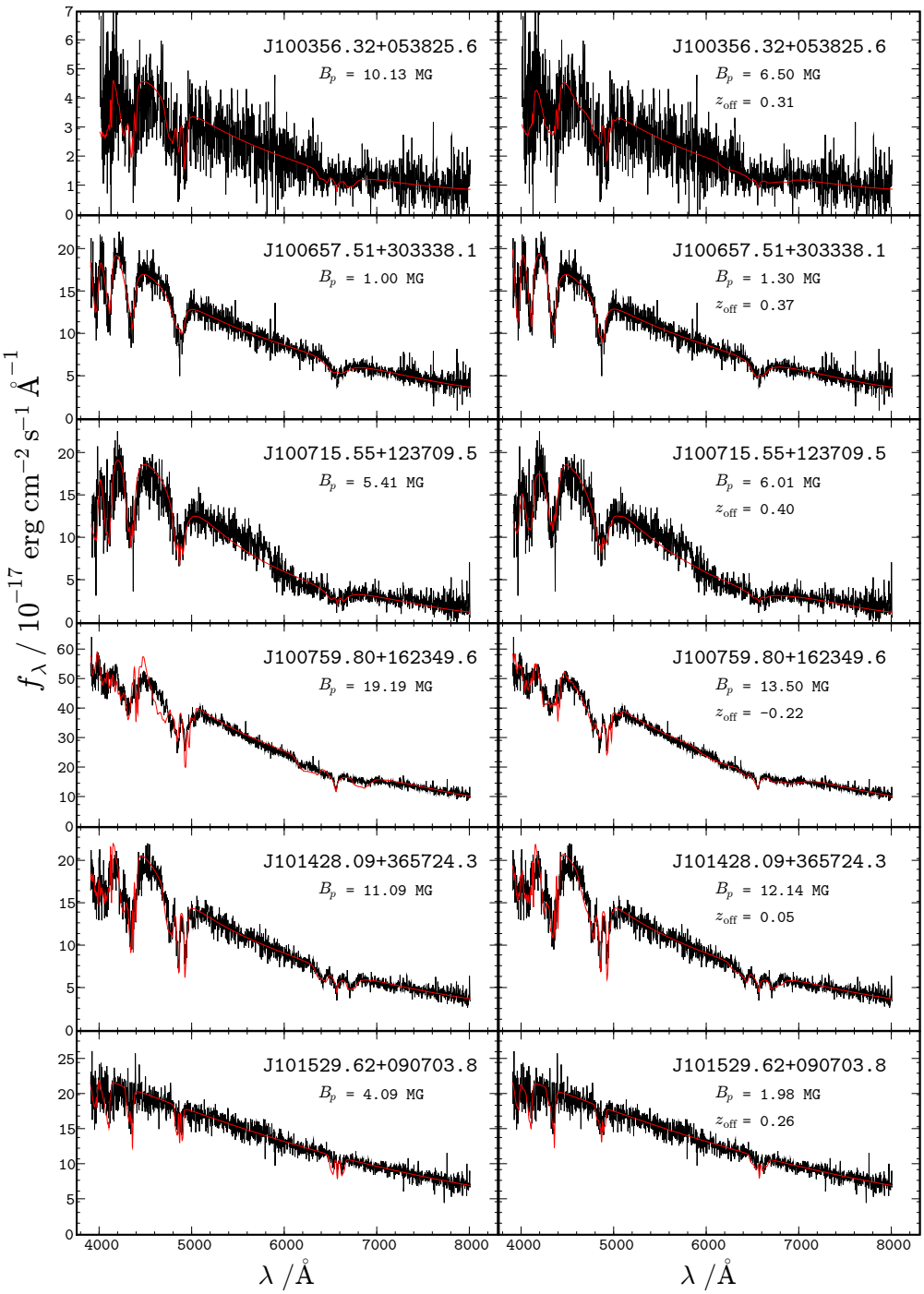

Figure B.8: Fits of observed spectra of DAHs from the SDSS to centered magnetic dipoles with a polar field strength B_p (left) and dipoles shifted by $z_{\rm off}$ stellar radii along the dipole axis (right).

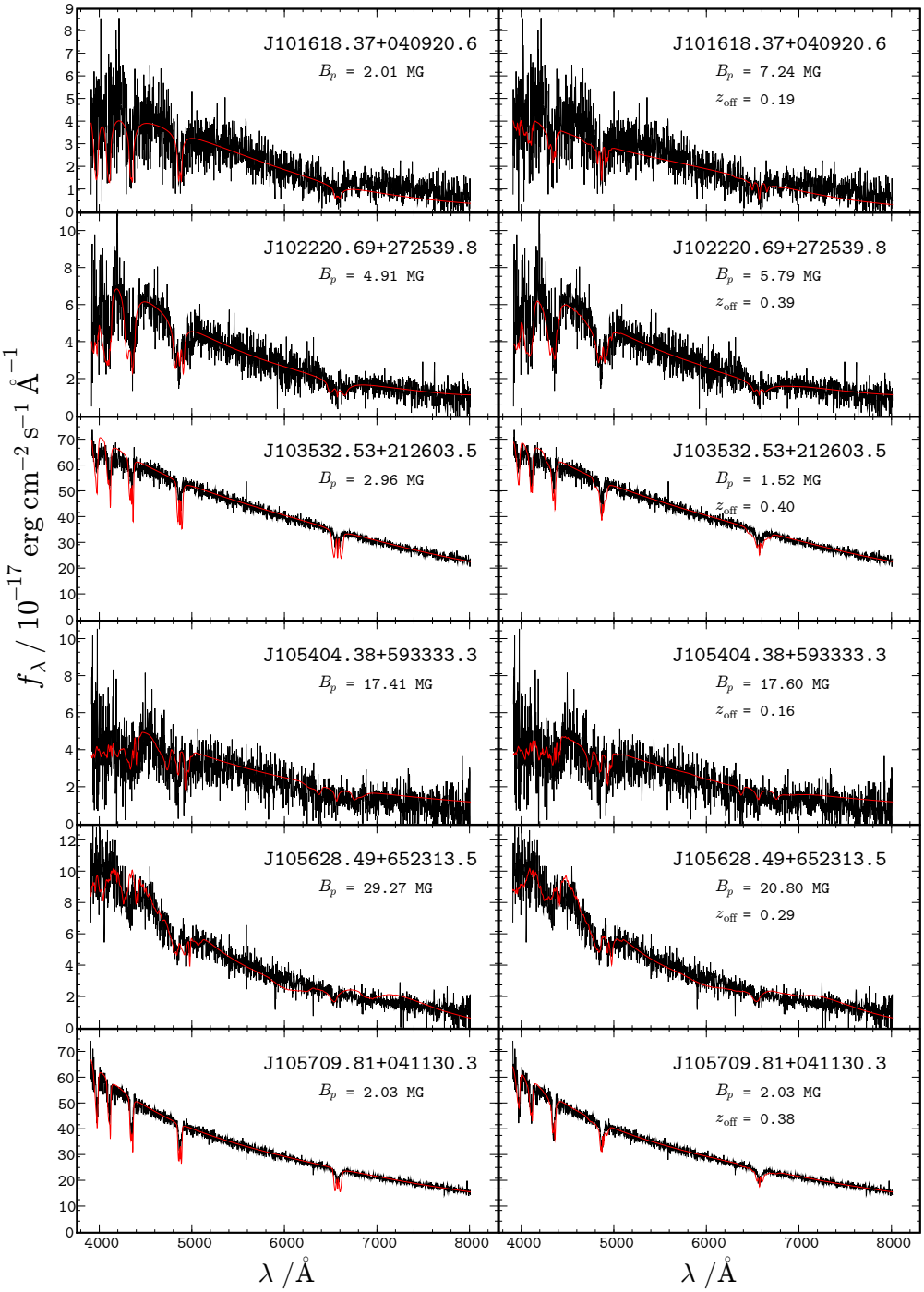

Figure B.9: Fits of observed spectra of DAHs from the SDSS to centered magnetic dipoles with a polar field strength B_p (left) and dipoles shifted by $z_{\rm off}$ stellar radii along the dipole axis (right).

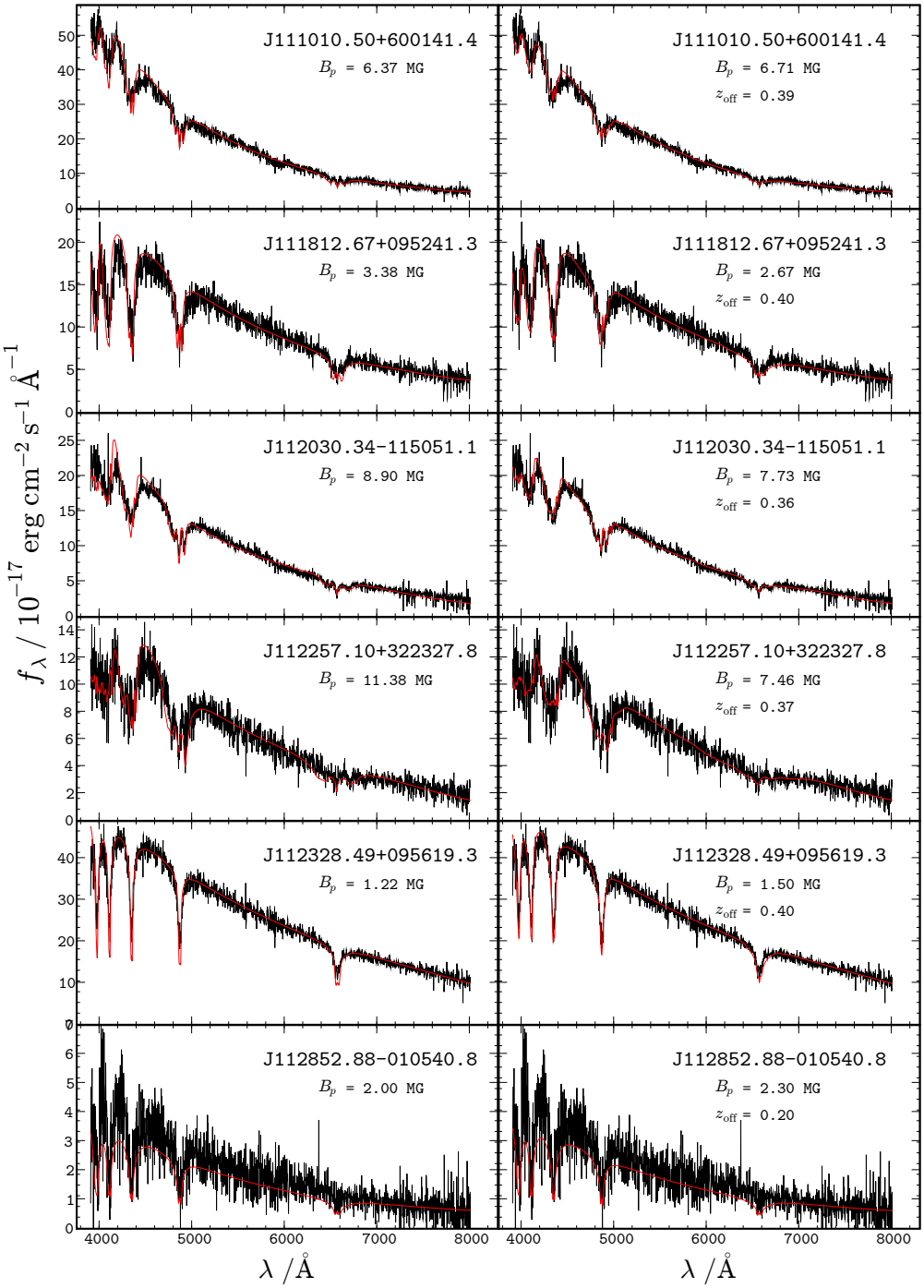

Figure B.10: Fits of observed spectra of DAHs from the SDSS to centered magnetic dipoles with a polar field strength B_p (left) and dipoles shifted by $z_{\rm off}$ stellar radii along the dipole axis (right).

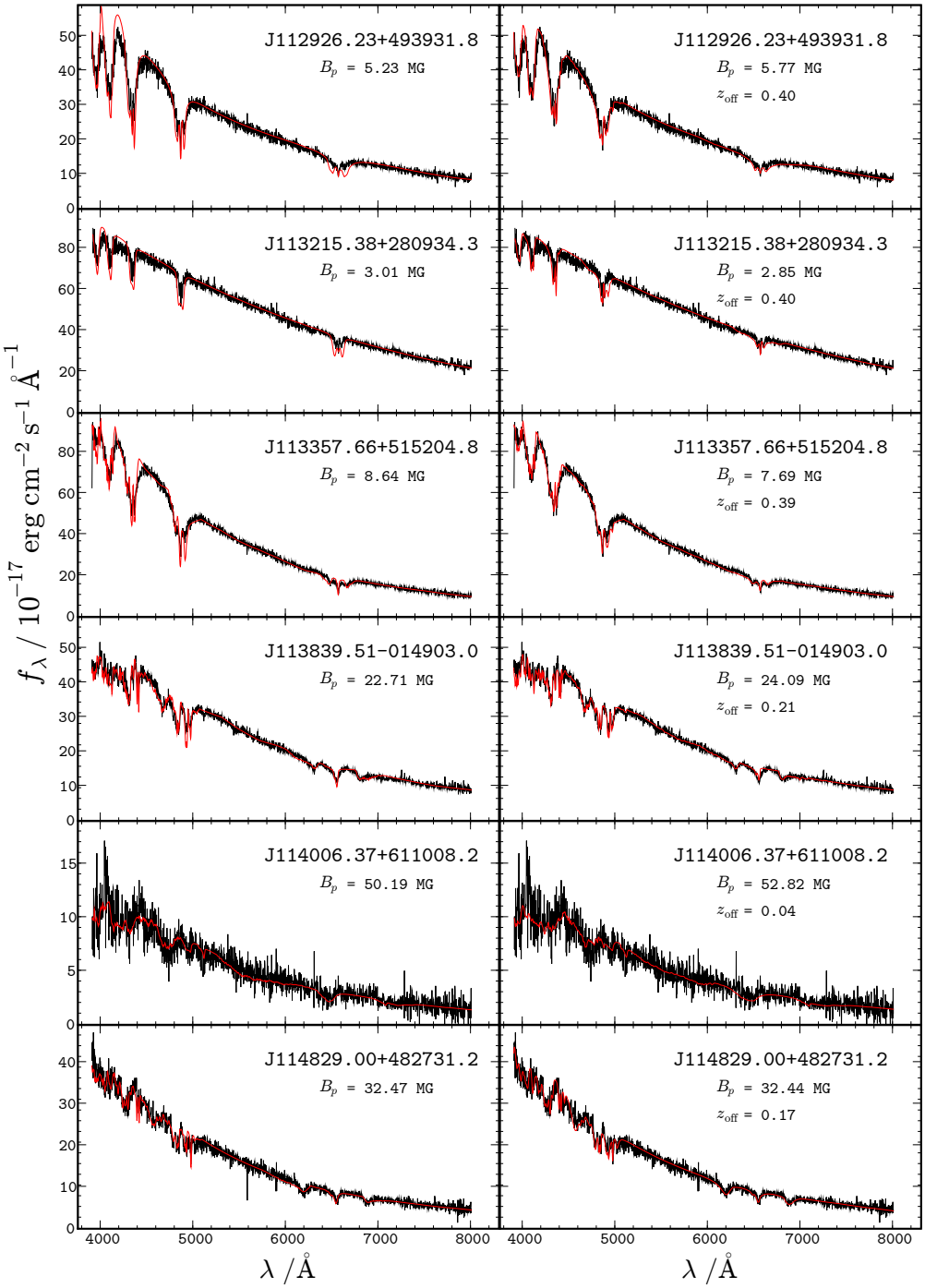

Figure B.11: Fits of observed spectra of DAHs from the SDSS to centered magnetic dipoles with a polar field strength B_p (left) and dipoles shifted by $z_{\rm off}$ stellar radii along the dipole axis (right).

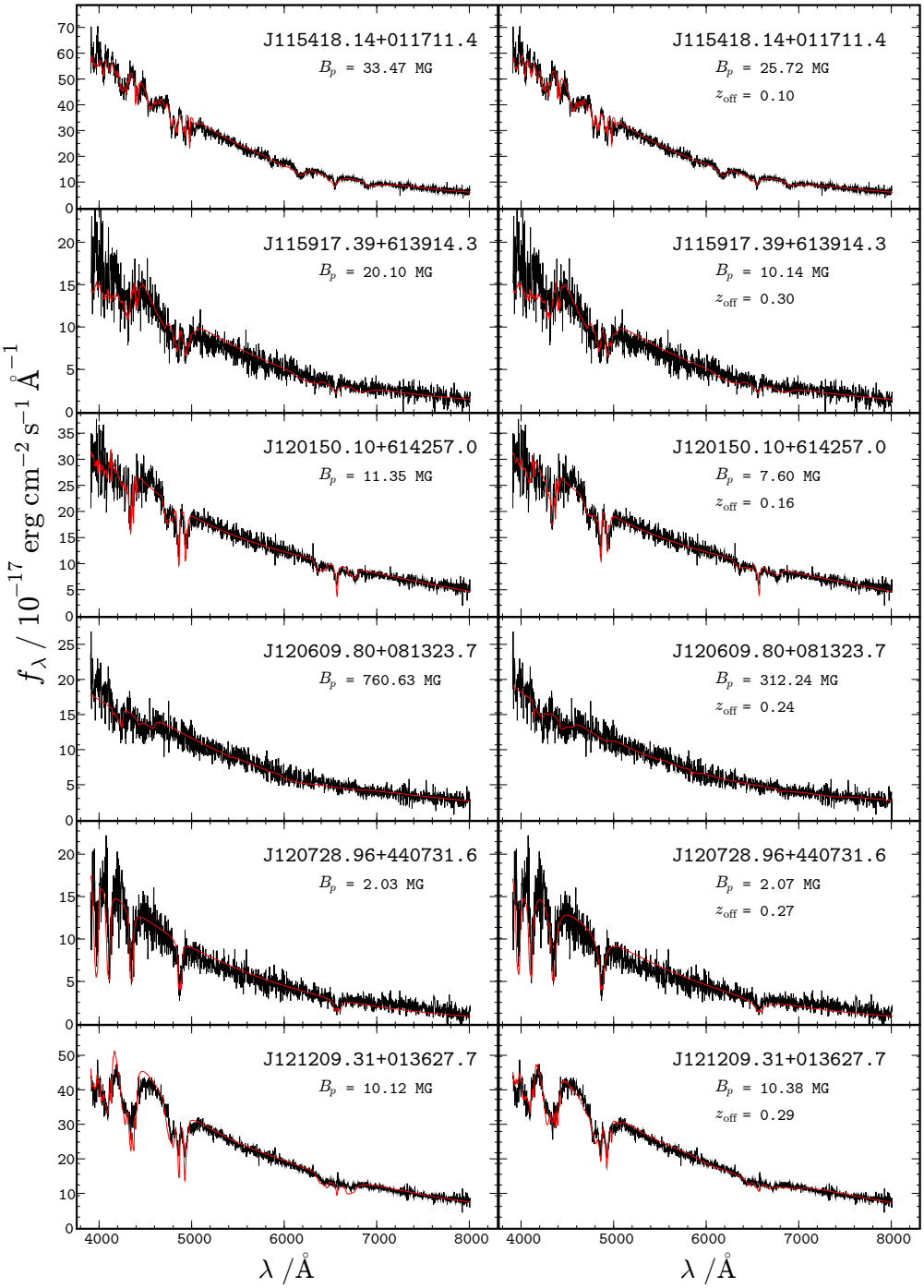

Figure B.12: Fits of observed spectra of DAHs from the SDSS to centered magnetic dipoles with a polar field strength B_p (left) and dipoles shifted by $z_{\rm off}$ stellar radii along the dipole axis (right).

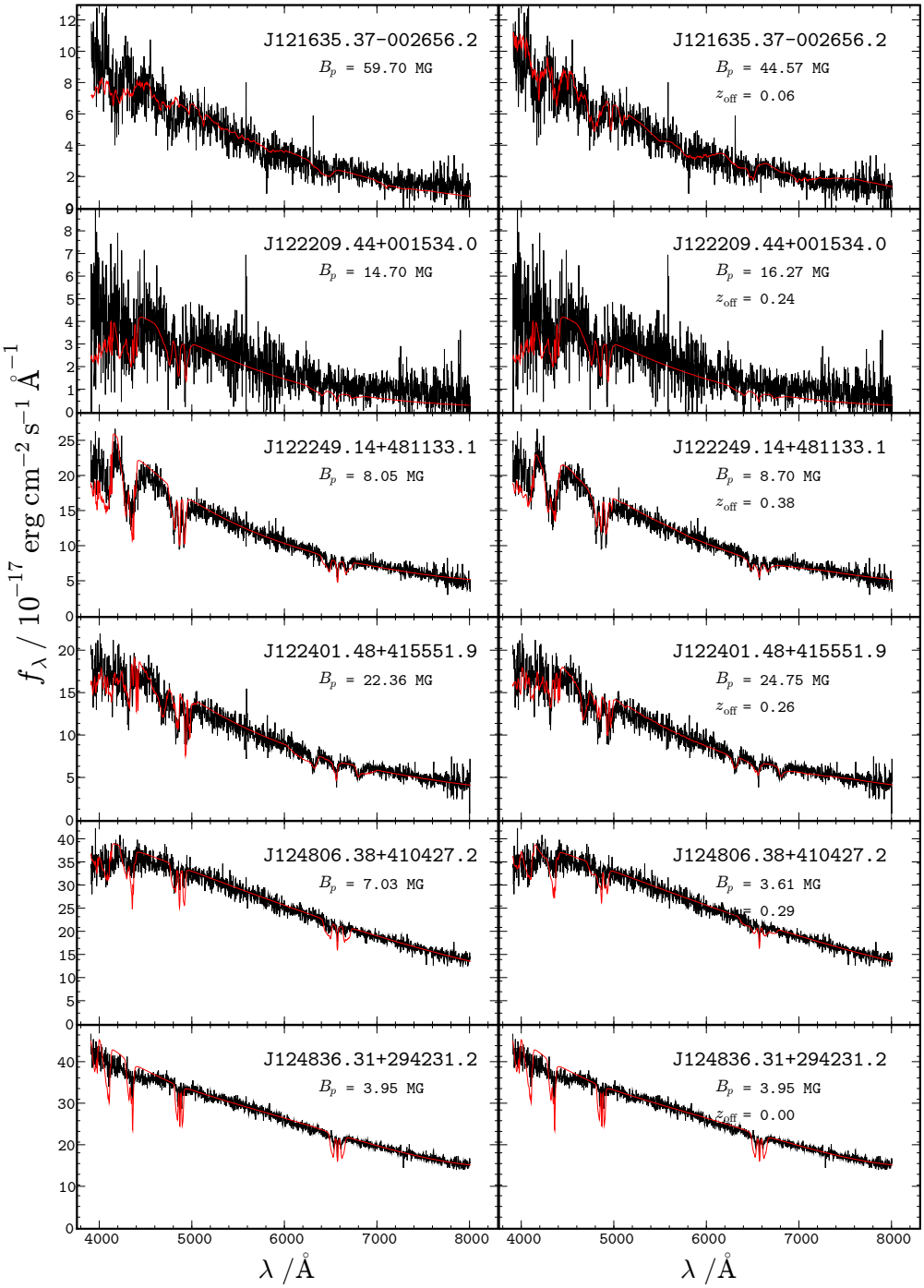

Figure B.13: Fits of observed spectra of DAHs from the SDSS to centered magnetic dipoles with a polar field strength B_p (left) and dipoles shifted by $z_{\rm off}$ stellar radii along the dipole axis (right).

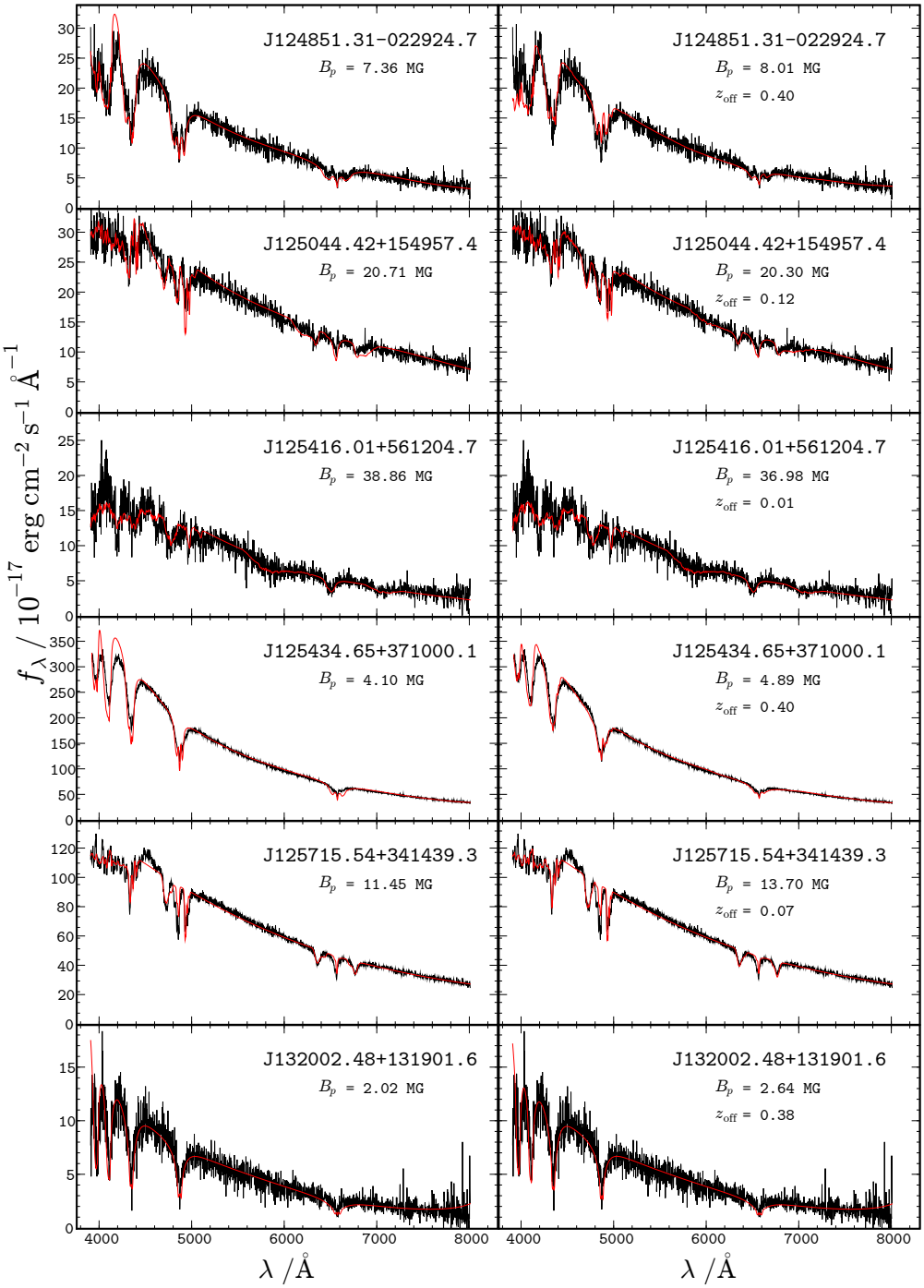

Figure B.14: Fits of observed spectra of DAHs from the SDSS to centered magnetic dipoles with a polar field strength B_p (left) and dipoles shifted by $z_{\rm off}$ stellar radii along the dipole axis (right).

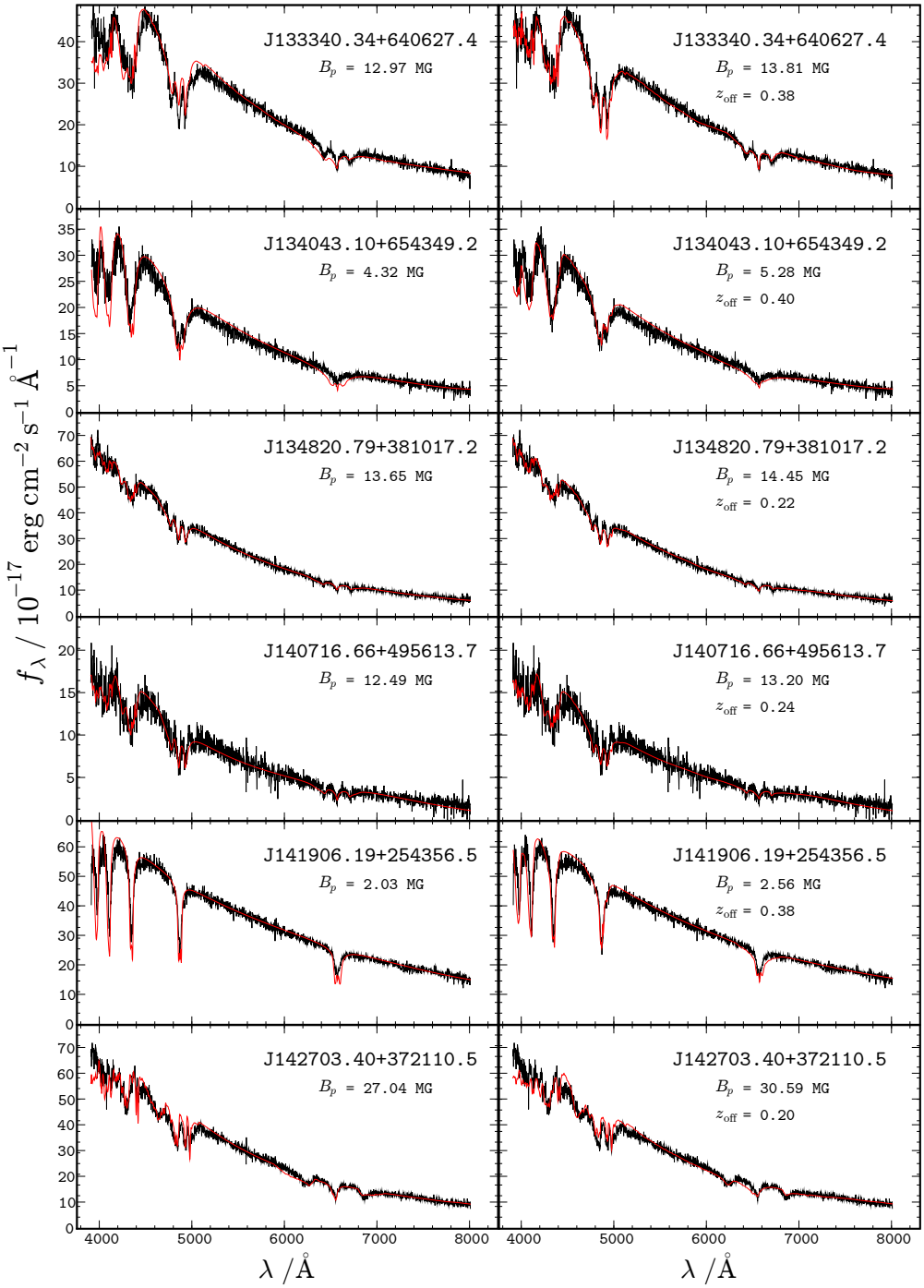

Figure B.15: Fits of observed spectra of DAHs from the SDSS to centered magnetic dipoles with a polar field strength B_p (left) and dipoles shifted by $z_{\rm off}$ stellar radii along the dipole axis (right).

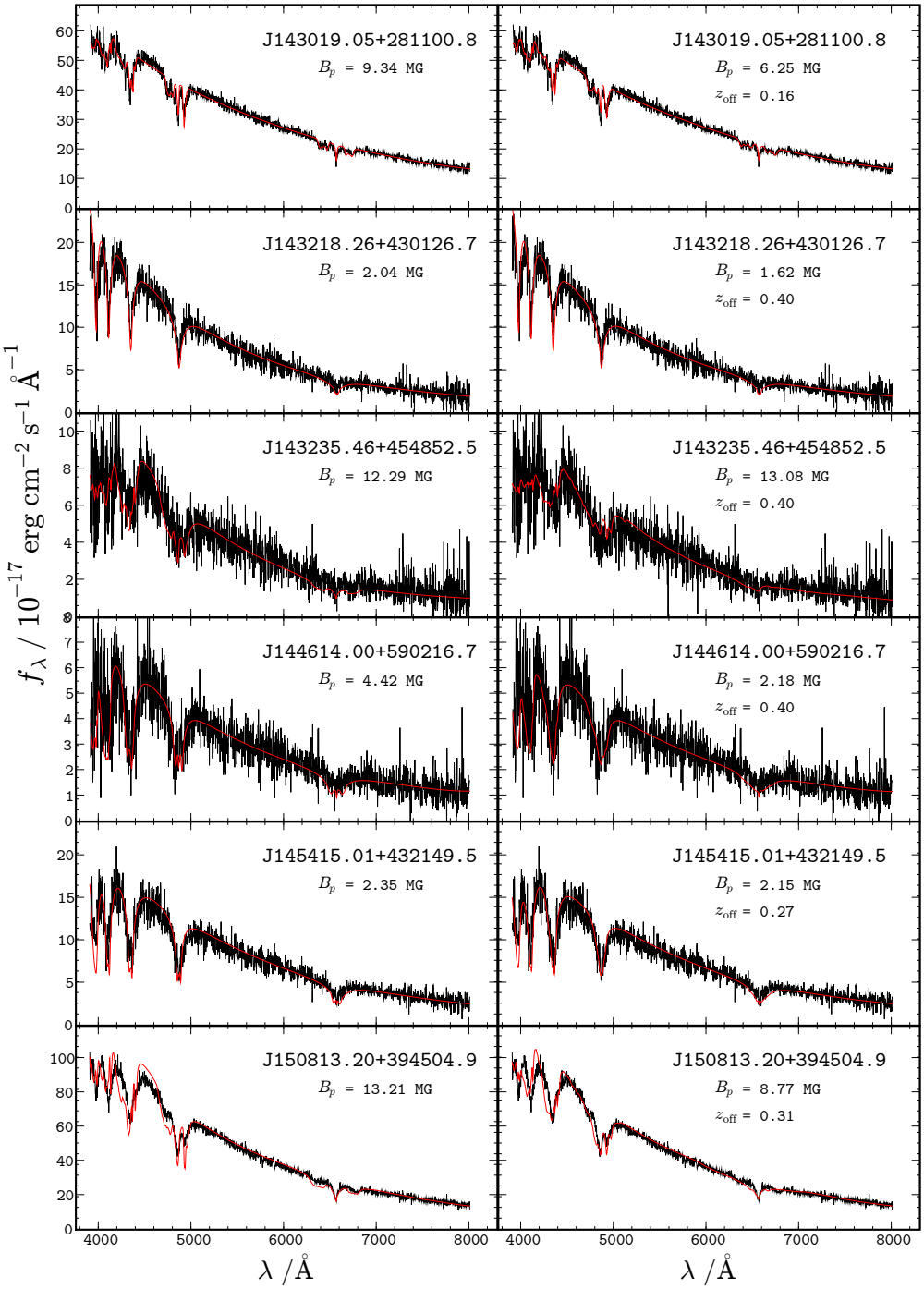

Figure B.16: Fits of observed spectra of DAHs from the SDSS to centered magnetic dipoles with a polar field strength B_p (left) and dipoles shifted by $z_{\rm off}$ stellar radii along the dipole axis (right).

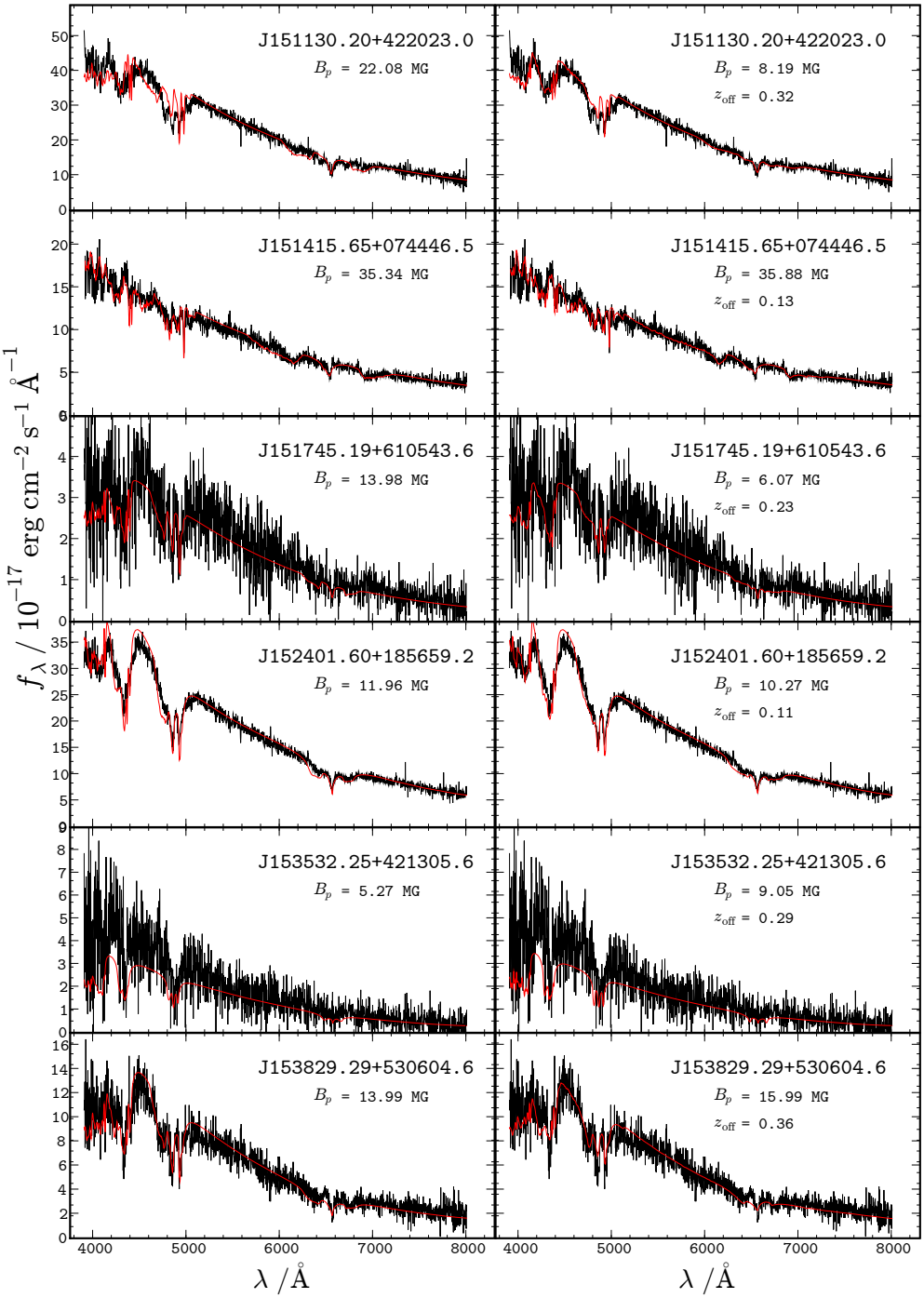

Figure B.17: Fits of observed spectra of DAHs from the SDSS to centered magnetic dipoles with a polar field strength B_p (left) and dipoles shifted by $z_{\rm off}$ stellar radii along the dipole axis (right).

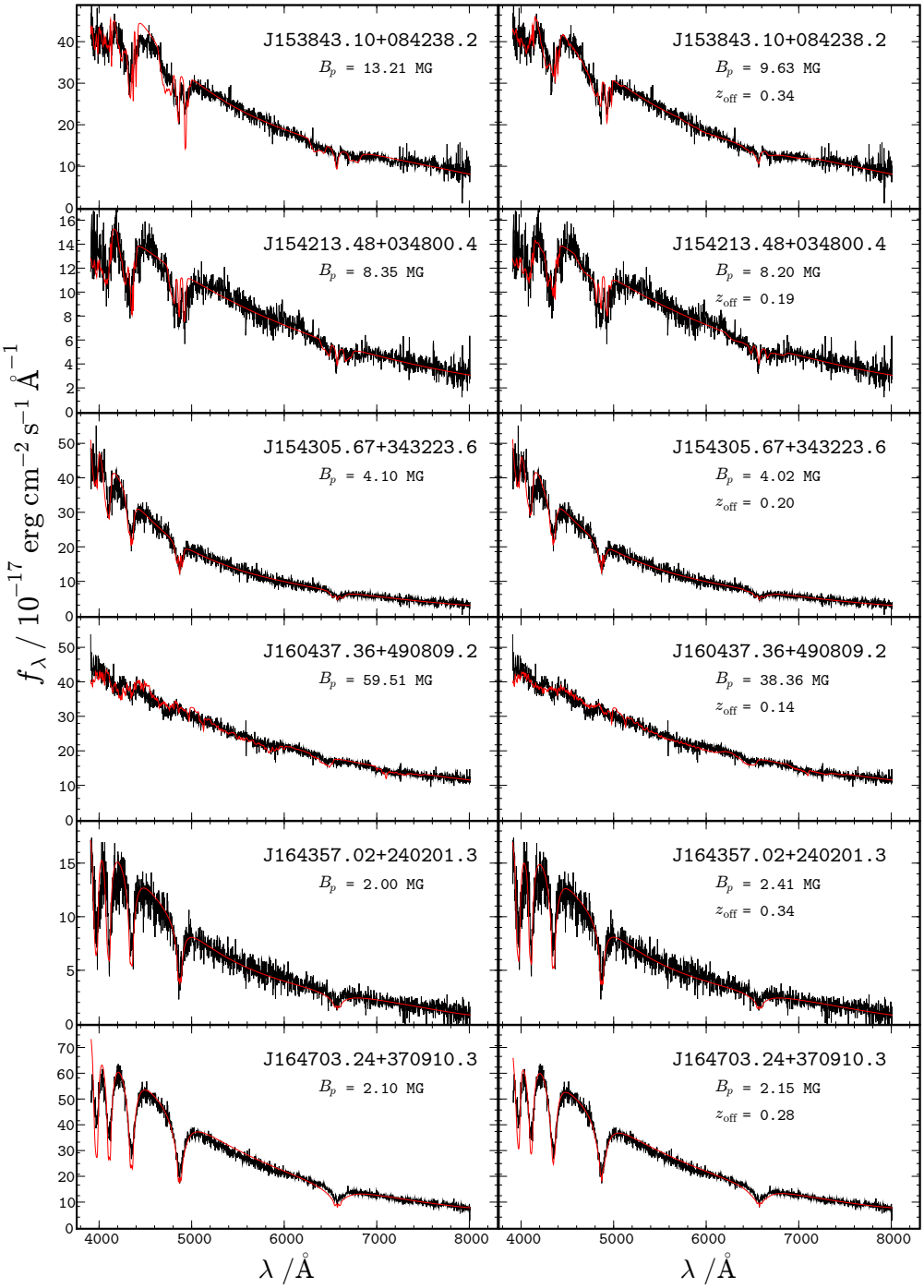

Figure B.18: Fits of observed spectra of DAHs from the SDSS to centered magnetic dipoles with a polar field strength B_p (left) and dipoles shifted by $z_{\rm off}$ stellar radii along the dipole axis (right).

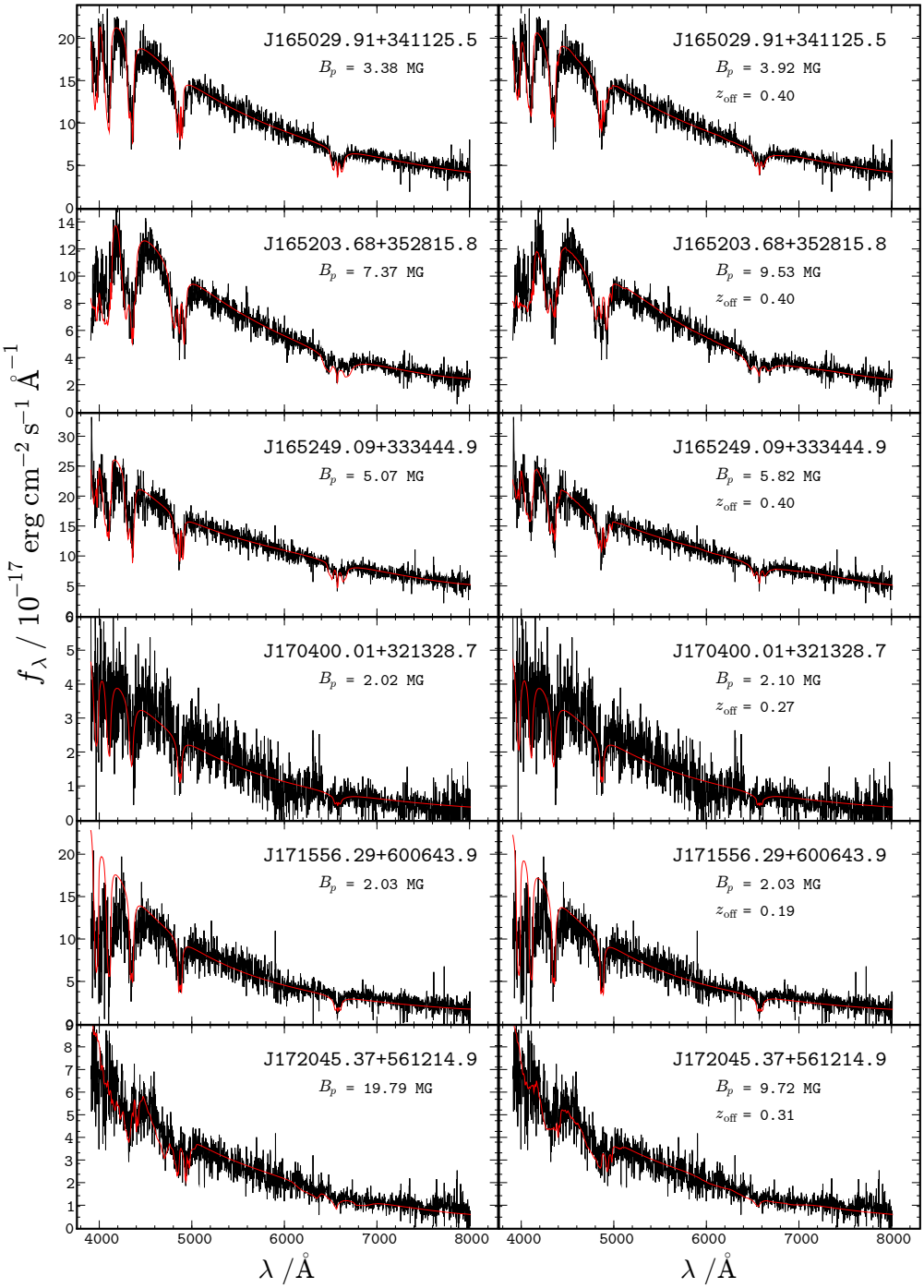

Figure B.19: Fits of observed spectra of DAHs from the SDSS to centered magnetic dipoles with a polar field strength B_p (left) and dipoles shifted by $z_{\rm off}$ stellar radii along the dipole axis (right).

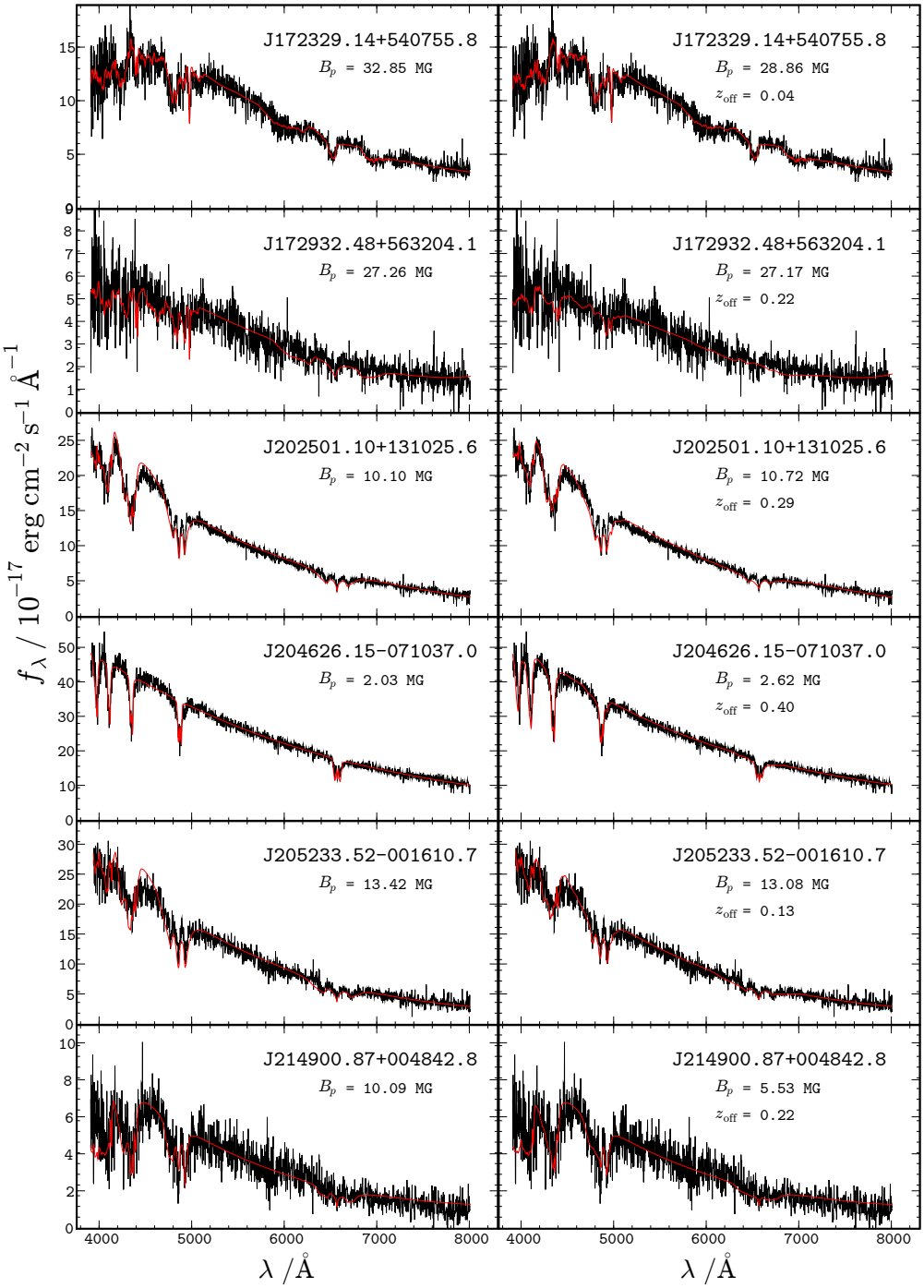

Figure B.20: Fits of observed spectra of DAHs from the SDSS to centered magnetic dipoles with a polar field strength B_p (left) and dipoles shifted by $z_{\rm off}$ stellar radii along the dipole axis (right).

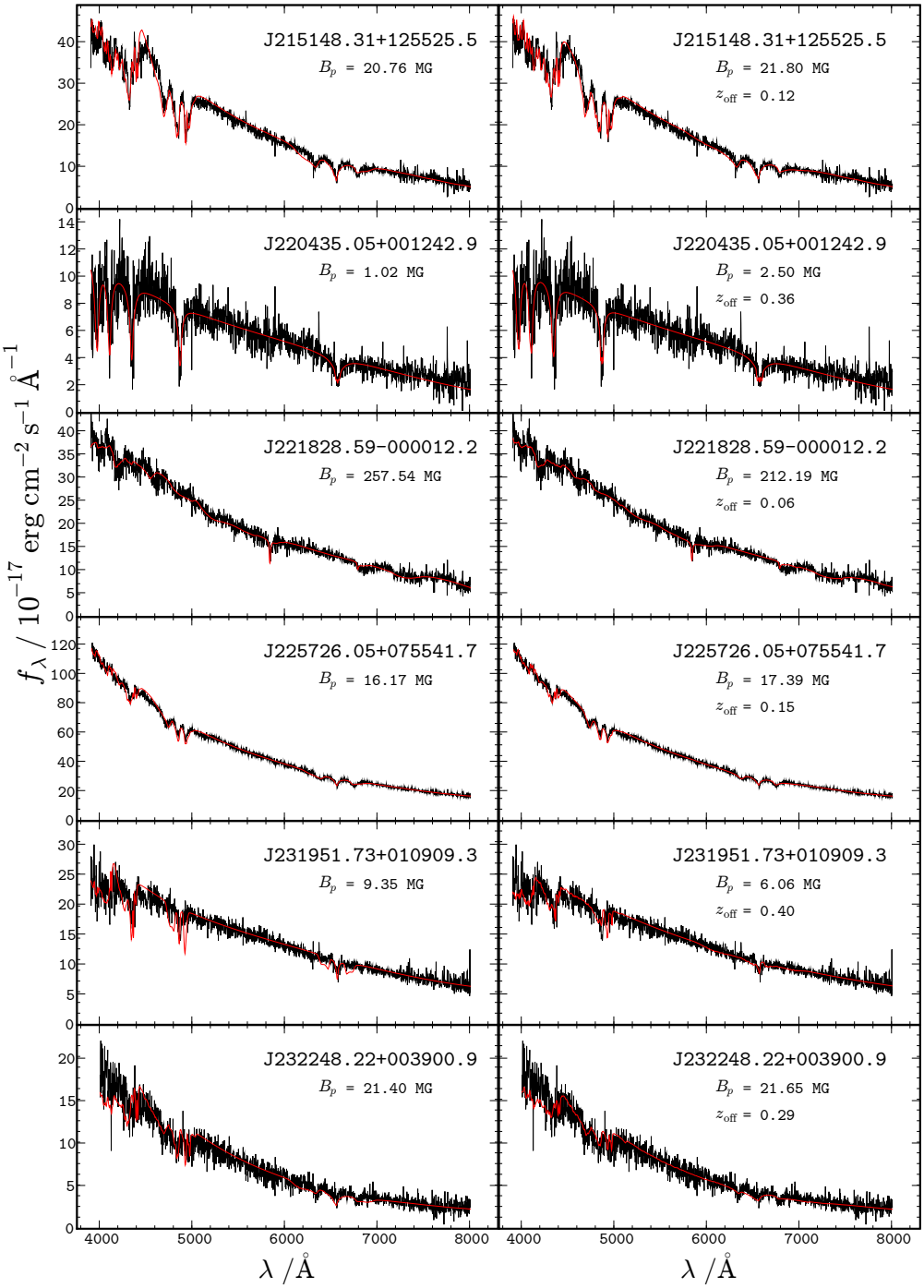

Figure B.21: Fits of observed spectra of DAHs from the SDSS to centered magnetic dipoles with a polar field strength B_p (left) and dipoles shifted by $z_{\rm off}$ stellar radii along the dipole axis (right).

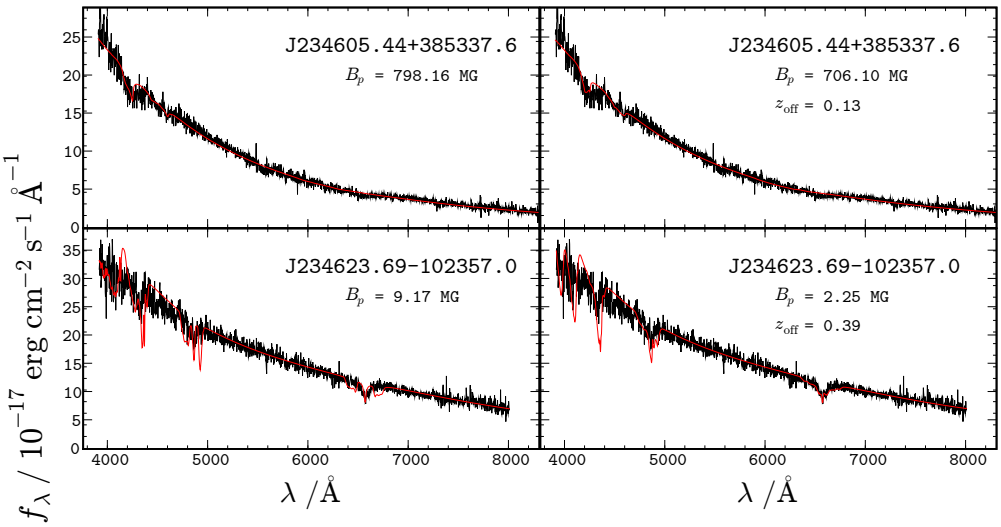

Figure B.22: Fits of observed spectra of DAHs from the SDSS to centered magnetic dipoles with a polar field strength B_p (left) and dipoles shifted by $z_{\rm off}$ stellar radii along the dipole axis (right).

Appendix C

Magnetic Model Parameters of Hydrogen-rich Magnetic White Dwarfs in Sloan Digital Sky Survey

Table C.1: Model fits with centered dipole and offset dipole models with comparison to literature values. The columns indicate the SDSS name of the object; the plate, Modified Julian Date and fiber ids of the observations; the dipole magnetic field strength of the centered dipole, the inclination with respect to the line of sight of the centered dipole, the dipole magnetic field strength of the offset dipole, the inclination with respect to the line of sight of the offset dipole, the offset along the axis of the magnetic field in terms of the stellar radius, and finally comments indicate the model parameters from the literature (i.e. Gänsicke et al., 2002; Schmidt et al., 2003; Vanlandingham et al., 2005)

MWD (SDSS+)	Plate-MJD-FiberID	B_p / MG	i / deg	$B_{\rm off}$ / MG	$z_{\rm off}$ / $r_{\rm WD}$	i / deg	fits
J002129.00+150223.7	753-52233-432	530.69±63.56	53.19 ± 25.64	527.33±97.98	0.16±0.08	28.05 ± 51.8	550 MG, ...
J004248.19+001955.3	690-52261-594	2.00 ± 0.00[2]	88.22 ± 43.37	2.58[1]	0.35±0.82	0.00 ± 23.66	14 MG, 30°
J021116.34+003128.5	405-51816-382	341.31±54.34	37.73 ± 27.71	281.34±186.95	0.32±0.14	9.59 ± 62.99	490 MG, ...
J021148.22+211548.2	246-53327-048	166.16 ± 7.41	48.89 ± 5.67	180.47 ± 13.15	0.27 ± 0.02	33.23 ± 10.05	210 MG, 90°
J023420.63+264801.7	2399-53764-559	32.82 ± 6.26	42.08 ± 8.09	21.17 ± 2.02	0.38 ± 0.04	17.17 ± 10.92	
J030407.40-002541.7	411-51817-172	10.95±0.98	48.57 ± 5.72	11.13±0.97	0.27±0.10	51.51 ± 17.26	11 MG, 60°
J031824.19+422651.0	2417-53766-568	10.12±0.10	54.6 ± 4.7	10.77±0.10	0.29±0.05	61.1 ± 10.0	
J032628.17+052136.3	2339-53729-515	16.87 ± 2.41	53.06 ± 26.65	17.49 ± 8.32	0.34 ± 0.12	44.62 ± 42.63	
J033145.69+004517.0	415-51879-378	13.13±1.00	49.41 ± 38.17	12.12±9.98	0.21±0.02	47.43 ± 38.49	12 MG, 60°
J033320.36+000720.6	0415-51879-485	849.30 ± 51.75	50.92 ± 8.75	784.22 ± 83.98	0.19 ± 0.05	6.29 ± 6.42	
J034308.18-064127.3	462-51909-117	9.96±2.06	41.96 ± 9.80	9.18±2.11	0.23±0.04	12.59 ± 8.55	13 MG, 45
J034511.11+003444.3	416-51811-590	1.96±0.42	49.01 ± 11.56	1.46±0.36	0.34±0.08	16.38 ± 6.43	1.5 MG, 0°
J074850.48+301944.8	889-52663-507	6.75±0.41	40.65 ± 7.59	8.03±0.66	0.40±0.14	43.85 ± 10.55	10 MG, 60°
J074924.91+171355.4	2729-54419-282	13.99 ± 1.30	46.00 ± 15.07	13.62 ± 1.86	0.27 ± 0.05	44.02 ± 53.16	
J075234.96+172525.0	1920-53314-106	10.30±1.23	72.4 ± 22.4	11.73±1.05	0.26±0.05	58.7 ± 38.1	
J075819.57+354443.7	757-52238-144	26.40±3.94	37.62 ± 22.98	32.42±5.65	0.39±0.07	54.51 ± 19.44	27 MG, 30°
J080359.93+122944.0	2265-53674-033	40.7 ± 2.13	42.97 ± 8.44	26.6 ± 11.8	0.26±0.04	17.71 ± 7.21	
J080440.35+182731.0	2081-53357-442	48.47±2.93	35.67 ± 7.59	29.26±3.18	0.16±0.02	33.97 ± 8.47	49 MG, 30°
J080502.29+215320.5	1584-52943-132	6.11±1.29	54.76 ± 14.52	3.13±0.59	0.39±0.06	86.79 ± 59.37	5 MG, 60°
J080743.33+393829.2	545-52202-009	65.75±18.52	78.07 ± 35.46	64.74±12.14	−0.01±0.01	8.25 ± 17.26	49 MG, 30°
J080938.10+373053.8	758-52253-044	39.74±5.41	41.89 ± 14.11	30.60±5.66	0.20±0.10	15.15 ± 75.23	40 MG, 30°
J081648.71+041223.5	1184-52641-329	10.13±8.03	48.82 ± 29.96	6.50±2.73	0.31±0.12	0.28 ± 27.06	10* MG, 30*°
J081716.39+200834.8	2082-53358-444	3.37 ± 0.44	49.02 ± 10.78	3.37 ± 1.09	0.39±0.10	34.05 ± 30.78	

Table C.1: continued.

MWD (SDSS+)	Plate-MJD-FiberID	B_p / MG	i / deg	$B_{\rm off}$ / MG	$z_{\rm off}$ / $r_{\rm WD}$	i / deg	Comments
J082835.82+293448.7	1207-52672-635	33.40±10.53	68.57 ± 33.47	34.60±6.91	0.17±0.05	50.3 ± 36.21	30 MG, 90*°
J083448.63+821059.1	2549 54523 135	14.44 ± 4.57	54.30 ± 66.45	14.36 ± 4.08	0.28 ± 0.09	48.58 ± 70.00	
J083945.56+200015.7	2277-53705-484	3.38±0.49	48.6 ± 7.7	2.15±0.10	0.29±0.08	49.9 ± 90^1	
J084155.74+022350.6	564-52224-248	5.00±0.99	49.35 ± 17.53	2.94±0.72	0.16±0.04	15.89 ± 10.57	6 MG, 90°
J085106.12+120157.8	2430-53815-229	2.03±0.10	81.9 ± 90^1	2.47±0.10	0.35±0.06	72.8 ± 18.8	
J085523.87+164059.0	2431-53818-522	12.23±2.92	48.6 ± 8.6	7.86±1.63	0.36±0.06	10.8 ± 6.1	
J085550.67+824905.3	2549 54523 066	10.82 ± 2.99	54.81 ± 19.36	12.13 ± 4.30	62.89 ± 36.38	0.30 ± 0.14	
J085830.85+412635.1	830-52293-070	3.38±0.19	48.85 ± 5.86	2.15±0.34	0.24±0.07	36.25 ± 7.31	2 MG, 30°
J090632.66+080716.0	1300-52973-148	5.98 ± 3.02	88.00 ± 88.06	5.97 ± 3.13	0.18 ± 0.13	65.13 ± 82.65	10 MG, 90°
J090746.84+353821.5	1212-52703-187	22.40±8.80	48.57 ± 16.68	11.91±3.22	0.26±0.08	1.77 ± 2.72	15 MG, 60°
J091005.44+081512.2	1300-52973-639	1.01 ± 0.00^2	74.46 ± 42.54	1.27 ± 0.70	71.06 ± 32.03	0.35 ± 0.29	
J091124.68+420255.9	1200-52668-538	35.20±5.83	35.1 ± 39.48	18.85±4.86	0.23±0.06	14.23 ± 10.72	45 MG, 60°
J091437.40+054453.3	1193-52652-481	9.16±0.77	48.52 ± 4.56	8.93±0.93	0.38±0.04	48.35 ± 19.7	9.5 MG, 90°
J091833.32+205536.9	2288-53699-547	2.04±0.10	87.2 ± 41.9	2.66±1.71	0.39±0.17	70.3 ± 61.9	
J092527.47+011328.7	475-51965-315	2.04 ± 0.00^2	54.83 ± 14.14	3.14±1.10	0.33±0.13	47.34 ± 14.08	2.2 MG, ...
J093356.40+102215.7	1303-53050-525	2.11±0.49	72.05 ± 22.68	2.47 ± 0.00^2	0.37±0.12	52.39 ± 29.38	1.5 MG, 60*°
J093409.90+392759.3	1215-52725-241	1.01 ± 0.00^2	81.18 ± 23.30	1.35 ± 0.25	57.43 ± 29.65	0.39±0.13	
J093447.90+503312.2	901-52641-373	7.35±2.21	54.61 ± 37.93	4.29±1.06	0.28±0.07	46.87 ± 49.83	9.5 MG, 60°
J094235.02+205208.3	2292-53713-019	39.21 ± 4.55	3.73 ± 1.64	37.94 ± 9.07	0.04 ± 0.02	1.24 ± 13.74	
J094458.92+453901.2	1202-52672-577	15.91±9.10	68.35 ± 44.53	17.41±7.12	0.34±0.14	61.00 ± 90^1	14 MG, 90°
J100005.67+015859.2	500-51994-557	19.74±10.26	48.5 ± 33.13	8.10±3.23	0.34±0.13	4.21 ± 90^1	20 MG, 30°
J100356.32+053825.6	996-52641-295	672.07±118.63	40.8 ± 34.86	667.67±131.71	0.08±0.05	36.67 ± 23.11	900* MG, ...
J100657.51+303338.1	1953-53358-415	1.00±0.10	82.5 ± 30.8	1.30±1.23	−0.37±0.39	14.3 ± 13.1	
J100715.55+123709.5	1745-53061-313	5.41±67.28	68.6 ± 31.88	6.01±2.55	0.40±0.22	50.7 ± 90^1	7 MG, 60°
J100759.80+162349.6	2585 54097 030	19.18 ± 3.36	42.02 ± 17.48	13.50 ± 2.92	-0.22 ± 0.05	33.31 ± 21.38	
J101428.09+365724.3	1954-53357-393	11.09 ± 1.50	48.75 ± 11.72	12.14 ± 2.71	0.05 ± 0.04	56.81 ± 34.40	
J101529.62+090703.8	1237-52762-533	4.09±0.86	49 ± 15.27	1.98±0.35	0.26±0.08	1.48 ± 60.69	5* MG, 90*°

Table C.1: continued.

MWD (SDSS+)	Plate-MJD-FiberID	B_p / MG	i / deg	$B_{\rm off}$ / MG	$z_{\rm off}$ / $r_{\rm WD}$	i / deg	Comments
J101618.37+040920.6	574-52355-166	2.01 ± 0.00^{2}	88.16 ± 104.01	7.24±4.77	0.19±0.16	60.55 ± 63.4	7.5 MG, 30°
J101805.04+011123.5	503-51999-244	99.92 ± 5.90	27.24 ± 6.16	39.87±2.25	0.26 ± 0.02	14.85 ± 3.17	120 MG, ...
J102220.69+272539.8	2350-53765-543	4.91 ± 0.31	27.58 ± 30.65	5.79 ± 2.82	0.39 ± 0.27	54.97 ± 35.63	
J102239.06+194904.3	2374-53765-544	2.94±0.71	49.0 ± 13.0	3.87±1.11	0.40±0.07	51.3 ± 40.3	
J103532.53+212603.5	2376-53770-534	2.96 ± 0.33	49.01 ± 9.51	1.515 ± 0.313	0.39 ± 0.05	0.00 ± 57.44	
J105404.38+593333.3	561-52295-008	17.41±7.90	90.0 ± 25.54	17.60±10.22	0.16 ± 0.05	67.59±59.48	17 MG, 90°
J105628.49+652313.5	490-51929-205	29.27±5.78	41.74 ± 15.24	20.80±4.10	0.29±0.54	5.27 ± 12.8	28 MG, 60°
J105709.81+041130.3	580-52368-274	2.03 ± 0.00^{2}	48.99 ± 7.70	2.48 ± 0.0	41.40 ± 13.13	0.38 ± 0.06	
J111010.50+600141.4	950-52378-568	6.37±2.32	68.6 ± 16.26	6.71±1.58	0.39±0.08	49.08 ± 18.99	6.5 MG, 70°
J111812.67+095241.3	1222-52763-477	3.38±0.72	48.14 ± 32.44	2.67±0.60	0.40±0.10	51.09 ± 43.5	6 MG, 60*°
J112030.34-115051.1	2874-54561-512	8.90 ± 1.02	50.37 ± 20.24	7.72 ± 1.24	0.35 ± 0.10	38.69 ± 34.08	
J112257.10+322327.8	1979-53431-512	11.38±3.42	49.0 ± 12.3	7.46±1.68	0.37±0.11	4.2 ± 6.3	
J112328.49+095619.3	1222-52763-625	$1.21 \pm$ [2]	81.18 ± 17.28	1.50 ± 0.36	0.39 ± 0.06	50.93 ± 90^{1}	
J112852.88-010540.8	326-52375-565	2.00 ± 0.00^{2}	89.4 ± 85.15	2.30±5.02	0.20±0.14	23.15 ± 30.18	3 MG, 60°
J112926.23+493931.8	966-52642-474	5.31±0.64	48.72 ± 6.34	2.43±0.33	0.39±0.09	7.04 ± 12.45	5 MG, 60°
J113215.38+280934.3	2219-53816-329	3.01 ± 0.82	49.00 ± 17.43	2.84 ± 0.43	0.39 ± 0.049	18.60 ± 5.56	
J113357.66+515204.8	879-52365-586	8.64±0.78	74.55 ± 19.87	7.69±0.69	0.39±0.04	47.91 ± 19.99	7.5 MG, 90°
J113756.50+574022.4	1311-52765-421	5.00±0.34	33.45 ± 9.92	2.83±0.25	0.17±0.01	0.07 ± 0.06	9 MG, 60*°
J113839.51-014903.0	327-52294-583	22.71±1.26	54.31 ± 14.41	24.09±1.92	0.21±0.04	50.16 ± 61.4	24 MG, 60°
J114006.37+611008.2	776-52319-042	50.19±17.78	21.8 ± 42.46	52.82±8.82	0.04±0.02	36.88 ± 50.59	58 MG, 20°
J114829.00+482731.2	1446-53080-324	32.47±7.11	80.89 ± 45.93	32.44±2.70	0.17±0.09	69.98 ± 33.06	33 MG, 90°
J115418.14+011711.4	515-52051-126	33.47±2.07	88.14 ± 23.62	25.72±2.51	0.10±0.03	76.03 ± 32.13	32 MG, 45
J115917.39+613914.3	777-52320-69	20.10±6.70	50.63 ± 62.9	10.14±6.89	0.30±0.07	50.63 ± 62.9	15.5 MG, 60°
J120150.10+614257.0	778-52337-264	11.35±1.53	28.04 ± 10.98	7.60±0.87	0.16±0.02	18.59 ± 12.62	20 MG, 90°
J120609.80+081323.7	1623-53089-573	760.63±281.66	30.74 ± 36.38	312.24±73.90	0.24±0.13	25.69 ± 24.66	830* MG, ...
J120728.96+440731.6	1369-53089-048	2.03 ± 0.00^{2}	73.01 ± 29.93	2.07 ± 0.00^{2}	−0.27±0.59	10.16 ± 21.53	2.5 MG, 90°
J121209.31+013627.7	518-52282-285	10.12±0.93	48.8 ± 4.69	10.38±1.02	0.29±0.05	40.65 ± 13.27	13 MG, 80°

Table C.1: continued.

MWD (SDSS+)	Plate-MJD-FiberID	B_p / MG	i / deg	$B_{\rm off}$ / MG	$z_{\rm off}$ / $r_{\rm WD}$	i / deg	Comments
J121635.37-002656.2	288-52000-276	59.70±10.23	37.85 ± 37.52	44.57±7.18	−0.06±0.01	20.15 ± 30.89	61 MG, 90°
J122209.44+001534.0	289-51990-349	14.70±4.70	82.52 ± 90^{1}	16.27±11.39	0.24±0.31	82.52 ± 90^{1}	14 MG, 80°
J122249.14+481133.1	1451-53117-582	8.05±2.24	56.67 ± 13.05	8.70±3.90	−0.38±0.08	53.05 ± 18.28	8 MG, 90*°
J122401.48+415551.9	1452-53112-181	22.36±3.02	66.08 ± 23.71	24.75±5.76	0.26±0.06	58.28 ± 23.89	23* MG, 60°
J123414.11+124829.6	1616-53169-423	4.32±0.27	49.35 ± 9.82	2.40±0.56	0.40±0.05	9.99 ± 2.72	7 MG, 60*°
J124806.38+410427.2	1456-53115-190	7.03±1.19	48.81 ± 9.27	3.61±0.47	0.29±0.06	5.5 ± 10.08	8 MG, 90°
J124836.31+294231.2	2457-54180-112	3.95 ± 0.25	48.93 ± 4.93	-	-	-	
J124851.31-022924.7	337-51997-264	7.36±2.19	48.9 ± 10.11	8.01±1.46	0.40±0.09	49.97 ± 27.39	7 MG, 40°
J125044.42+154957.4	1770-53171-530	20.71±3.66	56.7 ± 11.21	20.30±2.43	0.12±0.02	53.83 ± 38.18	20 MG, 60°
J125416.01+561204.7	1318-52781-299	38.86±9.03	20.97 ± 40.41	36.98±9.20	$0.01 \pm 1e+99$	10.25 ± 21.24	52 MG, 30°
J125434.65+371000.1	1989-53772-041	4.10±0.35	41.9 ± 19.2	4.89±0.42	0.40±0.03	50.1 ± 21.0	
J125715.54+341439.3	2006-53476-332	11.45±0.71	0.5 ± 0.6	13.70±1.69	0.07±0.02	7.7 ± 12.0	
J132002.48+131901.6	1773-53112-011	2.02 ± 0.00^{2}	88.21 ± 80.46	2.64±4.88	−0.38±0.52	6.99 ± 35.73	5 MG, 60°
J133340.34+640627.4	603-52056-112	10.71±1.03	50.29 ± 11.45	13.81±1.36	0.38±0.07	55.7 ± 24.63	13 MG, 60°
J134043.10+654349.2	497-51989-182	4.32±0.76	49.04 ± 9.75	5.28±1.07	0.40±0.06	34.03 ± 6.8	3 MG, 60°
J134820.79+381017.2	2014-53460-236	13.65±2.66	89.4 ± 90^{1}	14.45±4.65	0.22±0.04	54.8 ± 25.3	
J135141.13+541947.4	1323-52797-293	761.00±56.42	74.18 ± 21.65	772.73±94.41	−0.03±0.01	68.25 ± 62.04	760 MG, 20°
J140716.66+495613.7	1671-53446-453	12.49±6.20	88.1 ± 90^{1}	13.20±4.21	0.24±0.10	63.3 ± 81.1	
J141906.19+254356.5	2131-53819-317	2.03±0.10	81.2 ± 8.7	2.56±0.10	0.38±0.03	54.8 ± 10.4	
J142703.40+372110.5	1381-53089-182	27.04±3.20	56.89 ± 12.61	30.59±2.34	0.20±0.02	6.39 ± 22.5	30 MG, 60*°
J143019.05+281100.8	2134-53876-423	9.34±1.44	5.6 ± 4.5	6.25±0.75	0.16±0.03	5.6 ± 4.5	
J143218.26+430126.7	1396-53112-338	1.01 ± 0.00^{2}	78.3 ± 90^{1}	1.48^{1}	−0.39±0.56	55.37 ± 81.19	1.5 MG, 90°
J143235.46+454852.5	1288-52731-449	12.29±6.98	50.62 ± 88.7	13.08±4.78	0.40±0.11	25.84 ± 33.41	10 MG, 30°
J144614.00+590216.7	608-52081-140	4.42±3.79	48.9 ± 31.58	2.18 ± 0.00^{2}	0.40±0.26	4.72 ± 13.13	7 MG, 70°
J145415.01+432149.5	1290-52734-469	2.35±0.88	49.04 ± 17.87	2.15±1.09	0.27±0.11	53.38 ± 22.89	5 MG, ...
J150813.20+394504.9	1398-53146-633	13.23±3.11	37.55 ± 4.17	7.96±0.76	0.40±0.04	24.68 ± 5.61	20 MG, 90°
J151130.17+422023.0	1291-52735-612	22.40±9.41	48.6 ± 19.5	8.37±1.07	0.31±0.06	5.8 ± 21.1	12 MG, 60°

Table C.1: continued.

MWD (SDSS+)	Plate-MJD-FiberID	B_p / MG	i / deg	$B_{\rm off}$ / MG	$z_{\rm off}$ / $r_{\rm WD}$	i / deg	Comments
J151415.65+074446.5	1817-53851-534	35.34 ± 2.80	56.59 ± 17.23	35.88 ± 3.75	0.12 ± 0.043	56.08 ± 22.18	
J151745.19+610543.6	613-52345-446	13.98 ± 7.36	60.07 ± 196.18	6.07 ± 3.24	0.23 ± 0.35	24.86 ± 47.72	17 MG, 30°
J152401.60+185659.2	2794-54537-410	11.96 ± 1.85	41.53 ± 8.79	10.27 ± 3.12	0.11 ± 0.02	33.40 ± 6.58	
J153532.25+421305.6	1052-52466-252	5.27 ± 4.05	0.35 ± 41.68	9.05 ± 5.27	-0.29 ± 0.12	0.13 ± 0.37	4.5 MG, 60°
J153829.29+530604.6	795-52378-637	13.99 ± 3.82	48.96 ± 15.69	15.99 ± 3.03	0.36 ± 0.11	53.36 ± 29.05	12 MG, 30°
J153843.10+084238.2	1725 54266 297	13.20 ± 4.34	41.09 ± 90[1]	$9.63 \pm$	24.98 ± 34.53	0.33 ± 0.08	
J154213.48+034800.4	594-52045-400	8.35 ± 2.60	54.34 ± 35.5	8.25 ± 2.72	0.19 ± 0.16	44.48 ± 30.63	8 MG, 60°
J154305.67+343223.6	1402-52872-145	4.09 ± 2.67	62.06 ± 158.24	4.02 ± 1.09	0.20 ± 0.06	62.67 ± 22.69	
J160437.36+490809.2	622-52054-330	59.51 ± 4.64	40.83 ± 28.87	38.36 ± 3.61	0.14 ± 0.02	7.95 ± 10.24	53 MG, 0°
J164357.02+240201.3	1414-53135-191	2.00 ± 0.00[2]	88.01 ± 56.93	2.41 ± 10.10	-0.34 ± 0.99	18.54 ± 33.29	4 MG, 90°
J164703.24+370910.3	818-52395-026	2.10 ± 0.67	68.39 ± 18.11	2.15 ± 1.21	0.28 ± 0.10	72.53 ± 18.41	2* MG, 90*°
J165029.91+341125.5	1175-52791-482	3.38 ± 0.67	48.78 ± 13.64	3.92 ± 1.05	0.40 ± 0.12	57.74 ± 32.5	3* MG, 0*°
J165203.68+352815.8	820-52438-299	7.37 ± 2.92	48.98 ± 11.77	9.53 ± 3.53	0.40 ± 0.08	51.15 ± 30.36	9.5 MG, 60°
J165249.09+333444.9	1175-52791-095	5.07 ± 4.18	54.25 ± 28.04	5.82 ± 1.90	0.39 ± 0.11	49.85 ± 36.73	
J170400.01+321328.7	976-52413-319	50.11 ± 25.08	54.87 ± 118.04	56.16 ± 8.84	0.27 ± 0.05	0.34 ± 53.88	5 MG, 90*°
J171556.29+600643.9	354-51792-318	2.03 ± 0.00[2]	86.63 ± 31.39	2.03 ± 0.00[2]	-0.19 ± 0.09	60.85 ± 35.29	4.5 MG, 60°
J172045.37+561214.9	367-51997-461	19.79 ± 5.42	56.7 ± 21.33	9.72 ± 2.68	0.31 ± 0.18	0.85 ± 36.62	7 MG, 30°
J172329.14+540755.8	359-51821-415	32.85 ± 3.56	37.43 ± 26.52	28.86 ± 2.71	0.04 ± 0.03	25.4 ± 27.51	35 MG, 10°
J172932.48+563204.1	358-51818-239	27.26 ± 7.04	51.19 ± 67.41	27.17 ± 18.71	0.22 ± 0.10	41.74 ± 90[1]	35 MG, ...
J202501.10+131025.6	2257-53612-167	10.10 ± 1.76	68.5 ± 9.1	10.72 ± 1.71	0.29 ± 0.04	53.7 ± 9.0	
J204626.15-071037.0	635-52145-227	2.03 ± 0.00[2]	49.33 ± 25.34	2.62 ± 0.53	0.40 ± 0.06	54.97 ± 17.54	2 MG, 60°
J205233.52-001610.7	982-52466-019	13.42 ± 3.73	68.57 ± 12.86	1.31 ± 0.23	$0.130.03$	56.97 ± 16.83	13 MG, 80°
J214900.87+004842.8	1107-52968-374	10.09 ± 4.71	46.97 ± 99.7	5.53 ± 2.90	0.22 ± 0.11	5.00 ± 9.13	10 MG, 60°
J214930.74-072812.0	644-52173-350	44.71 ± 1.92	67.27 ± 26.38	44.71 ± 2.80	0.06 ± 0.05	60.11 ± 16.52	42 MG, 30°
J215148.31+125525.5	733-52207-522	20.76 ± 1.39	68.3 ± 12.21	21.80 ± 3.09	0.12 ± 0.03	68.66 ± 19.04	21 MG, 90°
J220435.05+0012 42.9	372-52173-626	1.02 ± 0.10	71.2 ± 90[1]	2.50 ± 5.47	-0.36 ± 0.69	3.1 ± 13.6	
J221828.59-000012.2	374-51791-583	257.54 ± 48.71	17.68 ± 17.63	212.18 ± 34.78	0.06 ± 0.02	17.09 ± 27.01	225 MG, 30°

Table C.1: continued.

MWD (SDSS+)	Plate-MJD-FiberID	B_p / MG	i / deg	$B_{\rm off}$ / MG	$z_{\rm off}$ / $r_{\rm WD}$	i / deg	Comments
J224741.46+145638.8	740-52263-444	42.11 ± 2.83	53.02 ± 9.70	46.95 ± 4.30	-0.17 ± 0.02	33.16 ± 9.84	560 MG, ...
J225726.05+075541.7	2310-53710-420	16.17 ± 2.81	74.9 ± 16.1	17.39 ± 3.21	0.15 ± 0.05	78.5 ± 34.8	
J231951.73+010909.3	382-51816-565	9.35 ± 31.50	48.98 ± 11.36	6.06 ± 1.24	0.40 ± 0.09	12.48 ± 50.66	1.5* MG, 90*°
J232248.22+003900.9	383-51818-421	21.40 ± 3.36	49.00 ± 15.42	21.65 ± 4.48	0.29 ± 0.07	44.174 ± 25.58	19 MG, 60°
J234605.44+385337.6	1883-53271-272	798.1 ± 163.6	2.50 ± 1.07	706.0 ± 238.9	0.12 ± 0.06	86.6 ± 15.4	1000* MG, ...
J234623.69-102357.0	648-52559-142	9.17 ± 1.58	48.78 ± 9.62	2.25 ± 0.29	0.39 ± 0.07	8.42 ± 2.6	2.5 MG, 90*°

Asterisks indicate field strengths or inclinations with uncertainties greater than 10% in Vanlandingham et al. (2005).
[1] The errors are very large.
[2] The errors are very small.

List of Figures

List of Tables

Bibliography

Abazajian, K. N., Adelman-McCarthy, J. K., Agüeros, M. A., et al. 2009, ApJS, 182, 543 56

Abt, H. A. & Cardona, O. 1984, ApJ, 276, 266 67

Adams, J. D., Stauffer, J. R., Monet, D. G., Skrutskie, M. F., & Beichman, C. A. 2001, AJ, 121, 2053 62

Adams, W. S. 1915, PASP, 27, 236 5

Adams, W. S. 1925, Proceedings of the National Academy of Science, 11, 382 5

Althaus, L. G., Córsico, A. H., Isern, J., & García-Berro, E. 2010, A&A Rev., 10 8

Althaus, L. G., García-Berro, E., Isern, J., & Córsico, A. H. 2005, A&A, 441, 689 19, 55, 119, 120, 121

Althaus, L. G., García-Berro, E., Isern, J., Córsico, A. H., & Rohrmann, R. D. 2007, A&A, 465, 249 19, 55, 119, 120

An, D., Terndrup, D. M., Pinsonneault, M. H., et al. 2007, ApJ, 655, 233 60

Anderson, W. 1929, Zeitschrift fur Physik, 54, 433 5

Angel, J. R. P., Borra, E. F., & Landstreet, J. D. 1981, ApJS, 45, 457 2

Araujo-Betancor, S., Gänsicke, B. T., Hagen, H., et al. 2005, A&A, 430, 629 69

Aurière, M., Wade, G. A., Silvester, J., et al. 2007, A&A, 475, 1053 49

Babcock, H. W. 1947a, PASP, 59, 112 6

Babcock, H. W. 1947b, ApJ, 105, 105 6

Babcock, H. W. 1948, PASP, 60, 368 6

Bagnulo, S., Landi Degl'Innocenti, M., & Landi Degl'Innocenti, E. 1996, A&A, 308, 115 50

Bagnulo, S., Landi Degl'Innocenti, M., Landolfi, M., & Mathys, G. 2002, A&A, 394, 1023 50, 51, 131

Bagnulo, S., Landstreet, J. D., Mason, E., et al. 2006, A&A, 450, 777 50

Barstow, M. A., Jordan, S., O'Donoghue, D., et al. 1995, MNRAS, 277, 971 54, 68, 103, 104, 105, 106, 110, 113, 118, 119, 122, 129

Becken, W. & Schmelcher, P. 2001, Phys. Rev. A, 63, 053412 7

Beckers, J. M. 1969, Sol. Phys., 9, 372 33, 34

Bekefi, G. 1966, Radiation Processes in Plasmas (John-Wiley and Sons, Inc., New York . London . Sydney) 33, 73, 92

Benedict, G. F., McArthur, B. E., Feast, M. W., et al. 2007, AJ, 133, 1810 114

Benvenuto, O. G. & Althaus, L. G. 1999, MNRAS, 303, 30 104, 121, 128

Berdyugina, S. V., Berdyugin, A. V., & Piirola, V. 2007, Physical Review Letters, 99, 091101 7

Bergeron, P., Kidder, K. M., Holberg, J. B., et al. 1991, ApJ, 372, 267 70, 125

Bergeron, P., Liebert, J., & Greenstein, J. L. 1990, ApJ, 361, 190 46

Bergeron, P., Ruiz, M., & Leggett, S. K. 1993, ApJ, 407, 733 69

Bertelli, G., Nasi, E., Girardi, L., & Marigo, P. 2009, A&A, 508, 355 60, 123, 125

Bespalov, P. A. & Zheleznyakov, V. V. 1990, Soviet Astronomy Letters, 16, 442 129

Beuermann, K., Euchner, F., Reinsch, K., Jordan, S., & Gänsicke, B. T. 2007, A&A, 463, 647 129

Beuermann, K., Wheatley, P., Ramsay, G., Euchner, F., & Gänsicke, B. T. 2000, A&A, 354, L49 54

Bhatnagar, P. L., Gross, E. P., & Krook, M. 1954, Phys. Rev., 94, 511 95

Blackett, P. M. S. 1947, Nature, 159, 658 6

Born, M., Wolf, E., & Bhatia, A. B. 1959, Principles of Optics (Cambridge University Press, Oxford) 33, 34

Braithwaite, J. & Nordlund, Å. 2006, A&A, 450, 1077 51, 132

Braithwaite, J. & Spruit, H. C. 2004, Nature, 431, 819 51, 132

Brinkworth, C. S., Burleigh, M. R., Wynn, G. A., & Marsh, T. R. 2004, MNRAS, 348, L33 69

Brinkworth, C. S., Marsh, T. R., Morales-Rueda, L., et al. 2005, MNRAS, 357, 333 69

Burleigh, M. R., Jordan, S., & Schweizer, W. 1999, ApJ, 510, L37 68, 103, 105, 106, 110

Burleigh, M. R., Marsh, T. R., Gänsicke, B. T., et al. 2006, MNRAS, 373, 1416 44

Casewell, S. L., Dobbie, P. D., Napiwotzki, R., et al. 2009, MNRAS, 395, 1795 56, 57, 60, 61, 70, 104, 123

Catalán, S., Isern, J., García-Berro, E., & Ribas, I. 2008, MNRAS, 387, 1693 56, 57, 60, 61, 63, 123

Chandrasekhar, S. 1931, ApJ, 74, 81 1, 5, 8, 15

Chandrasekhar, S. 1956, Proceedings of the National Academy of Science, 42, 1 17

Chandrasekhar, S. 1960, Radiative transfer, ed. Chandrasekhar, S. 20

Chandrasekhar, S. 1964, ApJ, 140, 417 16, 122

Chandrasekhar, S. & Prendergast, K. H. 1956, Proceedings of the National Academy of Science, 42, 5 17

Chandrasekhar, S. & Tooper, R. F. 1964, ApJ, 139, 1396 16, 122

Chanmugam, G. 1980, ApJ, 241, 1122 82

Chanmugam, G., Wu, K., Courtney, M. W., & Barrett, P. E. 1989, ApJS, 71, 323 73, 82

Chelouche, D., Rabadán, R., Pavlov, S. S., & Castejón, F. 2009, ApJS, 180, 1 132

Chow, T. L. 1969, Astrophys. Lett., 3, 85 6

Claver, C. F., Liebert, J., Bergeron, P., & Koester, D. 2001, ApJ, 563, 987 56, 57, 61

Cohen, J. M., Lapidus, A., & Cameron, A. G. W. 1969, Ap&SS, 5, 113 16, 128

Cowling, T. G. 1945, MNRAS, 105, 166 7

Cox, A. N. 2000, Allen's astrophysical quantities, ed. Cox, A. N. 112

Dahn, C. C., Bergeron, P., Liebert, J., et al. 2004, ApJ, 605, 400 104

Davis, D. S., Richer, H. B., King, I. R., et al. 2008, MNRAS, 383, L20 62

Debes, J. H., López-Morales, M., Bonanos, A. Z., & Weinberger, A. J. 2006, ApJ, 647, L147 44

Deetjen, J. L., Dreizler, S., Jordan, S., & Werner, K. 2003, in Astronomical Society of the Pacific Conference Series, Vol. 288, Stellar Atmosphere Modeling, ed. I. Hubeny, D. Mihalas, & K. Werner, 617–+ 24

Delande, D., Bommier, A., & Gay, J. C. 1991, Physical Review Letters, 66, 141 32

Dobbie, P. D., Napiwotzki, R., Burleigh, M. R., et al. 2006, MNRAS, 369, 383 56, 104

Dominguez, I., Straniero, O., Tornambe, A., & Isern, J. 1996, ApJ, 472, 783 56, 71, 123

Donati, J. F., Achilleos, N., Matthews, J. M., & Wesemael, F. 1994, A&A, 285, 285 47

Dufour, P., Fontaine, G., Liebert, J., Schmidt, G. D., & Behara, N. 2008, ApJ, 683, 978 7

Dufour, P., Liebert, J., Fontaine, G., & Behara, N. 2007, Nature, 450, 522 7

Eggen, O. J. & Greenstein, J. L. 1965, ApJ, 142, 925 57

Eisenstein, D. J., Liebert, J., Harris, H. C., et al. 2006, ApJS, 167, 40 7

Euchner, F., Jordan, S., Beuermann, K., Gänsicke, B. T., & Hessman, F. V. 2002, A&A, 390, 633 38, 40, 41, 44, 106, 110

Euchner, F., Jordan, S., Beuermann, K., Reinsch, K., & Gänsicke, B. T. 2006, A&A, 451, 671 41, 44, 129

Euchner, F., Reinsch, K., Jordan, S., Beuermann, K., & Gänsicke, B. T. 2005, A&A, 442, 651 41, 44, 129

Farihi, J., Becklin, E. E., & Zuckerman, B. 2005, ApJS, 161, 394 65, 69

Farihi, J., Becklin, E. E., & Zuckerman, B. 2008, ApJ, 681, 1470 44, 104, 126

Fellhauer, M., Lin, D. N. C., Bolte, M., Aarseth, S. J., & Williams, K. A. 2003, ApJ, 595, L53 62

Fendt, C. & Dravins, D. 2000, Astronomische Nachrichten, 321, 193 129, 132

Ferrario, L., Vennes, S., Wickramasinghe, D. T., Bailey, J. A., & Christian, D. J. 1997, MNRAS, 292, 205 2, 68, 105, 106, 110, 119, 123, 125, 128

Ferrario, L., Wickramasinghe, D., Liebert, J., & Williams, K. A. 2005a, MNRAS, 361, 1131 56

Ferrario, L., Wickramasinghe, D., Liebert, J., & Williams, K. A. 2005b, MNRAS, 361, 1131 124

Finley, D. S. & Koester, D. 1997, ApJ, 489, L79+ 67

Forster, H., Strupat, W., Rosner, W., et al. 1984, Journal of Physics B Atomic Molecular Physics, 17, 1301 26, 29

Fowler, R. H. 1926, MNRAS, 87, 114 5

Friedrich, S., Ostreicher, R., Ruder, H., & Zeller, G. 1994, A&A, 282, 179 40, 58

Fukugita, M., Ichikawa, T., Gunn, J. E., et al. 1996, AJ, 111, 1748 38

Gänsicke, B. T., Euchner, F., & Jordan, S. 2002, A&A, 394, 957 3, 37, 38, 46, 48, 58, 66, 166

Gänsicke, B. T., Koester, D., Girven, J., Marsh, T. R., & Steeghs, D. 2010, Science, 327, 188 7

Gänsicke, B. T., Schmidt, G. D., Jordan, S., & Szkody, P. 2001, ApJ, 555, 380 41

García-Berro, E., Ritossa, C., & Iben, Jr., I. 1997, ApJ, 485, 765 7, 123, 128

Garstang, R. H. 1977, Reports on Progress in Physics, 40, 105 26, 31

Garstang, R. H. & Kemic, S. B. 1974, Ap&SS, 31, 103 29

Gatewood, G. & de Jonge, J. K. 1994, ApJ, 428, 166 60

Giclas, H. L., Burnham, R., & Thomas, N. G. 1967, Lowell Observatory Bulletin, 7, 49 65

Ginzburg, V. 1964, The Propagation of Electromagnetic Waves in Plasmas (Translated by J.B. Sykes and R.J. Tayler, Pergamon Press, Oxford, London, Edinbugh, New York, Paris, Frankfurt.) 74, 82, 94, 95

Ginzburg, V. L., Zheleznyakov, V. V., & Zaitsev, V. V. 1969, Ap&SS, 4, 464 6

Girven, J., Gänsicke, B. T., Külebi, B., et al. 2010, MNRAS, 404, 159 3, 64, 65, 66, 68

Glenn, J., Liebert, J., & Schmidt, G. D. 1994, PASP, 106, 722 68

Greenstein, J. L., Henry, R. J. W., & Oconnell, R. F. 1985, ApJ, 289, L25 7

Hall, P. B. & Maxwell, A. J. 2008, ApJ, 678, 1292 7

Hamada, T. & Nakamura, Y. 1973, PASJ, 25, 527 29

Hamada, T. & Salpeter, E. E. 1961, ApJ, 134, 683 8, 12, 16, 128

Hansen, B. M. S., Kulkarni, S., & Wiktorowicz, S. 2006, AJ, 131, 1106 126

Hardorp, J., Shore, S. N., & Wittmann, A. 1976, in IAU Colloq. 32: Physics of Ap Stars, ed. W. W. Weiss, H. Jenkner, & H. J. Wood, 419–+ 24

Harris, H. C., Liebert, J., Kleinman, S. J., et al. 2003, AJ, 126, 1023 38

Henry, R. J. W. & Oconnell, R. F. 1984, ApJ, 282, L97+ 26, 29

Henry, R. J. W. & Oconnell, R. F. 1985, PASP, 97, 333 26, 29

Heyl, J. S. & Thirumalai, A. 2010, MNRAS, 407, 590 29

Hillebrandt, W. & Niemeyer, J. C. 2000, ARA&A, 38, 191 2

Høg, E., Kuzmin, A., Bastian, U., et al. 1998, A&A, 335, L65 113

Holberg, J. B. & Bergeron, P. 2006, AJ, 132, 1221 19, 41, 44, 55, 60, 66, 119, 120

Howell, D. A., Sullivan, M., Nugent, P. E., et al. 2006, Nature, 443, 308 133

Huang, K. 1987, Statistical Mechanics, 2nd Edition, ed. Huang, K. 93

Iben, Jr., I., Ritossa, C., & Garcia-Berro, E. 1997, ApJ, 489, 772 7

Iben, Jr., I. & Tutukov, A. V. 1984, ApJS, 54, 335 63, 125, 127

Iben, Jr., I. & Tutukov, A. V. 1985, ApJS, 58, 661 125, 126

Jacobs, J. A. 1987, Geomagnetism, Volume 1 (Academic Press, 1987, University of California) 40

Jefferys, W. H., Fitzpatrick, M. J., & McArthur, B. E. 1988, Celestial Mechanics, 41, 39 114

Jordan, S. 1992, A&A, 265, 570 7, 31, 38, 41, 58, 74, 104, 106, 129

Jordan, S. 2001, in Astronomical Society of the Pacific Conference Series, Vol. 226, 12th European Workshop on White Dwarfs, ed. J. L. Provencal, H. L. Shipman, J. MacDonald, & S. Goodchild, 269–+ 37

Jordan, S. 2009, ArXiv e-prints 49

Jordan, S. & Burleigh, M. R. 1999, in Astronomical Society of the Pacific Conference Series, Vol. 169, 11th European Workshop on White Dwarfs, ed. S.-E. Solheim & E. G. Meistas, 235–+ 104, 105

Jordan, S., O'Connell, R. F., & Koester, D. 1991, A&A, 242, 206 34, 94, 101, 106, 107

Jordan, S. & Schmidt, H. 2003, in Astronomical Society of the Pacific Conference Series, Vol. 288, Stellar Atmosphere Modeling, ed. I. Hubeny, D. Mihalas, & K. Werner, 625–+ 25, 38, 58

Kalirai, J. S., Bergeron, P., Hansen, B. M. S., et al. 2007, ApJ, 671, 748 56

Kalirai, J. S., Hansen, B. M. S., Kelson, D. D., et al. 2008, ApJ, 676, 594 56, 67

Kalirai, J. S., Richer, H. B., Reitzel, D., et al. 2005, ApJ, 618, L123 71

Kaplan, S. A. 1949, Zhurnal Eksperimental noi i Teoreticheskoi Fiziki, 19, 951 16

Kara, S. M. & McDowell, M. R. C. 1981, Journal of Physics B Atomic Molecular Physics, 14, 1719 31

Kawka, A., Vennes, S., Schmidt, G. D., Wickramasinghe, D. T., & Koch, R. 2007, ApJ, 654, 499 2, 37, 49, 103, 104, 110, 119, 122

Kemp, J. C. 1970, ApJ, 162, 169 7, 74

Kemp, J. C. & Swedlund, J. B. 1970, ApJ, 162, L67+ 74

Kharchenko, N. V., Piskunov, A. E., Röser, S., Schilbach, E., & Scholz, R. 2005, A&A, 438, 1163 56, 57

Kleinman, S. J., Harris, H. C., Eisenstein, D. J., et al. 2004, ApJ, 607, 426 7, 38

Koester, D. 2002, A&A Rev., 11, 33 1

Koester, D. & Chanmugam, G. 1990, Reports on Progress in Physics, 53, 837 16, 122

Koester, D., Napiwotzki, R., Voss, B., Homeier, D., & Reimers, D. 2005, A&A, 439, 317 65

Koester, D. & Weidemann, V. 1980, A&A, 81, 145 1, 56

Külebi, B., Jordan, S., Euchner, F., Gänsicke, B. T., & Hirsch, H. 2009, A&A, 506, 1341 3, 7, 55, 103

Külebi, B., Jordan, S., Nelan, E., Bastian, U., & Altmann, M. 2010, A&A, *in press*, arXiv:1007.4978 4

Lamb, F. K. & Sutherland, P. G. 1971, in Conference on Line Formation in the Presence of Magnetic Fields, High Altitude Observatory, Boulder, Colorado 32, 73, 92

Lamb, F. K. & Sutherland, P. G. 1974, in IAU Symposium, Vol. 53, Physics of Dense Matter, ed. C. J. Hansen, 265–+ 30, 31, 32, 73, 99

Landau, L. 1932, Phys. Z. Sowjetunion, 1, 285 1, 5

Landau, L. 1938, Nature, 141, 333 5

Landau, L. D. & Lifshitz, E. M. 1968, Statistical Physics (Pergamon Press, Oxford, 1968, second revised and enlarged edition) 9, 12, 13

Landau, L. D. & Lifshitz, E. M. 1977, Quantum Mechanics (Pergamon Press, Oxford, 1977, third edition) 31

Landolfi, M., Bagnulo, S., & Landi Degl'Innocenti, M. 1998, A&A, 338, 111 50

Landstreet, J. D. 1987, MNRAS, 225, 437 129

Lang, K. R. 1992, Astrophysical Data I. Planets and Stars., ed. Lang, K. R. 112

Latter, W. B., Schmidt, G. D., & Green, R. F. 1987, ApJ, 320, 308 37

Li, N. & Thakar, A. R. 2008, Computing in Science and Engineering, 10, 18 57

Liebert, J. 1988, PASP, 100, 1302 2, 6

Liebert, J., Bergeron, P., & Holberg, J. B. 2003, AJ, 125, 348 2, 37, 71

Liebert, J., Bergeron, P., Schmidt, G. D., & Saffer, R. A. 1993a, ApJ, 418, 426 46

Liebert, J., Bergeron, P., Schmidt, G. D., & Saffer, R. A. 1993b, ApJ, 418, 426 67, 68

Liebert, J., Wickramasinghe, D. T., Schmidt, G. D., et al. 2005, AJ, 129, 2376 65

Lorén-Aguilar, P., Isern, J., & García-Berro, E. 2009, A&A, 500, 1193 126

Luyten, W. J. 1962, in The Observatory, Univ. Minnesota, Minneapolis,1953, 31, 1 (1962), 1–+ 57

Marigo, P. 2001, A&A, 370, 194 56

Marsh, M. C., Barstow, M. A., Buckley, D. A., et al. 1997, MNRAS, 287, 705 70, 125

Martin, B. & Wickramasinghe, D. T. 1979, MNRAS, 189, 69 24, 33, 97

Martin, B. & Wickramasinghe, D. T. 1981, MNRAS, 196, 23 34

Martin, B. & Wickramasinghe, D. T. 1982, MNRAS, 200, 993 101

Maxted, P. F. L., Marsh, T. R., Moran, C. K. J., & Han, Z. 2000, MNRAS, 314, 334 69

Meggitt, S. M. A. & Wickramasinghe, D. T. 1982, MNRAS, 198, 71 82

Merani, N., Main, J., & Wunner, G. 1995, A&A, 298, 193 32, 73

Mermilliod, J., Turon, C., Robichon, N., Arenou, F., & Lebreton, Y. 1997, in ESA Special Publication, Vol. 402, Hipparcos - Venice '97, ed. R. M. Bonnet, E. Høg, P. L. Bernacca, L. Emiliani, A. Blaauw, C. Turon, J. Kovalevsky, L. Lindegren, H. Hassan, M. Bouffard, B. Strim, D. Heger, M. A. C. Perryman, & L. Woltjer, 643–650 60

Mermilliod, J., Weis, E. W., Duquennoy, A., & Mayor, M. 1990, A&A, 235, 114 62

Mestel, L. 1965, Stars in Stellar Systems, ed. Aller, L. H. & McLaughlin D. B. 17, 18, 121, 126

Mészáros, P. 1992, High-energy radiation from magnetized neutron stars., ed. Mészáros, P. 73

Mihalas, D. 1978, Stellar atmospheres /2nd edition/, ed. Hevelius, J. 18, 26, 31

Minkowski, R. 1938, Ann. Rep. Mt. Wilson Obs., 55, 44 6

Mitrofanov, I. G. & Pavlov, G. G. 1982, MNRAS, 200, 1033 129

Mochkovitch, R. & Livio, M. 1990, A&A, 236, 378 126

Monet, D. G., Levine, S. E., Canzian, B., et al. 2003, AJ, 125, 984 57

Moran, C., Maxted, P., Marsh, T. R., Saffer, R. A., & Livio, M. 1999, MNRAS, 304, 535 65

Muslimov, A. G., van Horn, H. M., & Wood, M. A. 1995, ApJ, 442, 758 48, 51

Należyty, M. & Madej, J. 2004, A&A, 420, 507 71

Nauenberg, M. 1972, ApJ, 175, 417 18

Nelan, E. 2010, Fine Guidance Sensor Instrument Handbook, Version 17.0 (Baltimore, MD: STScI) 111

Nelan, E. & Makidon, R. 2002, HST Data Handbook: Introduction to Reducing HST Data, Volume 1, Version 4.0, ed. Mobasher, B. 114

Nelan, E. P. 2007, AJ, 134, 1934 68, 69

Nelan, E. P., Lupie, O. L., McArthur, B., et al. 1998, in Presented at the Society of Photo-Optical Instrumentation Engineers (SPIE) Conference, Vol. 3350, Society of Photo-Optical Instrumentation Engineers (SPIE) Conference Series, ed. R. D. Reasenberg, 237–247 111

Oestreicher, R., Seifert, W., Friedrich, S., et al. 1992, A&A, 257, 353 110

Oppenheimer, J. R. & Volkoff, G. M. 1939, Physical Review, 55, 374 5

Ostriker, J. P. & Bodenheimer, P. 1968, ApJ, 151, 1089 8, 16

Ostriker, J. P., Bodenheimer, P., & Lynden-Bell, D. 1966, Physical Review Letters, 17, 816 16

Ostriker, J. P. & Hartwick, F. D. A. 1968, ApJ, 153, 797 6, 8, 17, 124, 127

Ostriker, J. P. & Mark, J. 1968, ApJ, 151, 1075 8

Oswalt, T. D., Hintzen, P. M., & Luyten, W. J. 1988, ApJS, 66, 391 63

Pacholczyk, A. G. 1977, Radio galaxies (Pergamon Press, University of Michigan, 1977) 34

Pavlov, G. G., Mitrofanov, I. G., & Shibanov, I. A. 1980, Ap&SS, 73, 63 82, 90, 97

Perryman, M. A. C., Brown, A. G. A., Lebreton, Y., et al. 1998, A&A, 331, 81 60

Pickles, A. J. 1998, PASP, 110, 863 112

Piro, A. L. 2008, ApJ, 679, 616 71, 133

Piskunov, A. E., Schilbach, E., Kharchenko, N. V., Röser, S., & Scholz, R. 2007, A&A, 468, 151 62

Piskunov, A. E., Schilbach, E., Kharchenko, N. V., Röser, S., & Scholz, R. 2008, A&A, 477, 165 57, 62

Pols, O. R., Schroder, K., Hurley, J. R., Tout, C. A., & Eggleton, P. P. 1998, MNRAS, 298, 525 67, 68

Portegies Zwart, S. F., McMillan, S. L. W., Hut, P., & Makino, J. 2001, MNRAS, 321, 199 57

Praddaude, H. C. 1972, Phys. Rev. A, 6, 1321 29

Preuss, O., Solanki, S. K., Haugan, M. P., & Jordan, S. 2005, Phys. Rev. D, 72, 042001 105

Putney, A. 1995, ApJ, 451, L67+ 44

Ramaty, R. 1969, ApJ, 158, 753 25, 82

Ramsey, W. H. 1950, MNRAS, 110, 444 15

Rebassa-Mansergas, A., Gänsicke, B. T., Rodríguez-Gil, P., Schreiber, M. R., & Koester, D. 2007, MNRAS, 382, 1377 65

Rechenberg, I. 1994, Werkstatt Bionik und Evolutionstechnik No. 1 (Stuttgart: frommann-holzboog 40

Reimers, D., Jordan, S., Beckmann, V., Christlieb, N., & Wisotzki, L. 1998, A&A, 337, L13 46

Ritossa, C., Garcia-Berro, E., & Iben, Jr., I. 1996, ApJ, 460, 489 7, 123, 128

Roesner, W., Wunner, G., Herold, H., & Ruder, H. 1984, Journal of Physics B Atomic Molecular Physics, 17, 29 7, 26, 29

Russell, H. N. 1914, Popular Astronomy, 22, 275 5, 7

Saakyan, G. S. & Vartanyan, Y. L. 1964, AZh, 41, 193 16

Saio, H. & Nomoto, K. 2004, ApJ, 615, 444 7

Sakurai, J. J. & Tuan, S. F. 1994, Modern Quantum Mechanics, ed. Tuan, S. F. (Addison Wesley Pub. Co.) 28

Salaris, M., Serenelli, A., Weiss, A., & Miller Bertolami, M. 2009, ApJ, 692, 1013 104, 123

Salpeter, E. E. 1961, ApJ, 134, 669 15

Salpeter, E. E. & Zapolsky, H. S. 1967, Physical Review, 158, 876 15

Schmidt, G. D., Bergeron, P., Liebert, J., & Saffer, R. A. 1992, ApJ, 394, 603 104

Schmidt, G. D., Harris, H. C., Liebert, J., et al. 2003, ApJ, 595, 1101 3, 37, 38, 41, 44, 48, 49, 50, 166

Schmidt, G. D., Liebert, J., & Smith, P. S. 1998, AJ, 116, 451 67, 68

Schmidt, G. D., Szkody, P., Silvestri, N. M., et al. 2005, ApJ, 630, L173 44

Schmidt, G. D., Vennes, S., Wickramasinghe, D. T., & Ferrario, L. 2001, MNRAS, 328, 203 46

Schmidt, G. D., West, S. C., Liebert, J., Green, R. F., & Stockman, H. S. 1986, ApJ, 309, 218 41

Segretain, L., Chabrier, G., & Mochkovitch, R. 1997, ApJ, 481, 355 104

Shapiro, S. L. & Teukolsky, S. A. 1983, Black holes, white dwarfs, and neutron stars: The physics of compact objects, ed. Shapiro, S. L. & Teukolsky, S. A. 17, 18, 124, 127

Shorlin, S. L. S., Wade, G. A., Donati, J.-F., et al. 2002, A&A, 392, 637 50

Smith, E. R., Henry, R. J., Surmelian, G. L., O'Connell, R. F., & Rajagopal, A. K. 1972, Phys. Rev. D, 6, 3700 29

Smith, S. 1966, Magneto-Optics in Crystals (Herausg. S. Flügge) 34

Somerville, R. S. & Primack, J. R. 1999, MNRAS, 310, 1087 55

Spitzer, L. 1956, Physics of Fully Ionized Gases, ed. Spitzer, L. 75, 94

Stepien, K. 1978, A&A, 70, 509 129

Stoughton, C., Lupton, R. H., Bernardi, M., et al. 2002, AJ, 123, 485 38

Takeda, Y. 1991, PASJ, 43, 823 25

Thackeray, A. D. 1947, MNRAS, 107, 463 6

Thirumalai, A. & Heyl, J. S. 2009, Phys. Rev. A, 79, 012514 29

Thompson, C. & Duncan, R. C. 1993, ApJ, 408, 194 2

Tillich, A., Geier, S., Heber, U., et al. 2009, ArXiv e-prints; arXiv:0901.1030 38

Tout, C. A., Wickramasinghe, D. T., Liebert, J., Ferrario, L., & Pringle, J. E. 2008, MNRAS, 387, 897 2, 3, 51, 70

Unno, W. 1956, PASJ, 8, 108 24

van den Bergh, S. & Tammann, G. A. 1991, ARA&A, 29, 363 55

Vanlandingham, K. M., Schmidt, G. D., Eisenstein, D. J., et al. 2005, AJ, 130, 734 3, 37, 38, 41, 44, 48, 166, 171

Vennes, S., Ferrario, L., & Wickramasinghe, D. T. 1999, MNRAS, 302, L49 69

Vennes, S. & Kawka, A. 2008, MNRAS, 389, 1367 2, 104, 133

Vennes, S., Schmidt, G. D., Ferrario, L., et al. 2003, ApJ, 593, 1040 68, 69, 74, 103, 105, 106, 125, 128

Vornanen, T., Berdyugina, S. V., Berdyugin, A. V., & Piirola, V. 2010, ApJ, 720, L52 7

Watson, G. N. 1966, A Treatise on the Theory of Bessel Functions (Cambridge University Press, Cambridge, UK) 87

Webbink, R. F. 1984, ApJ, 277, 355 125

Wegner, G. 1973, MNRAS, 165, 271 63

Weidemann, V. 1977, A&A, 59, 411 55, 56, 62

Weidemann, V. 2000, A&A, 363, 647 1, 55, 128

Weidemann, V., Jordan, S., Iben, Jr., I., & Casertano, S. 1992, AJ, 104, 1876 57, 62

Wentzel, D. G. 1961, ApJ, 133, 170 17

West, S. C. 1989, ApJ, 345, 511 32

Wickramasinghe, D. T. & Ferrario, L. 1988, ApJ, 327, 222 7

Wickramasinghe, D. T. & Ferrario, L. 2000, PASP, 112, 873 1, 37

Wickramasinghe, D. T. & Ferrario, L. 2005, MNRAS, 356, 1576 2, 49, 50, 124

Williams, K. A. 2002, PhD thesis, UNIVERSITY OF CALIFORNIA, SANTA CRUZ 62

Winget, D. E., Hansen, C. J., Liebert, J., et al. 1987, ApJ, 315, L77 2

Wittmann, A. 1974, Sol. Phys., 35, 11 34, 101

Woltjer, L. 1960, ApJ, 131, 227 17

Wood, M. A. 1992, ApJ, 386, 539 104

Wood, M. A. 1995, in Lecture Notes in Physics, Berlin Springer Verlag, Vol. 443, White Dwarfs, ed. D. Koester & K. Werner, 41–+ 19, 55, 60, 61, 104, 119, 120, 121, 128

Wunner, G., Roesner, W., Herold, H., & Ruder, H. 1985, A&A, 149, 102 26, 29

Wunner, G. & Ruder, H. 1987, Phys. Scr, 36, 291 26, 29

Yafet, Y. 1956, Journal of Physics and Chemistry of Solids, 1, 137 29

Yoon, S. & Langer, N. 2005, A&A, 435, 967 126, 133

Zacharias, N., Urban, S. E., Zacharias, M. I., et al. 2004, AJ, 127, 3043 56

Zhang, E.-H., Robinson, E. L., & Nather, R. E. 1986, ApJ, 305, 740 41

Zhao, L. B. & Stancil, P. C. 2006, Phys. Rev. A, 74, 055401 58, 73

Zhao, L. B. & Stancil, P. C. 2007, ApJ, 667, 1119 32

Zhelezniakov, V. V. & Zlotnik, E. I. 1980, in IAU Symposium, Vol. 86, Radio Physics of the Sun, ed. M. R. Kundu & T. E. Gergely, 87–99 90

Zheleznyakov, V. V., Koryagin, S. A., & Serber, A. V. 1999, Astronomy Letters, 25, 437 95

Zheleznyakov, V. V. & Serber, A. V. 1994, ApJS, 90, 783 129

Zheleznyakov, V. V., Serber, A. V., & Kuijpers, J. 1996, A&A, 308, 465 129

Acknowledgements

First and foremost I want to thank my supervisor Stefan Jordan, who gave me a job, a topic to work on, his time, supervision and most importantly my scientific "trade". All that will be left with me in the end will not be papers, not the thesis but the skills and experience that I gained in the meanwhile, hence I will forever be indebted to him for the things I have learned during this process.

That being said, the second in line are my scientific collaborators: Fabian Euchner, without his code and help during the initial phases this work would not have been possible. Boris Gänsicke, provided us not just with the much needed observations, but throughout my research he was one of the major motivators with his invaluable questions and wide perspective. I thank Tommi Vornanen whom I deeply respect as an observer, as an astronomical laborer, but I am grateful mostly for his unending enthusiasm which provided my work with very interesting questions. Finally I would like to thank George Pavlov for his brief but important guidance during the plasma calculations.

Wolfgang Löffler and Robert Schmidt welcomed me to Astronomisches Rechen-Institut (ARI) and helped me in their best during the initial stages of my experience. Without their patience and good suggestions, my scientific experience in Heidelberg would not have been this positive. On this note, I would like to mention my thesis committee Peter Schmelcher, Uli Bastian and during the late stages Thorsten Lisker who were attentive to my questions and interested in my work both inside and outside the committee duties. Their advice was invaluable.

It is hard to mention all the support I received from my fellow colleagues, be it scientific resulting from random discussions or specific problems, be it personal support: Katrin Jordi, Shoko Jin, Sonia Duffau, Raoul Haschke, Katharina Glatt I am grateful to you all. I should especially mention Raoul for single-handedly integrating me into the German society and Katharina Glatt in addition to her friendship of everything "nerdy," for her gracious help with German, consisting the zusammenfassung of this work.

Additionally I would like to thank all the administrative and technical help in ARI: Saskia Mayer, Diana Schwalbe and Hildrun Pisch who were always more than helpful to the problems of an immigrant fumbling his way through the German language. And one should never forget Peter Schwekendiek's diligent work on maintaining our servers, without which no scientific activity would be possible; Gernot Burkhardt's maintenance of the printers and finally Markus Demleitner, who is ever helpful without hesitation on both technical and employment related issues.

If I start with the personal aspect of my life that contributed the basis for this work to happen, I should start with thanking my mother Oya Külebi, for her education that brought me to this day and her understanding for the lonely and thorny path I chose for my life.

My dear friend and housemate Thomas Splettößer whom I appreciate his patience with

my non-existence in house related issues, but more importantly I thank for the arts that I learned from him; be it prop building or poster designing, and most importantly the ability to learn something from scratch and create something phenomenal in the end. Your accomplishments are and will be a constant source of inspiration for me.

I think I should not be afraid to say that, Özgen Deniz, Giulia Vannoni and most importantly Federica Capranico were the main people who made my life bearable in Heidelberg. I thank you all for sharing a part of your lives with me, for good or for worse.

And finally, I need to mention my partners in crime, the *post-modern immigrant workers* with whom I shared my misery and my euphoria; firstly Denija Crnojevic for her wisdom that she is unaware of and Giovanni Natale for his lust-for-life hidden under his *para-* behaviour. I appreciate the company of fellow Turkish bio friends; Ebru Ercan and Güneş Bozkurt with whom I had the regular cultural relief (a.k.a. *deer talk*). Additionally within this group I am proud to mention my comrades at arms; Kelly Foyle, Patrick Plötz and lastly but certainly not the least Massimo Viola. They are the truly patient ones who had to put up with my ups and downs, listen to my adventures and misadventures on all the aspects of my PhD life. Scientifically; Kelly you have been always been an inspiration with your self-discipline and perspective of science, while Patrick and Massimo, you have never been afraid to sit down and *derive*, and most importantly ask the right questions. Personally; in addition to Kelly and Patrick's camaraderie, Massimo gets a special mention for *sacrificing himself for my sins*. And finally politically; without their determination, interest and motivation we could not have accomplished the little we did. Thanks for playing "revolution" with me. Without your sobriety and affection my friends provided during this phase of my life, I can not imagine what kind of a person I would have turned out to be.

Heidelberg, October 2010